


國立交通大學

電子工程學系 電子研究所

博 士 論 文

藉助催化金屬與元件結構以增進奈米碳管場發
射特性之研究



**Study on the Improvements of Field-Emission
Characteristics of the Carbon Nanotubes via
Modifying the Catalyst and Device Structures**

研 究 生：賴瑞霖

Rui-Ling Lai

指 導 教 授：鄭晃忠 博士

Dr. Huang-Chung Cheng

中 華 民 國 九 十 六 年 九 月

藉助催化金屬與元件結構以增進奈米碳管場發射特性之研究

**Study on the Improvements of Field-Emission Characteristics of
the Carbon Nanotubes via Modifying the Catalyst and Device
Structures**

研究生：賴瑞霖

Student : Rui-Ling Lai

指導教授：鄭晃忠 博士

Advisor : Dr. Huang-Chung Cheng

國立交通大學

電子工程學系 電子研究所

博士論文

A Dissertation

Submitted to Department of Electronics Engineering
and Institute of Electronics

College of Electrical and Computer Engineering
National Chiao Tung University

In Partial Fulfillment of the Requirements

for the Degree of

Doctor of Philosophy

in Electronics Engineering

2006

Hsinchu, Taiwan, Republic of China

中華民國 九十六 年 九 月


藉助催化金屬與元件結構以增進奈米碳管場發射特性之研究

研究生：賴瑞霖

指導教授：鄭晃忠 博士

國立交通大學電子工程學系暨電子研究所博士班

摘要



在本篇論文當中，我們利用奈米碳管為場發射元件之電子源，並藉由改善催化金屬材料及其元件結構以改善場發射特性。於此研究中，我們運用金屬鈦覆蓋或摻雜於催化金屬鐵以控制催化金屬之活性、大小以及分佈，進而增進場發射電流密度、增強元件可靠度或是改善場發射電流之均勻性。此外，我們亦藉由微影的方式製作柱狀之奈米碳管場發射源，藉由人造結構來得到均勻之場發射電子源分佈，並有效控制柱狀場發射源之間距以降低電場遮蔽效應，而得到最佳化之場發射電流以及啟始電場。最後，於三極場發射元件中加入一層氮化矽以阻絕閘極與陰極間之漏電，進而改善三極場發射元件效率不佳之缺點。

首先，在場發射電流密度方面，對於奈米碳管而言，影響其電流密度之主要原因在於過高的奈米碳管密度所導致的電場屏蔽效應。對此，我們在經過氫氣前處理之鐵奈米顆粒上沈積一層微薄之金屬鈦，藉助鈦阻擋含碳之反應物質進入鐵催化金屬進而抑制奈米碳管之生成以降低奈米碳管的密度。藉由沈積不同厚度之金屬鈦，我們可以有效地控制奈米碳管之密度以增進其場發射電流密度並降低其啟始電場。此外，藉由所沈積之金屬鈦在奈米碳管成長過程中受熱部分融化並包圍鐵催化金屬奈米顆粒，我

們發現元件在量測過程所發生之電流崩潰現象有效地被抑制了，而其場發射電流在高電場下之劣化現象亦有效地被改善，針對此一結果，我們認為金屬鈦之包圍使得奈米碳管與基板之間的附著性被增強且降低其接觸電阻，因此改善了元件的可靠度。

然而，雖然電流密度與可靠度被改善了，其均勻性不佳之現象依然無法得到解決，是以我們利用金屬鈦與催化金屬鐵共鍍作為成長奈米碳管之催化金屬層，藉此使催化金屬顆粒之形成更為均勻，並藉由金屬鈦抑制催化金屬顆粒的聚集以得到小尺寸、且尺寸均勻之催化金屬奈米顆粒，最後成長出長度均勻之奈米碳管並在塗佈螢光粉之陽極板上得到均勻之光源。此外，因為鐵催化金屬顆粒於催化金屬層中受熱析出而形成部分被埋於催化金屬層中之結構，其可靠度亦大為改善。

接著，我們利用微影的方式以鐵鈦共鍍為催化金屬製作柱狀奈米碳管之場發射元件。藉由鐵鈦共鍍以得到均勻、筆直且具有穩定場發射電流之奈米探管；利用微影控制其間距，以有效降低電場屏蔽效應並且避免距離過大而減少場發射區域之總面積。是以，得到一個均勻分佈且具有較高場發射電流密度之場發射電子源。

最後，針對三極式場發射電子元件效率不佳之缺點，我們在元件中增加一層氮化矽絕緣層於閘極之上或閘極之下，以阻絕由陰極被閘極電場所吸引出來的電子電流，藉此改善電流效率以及功率效能。

在本論文中，我們提出了簡單、便宜且不會對場發射源奈米碳管造成結構損傷之方式來改善場發射電子元件之場發射特性。是以相當具有應用於場發射平面顯示器或是液晶螢幕背光模組之潛力。

Study on the Improvements of Field-Emission Characteristics of the Carbon Nanotubes via Modifying the Catalyst and Device Structures

Student: Rui-Ling Lai

Advisor: Dr. Huang-Chung Cheng

Department of Electronics Engineering & Institute of Electronics

College of Electrical Engineering and Computer Science

National Chiao Tung University

ABSTRACT

In this dissertation, the carbon nanotubes (CNTs) were utilized as the electron source in field-emission devices. By modifying the metallic catalysts and the device structures, the field-emission characteristics were greatly improved. In this research, Ti capping layer and Ti codeposited with Fe were used to control the activity, size, and distribution of the Fe catalytic nanoparticles for improving the emission current density, reliability, and uniformity of the devices. Moreover, the diameter and position of pillar-like CNTs synthesized from Fe-Ti codeposited catalyst were controlled by lithography. Therefore, a uniform distribution of emitters with suppressed screening effect was obtained for high emission current density and low turn-on field. Finally, a silicon nitride film was added into the triode-type field-emission devices to block the leakage current between the gate and the cathode for improving the power efficiency.

For emission current density, the high density of CNTs caused a serious screening effect which could greatly decrease the emission current density. Accordingly, a thin Ti

capping layer was deposited on the hydrogen pretreated Fe nanoparticles to resist the diffusion of the carbon radicals and effectively reduce the density of emitters. By altering the thickness of the Ti capping layer, a suitable density of CNTs was obtained with high emission current density and low turn-on field. Moreover, the Ti capped on the Fe nanoparticles held the nanoparticles firmly to provide stronger adhesion and lower contact resistance than those synthesized from the pure Fe. It remarkably suppressed the breakdown of the field-emission devices and diminished the degradation of emission current density at high electric field. It might result from the improvements of the contact properties with the modification of metallic catalyst.

However, the problems of uniformity were still not solved by means of the thin Ti capping layer. Therefore, a Fe-Ti codeposited metal layer was utilized as the catalyst of CNTs. During being heated, the nucleation of Fe atoms formed smaller nanoparticles with better uniformity due to the suppression of coalescence between Fe nanoparticles than those synthesized from pure Fe. A homogeneous light emission was therefore observed on the phosphor (P22) coated glasses. Furthermore, the nucleation of Fe nanoparticles resulted in a partially immersed structure of the CNTs which provided better contact properties between the CNTs and the substrates. As previous description, the reliability of the device could be improved.

Additionally, the lithography was utilized to form an artificial structure of pillar-like CNTs to control the diameter and distribution of emitters more precisely. The Fe-Ti codeposited catalyst was utilized for uniform CNTs with reliable emission current. A uniform distribution of emitters with low turn-on field was therefore achieved.

Finally, a silicon nitride layer was deposited on the poly-gate or under the poly-gate to block the electron emission from the cathode to the gate. Both of them could effectively improve the current efficiency and therefore increase the power efficiency of triode-type field-emission devices.

In this dissertation, simple, costless, and harmless methods have been proposed to improve the field-emission characteristics of CNTs. It showed a great potential in the applications of the field-emission displays and the back-light units in near future.



誌 謝

首先，要感謝我的指導教授 鄭晃忠 博士，在研究上給予我諄諄教誨，並適時地給予我專業的建議，使我能更清楚自己研究的目標與方向；此外，老師也時時關心我研究外生活的情況，常常教導我待人接物的道理，令我獲益良多，使我能順利地完成學業並獲得博士學位。也感謝在百忙之中抽空參加我論文口試的委員們，有了委員們專業的建議與熱心的指導，才能使我的論文更加地完整。

感謝實驗室的學長、同學以及學弟妹在生活上以及研究上的協助，令我在交通大學的學生生活更加地豐富也更加地順遂。鼎國學長在研究上的經驗談以及日常生活中的相處令我受惠良多；國基學長、全平學長以及高照學長在相關實驗上的經驗傳承以及教導令我更順利地進行相關的研究；感謝耀仁學弟、鈞凱學弟以及佩琪學妹的協助，共同在場發射元件的相關研究上貢獻心力，因為你們的付出才有今天的成果。也感謝宗穎學弟、翰忠學弟、依威學弟、建穎學弟、君翰學弟、育瑛學妹各位同組的成員在實驗上給予我建言與協助。

除此之外，也感謝交通大學奈米中心以及國家奈米實驗室能提供我最先進、最優良的實驗環境與設備。也感謝親切可愛的技術員徐秀巒小姐、黃月美小姐、范秀蘭小姐、鄭淑娟小姐、陳聯珠小姐、陳月婷小姐以及胡進章先生在技術上的協助，以及行政人員劉曉玲小姐與何惟梅小姐在行政事物上的協助。

還要感謝春乾學長、國瑞學長、逸哲學弟、育如學妹、可玉學妹、大傳學弟、瑛君學妹、旭信學弟、凱方學弟、祐圻學弟、心瑜學妹、仕偉學弟、序恆學弟以及偉凱學弟...等等實驗室成員在研究上以及生活上的協助。因為有了大家，才令我的論文能順利完成，生活才更加的豐富多姿。

最後，僅以此篇論文獻給我最敬愛的父母-賴德曙先生以及陳麗貞女士，因為父母的悉心栽培才能有今天的我，感謝他們在生活上令我無虞，隨時隨地支持我、鼓勵我，令我能有決心與毅力完成學業。也感謝我的女朋友以及妹妹，無時不刻給予我溫暖的

關懷，令我在灰心、氣餒的時候不被眼前的困難所打倒。

最後感謝身邊所有的親朋好友，謝謝你們一路以來的相挺以及協助，因為有了你們的關懷我才能順利完成博士學位，有機會我一定會請你們吃雞排加紅茶的(希望大家在得知我畢業的消息時不要太殘忍)。



Contents

Abstract (in Chinese).....	i
Abstract (in English).....	iii
Acknowledgments (in Chinese).....	vi
Contents.....	viii
Table Lists.....	xii
Figure Captions.....	xiii

Chapter 1 Introduction

1.1 Overview of Vacuum Microelectronics.....	1
1.1.1 Technologies of Vacuum Microelectronics.....	3
1.1.2 Applications of Vacuum Microelectronics in Field-Emission Displays.....	11
1.2 Theory of Field Emission.....	13
1.3 Carbon Nanotubes.....	17
1.3.1 Arc discharge.....	18
1.3.2 Laser Ablation.....	18
1.3.3 Chemical Vapor Deposition.....	18
1.4 Motivation.....	20
1.4.1 Reliability.....	20
1.4.2 Uniformity.....	21
1.5 Outline of Dissertation.....	21

Chapter 2 The Improvements of Emission Current Density and

Reliability for the CNTs Synthesized from the Ti-Capped Fe

Nanoparticles

2.1	Introduction.....	23
2.2	Experimental Procedures.....	26
2.2.1	Sample Fabrication.....	26
2.2.2	Material Analysis and Electrical Measurement.....	28
2.3	The Emission Current Density of the Carbon Nanotubes Synthesized from a Ti Capped Catalytic Nanoparticles.....	28
2.4	The Reliability Improvements of the Carbon Nanotubes by Modifying the Contact Properties.....	32
2.5	Summary.....	35

Chapter 3 The Improvements of Reliability and Uniformity for the CNTs Synthesized from the Fe-Ti Codeposited Catalyst

3.1	Introduction.....	37
3.2	Experimental Procedures.....	39
3.2.1	Sample Fabrication.....	39
3.2.2	Material Analysis and Electrical Measurement.....	40
3.3	The Partially Immersed Structure of the Carbon Nanotubes for the Reliability Improvements.....	41
3.4	The Suppression of the Coalescence between Fe Nanoparticles for a Uniform Light Emission.....	45
3.5	Summary.....	47

Chapter 4 The Synthesis and Characteristics of the Pillar-Like CNTs Synthesized from the Fe-Ti Codeposited Catalyst

4.1	Introduction.....	49
4.2	Experimental Procedures.....	50
4.2.1	Sample Fabrication.....	50
4.2.2	Material Analysis and Electrical Measurement.....	52
4.3	The Synthesis of the Pillar-Like Carbon Nanotubes by Utilizing the Fe-Ti Codeposited Catalyst.....	52
4.4	The Optimization of the Inter-Pillar Spacing Designed via the Lithography.....	54
4.5	Summary.....	56

Chapter 5 The Reduction of Gate Leakage for the CNTs-Based Triode Devices via Adding a Silicon Nitride Layer

5.1	Introduction.....	58
5.2	Experimental Procedures.....	60
5.2.1	Sample Fabrication.....	60
5.2.2	Material Analysis and Electrical Measurement.....	61
5.3	The Power Efficiency Improvements via Cutting Off the Leakage Paths.....	61
5.4	Summary.....	62

Chapter 6 Summary and Conclusions

.....	64
-------	----

Chapter 7 Future Prospects

.....67

References

.....69

Tables

.....92

Figures

.....98

Vita

.....197

Publication Lists

.....198



Table Lists

Chapter 1

Table 1.1	The timeline for the evolution of electronic technology.....	90
Table 1.2	The comparison of several flat panel displays.....	91
Table 1.3	The history of vacuum microelectronics.....	92
Table 1.4	The features of different field-emission technologies.....	93

Chapter 2

Table 2.1	The turn-on field and threshold field of samples with different thickness of Ti capping layer.....	94
Table 2.2	The densities of CNTs for samples with different thicknesses of Ti capping layer.....	94

Chapter 4

Table 4.1	The turn-on field and threshold field of the pillar-like CNTs with different intespacing.....	95
-----------	---	----

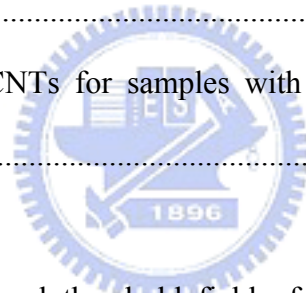


Figure Captions

Chapter 1

- Figure 1.1 The scheme of Spindt-type field emitter arrays. The height of the cones and thickness of the dielectric layer are both about 1 μm , the tip radius is about 20 nm, the gate aperture is about 0.5 μm , and the tip-to-tip spacing is about 1~5 μm96
- Figure 1.2 The processes of fabricating Spindt field emitter arrays: (a) etch cavities in the top two layers of a metal/dielectric/metal stack were formed by lithography and subsequent wet or dry etching, (b) a sacrificial lift-off layer is deposited onto the top layer and inner walls of the upper portion of the cavity by a tilted deposition with rotating the substrate on an axis perpendicular to the surface, (c) form metal cones in the cavities by depositing metal perpendicular to the substrate surface and the tilted deposition can be applied continuously or intermittently during this step to help to control the hole-closure rate and to manage stresses in the deposited layer as desired, and (d) a lift-off process is done by removing the sacrificial layer in a wet etching solution which only attacks the sacrificial layer without damage the metal cones seriously.....97
- Figure 1.3 The micrographs taken by SEM for (a) Spindt field emitter arrays and (b) device structure with higher resolution.....98
- Figure 1.4 The schematic illustration of orientation-dependant etching (ODE) method for fabricating silicon tips: (a) using lithography to pattern a etching mask to inhibit etching in locations where pyramids are desired and (b) etching of silicon is much faster at the (100) plane than at (111) plane, forming a (111) bounded pyramid in the end.....99

- Figure 1.5 The flowchart of the oxidation sharpening: (a) depositing a nitride layer on the silicon wafer and form an array of dots via lithography, (b) etch the nitride by dry etching and remove the photoresist, (c) undercut the silicon to form tips under the hard nitride mask by an isotropic etching (wet or dry etching), (d) form sharper silicon tips by oxidation at about 950 °C or lower, and (e) remove the nitride mask and thermal oxide to uncover the sharp silicon tips.....100
- Figure 1.6 The illustration of surface conduction emitters: (a) the device structure from top view with two ultrafine PdO films as cathode and gate electrodes and (b) the mechanism of surface conduction emission. A suitable voltage is applied between the two PdO films to extract electrons from cathode to gate and the electrons will be multi-scattered on the surface of PdO then extracted by the anode which is applied at a very high voltage.....101
- Figure 1.7 The schematic illustration of the ferroelectric emission mechanism. The screening charges are developed to compensate the net charges and a fast reversal of the polarization results a large electric field that ejects the electrons from the negative charged surface.....102
- Figure 1.8 The schematic depiction of (a) the MIM device structure and (b) the emission mechanism.....103
- Figure 1.9 A schematic illustration for the structures of a cathode-ray tube and a field-emission display. The left image shows that the electron source in the CRT is far from the anode but the electron source in the FED is just a millimeter away from the anode. The right-side figure demonstrates the cross-section view of a FED.....104
- Figure 1.10 The device structures of (a) diode-type and (b) triode-type in field-emission displays. The main differences between the diode-type and the triode-type

	device structure are the gate electrode around the emitter which can extract electrons from the cathodes at relative low electric field.....	105
Figure 1.11	The energy diagrams demonstrate the mechanisms of (a) thermionic-field emission and (b) field emission in semiconductor.....	106
Figure 1.12	The band diagram of the field-emission emitters in the vacuum environment (a) without applied electric field and (b) with applied electric field.....	107
Figure 1.13	The structure of the arc discharge system for synthesizing CNTs.....	108
Figure 1.14	The scheme for the structure of laser ablation system.....	109
Figure 1.15	The structure of chemical vapor deposition system for synthesizing CNTs..	110

Chapter 2

Figure 2.1	The schematic flowchart for the fabrication of experimental samples: (a) forming a 50×50 array of square holes with 10 μm in length and 10-um inter-space by the lithography system, (b) depositing a 50-nm-thick Ti buffer layer and a 5-nm-thick Fe catalytic layer subsequently by the dual-electron-gun deposition system, (c) removing the photoresist with Ti buffer layer and Fe catalytic layer by a lift-off process, (d) loading the samples into the thermal-CVD to be pretreated in hydrogen and form Fe nanoparticles, (e) depositing a thin Ti capping layer with 1 to 20 nm in thickness by the dual-electron-gun deposition system, and (f) synthesizing CNTs in the thermal-CVD.....	111
Figure 2.2	The samples were put on a glass substrate with a spacer of about 100 μm from the CNTs to the anode and the anode was a glass coated with a indium-tin-oxide (ITO) film and green phosphor (P22). The samples were loaded into a vacuum chamber with anode applied to the high-voltage source measurement unit, Keithley 237, and the cathode applied to the high-current	

	source measurement unit, Keithley 238, to measure the field-emission current at high vacuum environment.....	113
Figure 2.3	The pictures shown here were the images taken by SEM for the Fe nanoparticles that have been pretreated in hydrogen ambient for 5 min in the thermal-CVD with different thicknesses of the thin Ti capping layer: (a) 0 nm, (b) 1 nm, (c) 2 nm, (d) 4 nm, (e) 10 nm, and (f) 20 nm. With thicker Ti capping layer, the Fe nanoparticles were getting obscure in the micrographs due to being buried in the Ti capping layer.....	114
Figure 2.4	The surface morphologies taken by the SEM from top with 45° viewing angle for the CNTs of the samples with different thicknesses of the Ti capping layer: (a) 0 nm, (b) 1 nm, (c) 2 nm, (d) 4 nm, (e) 10 nm, and (f) 20 nm. It was obvious that the number density of the CNTs was decreased with the increasing thickness of the Ti capping layer.....	117
Figure 2.5	The scheme for the conditions of the Fe nanoparticles capped with thin Ti capping layer after being heated at 700 °C during the synthesis of the CNTs in the thermal-CVD: (a) the Fe nanoparticles capped with the thin Ti capping layer before growing the CNTs, (b) the deposited thin Ti capping layer was partially melted and getting thinner during the synthesis of CNTs at 700 °C, and (c) part of the Fe nanoparticle might even be exposed during the heating at 700 °C.....	120
Figure 2.6	The morphologies of CNTs synthesized with different materials as the capping layer: (a) Mo, (b) Ti, (c) Al, and (d) without capping layer.....	122
Figure 2.7	The SEM images of CNTs with different thickness of thin Ti capping layer from the top view: (a) 0 nm (b) 1 nm (c) 2 nm (d) 4 nm (e) 10 nm (f) 20 nm.....	124
Figure 2.8	The field-emission characteristics for the samples with different thicknesses of	

	the Ti capping layer: (a) the emission current density versus the electric field and (b) the F-N plot.....	127
Figure 2.9	The Raman spectra of the CNTs with no Ti capping layer and with Ti capping layer of 1 nm and 2 nm. The Raman spectra for the samples with thicker Ti capping layer were too weak to be detected here.....	128
Figure 2.10	(a) The micrograph of the CNTs taken by TEM and (b) The micrograph of CNTs taken by TEM with higher resolution.....	129
Figure 2.11	The analysis results of energy dispersive spectrometer for the nanoparticles enclosed in CNTs as shown in Fig. 2.10(a).....	131
Figure 2.12	The emission current density versus electric field for the samples without Ti capping layer (the conventional samples) and the samples with 5-nm-thick Ti capping layer (the proposed samples). An abrupt decrease in emission current density was observed in the conventional samples and no obvious decrease in emission current density was observed in the proposed samples. After the breakdown in the conventional samples, almost no emission current density was measured in the second measurements.....	132
Figure 2.13	The micrographs taken by the SEM for (a) the morphologies of the CNTs in the conventional samples after the electric breakdown and (b) the image with higher resolution.....	133
Figure 2.14	(a) the emission current density of both the conventional and the proposed samples over one hour (the emission current density of the conventional samples in the first 6 sec was removed) and (b) the emission current density of the conventional samples for the first 6 sec.....	134

Chapter 3

Figure 3.1	The flowchart of experiment: (a) an array of 5×5 square holes with 100 μm in
------------	--

length and 100 μm interspacing were patterned by the lithography system on a photoresist film, (b) a 50-nm-thick Ti layer was deposited by the dual-electron-gun physical vapor deposition system and a catalytic metal layer (Fe-Ti codeposited layer for proposed samples and pure Fe for conventional samples) was subsequently deposited in the same chamber, (c) the photoresist was removed by a lift-off process in acetone solution to leave the Ti buffer layer with the catalyst in the squared holes only, (d) loaded into the chamber of thermal-CVD to be pretreated in hydrogen ambient ($\text{H}_2/\text{N}_2 = 400/600$ s.c.c.m.) at 700 °C for 5 min, and (e) grew the CNTs in the same chamber with ethylene ($\text{C}_2\text{H}_4/\text{H}_2/\text{N}_2 = 5/100/10$ s.c.c.m.) at 700 °C for 15 min.....135

Figure 3.2	The images of SEM displayed the roots of the CNTs for both (a) the conventional specimens and (b) the proposed specimens with high resolution. The proposed specimens were cleaved across the patterned area and a CNT partially immersed into the codeposited metal layer on the cleaved edge was marked by a circle in (c).....137
Figure 3.3	The micrographs of the CNTs synthesized from the Fe-Ti codeposited catalyst taken by the TEM: (a) a CNT with an enclosed nanoparticle and (b) the multiwalled structure of the CNTs with higher resolution.....139
Figure 3.4	The phase diagram of Fe-Ti.....141
Figure 3.5	The results of energy dispersive spectrum for the enclosed nanoparticle in Fig. 3.8(a) where only signals of Fe, C, and Cu were detected.....142
Figure 3.6	The Raman spectrum of the CNTs in the conventional samples and the proposed samples.....143
Figure 3.7	The schemes of mechanisms illustrated the formation of nanoparticles during hydrogen pretreatment and the growth of CNTs for both (a) the conventional specimens and (b) the proposed specimens.....144

Figure 3.8	The surface energies of elements.....	146
Figure 3.9	The curves of emission current density versus electric field from 0 to 7 V/ μm for (a) the conventional samples and (b) the proposed samples before and after being stressed.....	147
Figure 3.10	The emission current density versus operating time of (a) the conventional samples and (b) the proposed samples for 2,500 sec.....	148
Figure 3.11	The micrographs taken by SEM displayed the morphologies of both the conventional and the proposed samples before and after being stressed.....	149
Figure 3.12	The micrographs of the catalytic nanoparticles taken by the SEM from top-view for (a) the conventional samples and (b) the proposed samples.....	150
Figure 3.13	The atomic force microscope images (scanning area of 10 μm \times 10 μm) of the catalytic nanoparticles for (a) the conventional samples and (b) the proposed samples.....	151
Figure 3.14	The micrographs of the CNTs taken by the SEM with 45° viewing angle for (a) the conventional samples and (b) the proposed samples. The cross-sections of the CNTs taken by the SEM: (c) the conventional samples and (d) the proposed samples.	152
Figure 3.15	The scheme for the formation of the catalytic nanoparticles in (a) the conventional samples and (b) the proposed samples.....	154
Figure 3.16	The curves of emission current density versus applied electric field for both the conventional and the proposed samples.....	155
Figure 3.17	(a) The luminescent images for the conventional samples operated at 500 V, 600 V, and 700 V of anode voltages and (b) The luminescent images for the proposed samples operated at 500 V, 600 V, and 700 V of anode voltages....	156

Chapter 4

Figure 4.1 The flowchart of experimental processes: (a) spin photoresist on N-type silicon wafers and then form a hole-array of circles with 6 μm in diameter and different inter spacing of 12, 15, 20, 25, 30, and 35 μm in a rectangular of 1 mm in width and 2 mm in length, (b) depositing a 50-nm-thick Ti metal as a buffer layer by dual electron-gun physical vapor deposition system and subsequently codeposited a 10-nm-thick Fe and Ti film as the catalyst of CNTs (Fe 64% w.t.), (c) the photoresist was removed by a lift-off process in an ultrasonic cleaner with acetone solution and only Ti buffer layer and Fe-Ti codeposited catalyst were left in the circle holes, (d) the samples were loaded into a thermal-CVD to be pretreated in hydrogen ambient ($\text{N}_2/\text{H}_2 = 500/100$ s.c.c.m.) at 700 $^\circ\text{C}$ for 8 min, and (e) finally synthesized CNTs with ethylene ($\text{C}_2\text{H}_4/\text{N}_2/\text{H}_2 = 20/500/100$ s.c.c.m.) at 700 $^\circ\text{C}$ for 15 min.....158

Figure 4.2 The cross-section view of pillar-like CNTs synthesized from the 5-nm-thick pure Fe catalytic film in the thermal-CVD for (a) 8 min, (b) 15 min, (c), 30 min, (d) 60 min, and (e) 120 min.....160

Figure 4.3 The cross-section view of pillar-like CNTs synthesized from the Fe-Ti codeposited catalytic film in the thermal-CVD for (a) 8 min, (b) 15 min, (c), 30 min, (d) 60 min, and (e) 120 min.....163

Figure 4.4 The relationship of the length of pillars versus the growth time for both the conventional and the proposed samples.....166

Figure 4.5 The morphologies of the hydrogen pretreated catalytic nanoparticles for both (a) the conventional samples and (b) the proposed samples.....167

Figure 4.6 The scheme of a sphere partially immersed in the substrate.....168

Figure 4.7 The surface to volume ratio of sphere in Fig. 5.6 versus the radius and the angle θ169

Figure 4.8 The images of CNTs with higher resolution for (a) the conventional samples

	and (b) the proposed samples.....	170
Figure 4.9	The micrographs of the pillar-like CNTs with different interpillar spacing, (a) 12 μm , (b) 15 μm , (c) 20 μm , (d) 25 μm , (e) 30 μm , and (f) 35 μm , taken by SEM with 45 ° viewing angle.....	171
Figure 4.10	The cross-section views of the pillar-like CNTs with different interpillar spacing, (a) 12 μm , (b) 15 μm , (c) 20 μm , (d) 25 μm , (e) 30 μm , and (f) 35 μm	174
Figure 4.11	The field-emission characteristics of the pillar-like CNTs (a) the emission current of samples versus applied voltage and (b) the Fowler-Nordhiem plot of each samples.....	177
Figure 4.12	The curve of the turn-on field versus the interpillar spacing for the pillar-like CNTs with different interpillar spacing.....	178
Figure 4.13	The average of the emission current density for all the samples with different interpillar spacing applied at 800 V for 1 hour.....	179
Figure 4.14	The luminescent image of the pillar-like CNTs applied at 800 V taken by digital camera.....	180

Chapter 5

Figure 5.1	The scheme of device structures in field-emission displays for (a) the diode-type and (b) the triode-type.....	181
Figure 5.2	(a) The flowchart of the conventional samples, (b) The flowchart of the OPN (oxide-poly-nitride) samples, and (c) The flowchart of the ONP (oxide-nitride-poly) samples.....	182
Figure 5.3	The device structures of the (a) conventional samples, (b) the OPN (oxide-poly-nitride) samples, and (c) the ONP (oxide-nitride-poly) samples.....	190

Figure 5.4 The vacuum measurement structure of the triode-type field-emission devices.....191

Figure 5.5 The cross-section views of (a) the conventional samples, (b) the OPN (oxide-poly-nitride) samples, and (c) the ONP (oxide-nitride-poly) samples taken by SEM. The insets were top views with 45° viewing angle for those samples that have undergone the process of CNTs synthesis.....192

Figure 5.6 The emission current density of anode versus gate voltage for the conventional samples, the OPN samples, and the ONP samples.....193

Figure 5.7 The leakage current paths between gate and cathode in (a) the conventional samples, (b) the OPN samples, and (c) the ONP samples.....194



Chapter 1

Introduction

1.1 Overview of Vacuum Microelectronics

The invention of vacuum tubes can be traced back to the observation of emission current by the research team of Thomas Edison during the experimental processes of finding proper materials for light bulb filament in early 1880. Although Thomas Edison could not figure out the mechanism of emission current passing through the evacuated bulb, he still filed a patent with no application purpose and, therefore, this phenomenon was also called “Edison Effect” nowadays. Until 1905, the first electronic diode vacuum tube was designed and fabricated by an English physicist, John Ambrose Fleming, and became a vital unit in radio receivers and radars for many decades afterwards. In 1906, an American electrical engineer, Lee De Forest, added a control “grid” into the Fleming diode to control the emission current between the cathode and the anode. It was the prototype of vacuum triode where a small voltage signal applied on the control grid can be amplified to be a large signal on the anode electrode with great linearity and large voltage swing. It was very essential in the creation of long-distance telephone, radio communications, radars, and early digital computers. However, due to the drawbacks of large, fragile, and needed to be heated to 1000 °C to extract electrons from the cathode, the vacuum tubes could not realize electric appliances easily. In 1947, William Shockley, Walter Brattain, and John Bardeen successfully invented the first point-contact bipolar transistor in Bell Lab[1.1]. After that, the concepts of integrated circuits (ICs) subsequently proposed

by Jack Kilby worked for Texas Instrument and Robert Noyce worked for Fairchild Semiconductor in 1960s. The invention of solid-state devices and concepts of ICs revealed the unpredictable potentials of solid-state electronics and, therefore, enter a new era[1.2-1.3]. As shown in the table 1.1, the solid-state electronics developed very rapidly with the improvements in semiconductor manufacturing technologies and almost replaced all the vacuum electronics in most applications and researches within several decades.

In the past few years, the vacuum electronic devices have been renewed by reducing the device scale down to micro-size with the improved manufacturing technologies and equipments of semiconductor. These new generated vacuum microelectronic devices have achieved significant progresses in the developments for the applications in field-emission displays (FEDs)[1.4-1.8], microwave amplifiers and generators[1.9-1.11], ultra-fast switches, intense electron/ion sources[1.12-1.13], electron source of scanning electron microscope (SEM) and e-beam lithography, micro-sensors[1.14-1.15], and devices needed to work in hostile environment. In fact, “vacuum state” devices have potentially a number of outstanding advantages with respect to the presently much popular “solid state” devices, including fast drift velocity and associated transit time, radiation hardness and temperature insensitivity, and higher output power. For example, the saturation drift velocity is limited to less than 3×10^7 cm/sec in all solid-state devices whereas the saturation electron velocity in vacuum is limited to 3×10^{10} cm/sec theoretically and practically to about $6-9 \times 10^8$ cm/sec[1.16]. The faster drift velocity of vacuum devices as compared with the solid-state devices results from less scattering in the channel of vacuum devices. The high mobility is the reason why even a manually assembled triode vacuum tube built in early 1950s with large mechanical tolerance still could operate at a very high frequency of 4 GHz[1.17]. Additionally, because there is no medium in the channel of

vacuum devices, temporary and permanent radiation effects should be neglected and the effects of temperature on performance are essentially none exists. With present availability of micro fabrication technologies, vacuum tubes were further improved into “vacuum microelectronics” with the feature of micro-size dimension and could overcome most of the mentioned drawbacks to make this technology much more potential in many interesting applications.

1.1.1 Technologies of Vacuum Microelectronics

The vacuum microelectronics has attracted a great deal of interests from many research groups due to many amazing characteristics since its invention. Several technologies have been investigated such as Spindt field emitter arrays, silicon field emitter arrays, diamond, diamond-like carbon (DLC), surface conduction emitters (SCE), ferroelectric emitters, metal-insulator-metal emitters (MIM), and carbon nanotubes (CNTs). Here, we make a brief introduction to these technologies:

● Spindt field emitter arrays

The cathodes of Spindt field emitter arrays are fabricated by forming metal cones on the conducting cathode electrodes as electron emitters by using thin film deposition processes. Each cone is surrounded by an accelerating grid electrode (gate) which is insulated from the conducting cathode electrode by a dielectric layer[1.18]. Typically, as shown in Fig. 1.1, the cone height and thickness of the dielectric layer are both about 1 μm , the tip radius of the cones is about 20 nm, the gate aperture is about 0.5 μm , and the tip-to-tip spacing is about 1~5 μm . In particular, the gate aperture can be reduced as small as 0.1 μm and the radius can also down to 5 nm. The cathode array features like a source of electrons with a positive voltage bias applied to

the surrounding gate electrode. The original idea for the development of microfabricated field emitter array (FEA) came from Ken Shoulders and Dubley Buck at Massachusetts Institute of Technology (MIT) in the 1950s[1.19] but it was realized 40 years later beyond the reach of technology. The basic concepts were brought by Shoulders to the Stanford Research Institute (SRI) to develop the microfabricated vacuum integrated circuits[1.20] and he also proposed a thin display tube base on matrix-addressed arrays of microfabricated field emitters, the field-emission displays (FEDs)[1.21]. As part of Shoulder's program, Capp Spindt proposed a smart method to form the arrays of miniature metal field emitter cones in microsize cavities with an surrounded extraction gate[1.22]. The processes of fabricating Spindt field-emitter arrays consists four steps as shown in Fig. 1.2. The first step is to etch the microsize cavities defined by lithography in the top two layers of a metal/dielectric/metal stack by using wet or dry etching. After that, a sacrificial layer is deposited onto the top layer and inner walls of the upper portion of the cavity by a tilted deposition with rotating the substrate on an axis perpendicular to the surface. Third step is to form metal cones in the cavities by depositing metal perpendicular to the substrate surface. The tilted deposition can be applied continuously or intermittently during this step to help to control the hole-closure rate and to manage stresses in the deposited layer as desired. Finally, a lift-off process is done by removing the sacrificial layer in a wet etching solution which attacks the sacrificial layer only without damage the metal cones seriously. The micrographs of Spindt field emitter arrays taken by SEM are shown in Fig. 1.3[1.20]. Although the Spindt type field emitter array provide a smart method to realize sharp metal tips with extraction gate electrode, it still has some drawbacks of needing huge metal depositing equipment, complex processes, requirement of high driving voltage, and reliability issues.

● silicon field emitter arrays

Sharp silicon tips of field emitter array are fabricated from crystalline silicon wafer by using oxidation processes to obtain silicon tips with small radius[1.18]. The processing steps of forming the silicon tips can be realized via standard semiconductor processes. According to some researches, the emission current from silicon tips can reach as high as 10 $\mu\text{A}/\text{tip}$ [1.23]. Furthermore, crystalline silicon is a good choice for the investigation of field emission array because of its great electronic, crystalline, mechanical properties, and availability. With well-developed techniques and equipments for fabrication, the apex radii of fabricated silicon tips can be below 10 nm with small deviation. One of the methods to form silicon tips is utilizing the orientation-dependant etching (ODE) which can form a convex pyramids structure[1.24-1.25]. This method is attractive since the pyramids structure with (111) crystal faces extending almost to the last atom which provide a highly uniform tip geometry with well-defined surfaces. Firstly, an array of dots are patterned by lithography processes on the (100) surface of silicon wafers over the points where the tips wanted to be formed. The dots are typically about 1 μm in diameter or even less. After that, the wafer is etched by KOH solution that dissolves the (100) crystal face much faster than the (111) crystal face. The etching process undercut the etching mask and leave a pyramid bounded by (111) in the end. To illustrate the processes with more detail, the flowchart of orientation-dependant etching (ODE) processes was displayed schematically in Fig. 1.4. Another way of fabricating silicon tips array is the oxidation sharpening process which is also the most used method in creating sharp tips on silicon wafers[1.26]. The first step is depositing a nitride layer on silicon as a hard mask to resist the following etching processes. A pattern of dots array is formed by using lithography processes and a dry etching process is applied to remove the nitride which is not under the patterned regions. An isotropic etching (wet or dry

etching) is applied to undercut the hard mask. To form the tip apex, this structure are thermally oxidized at about 950 °C or less and the silicon remained under the oxide become extremely sharp. The flowchart of the oxidation sharpening processes is shown in Fig. 1.5 to describe the processes schematically. However, the array of silicon tips still has the problem of local failure due to high emission current density. Local heating at the silicon tips due to high emission current passing through can result in a local evaporation of silicon tips to reduce its sharpness and, therefore, cause a gradual degradation in emission current. Moreover, the requirement of driving voltage is still too high for the applications of field-emission devices due to its high work function.

● **diamond emitters**

Diamond is one of the main crystalline allotropes of carbon, which is formed in an sp^3 tetrahedral bonded cubic structure. Due to negative work function, diamond possesses a very small barrier for its electrons to leave the surface and emit into the vacuum environment. When the surfaces of diamond are terminated with hydrogen atoms, the electron affinity, which is a measured energy barrier that electrons must overcome to escape from the surfaces of diamond into vacuum, can become negative[1.27]. Compared with other materials such as cesium (Cs) and barium (Ba) with low energy barrier for the emission of electrons, the diamond surfaces are chemically inert and mechanically strong. In fact, diamond is the only known material with negative electron affinity that is stable in air so far. According to the former properties, diamond is considered a very promising material of the electron emitters in vacuum microelectronics. The low energy barrier allows diamond to emit electrons at low applied electric field without the requirement of fabricating sharp microtips to enhance the local electric field. In addition, the excellent mechanical and chemical

stability of diamond leads to the highly durable and reliable emitters. Unfortunately, the conductivity of diamond is not good and, therefore, the maximum emission current from the diamond surface to the vacuum environment is limited. Additionally, the process temperature for diamond to be deposited via chemical vapor deposition is also usually higher than 700 °C. It makes the diamond electron emitters difficult to be fabricated on the glass substrates.

● **diamond-like carbon (DLC)**

Diamond-like carbon is another particular interesting material of three dimensional network of sp^3 and sp^2 bonded carbon atoms[1.28-1.30]. Due to good field emission properties and low deposition temperature, the DLC attracted a lot of interesting from many researches. The low deposition temperature allows them to be formed directly onto materials that can not sustain high temperature, such as glass substrate, for the applications of field-emission displays. Depending on the deposition conditions, the ratio of hydrogen carbon (a-C:H) and hydrogen-free carbon (a-C) can be altered in the DLC. It also means that different portions of sp^3 and sp^2 bonding can be achieved to dictate the field emission properties[1.31-1.32]. It is interesting that the emission properties of these amorphous carbon or DLC improve with increasing sp^3 content, while those of diamond materials deteriorate. It suggests that there is an optimal ratio of sp^3 and sp^2 bonding in order to obtain emitters with lowest turn-on field. If the sp^3 ratio is too high, the electrons in the substrate can be not transported to the surfaces of diamond effectively to provide a stable emission current. On the other hand, if the sp^2 is too high, the property of negative electron affinity of diamond would be suppressed and the tunneling barrier becomes too high for electron emission at low electric field. Therefore, the process of synthesizing the DLC is complex and sensitive to the growth conditions. As a significant drawback, a DLC film with small

variation is difficult to obtain in a single run or from run to run.

● **surface conduction emitters (SCE)**

Surface conduction emission is the phenomenon that electrons are emitted from a cathode when electric current flows through the cathode in parallel with the cathode surface[1.18]. It has attracted a great deal of attention since a 10-inch full color display incorporated a thin film PdO cathode based on the surface conduction emission mechanism was built by the researchers at Canon in Japan[1.33]. The device structure with two ultrafine PdO film as cathode and gate electrodes from top view is demonstrated in Fig. 1.6(a). The forming process of the gap between cathode and gate electrodes is to apply a voltage between two electrodes so that an electric current with high density flows through the PdO film in parallel with the surface. The thin film generates Joule heating when the electric current passing through and cause a fissure of nano scale between two electrodes. The fissure where be spatially discontinuous but electric continuous which causes field emissions because of high fields established across the cracks along the surface. The emitted electrons can be collected by the anode spaced apart from the surface of cathode after multiple scatterings on the cathode, as shown in Fig. 1.6(b). Due to the nanosize of the gap between cathodes and gates, the driving voltage can be greatly suppressed to several decades volt. The uniformity of emission current from device to device is also good resulting from the uniform PdO film. However, the emission current from cathode to anode is still low due to that most of the emitted electrons are collected by the gate electrode which only 10 nm apart from the cathode.

● **ferroelectric emitters**

About 40 years ago, it has been observed that electrons emitted from the surfaces

of ferroelectric materials during polarization reversal[1.34-1.35]. It was recognized that the polarization induces macroscopic charge separation on the two opposite surfaces of ferroelectric samples. As shown in Fig. 1.7, the screening charges are developed to compensate the net charges. A fast reversal (about sub-microseconds) of the polarization results a large electric field that ejects the electrons from the negative charged surface. By contrast, no external extraction field is required to overcome the surface work function to obtain electrons emission from ferroelectric emitters[1.36]. The emission depends on the polarization fields within the ferroelectric material and only excitation energies such as electrical, optical, thermal or mechanical energies are required to overcome the coercive fields. Ferroelectric emission is thus a transient unipolar effect generated from non-equilibrium charged ferroelectric surface. Ferroelectric cathodes have very robust surfaces that may be exposed to air and operated in poor vacuum conditions (up to 10^{-2} torr) or even in plasma. However, many issues in ferroelectric emissions such as polarization fatigue during multiple fast switching, emission current stability, and domain structure aging are still needed to be overcome before those envisioned devices could be realized.

● **metal-insulator-metal emitters (MIMs)**

Metal-insulator-metal cathodes are a kind of thin film tunneling device proposed by Mead in early 1960s and has been studied by many researchers[1.37-1.42]. Due to the stack structure, the buried cathode of MIM devices is less contamination and the electrons tunnel through interfacial Schottky barriers instead of surface barriers. This device consists of a thin insulating film (e.g. Al_2O_3) sandwiched between two metal electrodes, as shown in Fig. 1.18(a). The ultra-narrow insulating film allows the tunneling trough of electrons when a moderate electric field is applied across the layer. The energy diagram in Fig. 1.18(b) also shows that the tunneling electrons are

injected from the negative electrode (the emitter) through the insulating layer into the positive electrode (the gate) as hot electrons and are detected as diode current I_b . Part of the electrons have sufficient kinetic energy to overcome the surface energy of the Au and emit into the vacuum, which are collected as an emission current I_e . However, most of the tunneling electrons lose their kinetic energies while they pass through the structure due to scattering events in both the insulator and the gate metal. It is important to notice that the MIM structure requires a very precise control over the thickness of film to even atomic scale and the roughness of film is also very critical which can cause a very significant fluctuations in emission current and emission uniformity.

● **carbon nanotubes (CNTs)**

Carbon nanotubes has attracted a great deal of attention since its first observation in 1991 by Iijima[1.43]. Generally, they can be classified into single-walled nanotubes (SWNTs) and multi-walled nanotubes (MWNTs) depending on their structure. Due to high aspect ratio, strong mechanical strength, low work function, good thermal conductivity, and inert chemical properties, CNTs are recognized as a very wonderful material of electron emitters. Not only for the applications of field-emission devices, the CNTs were also thought to be very potential in many other researches such as microelectronics, hydrogen storage, scanning probes, bio-sensors, gas sensors, fuel cell, back-light units (BLUs), and field-emission displays (FEDs)[1.52-1.60]. From the report of De Heer, the emission current density of about 100 mA/cm^2 is measured from a partially aligned CNTs film prepared by drawing nanotube suspensions through 200 nm pore ceramic filters[1.61]. It has also been reported in many other researches that CNTs can provide a emission current with high density[1.62-1.63]. However, the growth mechanism of CNTs is still not very clear and there are still

issues of uniformity, stability, and reliability that should be overcome.

The previously mentioned technologies are very potential in the vacuum microelectronics and all of them are thought to be very promising techniques for the applications in field-emission displays. Among them, the CNTs show great field-emission characteristics and potential for the applications of the field-emission displays due to its high aspect ratio and relative low work function. In this dissertation, we will concentrate on the field-emission characteristics of CNTs synthesized by thermal-chemical vapor deposition (thermal-CVD) system. Several important issues are discussed and improved here to obtain better field-emission properties.

1.1.2 Applications of Vacuum Microelectronics in Field-Emission Displays

Owing to the requirement of displays with excellent image qualities and large image size, the development of flat-panel displays (FPDs) is one of the most important industries in the world now. Generally, the flat panel displays can be divided into two kinds, emissive-type and non-emissive-type. The non-emissive-type includes passive matrix-liquid crystal displays and active matrix-liquid crystal displays. Moreover, the emissive-type includes plasma display panel (PDP), organic light Emission display (OLED), light emission diode (LED), polymer light emitting diode (PLED), electro-luminescence display (EL display), vacuum fluorescent display (VFD), Flat cathode-ray tube (CRT), and field emission display (FED). Among them, field-emission displays were thought to be one of the most promising technologies that will be the major display technique in the near future due to its amazing properties of image. It has a simple structure with a baseplate formed by an array of

addressable gated emitters where emit electrons to a phosphor plate that is located in close proximity (0.2-2 mm) to the array. Unlike the traditional CRT display, each pixel in field-emission displays is constructed by a group of addressed field-emission emitters rather than pointed by a direction-controllable electron gun. It can provide a image with high resolution and avoid the distortion of image caused by external electric or magnetic field. The figure of field-emission displays and traditional CRTs shown in Fig. 1.9 illustrate the differences between these two displays schematically. The advantages of field-emission displays over other flat panel displays are higher brightness, better viewing angle, lower power consumption, less radiation, and larger operating range of temperature. The comparison for the characteristics of several flat panel displays is listed in table 1.2. The idea of the field-emission display was first proposed and described in U.S. patent 3,500,102 issued in 1970 by Crost, Shoulders, and Zinn. However, the first prototype was demonstrated in Japan Display until 1986 by a group from LETI and the first color display (6 inch) was demonstrated in 1993 by Pixel/LETI. To know the history of field-emission displays better, more relative events of field-emission displays were listed in the table 1.3.

Generally, the device structures of field-emission displays could be classified into two main categories, diode structure and triode structure. As shown in Fig. 1.10(a), the field emission current is emitted from the cathode to the anode in the diode structure and the emission current is controlled by the voltage applied on the anode electrode. It is a simpler structure as compared with the triode structure and easier to obtain a uniform emission current density. However, the driving voltage required to show a grayscale is too high which will increase the cost and complexity for the design of driving circuit. As a comparison, the triode structure of field-emission displays is demonstrated in Fig. 1.10(b). As shown in the picture, a gate electrode is added around the emitter to extract electrons from the cathode with

relative lower driving voltage and an insulating layer is also deposited under the gate electrode to separate the cathode and the gate. The emission current density from the cathodes to the anode is controlled by the voltage biased to the gate electrode. The electrons on the tip of emitters are extracted by the electric field induced from the gate voltage and parts of them are attracted by the electric field induced from the anode voltage. In the triode structure, a much lower driving voltage is required to realize a grayscale than the diode structure. So far, several technologies of field-emission displays have been developed to make it producible, such as Spint type, ballistic-electron surface-emitting device (BSD), surface conduction electron emitter (SCE), metal-insulator-semiconductor (MIS), metal-insulator-metal (MIM), diamond particles, and carbon nanotubes (CNTs). Most of them are base on the idea of triode structure and the relative information of those technologies is shown in table 1.4. Among them, the CNTs-based field-emission displays is one of the most promising technologies to realize a field-emission display with great image quality due to its high emission current density and relative low driving voltage. Many company such as Samsung of Korea, ITRI of Taiwan, NEC of Japan, etc. have taken a lot of resources to research and develop this amazing technology of field-emission display.

1.2 Theory of Field Emission

In semiconductor physics, the thermionic-field emission and field emission are both important mechanisms for the transport of electrons over the potential barrier between the metal and the semiconductor. In Schottky barriers on highly-doped silicon crystal as shown in Fig. 1.11(a), the depletion region is so narrow that the electrons can tunnel through the barrier near the top where the barrier is small enough which is called thermionic-field emission. On the other hand, in a degenerate silicon

crystal as shown in Fig. 1.11(b), the electrons can tunnel through the energy barrier even near the Fermi level which is called field emission. It can be found that the tunneling in thermionic-field emission process requires electrons with higher energy than in field emission process. The emission of electrons from a surface of conductive material such as metal or semiconductor into a vacuum environment at an extremely high electric field is also a quantum mechanical tunneling phenomenon. The energy diagram of a metal-vacuum system without external electric field is displayed in Fig. 1.12(a). As shown in Fig. 1.12(b), the vacuum level is bent at extremely high electric field and the energy barrier between the surface of metal and the vacuum become so narrow that the electron can tunnel through it easily, even at very low temperature. Here W_0 is the energy difference between an electron at rest outside the metal and an electron at rest inside the metal, whereas W_F is the energy difference between the Fermi level and the bottom of conduction band. The work function Φ defined as $\Phi = W_0 - W_F$. When a external electric field is applied, the vacuum level is reduced and the energy barrier at the surface of conductive metal or semiconductor becomes thinner. Then an electron having energy “ W ” has a finite probability of tunneling through the surface barrier. Fowler and Nordhiem derive the famous Fowler-Noedhiem equation (1.1) as below[1.64-1.65]:

$$J = \frac{aE^2}{\phi^2(y)} \exp\left[\frac{-b\phi^{3/2}v(y)}{E}\right], \quad (1.1)$$

where J is the current density (A/cm^2), E is the applied electric field (V/cm), Φ is the work function (eV), $a = 1.56 \times 10^{-6}$, $b = -6.831 \times 10^{-7}$, $y = 3.7947 \times 10^{-4} E^{1/2} / \Phi$, $t^2(y) \doteq 1.1$ and $v(y)$ can be approximated as [1.66]. Here

$$v(y) = \cos(0.5\pi y) \quad (1.2)$$

or

$$v(y) = 0.95 - y^2 \quad (1.3)$$

Typically, the field emission current is measured as a function of the applied voltage V . Substituting relationships of $J = I/\alpha$ and $E = \beta V$ into Eq. 1.1, where α is the emitting area and β is the local field enhance factor at the emitting surface, following equation can be obtained

$$I = \frac{A\alpha\beta^2V^2}{\phi^2(y)} \exp\left[\frac{-bv(y)\phi^{3/2}}{\beta V}\right]. \quad (1.4)$$

Then take the log. Form of Eq. 1.4

$$\log\left(\frac{I}{V}\right) = \log\left[1.54 \times 10^{-6} \frac{\alpha\beta^2}{\phi^2(y)}\right] - 2.97 \times 10^7 \left(\frac{\phi^{3/2}v(y)}{\beta V}\right), \quad (1.5)$$

from Eq. 1.5, the slope of a Fowler-Nordheim (F-N) plot is given by

$$S \equiv slope_{FN} = 2.97 \times 10^7 \left(\frac{\phi^{3/2}}{\beta}\right). \quad (1.6)$$

The parameter β can be evaluated from the slope S of the measured F-N plot if the work function Φ is known,

$$\beta \cong -2.97 \times 10^7 \left(\frac{\phi^{3/2}}{S}\right). \quad (1.7)$$

Emission area α can be subsequently extracted from a rearrangement of Eq. 1.5

$$\alpha = \left(\frac{I}{V^2}\right) \frac{\phi}{1.4 \times 10^{-6} \beta^2} \exp\left(\frac{9.89}{\sqrt{\phi}}\right) \exp\left(\frac{6.53 \times 10^7 \phi^{3/2}}{\beta V}\right). \quad (1.8)$$

For example, electric field at the surface of a spherical emitter of radius r concentric with a spherical anode (or gate) of radius $(r + d)$ can be represented analytically by

$$E = \frac{V}{r} \left(\frac{r+d}{d}\right). \quad (1.9)$$

Though a realistic electric field in the emitter tip is more complicated than the equation above, we can multiple Eq. 1.9 by a geometric factor β' to approximate the

real condition.

$$E_{tip} = F(r, d) = \beta' \frac{V}{r} \left(\frac{r+d}{d} \right), \quad (1.10)$$

where r is the tip radius of emitter, d is the emitter-anode(gate) distance, β' is a geometric correction factor[1.66], and $F(r,d)$ is a function of r and d .

For a very sharp conical emitter tip, where $d \gg r$, E_{tip} approached to $\beta'(V/r)$. Moreover, for $r \gg d$, E_{tip} approaches to $\beta'(V/d)$ which is the solution for parallel-plate capacitor and for a diode operation in a small anode-to-cathode spacing.

As the tip radius of the gated field-emission array is very small, Eq. 1.10 can be approximated as:

$$E_{tip} = \beta' \left(\frac{V}{r} \right). \quad (1.11)$$

Combining $E = \beta V$ and Eq. 1.11, we can obtain the relationship:

$$E_{tip} = \beta V = \beta' \left(\frac{V}{r} \right) \quad \text{and} \quad \beta' = \beta r, \quad (1.12)$$

the tip radius r is usually in the range from a few nm to 50 nm, corresponding to the parameter β' ranging from 10^{-1} to 10^{-2} .

Besides, transconductance g_m of a field emission device is defined as the change in anode current due to a change in gate voltage[1.67].

$$g_m = \left. \frac{\partial I_c}{\partial V_g} \right|_{V_c}. \quad (1.13)$$

Transconductance of a field-emission device is a figure of merit that gives as an indication of the amount of current charge that can be accomplished by a given change in gate voltage. The transconductance can be increased by using multiple tips or by decreasing the cathode-to-gate spacing for a given cathode-to-anode spacing.

1.3 Carbon Nanotubes

Since the first observation of CNTs in 1991 by Iijima[1.68], a great deal of attention has been attracted from many researchers due to its unique chemical and physical properties. Due to high aspect ratio, relative low work function, strong mechanical strength, inert chemical properties, good thermal conductivity, and good conductivity, the CNTs are recognized as a wonderful material of electron emitters in field-emission devices. The CNTs were observed as a by-product in the production of the fullerenes by utilizing the arc-discharge method. So far, it can be prepared by several kinds of methods including arc-discharge[1.45], laser ablation[1.69-1.72], and catalytic decomposition of hydrocarbon[1.73-1.80]. Here we make a brief introduction for the methods of CNTs synthesis.

1.3.1 Arc discharge

By keeping the gap between the carbon electrodes about 1 mm in the arc-discharge system, CNTs deposits on the surface of the cathode under the conditions that the diameter of the anode carbon is about 8 mm with arc-electric current of 80 A, voltage of 23.5 V, and He pressure of 300 Torr. The CNTs grow only inside the cathode deposit and not exist in other places in the reactor. The quality of CNTs depends on the pressure of He in the reactor and it is also the most important parameter. The optimized pressure of He is about 500 Torr and almost no CNTs are synthesized if the He pressure is below 100 Torr. Another important factor is the electric current for discharge which should be controlled well to keep the arc discharge stable and the electrode cool. The CNTs synthesized by using arc discharge are usually in bundles and need to be released by ultrasonic cleaner and particular etching solution. The arc discharge system is displayed in Fig. 1.13 schematically.

1.3.2 Laser Ablation

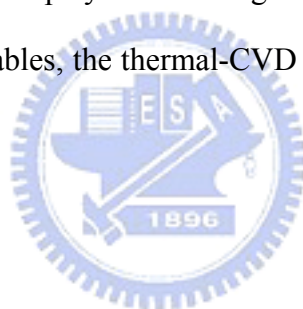
A pulsed or continue laser is applied to vaporize a graphite target in a chamber in He or Ar at about 500 Torr. As the vaporized graphite cooled rapidly, small carbon molecules or atoms condense quickly to form large clusters and then react with the catalyst to form CNTs. Laser ablation is very similar to arc discharge, because the optimum gas pressure and catalyst mix is close to those in the arc discharge process. This might be resulting from very similar reaction conditions required, and the reactions probably occur with the same mechanism. The structure of laser ablation system for synthesizing CNTs is displayed in Fig. 1.14 schematically.

1.3.3 Chemical Vapor Deposition

The process of synthesizing CNTs in chemical vapor deposition system includes heating a catalytic material at high temperature and flowing hydrocarbon gas through the reacting chamber for a period of time. The major parameters in the process are hydrocarbon, catalyst, and temperature. Additionally, the plasma enhanced-CVD was also applied to synthesis the CNTs at relative low temperature[1.82-1.83]. The active catalyst species are typically nanoparticles of transition-metal such as Fe, Ni, or Co. The general growth mechanism of CNTs in chemical vapor deposition system involves dissociation of hydrocarbon molecules catalyzed by the transition-metal, and dissolution and saturation of carbon atoms in the nanoparticles. After that, the carbon atoms precipitate from the saturated nanoparticles and form tubular carbon solids in sp^2 bonding. Due to containing no dangling bonds, tubule formation has lower formation energy and is favored over other forms of carbon such as graphite sheet with open edges. Moreover, the transition-metals, iron, nickel, and cobalt, are also catalyst used in laser ablation and arc discharge. It may hint that the growth

mechanisms of these three different methods are very similar although different approaches are used to provide carbon feedstock. The structure of the chemical vapor deposition system for synthesizing CNTs is shown in Fig. 1.15.

Generally, the CNTs synthesized by utilizing arc discharge and laser ablation feature with better crystallinity as compared with those synthesized by chemical vapor deposition. However, both the arc discharge and the laser ablation require high temperature processes that make it not possible to grow CNTs-based emitters on glass substrates. Moreover, the arc discharge and laser ablation methods also have the drawbacks of needing more expensive equipments and low throughput. Therefore, the method of synthesizing CNTs by chemical vapor deposition is more attractive for the applications of field-emission displays or back-light units. To make the experiments simpler without complex variables, the thermal-CVD is utilized in our experiments to synthesize the CNTs.



1.4 Motivation

Many relative researches for the synthesis or the field-emission characteristics improvements of the CNTs-based field-emission devices have been reported so far. However, only few of them discussed the problems of reliability and uniformity in the field-emission devices. For the purpose of applications, the issues of reliability and uniformity are two of the most critical keys for the commercialization of field-emission displays and back-light units. Therefore, we focus on the issues of reliability and uniformity of the CNTs-based field-emission devices. Furthermore, the increase of emission current density and power efficiency of the CNTs-based field-emission devices are also discussed here (in Chapter 2 and Chapter 5).

1.4.1 Reliability

Generally, two main problems of reliability for the CNTs-based field-emission devices are observed, an abrupt decrease in emission current with increasing applied electric field[1.84] and a gradual degradation of emission current for a long operating time[1.85-1.88]. These two different phenomena might result from different destruction induced from the applied electric field or the field emission current. As a speculation, the electrostatic force and the Joule heat generated by high current density might be the major factors that degrade the reliability of the field-emission devices. In Chapter 2 and Chapter 3, two novel methods are proposed to improve the contact properties, adhesion and contact resistance, between the CNTs and the substrates to suppress the abrupt decrease and gradual degradation of the emission current in the CNTs-based field-emission devices.



1.4.2 Uniformity

Uniformity is the most difficult challenge for the applications of field-emission displays and back-light units, especially for the displays with image size. Several factors could affect the length of CNTs, such as the thickness of catalyst film, the power of plasma, or distribution of hydrocarbon concentration[1.89-1.90]. Due to the difficulty of controlling the diameter, length, direction, and distribution of the CNTs, it is still hard to obtain a uniform emission current from the CNTs-based field-emission devices. Several methods have been proposed to improve the uniformity of the CNTs-based field-emission devices, such as post plasma treatment, modified catalyst, surface treatment, post laser treatment, critical biasing, and post particle blasting[1.91-1.96]. Part of them could improve the uniformity of the CNTs-based field-emission device, however, some of them had problems of complex

processes, causing defects to the CNTs, or increasing the cost. In Chapter 3, a novel method for the deposition of the catalytic metal layer is utilized to obtain CNTs with uniform morphologies. In Chapter 4, man-made emitters are defined by lithography to control the morphologies and distribution of the emitters precisely.

The main idea in this dissertation is to fabricate CNTs-based field-emission devices with reliable and uniform emission current. To achieve the targets here, additional processes or pretreatments before the growth of CNTs are preferred to avoid the damages caused by some post-treatments. Two novel methods of preparing the catalytic metal layer are proposed to improve the reliability and uniformity of the CNTs-based field-emission devices without generating defects in the CNTs seriously.

1.5 Outline of Dissertation

In the first chapter, the relative backgrounds of this dissertation are introduced briefly including the vacuum microelectronics, the field emission theory, and the technologies of field-emission devices. Here the motivation and main ideas for the design of our experiments are also described simply.

In Chapter 2, the mechanism for the destructions of CNTs in field-emission devices during the field-emission measurements are described according to the measurement data and the material analysis results. A method of thin Ti capping layer on the hydrogen pretreated nanoparticles is also proposed for better reliability. Moreover, this method is also applied to control the CNTs density for increasing the emission current density.

In Chapter 3, a Fe-Ti codeposited metal layer is utilized as the catalyst of the CNTs. For reliability issue, a partially immersed structure is achieved and therefore

suppresses the abrupt decrease and gradual degradation of the emission current density. Besides, for the uniformity issue, the coalescence between Fe nanoparticles is suppressed by the Ti in the codeposited layer and, therefore, uniform CNTs are obtained for homogeneous light emission.

In Chapter 4, the pillar-like CNTs are synthesized from the Fe-Ti codeposited catalyst. The growth rate and morphologies of the pillar-like CNTs are discussed here. Moreover, the optimal inter-pillar distance is also obtained via controlling the distance between pillars with lithography. The man-made structure provides uniform distributed electron emitters with small variation in morphologies and high emission current density.

In Chapter 5, a silicon nitride layer is added under the poly-Si gate or above the poly-Si gate in the triode-type field-emission devices to reduce the leakage current between the gates and the cathodes. By cutting off the current paths of the leakage current, the power efficiency of the triode-type field-emission devices was remarkably improved. It also shows a trade-off between the resisting of leakage current and the shielding of extracting electric field.

Finally, all experimental results in the previous chapters and all the suggested works for further researches are summarized in Chapter 6 and Chapter 7, respectively.

Chapter 2

The Improvements of Emission Current Density and Reliability for the CNTs Synthesized from the Ti-Capped Fe Nanoparticles

In this chapter, a novel method of preparing the catalytic metal layer was proposed for the synthesis of the CNTs in the thermal-CVD. By depositing a very thin Ti layer on the hydrogen pretreated Fe nanoparticles, part of the nanoparticles were covered and the density of CNTs was greatly reduced. With a suitable thickness of the thin Ti capping layer, the density of CNTs could be well controlled and suppress the screening effect which could reduce the emission current density seriously. Moreover, the Ti capped on the Fe nanoparticles also played a role of adhesive between the CNTs and the substrates after being heated to improve the contact properties. It suppressed the abrupt decrease and gradual degradation of the emission current.

2.1 Introduction

The emission current density between the cathodes and the anodes is one of the important features that can affect the performance of field-emission devices. With higher emission current density, the driving ability of vacuum microelectronics or the brightness of field-emission displays and back-light units can be greatly improved. According to the description of the field emission theory in chapter 1, there are

several factors that can seriously affect the emission current density, such as the strength of the applied electric field and the work-function Φ , field enhancement factor β , and emission area α of the electron emitters. Among them, the strength of the applied electric field and the work function of emitters have been defined by the architecture of field-emission devices and the chosen emitter material, respectively. The most effective way to increase the emission current density is to enlarge the local enhancement factor and emission areas of the electron emitters. It has been reported that the screening effect caused from the high density of electron emitters can greatly reduce the strength of local electric fields around the tips of emitters and, therefore, decrease the emission current density from the cathodes to the anodes[2.1-2.2]. According to the simulation results, the optimal distance between two CNTs is about two times of its length[2.1]. However, the densities of CNTs synthesized from chemical vapor deposition systems are generally much higher than the optimal density calculated from the simulation. It causes a very serious screening effect around the tips of the CNTs and decreases the local enhancement factor of emitters. The emission current density of CNTs-based emitters is therefore reduced seriously. Several methods have been reported to suppress the screening effect by reducing the density of CNTs in field-emission devices to a suitable value. Some of them separate or passivate the catalytic nanoparticles by adding some processes before synthesizing the CNTs to reduce the density of CNTs[2.2-2.11]. Some of them try to control the density of CNTs by changing the growth conditions during the synthesis processes[2.12-2.15]. The others make some post-treatments after the synthesis process to eliminate part of the grown CNTs[2.16-2.17]. However, some of them increase the complexity or cost of processes or cause defects in the crystal structure of CNTs.

Another critical issue of the CNTs-based field-emission devices is the reliability.

Although CNTs exhibit great mechanical strength and inert chemical properties, the degradation of the emission current density as being applied at high electric field or operated with high emission current density still occur and cause a fatal fail to the field-emission devices. According to several researches, the fails of CNTs during operation can generally be classified into two types: (i) a break of CNTs or a detachment between the CNTs and the substrate in high electric field[2.18] and (ii) a gradual degradation of emission current density for a long operating time or with high emission current density[2.19-2.22]. For the first type, mechanical damages cause an abrupt decrease in the field emission current when we apply a constant or an increasing electric field on the CNTs. It was also found that the CNTs are broken or pulled off from the substrate after being applied at high electric field and exhibit an abrupt drop in the emission current density. For the later one, a gradual degradation of the emission current density was found which might result from the Joule heat generated from high current density. At high temperature, the oxygen remained in the vacuum chamber tends to attack the defective regions in the CNTs. Additionally, the interface structure between the CNTs and the substrates is also getting loose at high temperature that makes the CNTs more easily to be pulled off from the substrate. It causes a gradual degradation of the field-emission current density.

Several methods have been reported to improve the reliability of the CNTs-based electron emitters via modifying the interface between the CNTs and the substrate such as utilizing different interfacial layers[2.23-2.24], making some post-treatments of the CNTs[2.25], and coating a binder or spin-on-glass (SOG) on the CNTs[2.26-2.27]. Via improving the adhesion between the CNTs and the substrate, the breakdown electric field could be increased to prevent from the abrupt decrease in emission current. On the other hand, the improvements of the contact resistance between the CNTs and the substrate could suppress the Joule heating generated with high current

density passing through the defective regions. However, some of the methods cause structural damages to the crystallinity of the CNTs and the others increase the complexity and cost of processes.

In this chapter, a thin Ti layer was capped on the hydrogen pretreated catalytic Fe nanoparticles before the growth of the CNTs. The Ti capping layer can effectively reduce the diffusion of the carbon radicals generated in the thermal-CVD to suppress the growth of CNTs. With different thicknesses of the Ti capping layer, the density of the CNTs was well controlled to a suitable density of about $2 \times 10^7 \text{ cm}^{-2}$. Furthermore, no obvious damage in the crystallinity of the CNTs was found according to the results of material analysis. By this way, the density of CNTs was greatly reduced and the turn-on field was greatly decreased from $3.8 \text{ V}/\mu\text{m}$ to $2.1 \text{ V}/\mu\text{m}$ with 2-nm-thick Ti capping layer.

Moreover, the abrupt decrease and gradual degradation in the emission current density was also suppressed with a 5-nm-thick Ti capping layer. Two different mechanisms were proposed and discussed here to describe the improvements of the reliability. One was the adhesion enhancement and the substrates and the other was the reduction of the contact resistance between the CNTs. According to the measurement results and the SEM images, the breakdown and degradation of the emission current density were both suppressed by depositing a thin Ti capping layer on the hydrogen pretreated Fe nanoparticles.

2.2 Experimental Procedures

2.2.1 Sample Fabrication

An N-type silicon wafer (100) with low resistance ($1\text{-}10 \text{ }\Omega/\text{cm}^2$) was utilized as the substrate. A 50×50 array of square holes with $10 \text{ }\mu\text{m}$ of length and $10 \text{ }\mu\text{m}$ of

inter-space was patterned by lithography system (Fig. 2.1(a)). A 50-nm-thick Ti layer was deposited by a dual-electron-gun physical vapor deposition system as a buffer layer and, then, a 5-nm-thick Fe film was deposited on the Ti layer as the catalyst for the synthesis of CNTs (Fig. 2.1(b)). After the depositions of metal films, the photoresist was removed by a lift-off process in an ultra-sonic vibration tank with acetone solution and only Fe/Ti (5 nm/50 nm) in the holes was left (Fig. 2.1(c)). Then, the samples were loaded into the thermal-CVD to be pretreated in hydrogen (500 s.c.c.m.) at 700 °C for 5 min and the Fe film formed catalytic nanoparticles after that (Fig. 2.1(d)). After the formation of catalytic nanoparticles, a thin Ti layer with different thicknesses, 1, 2, 4, 10, and 20 nm, was deposited on the Fe catalytic nanoparticles in a sputtering physical vapor deposition system (Fig. 2.1(e)). All the samples with different thicknesses of Ti capping layer were loaded into the thermal-CVD again to synthesize the CNTs in ethylene (5 s.c.c.m.) at 700 °C for 10 min (Fig. 2.1(f)). Besides, materials with different melting point such as Mo and Al were also utilized as the capping layer on the hydrogen pretreated nanoparticles to compare with the samples with Ti capping layer. For improving the reliability of the CNTs, the samples without depositing a Ti capping layer were called the conventional samples and the samples with a 5-nm-thick Ti capping layer were called the proposed samples. Here 5 nm was found as the suitable thickness for the Ti capping layer to improve the reliability with acceptable emission current density.

After the growth of the CNTs, both samples were loaded into the vacuum chamber to measure the emission current with an increasing electric field from 0 to 6.6 V/ μm . Moreover, both the samples were stressed at an extremely high electric field of 10 V/ μm for 1 hour. The SEM was utilized to analyze the morphologies of the CNTs before and after the field-emission measurements.

2.2.2 Material Analysis and Electrical Measurement

The micrographs of samples were taken by SEM to see the surface morphologies. Besides, the transmission electron microscope (TEM) and Raman spectra were also applied to analyze the structure and crystallinity of the CNTs. The morphologies of the samples capped with Mo and Al were also taken by the SEM. Furthermore, the energy dispersive spectrometer was applied to examine the nanoparticle enclosed in the CNTs. To obtain the field-emission characteristics, all the samples with different thicknesses of the Ti capping layer were loaded into a vacuum chamber to measure the emission current at about 5×10^{-6} torr. In the chamber, an Indium Tin Oxide (ITO) was utilized as the anode electrode with a distance of 100 μm from CNTs. Moreover, a high-voltage source measurement unit, Keithley 237, was applied on the anode and a high-current source measurement unit, Keithley 238, was applied to the cathode (silicon wafer), as shown in Fig. 2.2. For samples with different thicknesses of Ti capping layer, the samples were measured from 0 to 6 V/ μm to record the emission current density. For the reliability test, both the conventional samples and the proposed samples were measured from 0 to 6.6 V/ μm and stressed at 10 V/ μm for 1 hour.

2.3 The Emission Current Density of the Carbon Nanotubes Synthesized from a Ti Capped Catalytic Nanoparticles

The morphologies for the surface morphologies of the samples with different thicknesses of the thin Ti capping layer, 0, 1, 2, 4, 10, and 20 nm, were taken by the SEM and were shown in Figs. 2.3 (a), (b), (c), (d), (e), and (f), correspondingly.

Without thin Ti capping layer, the density of the Fe nanoparticles distributed on the Ti buffer layer was very high. From Fig. 2.3 (b) to (d), the Fe nanoparticles were getting larger and less with the increase of the Ti capping layer. As the thickness of the Ti capping layer was increased to 10 and 20 nm, the Fe nanoparticles were almost disappeared and only a rough surface of samples was observed in Figs. 2.3 (e) and (f). It resulted from that more Fe nanoparticles were buried under the Ti capping layer as the thickness of the Ti capping layer was increased and eventually totally being immersed into the Ti capping layer. After the deposition of the Ti capping layer, all these six different samples were loaded into the thermal-CVD to synthesize the CNTs in ethylene with the flow rate of 5 s.c.c.m. at 700 °C for 10 min. The surface morphologies of the CNTs were taken by the SEM and displayed in the Figs. 2.4 (a), (b), (c), (d), (e), and (f), respectively. It was very obvious that the number density of the CNTs in those six samples was getting lower with the increasing thickness of the Ti capping layer. In extreme case, there no CNT was observed with 20-nm-thick Ti capping layer in the Fig. 2.4 (f). The reduction of the number density resulted from that more Fe nanoparticles were covered by the Ti as the thickness of the Ti capping layer was increased. The Ti capping layer could reduce the diffusion of the carbon radicals generated at high temperature and therefore suppress the growth of the CNTs. As shown in Fig. 2.5 (a), the Fe nanoparticles were covered by a Ti capping layer. During the synthesis processes of the CNTs at 700 °C in the thermal-CVD, the thickness of the Ti capping layer would be thinner due to that the Ti capping layer was partially melted at 700 °C and tended to merge with the Ti buffer layer under the Fe nanoparticles, as shown in Fig. 2.5 (b). In this case, the carbon radicals with sufficient kinetic energy could penetrate the Ti metal and diffuse into the Fe nanoparticles. If the Ti capping layer was thin enough, the Fe nanoparticles might be exposed after being heated, as shown in Fig. 2.5 (c). In this situation, the carbon radicals could diffuse into

the Fe nanoparticles directly. The speculation for the partially melting of the Ti capping layer might be proved by utilizing other materials with different melting points as the capping layer. As shown in Figs. 2.6, the morphologies of CNTs synthesized from the Fe nanoparticles capped with 5-nm-thick Mo, Ti, and Al capping layer demonstrated that the density of CNTs was relative to the melting point of the capping material. The Mo capping layer with highest melting point showed a lowest density of CNTs and the melting points of these three different materials were 2623 °C for Mo, 1688 °C for Ti, and 660 °C for Al. The suppression for the growth of CNTs showed that the number density of the CNTs could be controlled by the thickness of the thin Ti capping layer. To count the number density of the CNTs, the images of the samples were taken from top view by the SEM and demonstrated in Figs. 2.7. The densities of CNTs for samples with different thickness of Ti capping layer were counted according to the images shown in Figs. 2.7 and listed in Table 2.1. The number density of the CNTs without Ti capping layer was about $10^8\sim 10^9$ cm⁻² and was getting less by increasing the thickness of Ti capping layer. When the thickness of Ti capping layer was increased to 20 nm, there no CNTs was observed in the micrograph of Fig. 2.7(f). It showed that the Ti capping layer could suppress the growth of CNTs and even control the density of CNTs by altering the thickness.

After the synthesis processes in the thermal-CVD, the field-emission characteristics of CNTs were measured in a vacuum chamber at about 5×10^6 torr. The emission current densities versus electric field were plotted in Fig. 2.8(a) and the Fowler-Nordheim plot for the field emission phenomenon was also displayed in Fig. 2.8(b). It can obviously be observed that the emission current densities were varied with different thicknesses of the Ti capping layer and the maximum emission current density was observed in the samples with 2-nm-thick Ti capping layer. Here the turn-on field (E_{on} , V/ μ m) was defined as the required applied electric field for the

emission current density of $10 \mu\text{A}/\text{cm}^2$ and the threshold field (E_{th} , $\text{V}/\mu\text{m}$) was defined as the required applied electric field for the emission current density of $10 \text{mA}/\text{cm}^2$. The turn-on fields and threshold fields of those samples with different thicknesses of the Ti capping layer were listed in Table 2.2 to show the field-emission characteristics of each sample. According to the simulation results[2.1], the local enhancement factor is increased as the screening effect reduced by increasing the inter-emitter distance and the turn-on field is therefore reduced and limited to a constant as the inter-emitter distance approaching to infinite. It was very similar to the experimental results shown in Table 2.2. For the samples with 10-nm- and 20-nm-thick Ti capping layer, the high turn-on and threshold field might due to the reduction of the total emission area and the shorten of the CNTs. An optimal thickness of 2 nm for the thin Ti capping layer with low turn-on field and high emission current density was obtained resulting from the trade-off between the suppression of screening effect and the reduction of total emission area caused by the reduction of the CNTs density.

The analysis results of Raman spectrum for samples with 0, 1, and 2 -nm-thick Ti capping layer were shown in Fig. 2.9 and the signals of samples with thicker Ti capping layers were too weak to be detected. It showed that the Raman analysis results for the CNTs with or without Ti capping layer were very similar. Additionally, the crystal structure of CNTs was also analyzed by TEM after the synthesis process. As shown in Fig. 2.10(a), the CNTs contained a nanoparticle enclosed in the nanostructure. With higher resolution, the image shown in Fig. 2.10(b) demonstrated a multiwalled structure of CNTs clearly. To identify the nanoparticle enclosed in CNTs as shown in Fig. 2.10(a), an analysis of energy dispersive spectrometer was also applied and the results was displayed in Fig. 2.11. In this analysis, only signals of iron, copper, and carbon were detected which implied that the Ti deposited as a capping layer on the Fe nanoparticles seemed not to involve the growth of CNTs in the

thermal-CVD. The peaks of copper here resulted from the copper mesh used in the TEM system as a supporter. According to the material analysis results shown above, the Ti deposited as a capping layer here seemed not to participate in the growth of CNTs or affected the crystallinity of the CNTs seriously but acted as only a resistant layer for the diffusion of carbon radicals.

2.4 2.4 The Reliability Improvements of the Carbon Nanotubes by Modifying the Contact Properties

Referring to the previous section, the density of CNTs was controlled with the thickness of the Ti capping layer. Although the samples with 2-nm-thick Ti capping layer could provide good emission current density, it has no obvious improvement in the reliability of the devices. It has been found that, with 5-nm-thick Ti capping layer, the reliability of the field-emission devices was improved with acceptable emission current. The relationships of the emission current density versus the applied electric field for both the samples without Ti capping layer (here called the conventional samples) and the samples with a 5-nm-thick Ti capping layer (here called the proposed samples) were measured with an increasing applied electric field and the curves were plotted in Fig. 2.12. The measurement results showed that an abrupt decrease of emission current density occurred in the conventional samples as the applied electric field was increased to about 6 V/ μm but no obvious decrease of emission current density was observed in the proposed ones. It also showed that there was almost no emission current was measured in the conventional samples in the second measurement which implied that it was an unrecoverable damage. The morphologies of the conventional samples were taken by the SEM and displayed in

Figs. 2.13. Part of the CNTs in the conventional samples were pulled off from the substrates, as shown in the Fig. 2.13 (a). With higher resolution, the destruction caused from the electrical breakdown could obviously be observed. These micrographs demonstrated that mechanical damages broke the CNTs during the electric breakdown at high electric field which is very similar to the results in the work of Makoto Okai, et al.[2.18]. According to the micrographs in Fig. 2.13, the damages of the CNTs might result from the electrostatic force induced from the applied electric field. The CNTs with weak adhesion for the substrates would be detached when the electrostatic force exceeded the strength of the contact between the CNTs and the substrates and, therefore, cause an abrupt decrease in emission current density. The suppression of the abrupt decrease in emission current density might due to that the adhesion between the CNTs and the substrates was enhanced by depositing a Ti capping layer before growing the CNTs. As described in previous section, the Ti was partially melted and tended to merge with the Ti buffer layer under the Fe nanoparticles. Therefore, the melted Ti held the Fe nanoparticles more firmly as compared with the samples with no Ti capping layer. It helped the CNTs to sustain the electrostatic force induced from the applied electric field and suppresses the breakdown of the CNTs.

Furthermore, the emission current of both the conventional and proposed samples were measured at a very high electric field of $10 \text{ V}/\mu\text{m}$ for 1 hour and the curves of emission current density versus time were displayed in Fig. 3.4(a). The emission current density of the conventional samples in the first 6 sec was so high that the variation in the curve of emission current density after 6 sec could not be observed clearly, as shown in Fig. 3.4(b), and therefore the points of the first 6 sec were removed from the Fig. 3.4(a). According to the curves shown in Fig. 3.4(a), the emission current density of the conventional samples dropped to almost zero in the

first few seconds but the emission current density of the proposed samples was kept about 7 mA/cm^2 for first 5 min and then dropped to 3 mA/cm^2 . Although the emission current density of the proposed samples gradually degraded in the next 55 min to about 3 mA/cm^2 , the CNTs in the proposed samples still showed better reliability than those in the conventional samples. The high emission current density for the conventional samples might result from that the screening effect was a relative minor factor at high electric field for the emission current density so that the higher density of CNTs could provide much larger emission area than those in the proposed samples and. Additionally, the morphologies of the CNTs in both samples were taken by the SEM before and after being stressed for 1 hour and displayed in Figs. 3.5. Interestingly, the CNTs in the proposed samples showed only slightly difference in the density of CNTs before and after being stressed for 1 hour, as shown in Figs. 3.5(b). However, as displayed in Figs. 3.5(a), the CNTs in the conventional samples were transformed into amorphous-like carbon after being stressed for 1 hour. It might be due to the Joule heat generated with a high current density passing through the defective regions of the CNTs during the stress. If the contact properties between the CNTs and the substrates were not very well, the contact resistance will be high and a great deal of heat would be generated with high current density passing through and cause a high temperature in the defective regions. At extreme high temperature, the CNTs might evaporate and form amorphous-like material during the stress and the oxygen remained in the vacuum chamber also tend to react with the defective regions in the CNTs. The strength of the contact structure would also be degraded at high temperature and the CNTs could subsequently be detached by the electrostatic force induced from the applied electric field. All of them caused an unrecoverable destruction that degraded the emission current density of the field-emission devices. A Ti capping layer could improve the contact properties between the CNTs and the

substrates after being heated which reduced the contact resistance between the CNTs and the substrates and suppressed the Joule heat generated with high current density.

2.5 Summary

By depositing a thin Ti capping layer on the hydrogen pretreated Fe nanoparticles, the diffusion of the carbon radicals generated in the thermal-CVD was resisted. The density of the CNTs was greatly reduced to a suitable density of $2 \times 10^7 \text{ cm}^{-2}$ with an optimal thickness of the Ti capping layer, 2 nm. The screening effect caused from the high density of the CNTs was effectively suppressed and therefore increase the local enhancement factor on the tips of the CNTs. By this way, the turn-on field was greatly reduced from $3.8 \text{ V}/\mu\text{m}$ to $2.5 \text{ V}/\mu\text{m}$. On the other hand, from the results of the material analysis, the CNTs synthesized from the Fe nanoparticles capped by a thin Ti metal layer showed a well multiwalled structure with no obvious difference from those synthesized from the Fe nanoparticles without capping layer. The Ti capped on the nanoparticles seemed not involve in the growth of the CNTs.

Furthermore, the Ti capping layer would melt and hold the Fe nanoparticles after being heated. It enlarged the contact area between the CNTs and the substrates to enhance the adhesion and reduce the contact resistance. With strong adhesion between the CNTs and the substrates, the CNTs could sustain large electrostatic force induced from the applied electric field and therefore suppressed the abrupt decrease in the emission current density. Moreover, the reduction of contact resistance also ease the Joule heat generated with high current density passing through the high resistive regions. The high temperature due to the Joule heat could make the remained oxygen react with defective regions in the CNTs, cause the evaporation of the CNTs, or

degrade the interfacial structure between the CNTs and the substrates. Therefore, the abrupt decrease or gradual degradation of the emission current density were both suppressed by means of utilizing the Ti capping layer.



Chapter 3

The Improvements of Reliability and Uniformity for the CNTs Synthesized from the Fe-Ti Codeposited Catalyst

In this chapter, a novel method of preparing the catalyst was proposed for improving the reliability and uniformity of the CNTs synthesized in the thermal-CVD. A partially immersed structure of the CNTs was achieved by using this novel method which enlarged the contact area to enhance the adhesion and reduce the contact resistance. The abrupt decrease and the gradual degradation of the emission current density were both suppressed by this way. Moreover, the coalescence between the Fe nanoparticles was also reduced to obtain the uniform nanoparticles in size and location distribution and, therefore, gained a uniform light emission.

3.1 Introduction

As discussed in the previous chapter, the reliability of the CNTs -based field-emission devices is one of the most critical keys that greatly determines the commercialization of the field-emission displays or the back-light units. Another critical issue that also plays a very important role for the applications of the CNTs in the field-emission displays or the back-light units is the uniformity of the CNTs in the field-emission devices. The uniformity of light emission in a CNTs-based field-emission displays and back-light units is the most difficult and emergent problems that needed to be solved. Especially for the field-emission displays, the

precise control of light intensity is required to obtain a display with high image quality. However, the lack in the mechanisms of the growth of CNTs leads to large variations of the CNTs in length, diameter, direction, and structure during the synthesis processes. The length of the CNTs, especially, affects the field-emission characteristics most seriously. It is hard to fabricate CNTs with uniform length, diameter, and distribution no matter what synthesis method is used, arc discharge, laser ablation, or chemical vapor deposition. For the screening printing technologies, the CNTs with good crystallinity synthesized from arc discharge, laser ablation, or other high temperature processes are dealt with some physical and/or chemical post-treatments to get similar length and diameter but the uniformity of light intensity is still poor in general cases owing to the random distribution of the CNTs after the screen printing. For the CNTs grown on the substrates by chemical vapor deposition systems directly, it is still difficult to control the length, diameter, or morphologies of the CNTs to be uniform due to the diameter variation of the catalytic nanoparticles. The non-uniformity in length, diameter, and location distributions of the CNTs could greatly affect the uniformity of the light intensity in the field-emission displays or back-light units. It has been reported that the non-uniformity of the light emission is greatly attributed to the emission current density which is strongly affected by the aspect ratio of the CNTs[3.1]. Several methods, like post plasma treatment[3.2], catalyst pretreatment[3.3], surface treatment[3.4], critical bias applying[3.5], post laser treatment[3.6], post particle blasting[3.7] have been proposed to improve the uniformity of luminance in the CNTs-based field-emission displays or back-light units. Unfortunately, the some of them cause structural damages by utilizing the post-treatments and the others require more complex processes that may increase the cost or reduce the throughput of products.

In this chapter, an Fe codeposited with Ti was utilized as a novel catalyst for the

synthesis of CNTs in the thermal-CVD. By this way, the coalescence between the Fe nanoparticles during the hydrogen pretreatment and the growth of the CNTs is suppressed and uniform Fe catalytic nanoparticles are observed. Therefore, uniform CNTs with small variation in length and uniform location distribution are gained after the synthesis process. A homogeneous light emission is observed on the glass coated with indium-tin-oxide (ITO) and green phosphor (P22) by using the CNTs synthesized from the Fe-Ti codeposited catalyst. Here the CNTs synthesized from pure Fe catalyst are called the conventional samples and those synthesized from the Fe-Ti codeposited catalyst are called the proposed samples. The percentages of the light emitting area for the proposed samples with the dimension of 1 cm×1 cm are improved from 12 % to 29 % at 500 V, from 41 % to 75 % at 600 V, and from 86 % to 100 % at 700 V as compared to the conventional samples with the same dimension. No extra mask and processes are required by using this novel Fe-Ti codeposited catalyst. Such a method exhibits its simplicity and merits which are very potential in the applications of the field-emission displays or back-light units to improve their luminescent uniformity.

3.2 Experimental Procedures

3.2.1 Sample Fabrication

The N-type silicon wafers (100) with low resistance ($1\sim 10 \Omega/\text{cm}^2$) were utilized as the substrates in this experiment. An array of 5×5 square holes with 100 μm in length and 100 μm interspacing were patterned by the lithography system on a photoresist film. After the lithography processes, a 50-nm-thick Ti layer was deposited by the dual-electron-gun physical vapor deposition system as a buffer layer between the CNTs and the substrate. To compare with the proposed method, two kinds of samples were prepared as the conventional samples and the proposed

samples. For the conventional samples, a 5-nm-thick pure Fe film was deposited by the dual-electron-gun physical vapor deposition system as the catalyst on the Ti buffer layer. On the other hand, Fe and Ti were codeposited by the dual-electron-gun physical vapor deposition system as a novel catalyst on the Ti buffer layer with weight percentage of 64% for Fe and 36% for Ti. Besides, the quantity of Fe was the same for the conventional samples. After the deposition of buffer layer and catalyst, the photoresist was removed by a lift-off process in acetone solution to leave the Ti buffer layer with the catalyst in the squared holes only. Both samples were loaded into the chamber of thermal-CVD to be pretreated in hydrogen ambient ($H_2/N_2 = 400/600$ s.c.c.m.) at $700\text{ }^\circ\text{C}$ for 5 min and subsequently grew the CNTs in the same chamber with ethylene ($C_2H_4/H_2/N_2 = 5/100/10$ s.c.c.m.) at $700\text{ }^\circ\text{C}$ for 15 min. To demonstrate the process steps more clearly, a flowchart was displayed in Figs. 3.1 schematically.

3.2.2 Material Analysis and Electrical Measurement

After the synthesis of CNTs, the images of the CNTs in both samples were taken by SEM and the crystallinity of the CNTs in the proposed samples was analyzed by TEM and Raman spectrum. An energy dispersive spectrometer was also applied to analyze the composition of the nanoparticles enclosed in the CNTs. The field-emission properties of the CNTs in both samples were measured in a vacuum chamber at 5×10^{-6} torr, as described in Chapter 2. Both the conventional and the proposed sample were measured from 0 to $7.7\text{ V}/\mu\text{m}$ 5 times and stressed at $7.7\text{ V}/\mu\text{m}$ for 2,500 sec. After the stress, both samples were measured from 0 to $7.7\text{ V}/\mu\text{m}$ again to estimate if the curves were changed after being stressed at $7.7\text{ V}/\mu\text{m}$ for 2,500 sec.

For the uniformity issue, the morphologies of the catalytic nanoparticles after the hydrogen pretreatment were analyzed by an atomic force microscope and SEM for

both samples before the synthesis of the CNTs. The morphologies of the CNTs in both samples were also analyzed by the SEM. Furthermore, the samples were loaded into a vacuum chamber to measure the field emission current at about 5×10^{-6} torr. The phosphor (P22) common used in the cathode-ray tube displays was deposited on a transparent conductive material, indium-tin-oxide (ITO), to be an anode electrode in the vacuum measurement system and the cathode voltage was applied to the silicon substrates. The measurement system was the same as that described in Chapter 2 (Fig. 2.2) schematically. To observe the images of luminescence, samples of a square with 1 cm^2 without pattern were also prepared by growing the CNTs with both the conventional and the proposed methods. The luminescent images of both samples were taken by a digital camera when the anode was applied at 500, 600, and 700 volts.

3.3 A Partially Immersed Structure of the Carbon Nanotubes for the Reliability Improvements

For both the conventional and the proposed samples, the micrographs of the CNTs synthesized in the thermal-CVD were taken by the SEM and displayed in Figs. 3.2. The micrograph for the conventional specimens in Fig. 3.2(a) displayed that the roots of the CNTs synthesized from the pure Fe catalyst seemed to terminate on the surface of the Ti buffer layer only. However, the micrograph of the proposed specimens in Fig. 3.2(b) showed that the CNTs synthesized from the Fe-Ti codeposited catalyst seemed to partially immerse into the codeposited metal layer. To check the partially immersed structure, the proposed specimens were cleaved across the patterned area and the micrograph along the cleaved edge was also taken by SEM. As shown in Fig. 3.2(c), a CNT partially immersed into the codeposited metal layer

was observed along the cleaved edge and marked by a circle. Moreover, the microstructure of the CNTs synthesized from the Fe-Ti codeposited catalyst was analyzed by the TEM and the images were displayed in Figs. 3.3. The micrograph shown in Fig. 3.3(a) demonstrated a CNT with an enclosed nanoparticle. With higher resolution, a multiwalled structure of CNTs was clearly observed in Fig. 3.3(b). According to the phase diagram of Fe-Ti shown in Fig. 3.4, the codeposited catalyst should form alloy FeTi during the growth process in the thermal-CVD at 700 °C[3.8]. To identify the composition of the enclosed nanoparticle in Fig. 3.3(a), an analysis of energy dispersive spectrum was also applied to the enclosed nanoparticles and the results were shown in Fig. 3.5. According to the results of the energy dispersive spectrum, only signals of Fe, Cu, and C were detected in the enclosed nanoparticles which implied that the Ti codeposited with the Fe in the catalyst seemed not to involve in the synthesis of the CNTs in the thermal-CVD. The signals of Cu originated from the Cu mesh used in the TEM as a supporter. Moreover, the Raman analysis was also applied to analysis the structure of the CNTs in the conventional samples and the proposed samples. As shown in Fig. 3.6, no obvious difference in the Raman analysis was observed which showed that the Ti codeposited with the Fe seemed not affect the crystallinity of the CNTs seriously. To illustrate the synthesis of the CNTs in both samples, the formation of the catalytic nanoparticles and the growth of the CNTs for both the conventional and the proposed samples were displayed in Fig. 3.7 (a) and 3.7 (b), correspondingly. As shown in Fig. 3.6(a), the Fe film formed Fe nanoparticles in the conventional samples resulting from that the surface energies of the Fe catalytic film was higher than the surface energies of the Ti buffer layer and, then, synthesized the CNTs which terminated on the surface of the Ti buffer layer only. However, as shown in Fig. 3.7(b), the Fe atoms nucleated in the codeposited metal layer due to higher surface energy than Ti and the Ti in the codeposited layer merged

with the Ti buffer layer at the same time in proposed specimens. The surface energies of Fe and Ti were shown in Fig. 3.8 where the surface energy of Fe is 2.9 J/m^2 and of Ti is 2.6 J/m^2 [3.9-3.10]. In the proposed samples, the Fe nanoparticles were partially buried in the codeposited metal layer and the CNTs synthesized from those embedded Fe nanoparticles partially immersed into the metal layer were observed after the growth process in the thermal-CVD. Figures 3.9(a) and 3.9(b) showed the curves of the emission current density versus the applied electric field for the five measurements before being stressed and one measurement again after being stressed for both the conventional and the proposed samples, correspondingly. In Fig. 3.9(a), the 1st curve exhibited an abrupt decrease in the emission current density (indicated by an arrow) while the other curves from 2nd to 5th measurement were smooth and had no obvious difference to each other. The abrupt decrease in emission current density in the 1st curve might resulted from that part of CNTs with weak adhesion were pulled off from the substrates and the CNTs with strong adhesion kept the curves unchanged in the subsequently four measurements. In Fig. 3.9(b), no abrupt decrease in the emission current density was observed and the curves from 2nd to 5th measurements were almost the same with only slight difference from the 1st measurement. It resulted from that the partially immersed structure in the proposed samples provided a stronger adhesion between the CNTs and the substrates than those in the conventional samples. After the five measurements, both specimens were stressed under a electric field of $7.7 \text{ V}/\mu\text{m}$ for 2,500 sec and the curves of emission current density versus operating time for both conventional and proposed specimens were plotted in Figs. 3.10(a) and 3.10(b) correspondingly. The emission current density of the conventional samples decreased from 60 mA/cm^2 to 20 mA/cm^2 after being stressed for 750 sec and the emission current density of the proposed ones maintained about 30 mA/cm^2 for 2,500 sec without obvious degradation. It may result

from that the reduction of the contact resistance between the CNTs and the substrates in proposed samples would suppress the Joule heating generated in the high resistive contact regions and, therefore, suppress the instability of emission current induced from high temperature. It showed that the CNTs synthesized from the Fe-Ti codeposited catalyst had the feature of better reliability than those synthesized from the pure Fe catalyst. After being stressed, the curves of emission current density versus applied electric field for both samples were measured again and plotted in Figs. 3.9. The emission current density was greatly reduced after being stressed for the conventional specimens as shown in Fig. 3.9(a). However, the curve for the proposed samples after being stressed was just slightly altered as shown in Fig. 3.9(b). Moreover, the morphologies of the CNTs before and after being stressed for both conventional and proposed samples were taken by SEM and demonstrated in Fig. 3.10. Obviously, the density of CNTs in the conventional samples was reduced after being stressed while the density of the CNTs in the proposed ones had no serious change in the morphology after being stressed. According to the curves in Figs. 3.9 and Figs. 3.10 and the micrographs in Fig. 3.11, the CNTs synthesized from the Fe-Ti codeposited catalyst could suppress both the abrupt decrease and the gradual degradation in the emission current density as compared to those synthesized from the pure Fe film. The improvements of the abrupt decrease in the emission current density for the proposed samples might result from that the enlarged contact area of the partially immersed structure could enhance the adhesion between the CNTs and the substrates to increase the mechanical strength of the emitters. Additionally, the enlarged area in the proposed samples also reduce the contact resistance between the CNTs and the substrates which could suppress the Joule heat generated with high current density passing through the high resistive regions and therefore ease the gradual degradation in the emission current density for a long operating time.

3.4 The Suppression of the Coalescence between Fe Nanoparticles for a Uniform Light Emission

The micrographs of the catalytic nanoparticles for the conventional and the proposed samples were taken by the SEM from top-view and displayed in Fig. 3.12 (a) and 3.11(b), respectively, after being pretreated in hydrogen ambient at 700 °C for 5 min in the thermal-CVD. As shown in Figs. 3.12, the catalytic nanoparticles in the conventional samples have larger diameter and diameter variation than those in the proposed samples. Additionally, the atomic force microscope analysis was also applied to the nanoparticles in both the conventional and the proposed samples and the results were shown in Figs. 3.13(a) and 3.13(b), correspondingly. A more uniform distribution of catalytic nanoparticles with smaller variation in diameter was also observed in the proposed samples, as shown in Fig. 3.13(b), as compared with the catalytic nanoparticles in the conventional samples, as shown in Fig. 3.13(a). After the synthesis of CNTs at 700 °C for 15 min, the morphological images of the CNTs were taken by the SEM and displayed in Figs. 3.13. With 45° viewing angle, the morphologies of the CNTs in both the conventional and the proposed samples were demonstrated in Fig. 3.14(a) and 3.14(b), respectively. Moreover, the cross-sections of the CNTs for both the conventional and the proposed samples were displayed in Fig. 3.14(c) and 3.14(d), correspondingly. According to the images in Fig. 3.14(a) and 3.14(b), the CNTs in the conventional samples showed a rough top plane and the proposed samples showed a flat top plane. From the comparison between the cross-sectional views of the CNTs of the conventional and the proposed samples in Figs. 3.14(c) and 3.14(d), the CNTs in the conventional samples also exhibited a

much larger length variation than the proposed ones. It had been reported that the growth rate of CNTs was dependent on the size of catalyst[3.11]. Therefore, the uniform CNTs in the proposed samples might contribute to the uniform distribution in the diameter of the catalytic nanoparticles after hydrogen pretreatment. Referring to the results of the material analysis in previous section, the Ti codeposited with the Fe seemed not involved in the synthesis of the CNTs or affected its crystallinity seriously. To explain the uniform catalytic nanoparticles in the proposed sample, the formation schemes of the nanoparticles for the conventional samples and the proposed ones were plotted in Figs. 3.15(a) and 3.15(b), respectively. For the conventional samples, the Fe catalyst transferred from a film to nanoparticles directly at 700 °C due to the higher surface energy of Fe than Ti and subsequently the coalescence of these nanoparticles proceeded, as shown in Fig.3.15(a). However, in the proposed samples, Fe atoms nucleated at 700 °C to form nanoparticles due to the higher surface energy of Fe than Ti and the codeposited Ti atoms merged with the underlaid Ti buffer layer, as shown in Fig. 3.15(b). Owing to the existence of the codeposited Ti, the coalescence of the Fe nanoparticles was retarded and suppressed during the pretreatment process or the synthesis process. Hence, the catalytic nanoparticles in the proposed samples were much smaller in diameter distribution and more uniform in location distribution as compared with those in the conventional ones. The emission current densities of both samples were thus measured by 0 to 7.7 V/ μm with the cathode-anode distance as 130 μm and the curves of emission current density versus applied electric field were shown in Fig. 3.16. The emission current density was about 65 mA at 7.7 V/ μm for the conventional samples and about 46 mA at 7.7 V/ μm for the proposed ones. The slightly higher emission current density of the conventional samples than the proposed ones may attribute to the milder screening effect induced from the CNTs in the conventional samples. However, for application purposes, the

emission current density of the proposed samples is none the less high enough. In contrast, the luminescent images for the conventional samples operated at 500, 600, and 700 anode voltages were displayed in Figs. 3.17(a) and those for the proposed samples operated at the same conditions were shown in Figs. 3.17(b). Both the conventional and the proposed samples had a CNTs film with 1 cm² area. As compared to the conventional samples, the percentages of emission area for the proposed samples were improved from 12% to 29% at 500 V, from 41% to 75% at 600 V, and from 86% to 100% at 700 V. The improvement of emission uniformity for the proposed samples may due to that a uniform CNTs film in proposed samples can prevent from non-uniform electric field distribution as compared to a rough CNTs film in the conventional ones. A non-uniform local field enhancement could cause a non-uniform emission current here. Obviously, the uniformities of the light emissions under the corresponding conditions were significantly improved for the proposed samples as compared with the conventional ones.

3.5 Summary

By utilizing a Fe-Ti codeposited metal layer as the catalyst of the CNTs, a partially immersed structure was achieved which enlarge the contact area between the CNTs and the substrates. An abrupt decrease in the emission current density due to weak adhesion between the CNTs and the substrates was therefore suppressed. Moreover, the gradual degradation in the emission current density was also improved by this way. It might result from that the Joule heat generated in the high resistive contact regions with high current density passing through caused some high temperature induced structural destructions to the CNTs. A relative stable emission current was obtained and no obvious change in the curve of emission current density

versus electric field was observed after being stressed at $7 \text{ V}/\mu\text{m}$ for 2,500 sec.

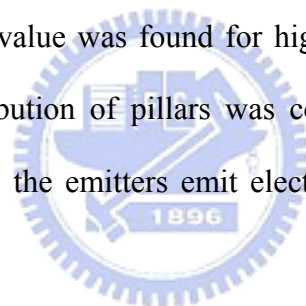
Furthermore, the coalescence between the Fe nanoparticles in the proposed samples was also suppressed by the codeposited Ti. The uniform and small Fe nanoparticles were observed after being pretreated in hydrogen ambient and, therefore, obtained the CNTs with small variation in length. It resulted in a flat top plane of the CNTs in the proposed samples which could reduce the variation of the local field enhancement and provide a uniform emission current. As compared to the conventional samples, the percentages of emission area for the proposed samples were improved from 12% to 29% at 500 V, from 41% to 75% at 600 V, and from 86% to 100% at 700 V.

According to the results of material analyses, the TEM, Raman spectrum, and energy dispersive spectrum, the Ti codeposited with the Fe seemed not involved the synthesis of the CNTs in the thermal-CVD. A well multiwalled structure was observed with no obvious structural damages. This simple and costless method showed a great potential in the applications of the field-emission displays and the back-light units.

Chapter 4

The Synthesis and Characteristics of the Pillar-Like CNTs Synthesized from the Fe-Ti Codeposited Catalyst

To obtain electron emitters with low turn-on field, high emission current density, and uniform emission current, pillar-like CNTs were formed in the thermal-CVD from an Fe-Ti codeposited catalyst. By controlling the ratio of distance between pillars (R) to its height (H), an optimal value was found for high emission current density and low turn-on field. The distribution of pillars was controlled by lithography and it could also make sure that all the emitters emit electrons without being affected by serious screening effect.



4.1 Introduction

Screening effect is a very important factor that can reduce the emission current density of CNTs seriously. Several methods, as mentioned in chapter 2, have been proposed to optimize the density of CNTs for suppressing the screening effect. Nevertheless, a high emission current density shown in the measurement results does not mean that a more uniform distribution of emission current can be obtained. If the distribution of emission sites is not uniform, it is still hard to achieve a uniform emission current even the total emission current measured over a certain area is very high. In chapter 4, a uniform emission current was shown by using CNTs synthesized from an Fe-Ti codeposited catalyst as emitters but the emission current density was also

obviously reduced due to serious screening effect resulting from the high density of the CNTs. To possess both the properties of low turn-on field and uniform emission current, pillar-like CNTs were formed by lithography to control the position of emitters. The synthesis and properties of pillar-like CNTs have been reported in several researches[4.1-4.4]. A very high emission current density (100 mA/cm^2 at $1.7 \text{ V}/\mu\text{m}$) with ultra-low turn-on field ($0.4 \text{ V}/\mu\text{m}$) was demonstrated for pillars of $50 \mu\text{m}$ diameter, $250 \mu\text{m}$ interpillar spacing, and $125 \mu\text{m}$ height[4.4]. Moreover, an image of uniform light emission was also obtained with very strong intensity. It is a very promising electron source in field-emission displays[4.5], flat lamp[4.6], or back-light units[4.7].

However, for application purpose, the length of pillar-like CNTs should be controlled to a proper value to make the design of the field-emission devices more easily. For example, a long pillar-like CNTs is hard to realize a typical triode-type field-emission device due to the difficulty of depositing such a thick insulating layer. Besides, length variation resulting from the difference of growth rate locally might be serious if the length of CNTs is too long. In this chapter, pillar-like CNTs of $12 \mu\text{m}$ in height were formed with different interpillar spacing to gain an optimal R/H ratio. A relative low turn-on field of $0.82 \text{ V}/\mu\text{m}$ was obtained with R/H ratio of 2.5 which is similar as the prediction of Nilsson et al.[4.8]. Furthermore, pillar-like CNTs synthesized from a 5-nm-thick pure Fe catalyst were also prepared to compare with those grown from the Fe-Ti codeposited catalyst.

4.2 Experimental Procedures

4.2.1 Sample Fabrication

The substrates utilized in this experiment were N-type silicon wafers with low

resistance. By using a lithography system, an array of circle holes with 6- μm diameter and 9- μm inter spacing in a rectangular of with 1-mm width and 2-mm length was formed on the silicon substrates. After that, a 50-nm-thick Ti metal layer was deposited by the dual-electron-gun physical vapor deposition system as a buffer layer between the CNTs and the silicon substrates. To compare the CNTs synthesized from the pure Fe catalytic film and from the Fe-Ti codeposited catalytic film, both a 5-nm-thick Fe metal film and a Ti-Fe codeposited film were deposited on the Ti buffer layer in the same system. Here the samples with pure Fe catalytic film were named as conventional samples and those with Fe-Ti codeposited film were named as proposed samples. Additionally, the Fe in the proposed samples kept a constant quantity as compared with the conventional ones. For both samples, the photoresist was removed by a lift-off process in an acetone solution to leave the Ti buffer layer with catalyst in circle holes only. After the lift-off process, both samples were loaded into a thermal-CVD to be pretreated in hydrogen ambient ($\text{N}_2/\text{H}_2 = 500/100$ s.c.c.m.) at 700 °C for 8 min and then synthesized CNTs with ethylene ($\text{C}_2\text{H}_4/\text{N}_2/\text{H}_2 = 20/500/100$ s.c.c.m.) at 700 °C for 8, 15, 30, 60, and 120 min. The flowchart of experiment was demonstrated in Figs. 4.1 schematically.

For the optimization of the inter-pillar distance, the experimental procedures were the same as described in previous section. A hole-array of circles with 6 μm in diameter and different inter spacing of 12, 15, 20, 25, 30, and 35 μm were form by lithography. The dimension of hole-array is 1 mm in width and 2 mm in length. A 50-nm-thick Ti was deposited by dual electron-gun physical vapor deposition system as a buffer layer. Subsequently, a 10-nm-thick Fe-Ti codeposition was also deposited by dual E-gun as the catalyst of pillar-like CNTs. The weight percentage of Fe in the codeposited catalyst is 64%. Then, the photoresist was removed by a lift-off process in an ultrasonic cleaner with acetone solution and only Ti buffer layer and Fe-Ti

codeposited catalyst were left in the circle holes. After that, the samples were loaded into the thermal-CVD to be pretreated in hydrogen ambient ($N_2/H_2 = 500/100$ s.c.c.m.) at $700\text{ }^\circ\text{C}$ for 8 min and then synthesized CNTs with ethylene ($C_2H_4/N_2/H_2 = 20/500/100$ s.c.c.m.) at $700\text{ }^\circ\text{C}$ for 15 min. The processes of experiment here was the same with the processes in previous section as shown in Figs. 4.1.

4.2.2 Material Analysis and Electrical Measurement

After the synthesis of pillar-like CNTs, the images of morphologies were taken by a SEM. The field-emission characteristics were measured in a high vacuum environment of 5×10^{-6} Torr as described in Chapter 2. A glass coated with indium-tin-oxide was positioned 150 μm above the tip of the pillar-like CNTs as the anode electrode. The anode voltage was applied by a Keithley 237 high-voltage source measurement unit and the cathode voltage was applied by a Keithley 238 high-current source measurement unit.

4.3 The Synthesis of the Pillar-Like Carbon Nanotubes by Utilizing the Fe-Ti Codeposited Catalyst

The cross-section views of the pillar-like CNTs synthesized in the thermal-CVD with different catalyst, the pure Fe film and the Fe-Ti codeposited film, were taken by SEM and displayed in Figs. 4.2 and Fig. 4.3, correspondingly. The lengths of the pillars synthesized from pure Fe film for different time were about 5.6 μm for 8 min, 15.7 μm for 15 min, 22.4 μm for 30 min, 47 μm for 60 min, and 69.8 μm for 120 min.

On the other hand, the lengths of the pillars grown from the Fe-Ti codeposited catalyst for different time were about 4.48 μm for 8 min, 12 μm for 15 min, 19.4 μm for 30 min, 52.2 μm for 60 min, and 118 μm for 120 min. The relationship between the length and the growth time for both samples were plotted in Fig. 4.4. As shown in Fig. 4.4, the growth rate of CNTs in the conventional samples seemed to saturate when the growth time was over 60 min and the growth rate of CNTs in the proposed samples sustained almost a constant in 120 min. The growth rate was about 0.78 $\mu\text{m}/\text{min}$ in the first 60 min and 0.38 $\mu\text{m}/\text{min}$ in the last 60 min for the conventional samples and was about 0.98 $\mu\text{m}/\text{min}$ for the proposed samples. The micrographs of the nanoparticles after being pretreated in hydrogen ambient for both the conventional and the proposed samples were shown in Figs. 4.5(a) and 4.5(b) respectively. Similar to the results shown in Chapter 3, the nanoparticles in the proposed samples were much smaller and more uniform than those in the conventional samples which resulted from the different mechanisms for the formation of nanoparticles as discussed in Chapter 3. From Fig. 4.4, the growth rate of the conventional samples was slightly faster than that of the proposed samples in the first few minutes. It might result from the higher surface to volume ratio in the conventional samples than in the proposed samples. A diagram was shown in Fig. 4.6, to calculate the surface to volume ratio of a sphere partially immersed in the substrate. The volume of the sphere is

$$\begin{aligned}
 & \text{Volume} \\
 &= \int_0^r \left(\int_0^\pi 2\pi(r \sin \theta)(r d\theta) \right) dr \\
 &= \int_0^r 4\pi r^2 dr \\
 &= \frac{4}{3} \pi r^3
 \end{aligned} \tag{4.1}$$

and the surface area appeared out of the substrate is

Surface

$$\begin{aligned} &= \int_0^\Phi 2\pi(r \sin \theta)(rd\theta) \\ &= 2\pi r^2(1 - \cos \Phi) \end{aligned} \quad (4.2)$$

The surface to volume ratio is obtained from Eq. 5.1 and Eq. 5.2:

$$\begin{aligned} S/V &= \frac{2\pi r^2(1 - \cos \Phi)}{\frac{4}{3}\pi r^3} \\ &= \frac{3(1 - \cos \Phi)}{2r} \end{aligned} \quad (4.3)$$

The surface to volume ratio versus radius of sphere and the angle θ was plotted in Figs. 4.7. Refer to the SEM image in Fig. 4.5, the radius of nanoparticles in the conventional samples was about 50 nm and that in the proposed samples was about 20 nm. If the θ in the proposed samples was less than 80° , the surface to volume ratio of the proposed samples was smaller than that of the conventional samples. The growth rate of CNTs was related to the diffusion rate of carbon radical which is also related to the surface to volume ratio. However, the growth rate in the conventional samples decreased after about 40 min which might result from that the smaller nanoparticles in the proposed samples could keep the activity during the synthesis process better than the conventional samples as compared with those in the conventional ones. Moreover, the CNTs in the proposed samples seemed straighter than in the conventional samples from the images taken by SEM with higher resolution, shown in Fig. 4.8. It may be due to the higher density of nanoparticles in the proposed samples which restricted the growth direction of the CNTs.

4.4 The Optimization of the Inter-Pillar Spacing Designed via the Lithography

The micrographs of the pillar-like CNTs with different interpillar spacing, 12, 15, 20, 25, 30, and 35 μm , were taken by SEM and shown in Figs. 4.9. Arrays of pillar-like CNTs in the shape of columns were observed. To show the height of pillars in different samples, cross-sectional views of the pillar-like CNTs were also displayed in Figs. 5.10. From the images displayed in Figs. 4.10, the height of pillar-like CNTs were all about 12 μm and the interpillar spacing was well-defined by lithography. The emission currents of samples were measured in a vacuum environment of 5×10^{-6} Torr and the curves of emission current of samples versus applying voltage were plotted in Fig. 4.11(a). Additionally, the Fowler-Nordheim plot for each sample was also demonstrated in Fig. 4.11(b) to show a Fowler-Nordheim field emission. The emission current of device was divided by the device area (0.02 cm^2) to get turn-on field and threshold field of one device and the results were shown in Table 4.1. The curve of the turn-on field versus the interpillar spacing was plotted in Fig. 4.12 and showed that the turn-on field remain almost a constant for the R/H ratio was larger than 2.5. As the simulation results shown in the work of Nilsson, et al., the screening effect is greatly reduced when the interspacing of emitters is two times of its height. The local enhancement factor will not be improved obviously even the interspacing between emitters was increase greatly. It also hinted that the turn-on field will not be decreased remarkably with increasing the interpillar spacing more. The emission currents of these samples were measured at 800 V for 1 hour and the average of emission current density versus interpillar spacing plotted in Fig. 4.13. As shown in this figure, the emission current density increased rapidly with enlarging interpillar spacing from 12 μm to 25 μm and then increased slowly even a slightly decreased with larger interpillar spacing. The increasing of emission current resulted from the suppression of screening effect by enlarging the interpillar spacing, however, the improvement in screening effect was getting unobvious and the emission areas was

also getting small that caused a reduction of the total emission current of the devices. The trade-off between the suppression of screening effect and the reduction of emission area led to an optimal interpillar spacing to obtain a maximum emission current and here was 30 μm , about 2.5 times of the height of pillars, in our experiments. The luminescent image of the pillar-like CNTs was also taken by a digital camera by applying the anode at 800 V, as shown in Fig. 4.14.

4.5 Summary

The pillar-like CNTs synthesized from the Fe-Ti codeposited catalyst exhibited a linear growth rate of 0.98 $\mu\text{m}/\text{min}$ in 2 hours but the growth rate of the pillar-like CNTs synthesized from the pure Fe catalyst tended to saturate after about 60 min. This phenomenon might be due to that the smaller dimension of the catalytic nanoparticles from the Fe-Ti codeposited metal layer could hold its activity at the same temperature better than the catalytic nanoparticles from the pure Fe metal layer. Moreover, the CNTs synthesized from the Fe-Ti codeposited catalyst also showed a straighter morphology as compared with those synthesized from the pure Fe catalyst. It might result from that the high density of the nanoparticles synthesized from the Fe-Ti codeposited catalyst restricted the growth direction of the CNTs. It was helpful to form pillars with better uniformity in direction and then gain a more uniform emission current. Additionally, an optimal inter-pillar spacing of 30 μm was also found for the pillars with the height of 12 μm to obtain a largest emission current density. It was attributed to the trade-off between the suppression of screening effect and the reduction of the total emission area caused by decreasing the inter-pillar spacing. A low turn-on field of 1 V/ μm was obtained for the pillar-like CNTs with inter-pillar spacing of 30 μm . Besides, a very bright light emission was also observed

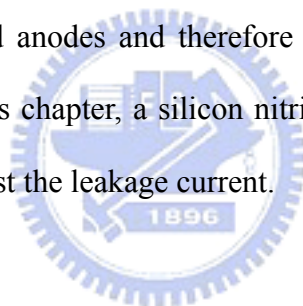
by applying the pillar-like CNTs at 800 V. The pillar-like CNTs showed its wonderful potential for the applications in the field-emission displays or the back-light units with simplicity. By this way, the field-emission characteristics could be well designed by the pattern of lithography.



Chapter 5

The Reduction of Gate Leakage for the CNTs-Based Triode Devices via Adding a Silicon Nitride Layer

For environment and economic issues, the power efficiency is an important feature of the field-emission displays. In typical triode-type field-emission devices, the leakage current between cathodes and gates could greatly reduce the emission current between cathodes and anodes and therefore reduce the power efficiency of field-emission displays. In this chapter, a silicon nitride film was deposited under or upon the gate electrode to resist the leakage current.



5.1 Introduction

Since the first observation of CNTs in 1991[5.1], it has attracted a lot of attention from different research fields. Owing to many unique properties, the CNTs has been utilized in various advanced investigations such as bio-sensors[5.2], gas sensors[5.3], transistors[5.4], back-light units[5.5], and field-emission displays[5.6-5.7]. Among them, CNTs-based field-emission displays was thought to be one of the most promising products in the near future and it was also a very popular technologies owing to the intense competition in the market of flat-panel displays nowadays. Due to several amazing characteristics such as high aspect ratio, low work function, great mechanical strength, and inert chemical properties, the CNTs have been considered as a very wonderful material of electron emitters in field-emission displays[5.8-5.9]. The

device structures of the CNTs-based electron emitters invented so far can generally be classified into two kinds, the diode-type electron emitters and the triode-type electron emitters[5.10] as shown in Fig. 5.1(a) and 5.1(b) respectively. Between them, the triode-type device structure was thought to be more reasonable to accomplish the field-emission displays due to the requirement of lower driving voltage as compared with the diode-type one[5.11-5.13]. It was due to that the intensity of emission current emitted from CNTs was controlled by the voltage of anode in the diode-type field-emission device and the required driving voltage of anode was very large because of the long distance between the anode and the cathode. On the other hand, the amount of emission current emitted from CNTs was controlled by the gate voltage in the triode-type field-emission device and the required driving voltage was relative small because of the short distance between the cathode and the gate. Moreover, by modifying the gate aperture and the distance between gate and cathode, the driving voltage can be greatly reduced to several decades volt. Unfortunately, the reduction of gate aperture and distance could result in stronger electric field between gate and cathode and, therefore, significantly increased the gate leakage current in the triode-type field-emission triodes. A few methods of suppressing the leakage current between gate and cathode have been reported, such as depositing an inside spacer to block the emission current[5.14-5.15], forming Spindt-type-like structures to counterbalance the horizontal electric field[5.16], and enlarging the distance between gate and cathode to reduce the imbalance of horizontal electric field around cathode[5.17-5.18]. However, some of them need to increase the complexity of processes, reduce the dimension of device, or raise the required voltage of driving circuits. In this experiment, a silicon nitride layer was deposited above or under the poly-Si gate to cut off the emission path between gate and cathode. Without adding any extra mask or complex process, the efficiency of emission current was improved

from 1.23% to 8.56% with a nitride layer deposited above the poly-Si gate and to 12.54% with a nitride layer sandwiched in between the oxide layer and the poly-Si gate.

5.2 Experimental Procedures

5.2.1 Sample Fabrication

The N-type silicon wafers (100) with low resistance ($1-10 \Omega/\text{cm}^2$) were applied as the substrates. A 1- μm -thick silicon dioxide was grown via wet oxidation process at $1050 \text{ }^\circ\text{C}$ as an insulating layer. For the conventional device structure, only a poly-Si film was deposited on the insulating layer as the gate electrode. For two proposed device structures, a silicon nitride layer was formed after the deposition of poly-Si gate in one case and before the deposition of poly-Si gate in the other. The poly-Si gate with 300 nm in thickness was deposited by low pressure-chemical vapor deposition system with silane (40 sccm) at $621 \text{ }^\circ\text{C}$ and subsequently heavily doped by phosphor to reduce the resistivity. The silicon nitride film with 300 nm in thickness was also formed by low pressure-chemical vapor deposition system with $\text{NH}_3/\text{Si}_2\text{H}_2\text{Cl}_2$ (105/35 sccm) at $800 \text{ }^\circ\text{C}$. By utilizing the lithography system, the gate holes of field-emission triodes in these three samples were all defined as an array of 25×25 squares with 10 μm in length and 10- μm interspace. The poly-Si and silicon nitride films in gate holes were removed by dry etching and the thermal oxide was removed by wet etching. After the etching processes, a 50-nm-thick Ti buffer layer and a 5-nm-thick Fe catalyst were deposited sequentially by electron-gun and then the metal films on gate were removed by a lift-off process to leave the Fe catalyst in gate holes only. The samples were all loaded into a quartz chamber to synthesize the CNTs in a thermal-CVD at $700 \text{ }^\circ\text{C}$ with ethylene (5 sccm) for 5 min. The flowcharts were

displayed in Figs. 6.2 schematically to illustrate the experiments. Figures 5.3(a), 5.3(b), and 5.3(c) depicted the device structures of conventional samples, samples with a nitride layer capped on the poly-Si gate, and samples with a nitride layer sandwiched in between the insulating layer and the poly-Si gate respectively. To simplify the description, these three device structures were named as conventional samples, OPN (oxide-poly-nitride) samples, and ONP (oxide-nitride-poly) samples accordingly.

5.2.2 Material Analysis and Electrical Measurement

The micrographs of device structures were taken by SEM and the emission currents were measured by applying anode voltage at 1000 V and altering gate voltage from 0 to 100 V in a high vacuum chamber (5×10^{-6} torr). The scheme of the vacuum measurement structure was demonstrated in the Fig. 5.4.

5.3 The Power Efficiency Improvements via Cutting Off the Leakage Paths

The cross-section views of the conventional samples, the OPN samples, and the ONP samples were taken by SEM before the synthesis of the CNTs and the images were shown in Figs. 5.5(a), 5.5(b), and 5.5(c) respectively. The insets in Figs. 5.5 displayed a top view with 45° viewing angle for the samples that have undergone the process of CNTs synthesis. It could be observed that the horizontal distance from CNTs to the poly-Si gate was about $2.5 \mu\text{m}$ in all the samples. The emission current densities of anode in these samples were measured by altering the gate voltage from 0 to 100 V when the anode was applied at 1000 V, as plotted in Fig. 5.6. According to the measurement results, the emission current density of anode was 0.81 mA/cm^2 in

conventional samples, 5.44 mA/cm² in the OPN samples, and 2.01 mA/cm² in the ONP samples when the gate was applied at 100 V. At the same time, the gate leakage current was 65.2 mA/cm² in conventional samples, 58.14 mA/cm² in the OPN samples, and 14.02 mA/cm² in the ONP samples. If the total emission current density from cathode was defined as the summation of anode current density and gate current density and the current efficiency was defined as the ratio of anode current density to total emission current density, the current efficiency was 1.23% in conventional samples, 8.56% in OPN samples, and 12.54% in the ONP samples. Accordingly, the power efficiency was 1.23% in conventional samples, 48.34% in the OPN samples, and 58.6% in the ONP samples. The improvement of current efficiency may result from that the nitride film could block part of the emission current between gate and cathode. As shown in Fig. 5.7(a), there might be two main paths of gate leakage in conventional samples. The proposed OPN samples, as shown in Fig. 5.7(b), could clog the emission current from upside to suppress the gate leakage current and the proposed ONP samples, as shown in Fig. 5.7(c), could clog the emission current from downside. The higher current efficiency of the ONP samples than the OPN samples indicated that the leakage current from downside was the major path of the gate leakage current. Moreover, the total emission current of conventional samples and the OPN samples were both about 65 mA/cm² but that of the ONP samples was only 16 mA/cm². It resulted from that the nitride film in the ONP samples could greatly decrease the electric field induced from poly-Si gate, therefore, reduce the total emission current extracted from the cathode.

5.4 Summary

The current efficiency of the CNTs -based field-emission triodes has been greatly

reduced from 1.23% to 8.56% by capping a silicon nitride film above the poly-Si gate to prevent the leakage current from upside in the OPN samples and to 12.54% by inserting a silicon nitride film under the poly-Si gate to prevent the leakage current from downside in the ONP samples. The improvements of current efficiency showed that the added nitride film could effectively reduce the leakage current between gate and cathode by moderating the electric field around the poly-Si gate. For the proposed two device structures, the OPN device structure could both increase the current efficiency and high emission current density of anode and the ONP device structure could provide even better current efficiency, however, the total emission current density was notably suppressed resulting from that the nitride film could also moderate the electric field around cathode. As compared with the conventional device structure, the OPN and the ONP structures could not only improve the current efficiency remarkably but also increase the emission current density of anode. It showed a great potential in the application of field-emission displays.

Chapter 6

Summary and Conclusions

In this dissertation, several field-emission characteristics of the CNTs were improved by modifying the catalyst and the device structures. By modifying the catalyst structures, the emission current density, reliability, and uniformity were improved without causing any obvious structural destruction to the CNTs-based emitters or increasing the complexity of process. The power efficiency was also improved by modifying the device structures.

In Chapter 2, a thin Ti capping layer was deposited on the Fe nanoparticles to reduce the density of the CNTs. With 2-nm-thick Ti capping layer, an optimal density of the CNTs of about $2 \times 10^7 \text{ cm}^{-2}$ was obtained with the lowering of the turn-on field from $3.8 \text{ V}/\mu\text{m}$ to $2.5 \text{ V}/\mu\text{m}$. It was due to the trade-off between the suppression of the screening effect and the reduction of the total emission area caused by the decrease of the density. Moreover, the abrupt decrease and the gradual degradation in the emission current density were also eased with the Ti capping layer. It might result from the improvements of the contact properties between the CNTs and the substrates. The Ti capping layer tended to merge with the Ti buffer layer under the Fe nanoparticles and held the Fe nanoparticles with large contact area. It could enhance the adhesion between the CNTs and the substrates and gained a strong contact structure to sustain the electrostatic force induced by the applied electric field from being pulled off from the substrates. Furthermore, the enlarged contact area also reduced the contact resistance between the CNTs and the substrates which could generate a great deal of Joule heat with high current density passing through. The high temperature induced

from the Joule heat would result in the attack from the oxygen remained in the vacuum chamber, cause an evaporation of the CNTs, or make the contact structure loose. It could cause a gradual degradation in the emission current density with the increase of operating time.

In Chapter 3, an Fe-Ti codeposited metal layer was utilized as the catalyst of the CNTs. By utilizing this novel catalyst, the reliability of the CNTs-based field-emission devices could be improved by enhancing the contact properties between the CNTs. No obvious abrupt decrease in the emission current density was observed in five measurements from 0 to 7.7 V/ μm and no serious degradation of the emission current density occurred during being stressed at 7.7 V/ μm for 2,500 sec. Additionally, the Ti codeposited with the Fe in the metal layer could suppress the coalescence of the Fe nanoparticles during being heated in the hydrogen pretreatment or the CNTs growth processes. Uniform CNTs with small variation in length were obtained. It could greatly reduce the local field enhancement due to the length variation of the CNTs and obtained a uniform emission current. As compared to the CNTs synthesized from the pure Fe catalyst, the percentages of emission area for the CNTs synthesized from the Fe-Ti codeposited catalyst was improved from 12% to 29% at 500 V, from 41% to 75% at 600 V, and from 86% to 100% at 700 V.

In Chapter 4, a man-made structure, the pillar-like CNTs, was synthesized from the Fe-Ti codeposited catalyst to obtain a reliable emission current from straight CNTs with small variation in its length. As compared with the pillar-like CNTs synthesized from the pure Fe catalyst, those synthesized from the Fe-Ti catalyst remained a constant growth rate in 2 hours. It was due to that the smaller catalytic nanoparticles synthesized from the Fe-Ti codeposited layer could keep the activity better than those synthesized from the pure Fe metal layer. To design the field-emission characteristics of the pillar-like CNTs, the diameter and the inter-pillar spacing of the pillar-like

CNTs were defined by the pattern. An optimal R/H ratio, 2.5, for the pillar-like CNTs of 12 μm high was obtained with low turn-on field of 1.01 $\text{V}/\mu\text{m}$. It was also due to the trade-off between the suppression of the screening effect and the reduction of the total emission current density as described in Chapter 2.

In Chapter 5, a silicon nitride layer was added into the triode-type CNTs -based field-emission devices to block the leakage current between the cathodes and the gates. The current efficiency of the CNTs-based field-emission triodes has been greatly reduced from 1.23% to 8.56% by capping a silicon nitride film above the poly-Si gate to prevent the leakage current from upside in the OPN samples and to 12.54% by inserting a silicon nitride film under the poly-silicon gate. For these two proposed device structures, the OPN device structure could both increase the current efficiency and high emission current density of anode and the ONP device structure could provide even better current efficiency. However, the total emission current density was notably suppressed resulting from that the nitride film could also moderate the electric field around cathode. For application purpose, the ONP device structure showed more potential in the triode-type field-emission devices.

Chapter 7

Future Prospects

For further research, some important topics about the CNTs-based field-emission devices are suggested.

(1) Low Temperature Processes

Although some of the field-emission characteristics, the emission current density, reliability, and uniformity, were improved by the modification of the catalyst and device structures, the process temperature is still too high for practical application purposes. The high temperature during the processes of hydrogen pretreatment and CNTs synthesis makes it difficult to utilize a glass or even a plastic substrate. Glasses are the most common used substrates in flat-panel displays because of its flat and large area and also one of the most promising substrates for field-emission displays. However, the melting point of glasses is generally below 600 °C which is lower than the process temperature. Therefore, a low temperature process for the fabrication of CNTs is essential for the commercialization of the CNTs-based field-emission displays or back-light units.

For a catalytic nanoparticle with small diameter, the activity can be kept during the synthesis process of CNTs. In this dissertation, the Fe nanoparticles synthesized from the Fe-Ti codeposited layer also have the feature of small diameter. It shows a very great chance to synthesize the CNTs from the codeposited metal layer at relative low temperature. Moreover, it would be interesting to utilize other catalytic metal and codeposited metal as the catalyst for the low temperature purpose.

(2) Pillar-Like CNTs with Large Emission Area

In our work, the pillar-like CNTs with uniform length were achieved by using the Fe-Ti codeposited catalyst. It shows a very great potential in the application of back-light units or flat light source. Due to the limitation of the thermal-CVD in chamber size and the compliance of the measurement system, the pillar-like CNTs with large area are not fabricated. However, the reliability and uniformity for the pillar-like CNTs with large emission area still need to be studied.

For this purpose, we should build a thermal-CVD with large reaction chamber and a large vacuum measurement system which could sustain the high voltage and high emission current density.

(3) The Reliability and Uniformity of the Triode-Type Field-Emission Devices

In Chapter 5, the issues of the reliability and uniformity are not discussed for the triode-type field-emission devices. It would be helpful to utilize the Fe-Ti codeposited catalyst in the triode-type field-emission devices for a reliable and uniform emission current.

In addition to the topics mentioned above, there are still many interesting issues remained for the CNTs-based field-emission devices.

References

Chapter 1

- [1.1] J. Bardeen and W. H. Brattain, "The Transistor, A Semi-Conductor Triode," *Phys. Rev.*, Vol. 74, pp. 230-231, 1948.
- [1.2] R. N. Noyce, "Semiconductor Device-and-Lead Structure," *US Patent* 2,981,877, 1959.
- [1.3] J. S. Kilby, "Invention of the Integrated Circuit," *IEEE Trans. Electron. Dev.*, Vol. ED-23, No. 7, pp. 684-654, 1976.
- [1.4] P. Vaudaine and R. Myer, "Microtips Fluorescent Display," *International Electron Devices Meeting*, pp. 197-200, 1991.
- [1.5] C. Curtin, "The Field Emission Display: A New Flat Panel Technology," *Proceedings of the International Display Research Conference, SID*, pp. 12-15, 1991.
- [1.6] C. A. Spindt, C. E. Holland, I. Brodie, J. B. Mooney, and E. R. Westerburg, "Field-emitter Array to Vacuum Fluorescent Display," *IEEE Trans. Electron. Dev.*, Vol. 36, No. 1, pp. 225-228, 1989.
- [1.7] David A. Cathey. Jr., "Field Emission Displays," *International Symposium on VLSI Technology Systems, and Applications, Proceedings of Technical Papers, Taiwan*, pp. 131-136, 1995.
- [1.8] "Pixel Tech to produce color FEDs" *Nikkei Electronics ASIA*, p. 42, Nov., 1995.
- [1.9] H. G. Kosmahl, "A Wide-bandwidth High-gain Small Size Distributed Amplifier with Field Emission Triodes (FETRODE's) for the 10 to 300 GHz

- Frequency Range,” *IEEE trans. Electron. Dev.*, Vol. 36, No. 11, pp. 2728-2737, Nov. 1989.
- [1.10] P. M. Lally, E. A. Nettesheim, Y. Goren, C. A. Spindt, and A. Rosengreen, “A 10 GHz Tuned Amplifier Based on the SRI Thin Film Field-Emission Cathode,” *International Electron Devices Meeting*, p.522, 1998.
- [1.11] C. A. Spindt, C. E. Holland, A. Rosengreen, and I. Brodie, “Field-emitter-array Development for High Frequency Operation,” *J. Vac. Sci. Technol. B*, Vol. 11, pp. 468-473, 1993.
- [1.12] C. A. Spindt, “Microfabricated Field-emission and Field-ionization Sources,” *Surface Sci.*, Vol. 266, pp. 145-154, 1992.
- [1.13] T. H. P. Chang, D. P. Kern, et, al., “A Scanning Tunneling Microscope Controlled Field Emission Micro Probe System,” *J. Vac. Sci. Tech. B*, No. 9, pp. 438-443, 1991.
- [1.14] H. H. Busta, J. E. Pogemiller, and B. J. Zimmerman, “The Field-Emitter Triode as a Displacement/Pressure Sensor,” *J. Micromech. Microeng.*, Vol. 3, pp. 49-56, 1993.
- [1.15] H. C. Lee and R. S. Huang. “A Novel Field Emission Array Pressure Sensor,” *IEEE Transducers-International Solid-State Sensors and Actuators*, Vol. 126, pp. 241-244, 1991.
- [1.16] S. M. Sze, “Physics of Semiconductor Devices,” 2nd ed., John-Wiley & Sons publisher, New York, 648, 1991.
- [1.17] J. A. Morton and R. M. Ryder, “Design Factors of the Bell Laboratories 1553 Triode,” *Bell Sys. Tech. J.*, Vol. 29,p. 496, 1950.
- [1.18] Wei Zhu, “Vacuum Microelectronics,” John-Wiley & Sons publisher, New York, 2001.
- [1.19] D. A. Buck and K. R. Shoulders, “An Approach to Microminiature Printed

- Systems,” *Eastern Joint Computer Conference*, pp. 55-59, 1959.
- [1.20] K. R. Shoulders, “Microelectronics Using Electron Beam Activated Machining Technologies,” *Advances in Computers*, Vol. 2, pp. 135-293, 1961.
- [1.21] M. E. Crost, K. Shoulders, and M. E. Zinn, “Thin Electron Tube with Electron Emitters at the Intersection of Crossed Conductors,” *US Patent* 3,500, 102, 1970.
- [1.22] C. A. Spindt and K. R. Shoulders, “Research in Micro-size Field-Emission Tubes,” *IEEE Conference on Tube Techniques*, pp. 143-147, 1966.
- [1.23] K. Betsui, “Fabrication and Characteristics of Si Field Emitter Arrays,” *Tech. Dig. 4th Int. Vacuum Microelectronics Conf.*, Naghama, Japan, p.26-29, 1991.
- [1.24] H. F Gray, “Silicon Field Emitter Array Technology,” *Proc. 29th Int. Field Emission Symp.*, Stockholm, Sweden, p. 111, 1982.
- [1.25] G. J. Campisi, H. F. Gray, and R. F. Greene, “A Vacuum Field Effect Transistor Using Silicon Field Emitter Arrays,” *IEDM Technical Digest*, pp. 776-779, 1986.
- [1.26] P. B. Marcus and T. T. Sheng, “The Oxidation of Shaped Silicon Surface,” *J. Electrochem. Soc.*, Vol. 129, pp.1278-1282, 1982.
- [1.27] F. J. Himpsel, J. A. Knapp, J. A. van Vechten, and D. E. Eastman, “Quantum photoyield of diamond(111)—A stable negative-affinity emitter,” *Phys. Rev. B*, Vol. 20, pp. 624-627, 1979.
- [1.28] S. Lee, B. K. Ju, Y. H. Lee, D. Jeon, and M. H. Oh, “Fabrication and field emission study of gated diamondlike-carbon-coated silicon tips,” *J. Vac. Sci. Technol. B*, Vol. 15, p.425, 1997.
- [1.29] K. L. Park, J. H. Moon, S. J. Chung, J. Jang, M. H. Oh, and W. I. Milne,

- “Deposition of N-type Diamond-like Carbon by Using the Layer-by-layer Technique and its Electron Emission Properties,” *Appl. Phys. Lett.*, Vol. 70, pp. 1381-1383, 1997.
- [1.30] F. Y. Chuang, C. Y. Sun, T. T. Chen, and I. N. Lin, “Local Electron Field Emission Characteristics of Pulsed Laser Deposited Diamond-like Carbon Films,” *Appl. Phys. Lett.*, Vol. 69, pp. 3504-3506, 1996
- [1.31] J. Robertson, “Recombination and Photoluminescence Mechanism in Hydrogenated Amorphous Carbon,” *Phys. Rev. B*, Vol. 53, pp.16302-16305, 1996.
- [1.32] J. Rinstein, J. Schafer, and L. Ley, “Effective Correlation Energies for Defects in a-C:H from a Comparison of Photoelectron Yield and Electron Spin Resonance Experiments,” *Diam. Relat. Mater.*, Vol. 4, pp. 508-516, 1995.
- [1.33] E. Yamaguchi, K. Sakai, I. Nomura, T. Ono, M. Yamanobe, N. Abe, T. Hara, K. Hatanaka, Y. Osada, H. Yamamoto, and T. Nakagiri, “A 10-in. Surface-Conduction Electron-Emitter Display,” *J. SID*, Vol. 5, pp.345-348, 1997.
- [1.34] R. C. Miller and A. Savage, “Motion of 180° Domain Walls in Metal Electroded Barium Titanate Crystals as a Function of Electric Field and Sample Thickness,” *J. Appl. Phys.*, Vol. 31, pp. 662-669, 1960.
- [1.35] A. Koller and M. Beranek, “Einige neue Erkenntnisse über die Degradation von Titanaten im Zusammenhang mit der Exoemission,” *Czech. J. Phys.*, Vol. 9, pp.402-403, 1959.
- [1.36] G. Rosenman, D. Shur, Y. E. Krasik, and A. Dunaevsky, “Electron Emission from Ferroelectrics,” *J. Appl. Phys.*, Vol. 88, pp.6109-6161, 2000.
- [1.37] C. A. Mead, “Operation of Tunnel-Emission Devices,” *J. Appl. Phys.*, Vol. 32, pp.646-652, 1961.

- [1.38] Y. Kumagai, K. Kawarada, and Y. Shibata, "Energy Distribution of Electrons Tunneling through a Metal-Insulator-Metal Sandwich Structure," *Jpn. J. Appl. Phys.*, Vol. 6, pp.280-296, 1966.
- [1.39] J. G. Simmons, "Generalized Formula for the Electric Tunnel Effect between Similar Electrodes Separated by a Thin Insulating Film," *J. Appl. Phys.*, Vol. 34, pp.1793-1803, 1963.
- [1.40] K. Ohta, J. Nishida, and T. Hayashi, "Electron Emission Pattern of Thin-Film Tunnel Cathode," *Jpn. J. Appl. Phys.*, Vol. 7, pp. 784-784, 1968.
- [1.41] T. Kusunoki, M. Suzuki, S. Sasaki, T. Yaguchi, and T. Adia, "Fluctuation-Free Electron Emission from Non-Formed Metal-Insulator-Metal (MIM) Cathodes Fabricated by Low Current Anodic Oxidation," *Jpn. J. Appl. Phys.*, Vol. 32, pp.L1695-L1697, 1993.
- [1.42] H. Adachi, "Emission Characteristics of Metal-insulator-metal Tunnel Cathodes," *J. Vac. Sci. Technol. B*, Vol. 14, pp. 2093-2095, 1996.
- [1.43] S. Iijima, "Helical Microtubules of Graphitic Carbon," *Nature*, Vol. 354, pp. 56-58, 1991.
- [1.44] N. A. Kiselev, A. P. Moravsky, A. B. Ormontc, and D. N. Zakharov, "SEM and HREM Study of the Internal Structure of Nanotube Rich Carbon Arc Cathodic Deposits ," *Carbon*, Vol. 37, p0. 1093-1103, 1999.
- [1.45] Guo T., Nikolaev P., Rinzler A. G., TomBnek D., Colbert D. T., and Smalley R. E., "Self-assembly of Tubular Fullerenes," *J. Phys. Chem.*, Vol. 99, pp. 10694-10697, 1995.
- [1.46] A. M. Cassell, J. A. Raymarkers, J. King, and H. Dai, "Large Scale CVD Synthesis of Single-walled Carbon Nanotubes," *J. Phys. Chem. B*, Vol. 103, pp. 6484-6492, 1999.
- [1.47] L. Delzeit, B. Chen, A. M. Cassell, R. Stevens, C. Nguyen, and M.

- Meyyappan, "Multilayered Metal Catalysts for Controlling the Density of Single-walled Carbon Nanotubes Growth," *Chem. Phys. Lett.*, Vol. 348, pp. 368-374, 2001.
- [1.48] Kind H., Bonard J. M., Forro L., Kern K., Hernadi K., Nilsson L. O., Schlapbach L., "Printing Gel-like Catalysts for the Directed Growth of Multi-wall Carbon Nanotubes," *Langmuir*, Vol. 16, p. 6877-6883, 2000.
- [1.49] Bojan O. Boskovic, Vlad Stolojan, Rizwan U.A. Khan, Sajad Haq, and S. Ravi P. Silva., "Large-area Synthesis of Carbon Nanofibres at Room Temperature," *Nat. Mater.*, Vol. 1, pp. 165-168, 2002.
- [1.50] S. Hofmann, C. Ducati, J. Robertson, and B. Kleinsorge, "Low-temperature Growth of Carbon Nanotubes by Plasma-enhanced Chemical Vapor Deposition," *Appl. Phys. Lett.*, Vol. 83, pp. 135-137, 2003.
- [1.51] C. Bower, W. Zhu, D. Shalom, D. Lopez, L. H. Chen, P. L. Gammel, and S. Jin, "On-chip Vacuum Microtriode Using Carbon Nanotube Field Emitters," *Appl. Phys. Lett.*, Vol. 80, pp. 3820-3822, 2002.
- [1.52] W. A. de Heer, A. Chateline, D. Ugrate, "A Carbon Nanotube Field-emission Electron Source," *Science*, Vol. 270, pp. 1179-1180, 1995.
- [1.53] C Journet, Wk Maser, P Bernier, A Loiseau, M Lamy De La Chapelle, S Lefrant, P Deniard, R. Lee, and Je Fischer, "Large Scale Production of Single Walled Carbon Nanotubes by the Electric Arc Technique," *Nature*, Vol. 388, pp. 756-758, 1997.
- [1.54] Kanchan A. Joshi, Jason Tang, Robert Haddon, Joseph Wang, Wilfred Chen, and Ashok Mulchandani, "A Disposable Biosensor for Organophosphorus Nerve Agents Based on Carbon Nanotubes Modified Thick Film Strip Electrode," *Electroanalysis*, Vol. 17, pp. 54-58, 2005.
- [1.55] F. Yuan and H. Ryu, "Synthesis, Characterization, and Performance of

Carbon Nanotubes and Carbon Nanofibers with Controlled Size and Morphology as Catalyst Support Material for PEMFC,” *Nanotechnology*, Vol. 15, pp. S596-S602, 2004.

- [1.56] Y. C. Kim and E. H. Yoo, “Printed Carbon Nanotube Field Emitters for Backlight Applications,” *Jpn. J. of Appl. Phys.*, Vol. 44, pp. L454- L456, 2005.
- [1.57] W. B. Choi, Y. W. Jin, H. Y. Kim, S. J. Lee, M. Y. Yun, J. H. Kang, Y. S. Choi, N. S. Park, N. S. Lee, and J. M. Kim, “Electrophoresis Deposition of Carbon Nanotubes for Triode-type Field Emission Display,” *Appl. Phys. Lett.*, Vol. 78, pp. 1547-1549, 2001.
- [1.58] W. B. Choi, D. S. Chung, J. H. Kang, H. Y. Kim, Y. W. Jin, I. T. Han, Y. H. Lee, J. E. Jung, N. S. Lee, G. S. Park, and J. M. Kim, “Fully Sealed, High-brightness Carbon-nanotube Field-emission Display,” *Appl. Phys. Lett.*, Vol. 75, pp. 3129-3131, 1999.
- [1.59] F. Ito, Y. Tomihari, Y. Okada, K. Konuma, and A. Okamoto, “Carbon-Nanotube-Based Triode-Field-Emission Displays Using Gated Emitter Structure,” *IEEE Electron Device Lett.*, Vol. 22, pp. 426-428, 2001.
- [1.60] Q. H. Wang, M. Yan, and R. P. H. Chang, “Flat Panel Display Prototype Using Gated Carbon Nanotube Field Emitters,” *Appl. Phys. Lett.*, Vol. 78, pp. 1294-1296, 2001.
- [1.61] W. A. de Heer, A. Chateline, D. Ugrate, “A Carbon Nanotube Field-emission Electron Source,” *Science*, Vol. 270, pp. 1179-1180, 1995.
- [1.62] K. A. Dean and B. R. Chalamala, “Current Saturation Mechanisms in Carbon Nanotube Field Emitters,” *Appl. Phys. Lett.*, Vol. 76, pp. 375-377, 2000.
- [1.63] W. Zhu, C. Bower, O. Zhou, G. Kochanski, and S. Jin, “Large Current Density from Carbon Nanotube Field Emitters,” *Appl. Phys. Lett.*, Vol. 75,

pp. 873-875, 1999.

- [1.64] R. H. Fowler and L. W. Nordheim, "Electron Emission in Intense Field," *Proc. R. Soc. London Ser. A*, Vol. 119A, pp. 173-175, 1928.
- [1.65] Kevin L. Jensen, "Electron Emission Theory and its Application: Fowler-Nordheim Equation and Beyond," *J. Vac. Sci. Technol. B*, Vol. 21, 1528-1544, 2003.
- [1.66] R. E. Burgess, H. Kroemer, and J. M. Honston, "Corrected Value of Fowler-Nordheim Field Emission Function $v(y)$ and $s(y)$," *Phys. Rev.*, Vol. 90, p.515, 1953.
- [1.67] S. M. Sze, "Physics of Semiconductor Devices," 2nd ed., John-Wiley & Sons publisher, New York, 648, 1991.
- [1.68] S. Iijima, "Helical Microtubules of Graphitic Carbon," *Nature*, Vol.354, pp. 56, 1991.
- [1.69] H. W. Kroto, J. R. Heath, S. C. O'Brien, R. F. Curl, and R. E. Smalley, "Buckminsterfullerene," *Nature*, Vol. 318, pp. 162-163, 1985.
- [1.70] A. Thess, R. Lee, P. Nikolaev, H. Dai, P. Petit, J. Robert, C. Xu, Y. H. Lee, S. G. Kim, A. G. Rinzler, D. T. Colbert, G. E. Scuseria, D. Tomanek, J. E. Fischer, and R. E. Smalley, "Crystalline Ropes of Metallic Carbon Nanotubes," *Science*, Vol. 273, pp. 483-487, 1996.
- [1.71] M. Yudasaka, T. Komatsu, T. Ichihashi, and S. Iijima, "Single-wall Carbon Nanotube Formation by Laser Ablation Using Double-targets of Carbon and Metal," *Chem. Phys. Lett.*, Vol. 278, pp. 102-106, 1997.
- [1.72] M. Yudasaka, T. Komatsu, T. Ichihashi, Y. Achiba, and S. Iijima, "Pressure Dependence of the Structures of Carbonaceous Deposits Formed by Laser Ablation on Targets Composed of Carbon, Nickel and Cobalt," *J. Phys. Chem. B*, Vol. 102, pp. 4892-4896, 1998.

- [1.73] M. Endo, K. Takeuchi, K. Kobori, K. Takahashi, H. W. Kroto, and A. Sakar, "Pyrolytic Carbon Nanotubes from Vapor-grown Carbon Fibers," *Carbon*, Vol. 33, pp. 873-880, 1995.
- [1.74] A. Fonseca, K. Hernadi, P. Piedigrosso, and J. -F. Colomer, "Synthesis of Single and Multi-wall Carbon Nanotubes over Supported Catalysts," *J. Appl. Phys. A*, Vol. 67, pp. 11-22, 1998.
- [1.75] V. Ivanov, A. Fonseca, J. B. Nagy, A. Lucas, P. Lambin, D. Bernaerts, and X. B. Zhang, "Catalytic Production and Purification of Nanotubes Having Fullerene-scale Diameters," *Carbon*, Vol. 33, pp. 1727-1738, 1995.
- [1.76] T. E. Muller, D. G. Reid, W. K. Hsu, J. P. Hare, H. W. Kroto, and D. R. M. Walton, "Synthesis of Nanotubes via Catalytic Pyrolysis of Acetylene: A SEM study," *Carbon*, Vol. 35, pp. 951-966, 1997.
- [1.77] W. Z. Li, S. S. Xie, L. X. Qian, B. H. Chang, B. S. Zou, W. Y. Zhou, R. A. Zhao, and G. Wang, "Large-scale Synthesis of Aligned Carbon Nanotubes," *Science*, Vol. 274, pp. 1701-1703, 1996.
- [1.78] M. Terrones, N. Grobert, J. Olivares, J. P. Zhang, H. Terrones, K. Kordatos, W. K. Hsu, J. P. Hare, P. D. Townsend, K. Prassides, A. K. Cheetham, H. W. Kroto, and D. R. M. Walton, "Controlled Production of Aligned Nanotube Bundles," *Nature*, Vol. 388, pp. 52-55, 1997.
- [1.79] H. M. Cheng, F. Li, G. Su, H. Y. Pan, L. L. He, X. Sun, and M. S. Dresselhaus, "Large-scale and Low-cost Synthesis of Single-walled Carbon Nanotubes by the Catalytic Pyrolysis of Hydrocarbons," *Appl. Phys. Lett.*, Vol. 72, pp. 3282-3284, 1998.
- [1.80] Saito, Y. "Nanoparticles and Filled Nanocapsules," *Carbon*, Vol. 33, pp. 979-988, 1995.
- [1.81] L. Nilsson, O. Groening, C. Emmenegger, O. Kuettel, E. Schaller, L.

- Schlapbach, H. Kind, J-M. Bonard, and K. Kern, "Scanning Field Emission from Patterned Carbon Nanotube Films," *Appl. Phys. Lett.*, Vol. 76, pp. 2071-2073, 2000).
- [1.82] T.F. Kuo, Z.Y. Juang, C.H. Tsai, Y.M. Tsau, H.F. Cheng and I.N. Lin, "Microwave-assisted Chemical Vapor Deposition Process for Synthesizing Carbon Nanotubes," *J. Vac. Sci. Technol. B*, Vol. 19, No.3, pp. 1030-1033, 2001.
- [1.83] J.H. Huang, C.C. Chuang, C.H. Tsai and W.J. Chen, "Excellent Field Emission from Carbon Nanotubes Grown by Microwave-heated Chemical Vapor Deposition," *J. Vac. Sci. Technol. B*, Vol. 21, No. 4, pp. 1655-1659, 2003.
- [1.84] [2.18] Makoto Okai, Tadashi Fujieda, Kishio Hidaka, Takahiko Muneyoshi and Tomio Yaguchi, "In Situ Transmission Electron Microscope Observation of Carbon Nanotubes in Electric Fields," *Jpn. J. of Appl. Phys.*, Vol. 44, No. 4A, pp. 2051-2055, 2005.
- [1.85] [2.19] Kenneth A. Dean, Timothy P. Burgin, and Babu R. Chalamala, "Evaporation of Carbon Nanotubes During Electron Field Emission," *Appl. Phys. Lett.*, Vol. 79, No. 12, pp. 1873-1875 (2001)
- [1.86] [2.20] Jean-Marc Bonard, and Christian Klinke, "Degradation and Failure of Carbon Nanotube Field Emitters," *Physical Review B*, Vol. 67, pp. 115406 1-10, 2003.
- [1.87] [2.21] J. C. She, N. S. Xu, S. Z. Deng, Jun Chen, H. Bishop, S. E. Huq, L. Wang, D. Y. Zhong, and E. G. Wang, "Vacuum Breakdown of Carbon-nanotube Field Emitters on a Dilicon Tip," *Appl. Phys. Lett.*, Vol. 83, No. 13, pp. 2671-1673, 2003.
- [1.88] [2.22] P. Vincent, S. T. Purcell, C. Journet, and Vu Thien Binh,

- “Modelization of Resistive Heating of Carbon Nanotubes During Field Emission,” *Phys. Rev. B*, Vol. 66, pp. 075406 1-5, 2002.
- [1.89] C.C. Chuang, J.H. Huang, Z.Y. Juang, C.H. Tsai, S.P. Chen and I.N. Lin, ,
“The Effect of Nickel Thickness on the Structure and Field-emission Properties of Carbon Nanotubes,” *Journal of Materials Science and Engineering*, Vol. 34, No.2, pp. 112-116, 2002.
- [1.90] J.H. Huang, C.C. Chuang and C.H. Tsai, (2003), “Effect of Nickel Thickness and Microwave Power on the Growth of Carbon Nanotubes by Microwave-heated Chemical Vapor Deposition,” *Microelectronic Engineering*, Vol. 66, pp. 10-16, 2003.
- [1.91] [3.1] Ke Yu, Ziqiang Zhu, Min Xu, Qiong Li, Wei Liu, Qun Chen, “Soluble Carbon Nanotube Films Treated Using a Hydrogen Plasma for Uniform Electron Field Emission,” *Surface and Coating Technology*, Vol. 179, pp.63, 2004.
- [1.92] [3.2] Jong Hyung Choi, Sun Hong Choi, Jae Hee Han, Ji Beom Yoo, and Chong Yun Park, “Enhanced Electron Emission from Carbon Nanotubes through Density Control Using in situ Plasma Treatment of Catalyst Metal,” *Journal of Applied Physics*, Vol. 94, pp. 487, 2003.
- [1.93] [3.3] H. J. Lee, Y. D. Lee, W. S. Cho, B. K. Ju, Yun Hi Lee, J. H. Han, and J. K. Kim, “Field-emission Enhancement from Change of Printed Carbon Nanotube Morphology by an Elastomer,” *Applied Physics Letters*, Vol. 88, p. 093115, 2006.
- [1.94] [3.4] H. J. Lee, S. I. Moon, J. K. Kim, Y. D. Lee, S. Nahm, J. E. Yoo, J. H. Han, Y. H. Lee, S. W. Hwang, and B. K. Ju, “Improvement of Field Emission from Printed Carbon Nanotubes by a Critical Bias Field,” *Journal of Applied Physics*, Vol. 98, pp. 016107, 2005.

- [1.95] [3.5] Zhixin Yu, De Chen, Ba°rd Tøtdal, and Anders Holmen, “Effect of Catalyst Preparation on the Carbon Nanotube Growth Rate,” *Catalyst Today*, Vol. 100, pp. 261, 2005.
- [1.96] Mei-Chao Chiang, Chi-Neng Mo, and Ming Chang, “CNT-Cathode Manufacturing for Emission Display,” the IDMC 07, Wed-S03-05, 2007.



Chapter 2

- [2.1] L. Nilsson, O. Groening, C. Emmenegger, O. Kuettel, E. Schaller, L. Schlapbach, H. Kind, J-M. Bonard, and K. Kern, "Scanning Field Emission from Patterned Carbon Nanotube Films," *Appl. Phys. Lett.*, Vol. 76, No. 15, pp. 2071-2073, 2000.
- [2.2] X.Q. Wang, M. Wang, H.L. Ge, Q. Chen, and Y.B. Xu, "Modeling and Simulation for the Field Emission of Carbon Nanotubes Array," *Physica E*, Vol. 30, pp. 101-106, 2005.
- [2.3] Z. F. Ren, Z. P. Huang, D. Z. Wang, J. G. Wen, J. W. Xu, J. H. Wang, L. E. Calvet, J. Chen, J. F. Klemic, and M. A. Reed, "Growth of a Single Freestanding Multiwall Carbon Nanotube on Each Nanonickel Dot," *Appl. Phys. Lett.*, Vol. 75, No. 8, pp. 1086-1088, 1999.
- [2.4] Jean-Marc Bonard, Mirko Croci, Christian Klinke, Ralph Kurt, Olivier Noury, Nicolas Weiss, "Carbon Nanotube Films as Electron Field Emitters," *Carbon*, Vol. 40, pp. 1715-1728, 2002.
- [2.5] Jong Hyung Choi, Sun Hong Choi, Jae-Hee Han, Ji-Beom Yoo, Chong-Yun Park, Taewon Jung, SeGi Yu, In-Taek Han, and J. M. Kim, "Enhanced Electron Emission from Carbon Nanotubes through Density Control Using in situ Plasma Treatment of Catalyst Metal," *J. Appl. Phys.*, Vol. 94, No. 1, pp. 487-490, 2003.
- [2.6] B. Kim, and W. M. Sigmund, "Density Control of Self-aligned Shortened Single-wall Carbon Nanotubes on Polyelectrolyte-coated Substrates," *Colloids and Surf. A*, Vol. 266, pp. 91-96, 2005.
- [2.7] Cheng Hang Hsu, Chia-Fu Chen, Chien-Chung Chen, and Shih-Yu Chan, "Density-controlled Carbon Nanotubes," *Diamond Relat. Mater.*, Vol. 14, pp.

739-743, 2005.

- [2.8] Thomas Goislard De Monsabert, Jean Dijon, and Patrice Gadelle, "Density Control of Carbon Nanotubes and Filaments Films by Wet Etching of Catalyst Particles and Effects on Field Emission Properties," *Carbon*, Vol. 43, pp. 2441-2452, 2005.
- [2.9] Po-Lin Chen, Jun-Kai Chang, Fu-Ming Pan, and Cheng-Tzu Kuo, "Tube Number Density Control of Carbon Nanotubes on Anodic Aluminum Oxide Template," *Diamond Relat. Mater.*, Vol. 14, pp. 804-809, 2005.
- [2.10] L. Delzeit, B. Chen, A. Cassell, R. Stevens, C. Nguyen, and M. Meyyappan, "Multilayered Metal Catalyst for Controlling the Density of Single-Walled Carbon Nanotube Growth," *Chem. Phys. Lett.*, Vol. 348, pp. 368-374, 2001.
- [2.11] Chuan-Ping Juan, Kuo-Ji Chen, Chun-Chien Tsai, Kao-Chao Lin, Wei-Kai Hong, Chen-Yu Hsieh, Wen-Pin Wang, Rui-Ling Lai, Kuei-Hsien Chen, Li-Chyong Chen, and Huang-Chung Cheng, "Improved Field-Emission Properties of Carbon Nanotube Field-Emission Arrays by Controlled Density Growth of Carbon Nanotubes," *Jpn. J. Appl. Phys.*, Vol. 44, No. 1A, pp. 365-370, 2005.
- [2.12] Sung Hoon Lim, Kyu Chang Park, Jong Hyun Moon, Hyun Sik Yoon, Didier Pribat, Yvan Bonnassieux, and Jin Jang, "Controlled Density of Vertically Aligned Carbon Nanotubes in a Triode Plasma Chemical Vapor Deposition System," *Thin Solid Films*, Vol. 515, pp. 1380-1384, 2006.
- [2.13] K.-Y.Lee, S. Hond, M. Katayama, T.Hirao, H.Mori, and K.Oura, "Controlling the Density of Vertically Aligned Carbon Nanotubes by DC Bias Sputtering with Gas Mixtures," *Diamond Relat. Mater.*, Vol. 13, pp. 1228-1231, 2004.
- [2.14] Jong Hyung Choi, Tae Young Lee, Sun Hong Choi, Jae-Hee Han, Ji-Beom

- Yoo, Chong-Yun Park, Taewon Jung, Se Gi Yu, Whikun Yi, In-Taek Han, and J. M. Kim, "Control of Carbon Nanotubes Density through Ni Nanoparticle Formation Using Thermal and NH₃ Plasma Treatment," *Diamond Relat. Mater.*, Vol. 12, pp. 794-798, 2004.
- [2.15] Chuan-Ping Juan, Kao-Chao Lin, Rui-Ling Lai, Kuo-Jui Chang, and Huang-Chung Cheng, "Field Emission Improvement through Structure of Intermixture of Long and Short Carbon Nanotubes," *Jpn. J. Appl. Phys.*, Vol. 46, No. 2, pp. 859-862, 2007.
- [2.16] H. Busta, Z. Tolt, Montgomery and A. Feinerman, "Field Emission from Teepee-shaped Carbon Nanotube Bundles," *J. Vac. Sci. Technol. B*, Vol. 23, pp. 676-679, 2005.
- [2.17] Chuan-Ping Juan, Chun-Chien Tsai, Kuei-Hsien Chen, Li-Chyong Chen, and Huang-Chung Cheng, "Effects of High-Density Oxygen Plasma Posttreatment on Field Emission Properties of Carbon Nanotube Field-Emission Displays," *Jpn. J. Appl. Phys.*, Vol. 44, No. 11, pp. 8231-8236, 2005.
- [2.18] Makoto Okai, Tadashi Fujieda, Kishio Hidaka, Takahiko Muneyoshi and Tomio Yaguchi, "In Situ Transmission Electron Microscope Observation of Carbon Nanotubes in Electric Fields," *Jpn. J. of Appl. Phys.*, Vol. 44, No. 4A, pp. 2051–2055, 2005.
- [2.19] Kenneth A. Dean, Timothy P. Burgin, and Babu R. Chalamala, "Evaporation of Carbon Nanotubes During Electron Field Emission," *Appl. Phys. Lett.*, Vol. 79, No. 12, pp. 1873-1875 (2001)
- [2.20] Jean-Marc Bonard, and Christian Klinke, "Degradation and Failure of Carbon Nanotube Field Emitters," *Physical Review B*, Vol. 67, pp. 115406 1-10, 2003.

- [2.21] J. C. She, N. S. Xu, S. Z. Deng, Jun Chen, H. Bishop, S. E. Huq, L. Wang, D. Y. Zhong, and E. G. Wang, "Vacuum Breakdown of Carbon-nanotube Field Emitters on a Dilicon Tip," *Appl. Phys. Lett.*, Vol. 83, No. 13, pp. 2671-1673, 2003.
- [2.22] P. Vincent, S. T. Purcell, C. Journet, and Vu Thien Binh, "Modelization of Resistive Heating of Carbon Nanotubes During Field Emission," *Phys. Rev. B*, Vol. 66, pp. 075406 1-5, 2002.
- [2.23] Chao Liu, An-jen Cheng, Maurice Clark, and Yonhua Tzeng, "Effects of Interfacial Layers on Thermal Chemical Vapor Deposition of Carbon Nanotubes Using Iron Catalyst," *Diamond Relat. Mater.*, Vol. 14, pp. 835-840, 2005.
- [2.24] M. Wang, K. P. Pramoda, and S. H. Goh, "Enhancement of Interfacial Adhesion and Dynamic Mechanical Properties of Poly(methyl methacrylate)/Multiwalled Carbon Nanotube Composites with Amine-terminated Poly(ethylene oxide)," *Carbon*, Vol. 44, pp. 613-617, 2006.
- [2.25] J. H. Han, S. H. Lee, A. S. Berdinsky, Y. W. Kim, J. B. Yoo, C. Y. Park, J. J. Choi, T. Jung, I. T. Han, and J. M. Kim, "Effects of Various Post-treatments on Carbon Nanotube Films for Reliable Field Emission," *Diamond Relat. Mater.*, Vol. 14, pp. 1891-1896, 2005.
- [2.26] Paul C. P. Watts, Stephen M. Lyth, Ernest Mendoza, and S. Ravi P. Silva, "Polymer Supported Carbon Nanotube Arrays for Field Emission and Sensor Devices," *Appl. Phys. Lett.*, Vol. 89, pp. 103113 1-3, 2006.
- [2.27] J. H. Park, J. S. Moon, J. H. Han, A. S. Berdinskiy, D. G. Kuvshinov, J. B. Yoo, C. Y. Park, J. W. Nam, J. H. Park, C. G. Lee, and D. H. Choe, "Effects of Binders and Organic Vehicles on the Emission Properties of Carbon

Nanotube Paste,” *Diamond Relat. Mater.*, Vol. 14, pp. 1463-1468, 2005.



Chapter 3

- [3.1] Kenneth A. Dean, Bernard F. Coll, Larry Dworsky, Emmett Howard, Hao Li, Michael R. Johnson, Scott V. Johnson, and James E. Jaskie, "Performance of Nanotube Field Emission Displays," *the IDMC 07*, Wed-S06-01, 2007.
- [3.2] Ke Yu, Ziqiang Zhu, Min Xu, Qiong Li, Wei Liu, Qun Chen, "Soluble Carbon Nanotube Films Treated Using a Hydrogen Plasma for Uniform Electron Field Emission," *Surface and Coating Technology*, Vol. 179, pp.63, 2004.
- [3.3] Jong Hyung Choi, Sun Hong Choi, Jae Hee Han, Ji Beom Yoo, and Chong Yun Park, "Enhanced Electron Emission from Carbon Nanotubes through Density Control Using in situ Plasma Treatment of Catalyst Metal," *Journal of Applied Physics*, Vol. 94, pp. 487, 2003.
- [3.4] H. J. Lee, Y. D. Lee, W. S. Cho, B. K. Ju, Yun Hi Lee, J. H. Han, and J. K. Kim, "Field-emission Enhancement from Change of Printed Carbon Nanotube Morphology by an Elastomer," *Applied Physics Letters*, Vol. 88, p. 093115, 2006.
- [3.5] H. J. Lee, S. I. Moon, J. K. Kim, Y. D. Lee, S. Nahm, J. E. Yoo, J. H. Han, Y. H. Lee, S. W. Hwang, and B. K. Ju, "Improvement of Field Emission from Printed Carbon Nanotubes by a Critical Bias Field," *Journal of Applied Physics*, Vol. 98, pp. 016107, 2005.
- [3.6] Zhixin Yu, De Chen, Ba°rd Tøtdal, and Anders Holmen, "Effect of Catalyst Preparation on the Carbon Nanotube Growth Rate," *Catalyst Today*, Vol. 100, pp. 261, 2005.
- [3.7] Mei-Chao Chiang, Chi-Neng Mo, and Ming Chang, "CNT-Cathode Manufacturing for Emission Display," *the IDMC 07*, Wed-S03-05, 2007.

- [3.8] (<http://www.crct.polymtl.ca/>), Center for Research in Computational Thermochemistry.
- [3.9] F. J. Himpsel, J. E. Ortega, G. J. Mankey, and R. F. Willis, “Magnetic Nanostructures,” *Advances in Physics*, Vol. 47, No. 4, pp. 511-597, 1998.
- [3.10] A. Zangwill, “Physics at Surfaces”, Cambridge University Press, Cambridge ,1988.
- [3.11] Z. Yu, D. Chen, B. Tøtdal, and A. Holmen, “Effect of Catalyst Preparation on the Carbon Nanotube Growth rate” *Catal.Today*, Vol. 100, pp. 261-267, 2005.



Chapter 4

- [4.1] B. Q. Wei, Z. J. Zhang, P. M. Ajayan, and G. Ramanath, "Growing Pillars of Densely Packed Carbon Nanotubes on Ni-coated Silica," *Carbon*, Vol. 40, pp. 47-51, 2002 .
- [4.2] Michael J. Bronikowski, "CVD Growth of Carbon Nanotube Bundle Arrays," *Carbon*, Vol. 44, pp. 2822-2832, 2006.
- [4.3] Y. M. Wong, W. P. Kang, J. L. Davidson, B. K. Choi, W. Hofmeister, J. H. Huang, "Array Geometry, Size and Spacing Effects on Field Emission Characteristics of Aligned Carbon Nanotubes," *Diamond & Relat. Mater.*, Vol. 14, pp. 2078-2083, 2005.
- [4.4] M. Katayama, K. Y. Lee, S. I. Honda, T. Hirao, and K. Oura, "Ultra-Low-Threshold Field Electron Emission from Pillar Array of Aligned Carbon Nanotube Bundles," *Japanese Journal of Applied Physics*, Vol. 43, No. 6B, pp. L774-L776, 2004.
- [4.5] W. A. de Heer, A. Chatelain, D. Urgate, "A Carbon Nanotube Field-Emission Electron Source,," *Science*, Vol. 270, No. 5239, p. 1179, 1995.
- [4.6] Y. Cheng, O. Zhou, C. R., "Electron Field Emission from Carbon Nanotubes," *Physique*, Vol. 4, pp. 1021-1033, 2003.
- [4.7] D. J. Lee, S. I. Monn, Y. H. Lee, J. E. Yoo, J. H. Park, J. Jang, B. K. Ju, "The Vacuum Packaging of a Flat Lamp Using Thermally Grown Carbon Nano Tubes," *Vacuum*, Vol. 74, pp. 105-111, 2004.
- [4.8] L. Nilsson, O. Groening, C. Emmenegger, O. Kuettel, E. Schaller, L. Schlapbach, H. Kind, J-M. Bonard, and K. Kern, "Scanning Field Emission from Patterned Carbon Nanotube films," *Appl. Phys. Lett.*, No. 76, pp. 2071-2073, 2000.

Chapter 5

- [5.1] S. Iijima, "Helical Microtubules of Graphitic Carbon," *Nature*, Vol.354, pp. 56-58, 1991.
- [5.2] Y. Cui, Q. Wei, H. Park, Charles M. Lieber, "Nanowire Nanosensors for Highly Sensitive and Selective Detection of Biological and Chemical Species,," *Science*, Vol. 293, pp. 1289-1292, 2001.
- [5.3] S. Chopra, A. Pham, J. Gaillard, A. Parker, and A. M. Rao, "Carbon-nanotube-based Resonant-circuit Sensor for Ammonia,," *Appl. Phys. Lett.*, Vol. 80, pp. 4632-4634, 2002.
- [5.4] R. Martel, T. Schmidt, H. R. Shea, T. Hertel, and Ph. Avouris, "Single- and Multi-wall Carbon Nanotube Field-effect Transistors," *Appl. Phys. Lett.*, Vol. 73, pp. 2447-2449, 1998.
- [5.5] Y. C. Kim and E. H. Yoo, *Jpn. J.*, "Printed Carbon Nanotube Field Emitters for Backlight Applications,," *Appl. Phys.*, Vol. 44, No. 15, pp. L454-L456, 2005.
- [5.6] W. B. Choi, Y. H. Lee, N. S. Lee, J. H. Kang, S. H. Park, H. Y. Kim, D. S. Chung, S. M. Lee, S. Y. Chung, and J. M. Kim, *Jpn. J.*, "Carbon-Nanotubes for Full-Color Field-Emission Displays,," *Appl. Phys.*, Vol. 39, No. 5A, pp. 2560-2564, 2000.
- [5.7] Y. R. Cho, J. H. Lee, C. S. Hwang, Y. H. Song, H. S. Uhm, D. H. Kim, S. D. Ahn, C. H. Chung, B. C. Kim, and K. I. Cho, "Characterizations of Fine-pitched Carbon Nanotube Pixels for Field Emitter Arrays,," *Jpn. J. Appl. Phys.*, Vol. 41, No. 3A, pp. 1532-1535, 2002.
- [5.8] A. V. Melechko, V. I. Merkulov, T. E. McKnight, M. A. Guillorn, K. L. Klein, D. H. Lowndes, and M. L. Simpson, "Vertically Aligned Carbon Nanofibers

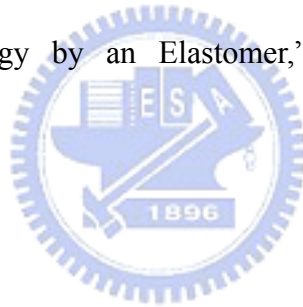
- and Related Structures: Controlled Synthesis and Directed Assembly,” *J. of Appl. Phys.*, Vol. 97, pp. 041301-39, 2005.
- [5.9] K. B. K. Teo, R.G. Lacerda, M. H. Yang, A. S. Teh, L. A. W. Robinson, S. H. Dalal, N. L. Rupesinghe, M. Chhowalla, S. B. Lee, D. A. Jefferson, D. G. Hasko, G. A. J. Amaratunga, W. L. Milne, P. Legagneux, L. Gangloff, E. Minoux, J. P. Schnell and D. Pribat, “Carbon Nanotube Technology for Solid State and Vacuum Electronics” *IEE Proc.-Circuits Devices Syst.*, Vol. 151, p. 443-451, 2004.
- [5.10] Y. M. Wong, W. P. Kang, J. L. Davidson, W. Hofmeister, S. Wei, J. H. Huang, “Growth and Profile Modification of Carbon Nanotubes Designed for Field Emission Applications by Hydrogen Plasma Pretreatment,” *Diamond Relat. Mater.*, Vol. 15, pp. 1132-1137, 2005.
- [5.11] C. G. Lee, S. J. Lee, S. H. Cho, E. J. Chi, B. G. Lee, S. H. Jeon, S. H. Ahn, S. B. Hong, and D. H. Choe, “Gated Carbon Nanotube Emitter with Low Driving Voltage” *IEEE Electron Device Lett.*, Vol. 25, pp. 605-607, 2004.
- [5.12] H. C. Cheng, K. J. Chen, W. K. Hong, F. G. Tantair, C. P. Lin, K. H. Chen, and Li-Chyong Chen, “Fabrication and Characterization of Low Turn-on Voltage Carbon Nanotube Field Emission Triodes,” *Electrochem. and Solid-State Lett.*, Vol. 4, No. 8, pp. H15-H17, 2001.
- [5.13] K. B. Kim, Y. H. Song, C. S. Hwang, C. H. Chung, J. H. Lee, I. S. Choi, and J. H. Park, “Efficient Electron Emissions from Printed Carbon Nanotubes by Surface Treatments,” *J. Vac. Sci. Technol. B*, Vol. 22, pp1331-1334, 2004.
- [5.14] David S. Y. Hsu, “Microgating Carbon Nanotube Field Emitters by in situ Growth Inside Open Aperture Arrays,” *Appl. Phys. Lett.*, Vol. 80, No. 16, pp.2988-2990, 2002
- [5.15] Y. T. Janga, C. H. Choi, B. K. Ju, J. H. Ahn, Y. H. Lee, “Simple Approach to

Fabricate Microgated Nanotubes Emitter with a Sidewall Protector,” *Physica B*, Vol. 334, pp. 9–12, 2003.

[5.16] M. Q. Ding, X. Li, G. Bai, J. J. Feng, F. Zhang, F. Liao, “Fabrications of Spindt-type Cathodes with Aligned Carbon Nanotube Emitters,” *Appl. Surf. Sci.*, Vol. 251, pp. 201–204, 2005.

[5.17] Y. M. Wong, W. P. Kang, J. L. Davidson, B. K. Choi, W. Hofmeister, J. H. Huang, “Array Geometry, Size and Spacing Effects on Field Emission Characteristics of Aligned Carbon Nanotubes,” *Diamond & Relat. Mater.*, Vol. 14, pp. 2078-2083, 2005.

[5.18] H. J. Lee, Y. D. Lee, W. S. Cho, B. K. Ju, Yun-Hi Lee, J. H. Han, and J. K. Kim, “Field-emission Enhancement from Change of Printed Carbon Nanotube Morphology by an Elastomer,” *Appl. Phys. Lett.*, Vol. 88, pp.093115 1-3, 2006.



Tables

Table 1.1 The timeline for the evolution of electronic technology

1900's: The Vacuum Tube.	
1905	First electronic diode vacuum tube is built by English physicist J. Ambrose Fleming, allowing the change of alternating current into a direct one-way signal.
1906	First electronic triode vacuum tube is built by American electrical engineer Lee DeForest, allowing signals to be controlled and amplified. Technology of electronics is born.
Late 1940's: The Transistor.	
1947	The point-contact bipolar transistor is invented by Bell Lab's Bardeen, Shockley, and Brattain
1951	Junction field-effect transistor (JFET) is invented.
1952	Single-crystal silicon is fabricated.
1954	Oxide masking process is developed.
Late 1950's: Key IC discoveries.	
1958	First silicon integrated circuit is built by Texas Instrument's Jack Kilby.
1959	Planar process to distribute transistors on silicon, with passive oxide layers to protect junctions, is developed by Fairchild Semiconductor's Noyce and Moore. A modern version of this process is used today.
1960's: Small Scale Integration (SSI), up to 20 gates per chip.	
1960	Metal-Oxide-Silicon (MOS) transistor is invented.
1962	Transistor-transistor Logic (TTL) is developed.
1963	Complementary Metal Oxide Silicon (CMOS) is invented.
Late 1960's: Medium Scale Integration (MSI), 20-200 gates per chip.	
1968	MOS memory circuits are introduced.
1970's: Large Scale Integration (LSI), 200-5000 gates per chip.	
1970	8-bit MOS calculator chips are introduced, 7 micrometer chip geometries.
1971	16-bit Microprocessors are introduced.
1980's: Very Large Scale Integration (VLSI), over 5000 gates per chip.	
1981	Very High Speed Integration (VHSIC), tens's of thousands of gates per chip, 1.5 micrometer chip geometries.
1984	0.5 micrometer chip geometries.

Table 1.2 The comparison of several flat panel displays

	FED	OLED	PDP	LCD	CRT
low cost	?	▲	▲	▲	★
viewing angle	★	★	★	×	★
life time	?	×	▲	★	★
response time	★	▲	★	×	★
power consumption	★	▲	×	★	×
resolution	▲	★	▲	★	×
weight	★	★	★	★	×
display area	★	▲	★	★	×

- ★ : good
- ▲ : medium
- × : bad
- ? : unsure

Table 1.3 The history of vacuum microelectronics

1950s	Foundations of field emission physics
1958	Buck and Shoulders (SRI) – proposals for fabricating vacuum microelectronics devices
1961	Shoulders (SRI) – proposals for vertical and lateral microtriodes
1968	Spint (SRI) –fabrication and operation of gated Mo-FEAs
1981	Henry Gary (NRL) – lateral vacuum triode using silicon field emitters
1985	Robert Meyer – demonstration of matrix addressable monochrome display with field-emission cathode array
1988	Meyer and Baptist (LETI) – Mo microtips with lateral resistive layer
1993	Pixtech Consortium – demonstration of full color FED
1993	Kumar (MCC) – demonstration of FED with carbon/diamond film
1995	Pixtech/Futaba – demonstration of low voltage color display
1997	Motorola – demonstration of high voltage full color FED
2000	Sony/Candescent – demonstration of full color 5.5” and 13.2” FED



Table 1.4 The features of different field-emission technologies

	BSD	Spindt	SCE	MIS	MIM	diamond particle	CNT
driving voltage	15~30 V	30~80 V	10~20 V	80~110 V	10 V	3500 V	hundreds to thousands V
emission current	2.6 mA/cm ²	50 A/cm ²	2 mA/cm ²	1.4 mA/cm ²	5.8 mA/cm ²	1 mA/cm ²	0.01~1 A/cm ²
vacuum degree	1~10 Pa	10 ⁻⁵ Pa	10 ⁻⁶ Pa	10 ⁻⁴ Pa	10 ⁻⁴ Pa	4×10 ⁻⁵ Pa	10 ⁻⁵ ~10 ⁻⁶ Pa
efficiency	1 %	--	< 1%	28 %	0.5 %	--	--
company	Panasonic	PixTech, Candescent, Motorola, Toshiba, Futaba, Sony, NEC, Fujitsu, Mitsubishi, Samsung	Canon, Toshiba	Pioneer	Hitachi	Panasonic, SI DIAMOND Tech	Noritake, NEC, Samsung, ERSO/ITRI

from Toray Research Center/PIDA

Table 2.1 The turn-on field and threshold field of samples with different thickness of Ti capping layer

	Thickness of thin Ti capping layer (Å)					
	0 Å	10 Å	20 Å	40 Å	100 Å	200 Å
E_{on} (V/μm)	3.8	2.6	2.5	2.1	3.9	4.7
E_{th} (V/μm)	5.9	5.2	3.5	4.6	6	N. A.

Table 2.2 The densities of CNTs for samples with different thicknesses of Ti capping layer

	Thickness of thin Ti capping layer (Å)					
	0 Å	10 Å	20 Å	40 Å	100 Å	200 Å
Density of CNTs (cm ⁻²)	10 ⁸ ~10 ⁹	10 ⁸	2×10 ⁷	7×10 ⁶	4×10 ⁶	0

Table 4.1 The turn-on field and threshold field of the pillar-like CNTs with different interspacing

Interpillar Spacing (μm)	R/H ratio	Turn-on Field ($\text{V}/\mu\text{m}$)	Threshold Field ($\text{V}/\mu\text{m}$)
12	1	1.87	3.4
15	1.25	1.73	3.25
20	1.67	1.3	3
25	2.08	1.21	2.87
30	2.5	1.01	2.67
35	2.92	1.1	2.85



Figures

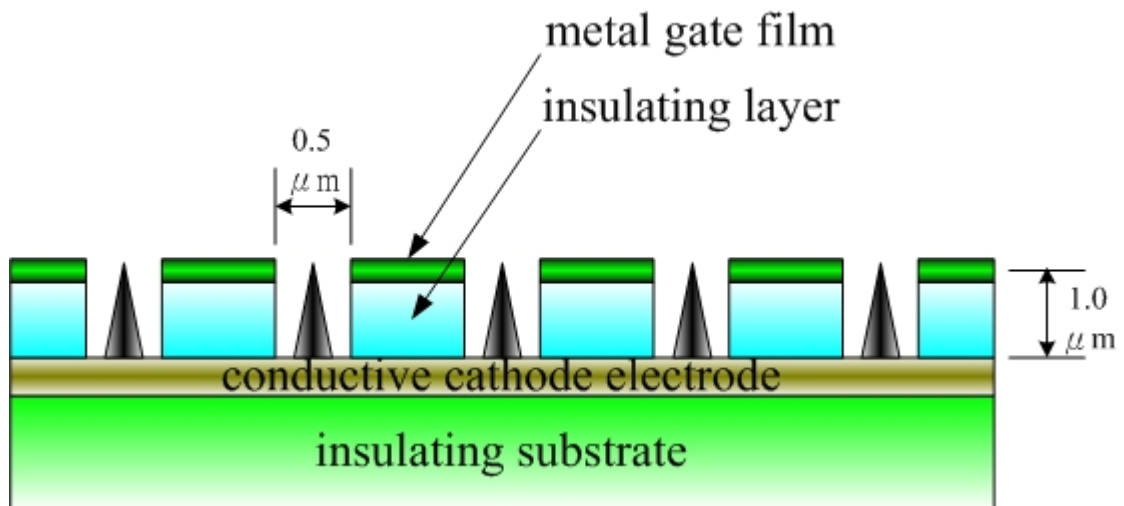


Figure 1.1 The scheme of Spindt-type field emitter arrays. The height of the cones and thickness of the dielectric layer are both about $1\ \mu\text{m}$, the tip radius is about $20\ \text{nm}$, the gate aperture is about $0.5\ \mu\text{m}$, and the tip-to-tip spacing is about $1\sim 5\ \mu\text{m}$.

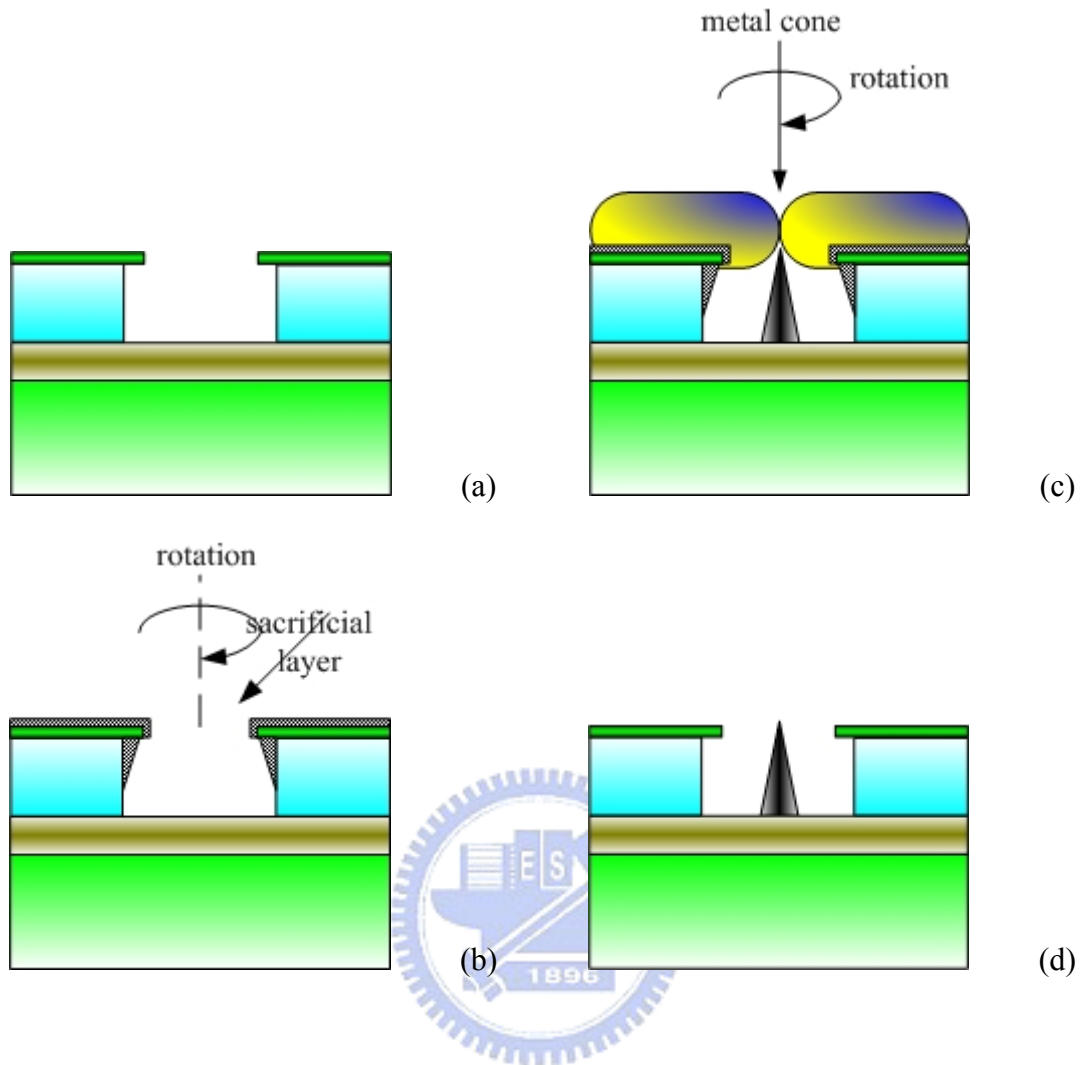
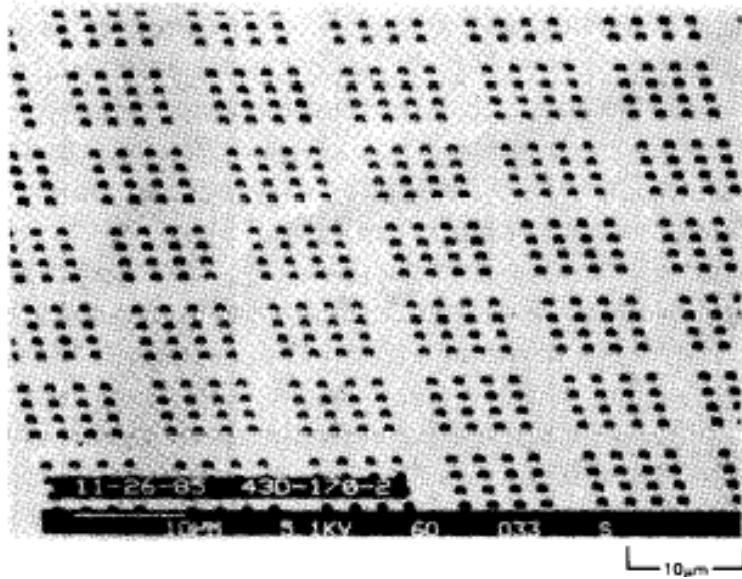


Figure 1.2 The processes of fabricating Spindt field emitter arrays: (a) etch cavities in the top two layers of a metal/dielectric/metal stack were formed by lithography and subsequent wet or dry etching, (b) a sacrificial lift-off layer is deposited onto the top layer and inner walls of the upper portion of the cavity by a tilted deposition with rotating the substrate on an axis perpendicular to the surface, (c) form metal cones in the cavities by depositing metal perpendicular to the substrate surface and the tilted deposition can be applied continuously or intermittently during this step to help to control the hole-closure rate and to manage stresses in the deposited layer as desired, and (d) a lift-off process is done by removing the sacrificial layer in a wet etching solution which only attacks the sacrificial layer without damage the metal cones seriously.

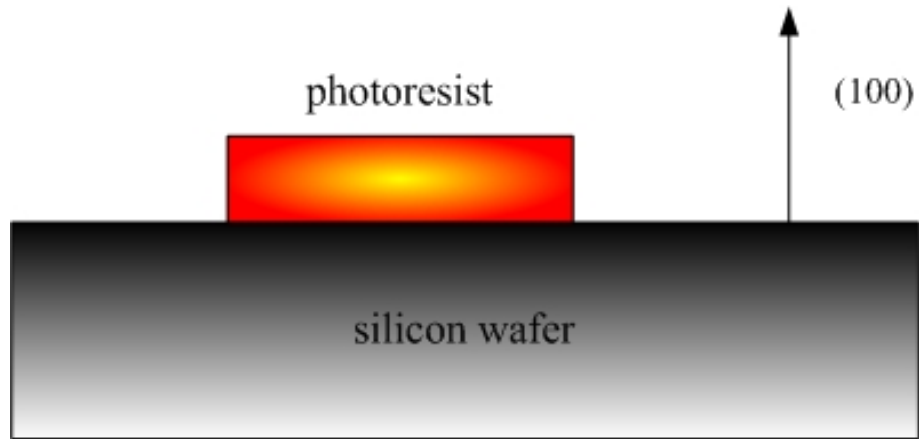


(a)

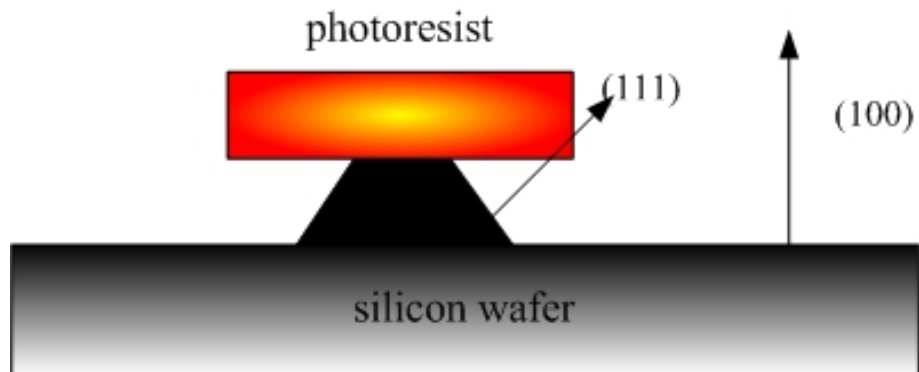


(b)

Figure 1.3 The micrographs taken by SEM for (a) Spindt field emitter arrays and (b) device structure with higher resolution.



(a)



(b)

Figure 1.4 The schematic illustration of orientation-dependant etching (ODE) method for fabricating silicon tips: (a) using lithography to pattern a etching mask to inhibit etching in locations where pyramids are desired and (b) etching of silicon is much faster at the (100) plane than at (111) plane, forming a (111) bounded pyramid in the end.

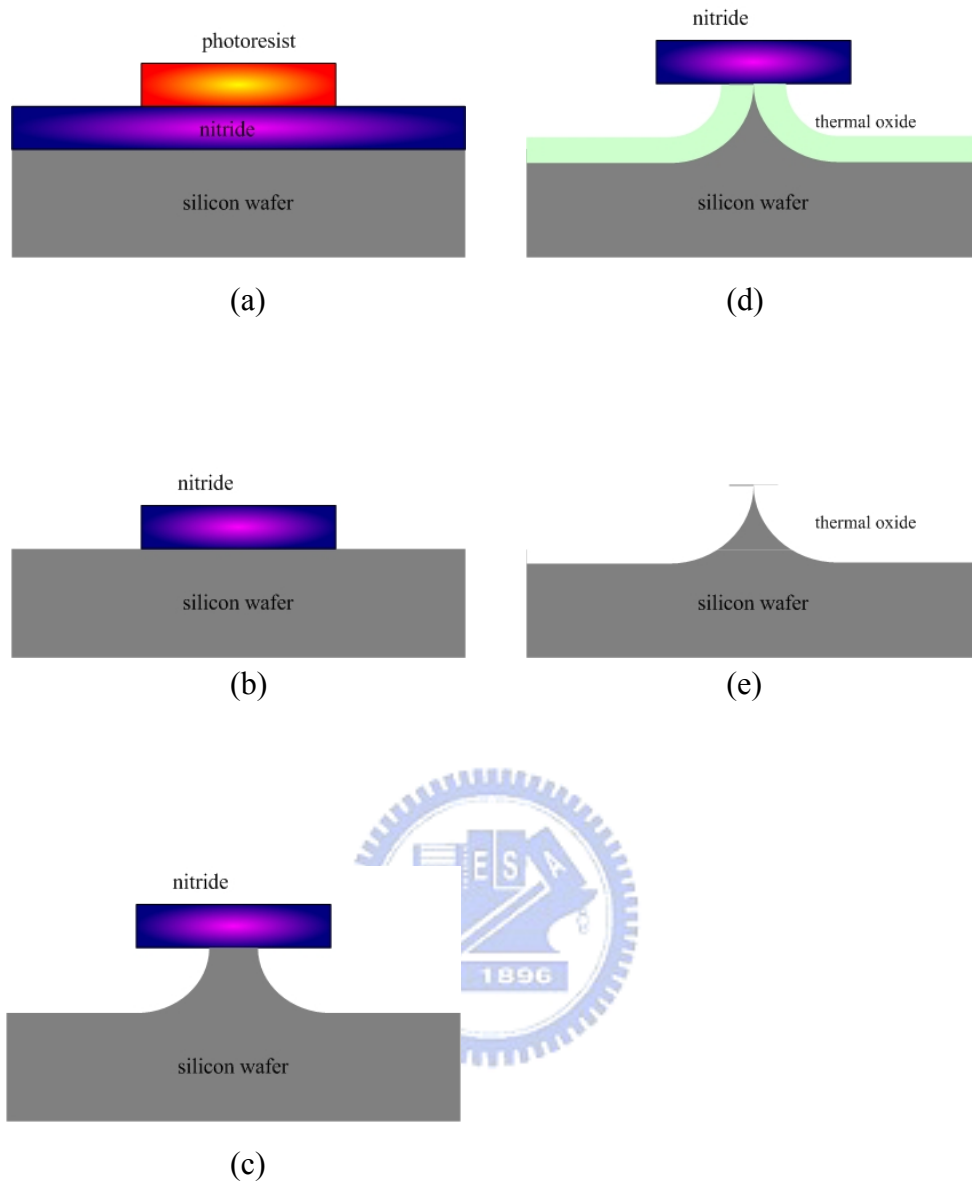


Figure 1.5 The flowchart of the oxidation sharpening: (a) depositing a nitride layer on the silicon wafer and form an array of dots via lithography, (b) etch the nitride by dry etching and remove the photoresist, (c) undercut the silicon to form tips under the hard nitride mask by an isotropic etching (wet or dry etching), (d) form sharper silicon tips by oxidation at about 950 °C or lower, and (e) remove the nitride mask and thermal oxide to uncover the sharp silicon tips.

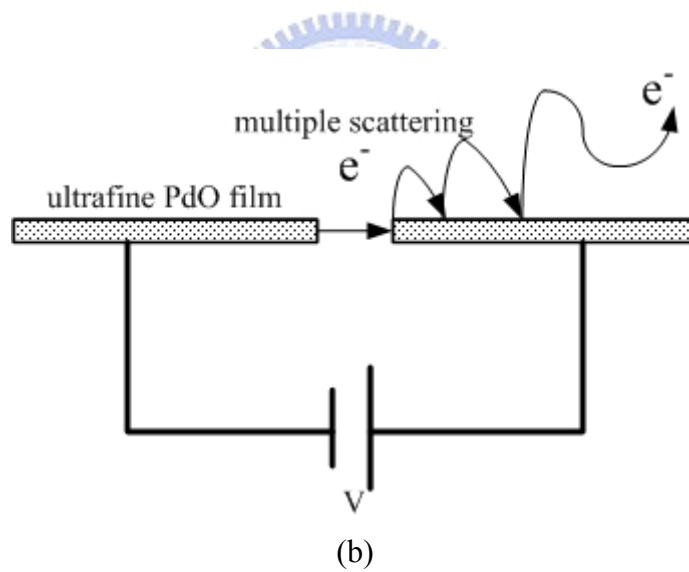
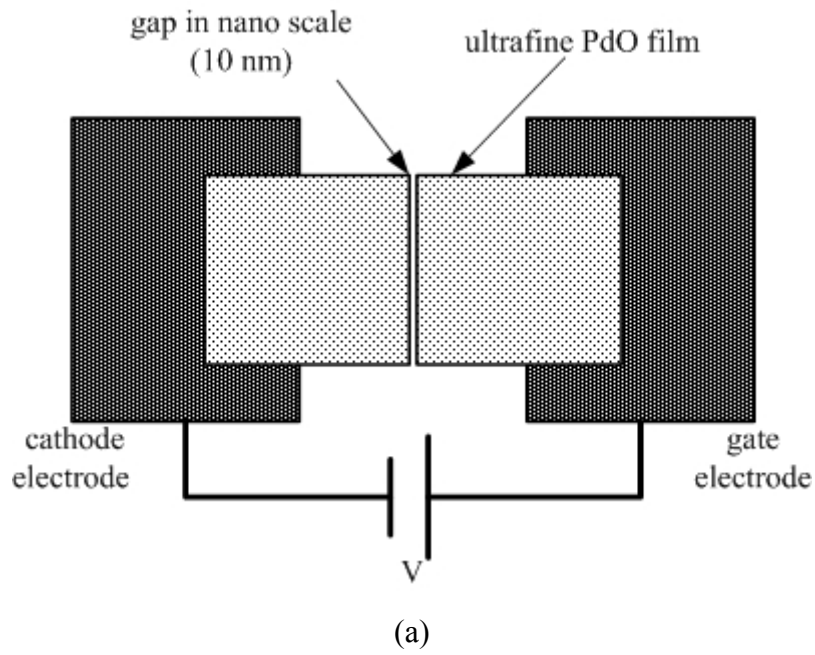


Figure 1.6 The illustration of surface conduction emitters: (a) the device structure from top view with two ultrafine PdO films as cathode and gate electrodes and (b) the mechanism of surface conduction emission. A suitable voltage is applied between the two PdO films to extract electrons from cathode to gate and the electrons will be multi-scattered on the surface of PdO then extracted by the anode which is applied at a very high voltage.

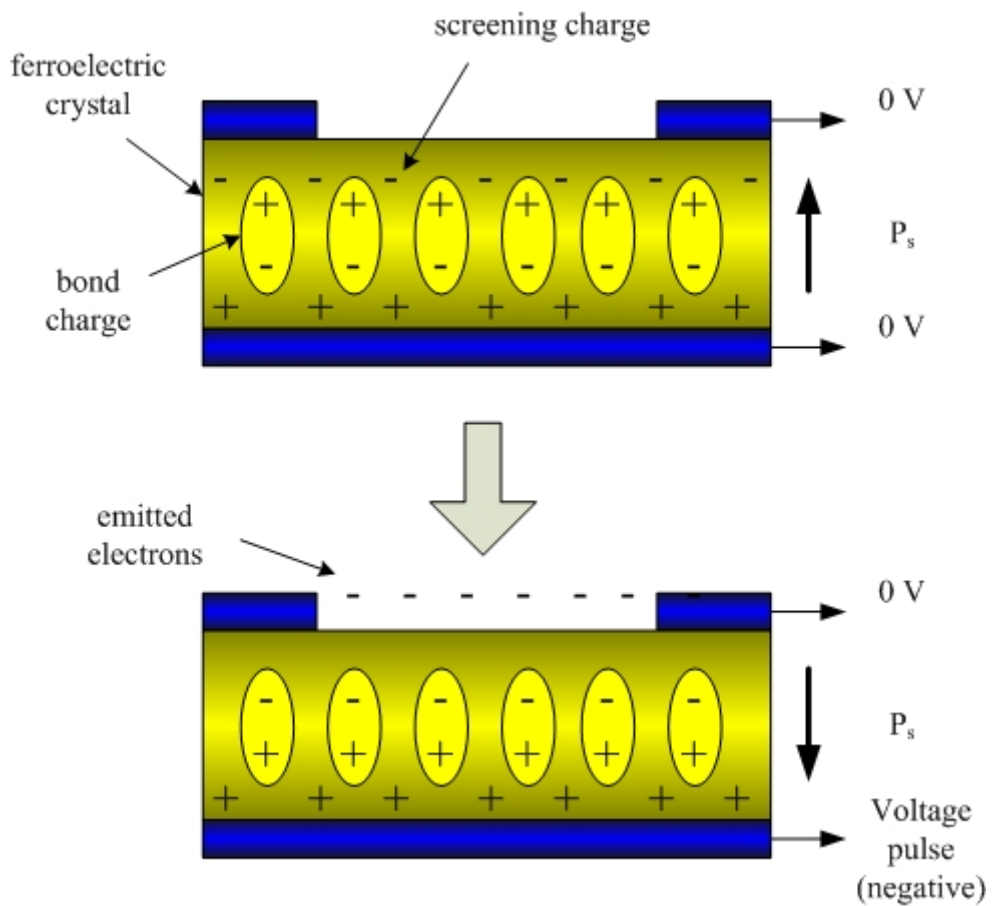
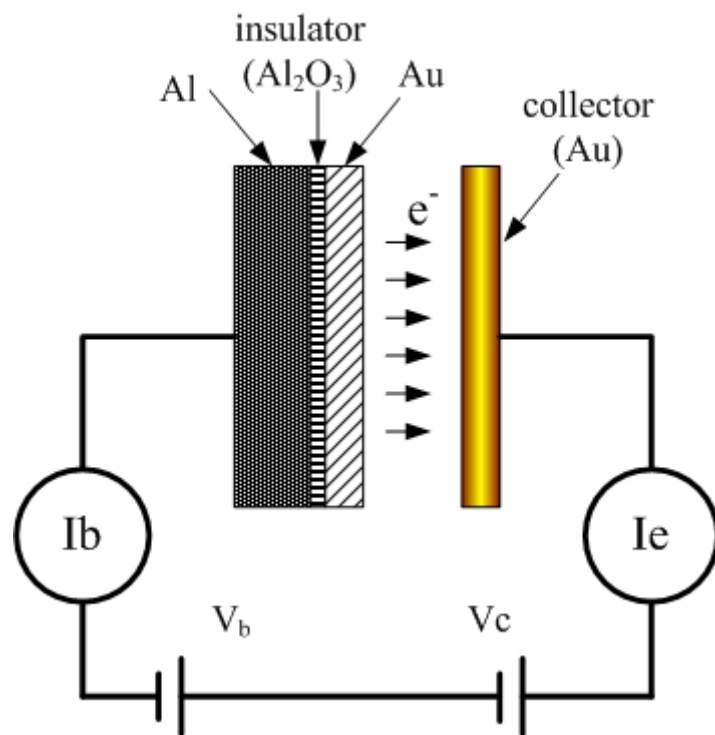
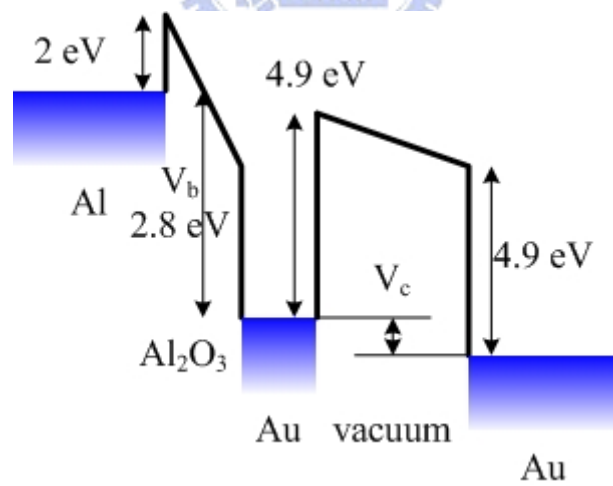


Figure 1.7 The schematic illustration of the ferroelectric emission mechanism. The screening charges are developed to compensate the net charges and a fast reversal of the polarization results a large electric field that ejects the electrons from the negative charged surface.



(a)



(b)

Figure 1.8 The schematic depiction of (a) the MIM device structure and (b) the emission mechanism.

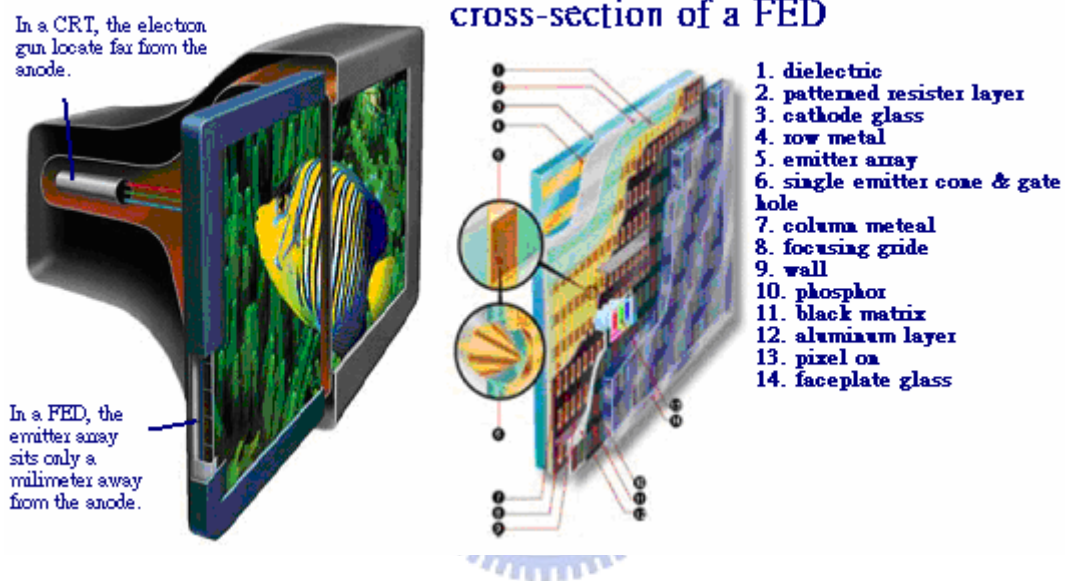
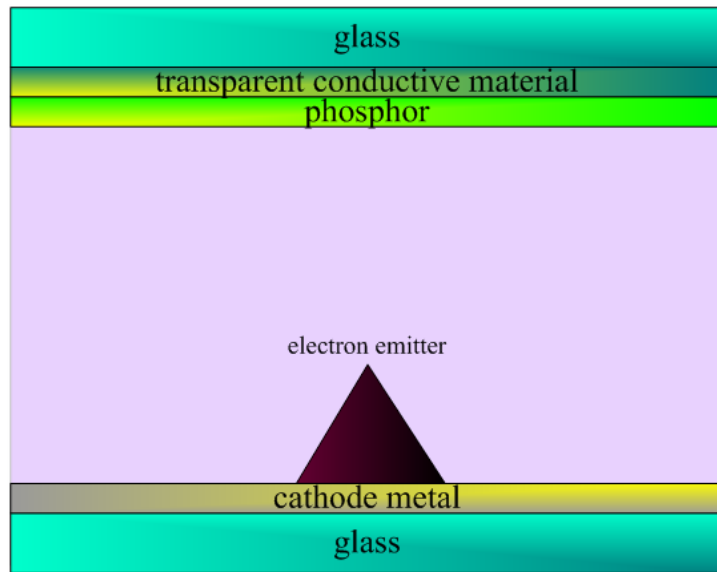
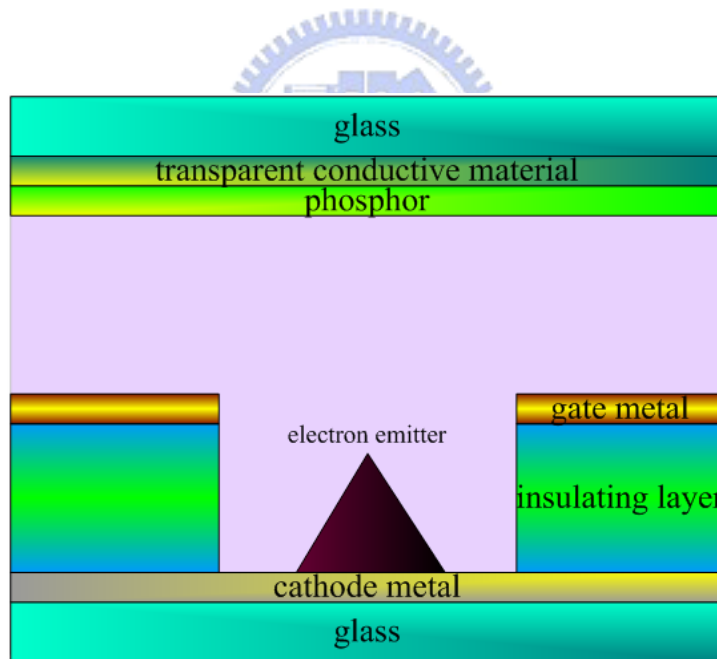


Figure 1.9 A schematic illustration for the structures of a cathode-ray tube and a field-emission display. The left image shows that the electron source in the CRT is far from the anode but the electron source in the FED is just a millimeter away from the anode. The right-side figure demonstrates the cross-section view of a FED.



(a)



(b)

Figure 1.10 The device structures of (a) diode-type and (b) triode-type in field-emission displays. The main differences between the diode-type and the triode-type device structure are the gate electrode around the emitter which can extract electrons from the cathodes at relative low electric field.

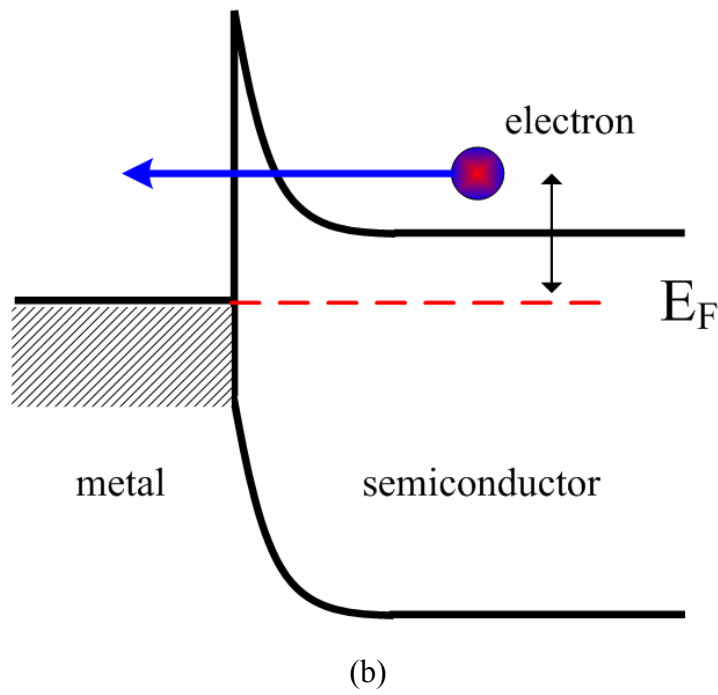
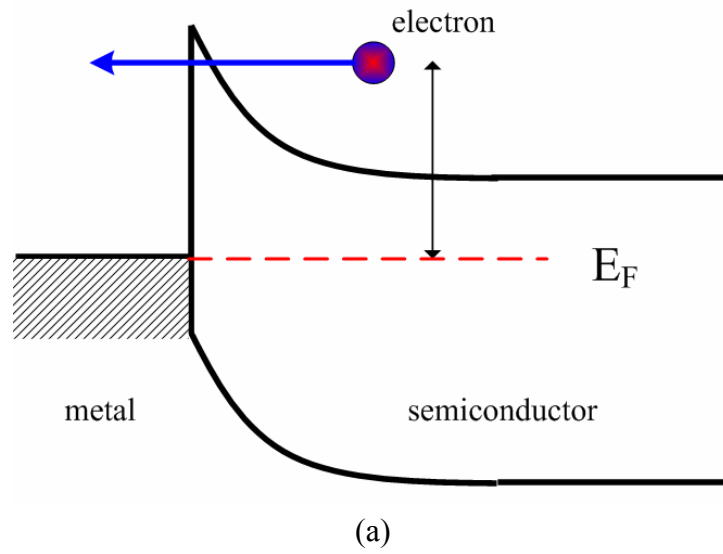
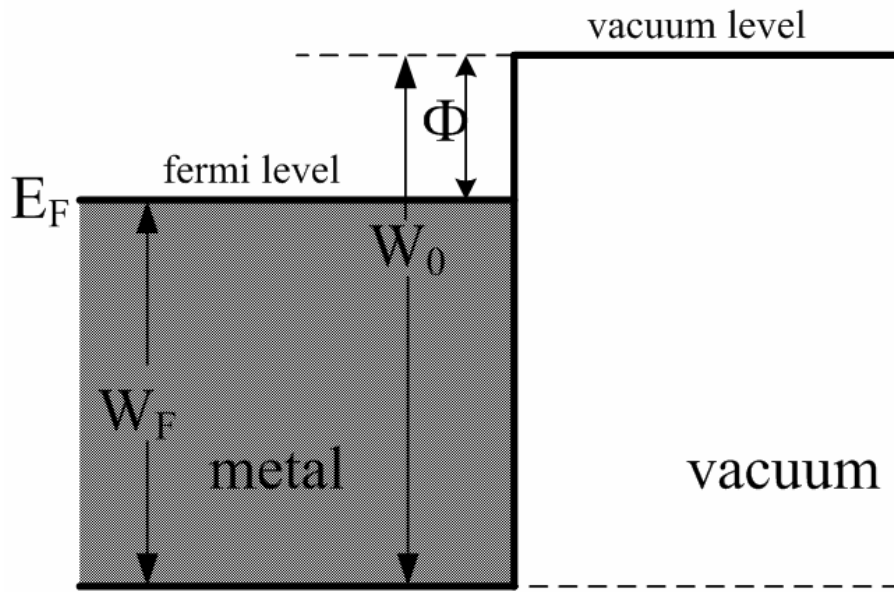
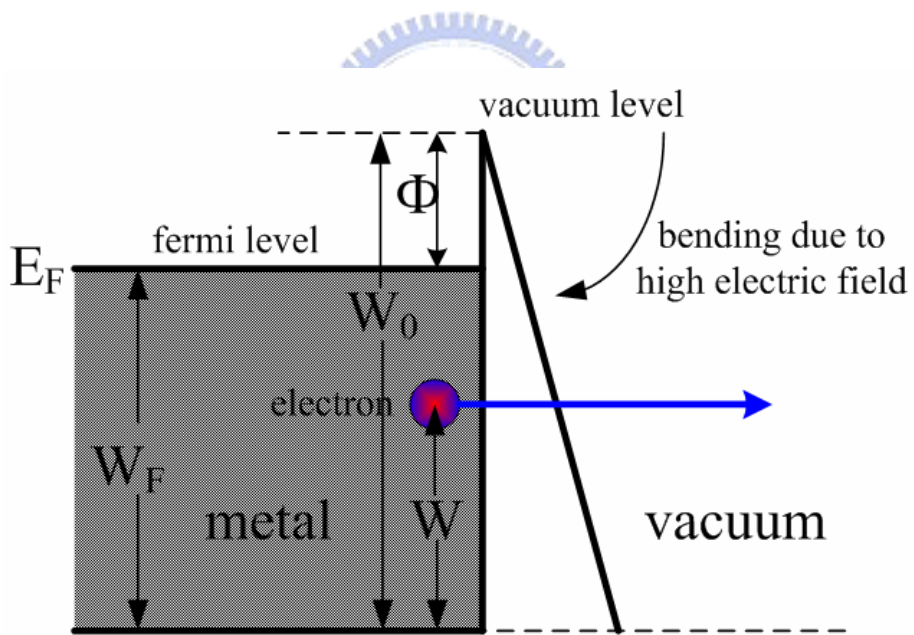


Figure 1.11 The energy diagrams demonstrate the mechanisms of (a) thermionic-field emission and (b) field emission in semiconductor.



(a)



(b)

Figure 1.12 The band diagram of the field-emission emitters in the vacuum environment (a) without applied electric field and (b) with applied electric field.

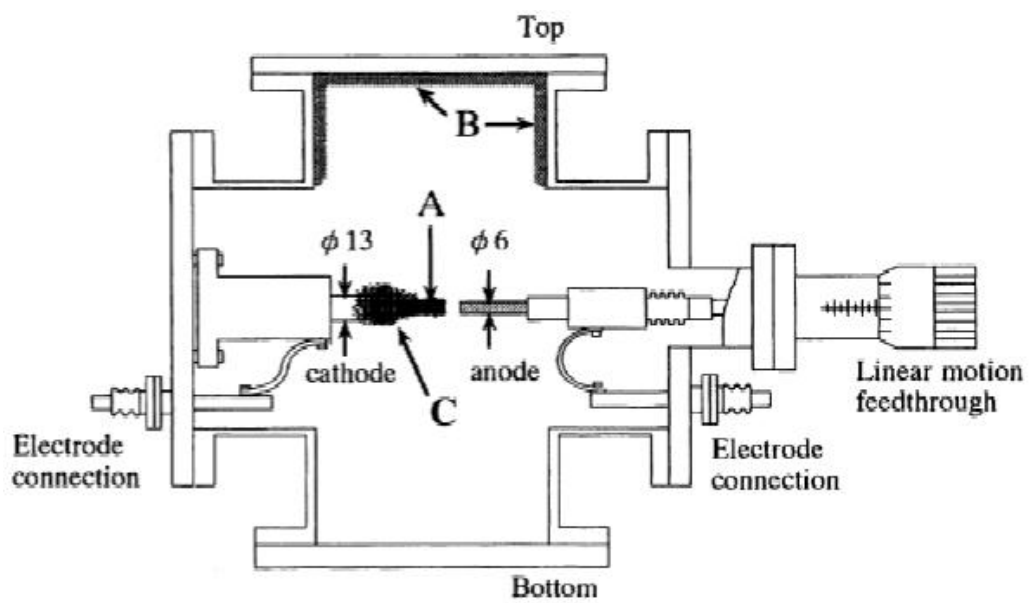


Figure 1.13 The structure of the arc discharge system for synthesizing CNTs.

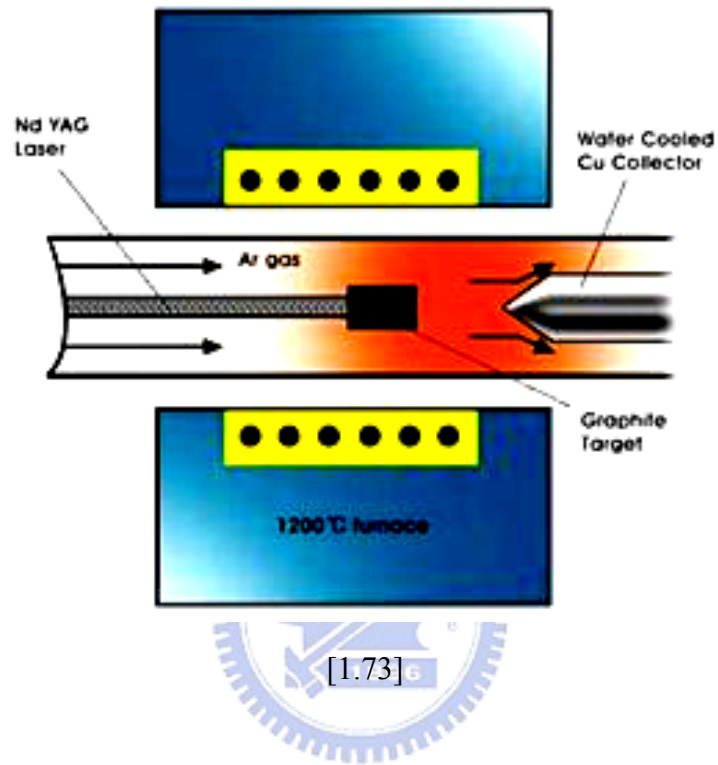


Figure 1.14 The scheme for the structure of laser ablation system.

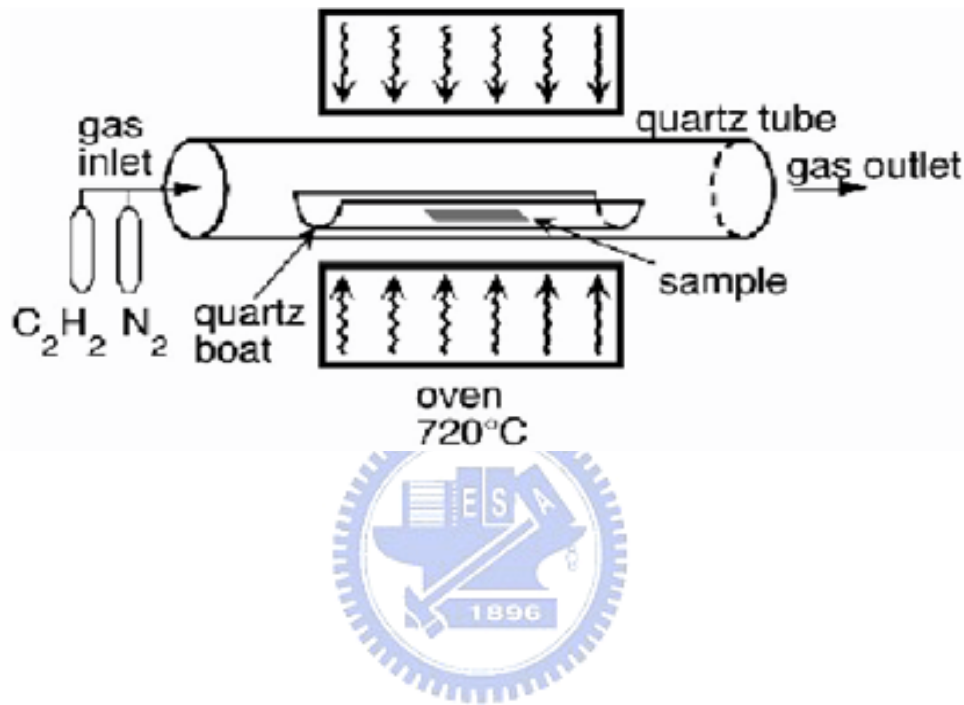


Figure 1.15 The structure of chemical vapor deposition system for synthesizing CNTs.

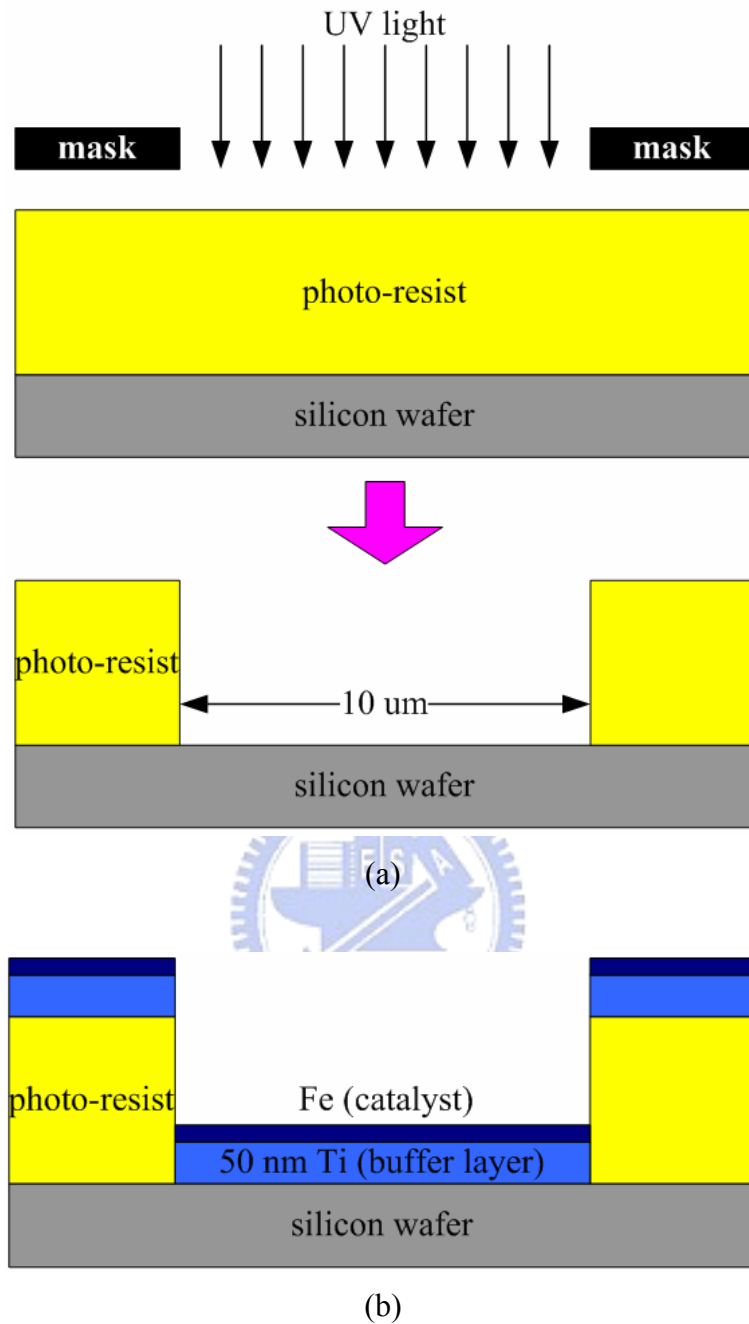
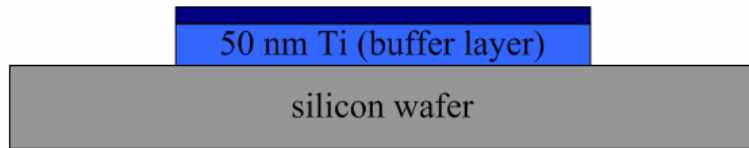
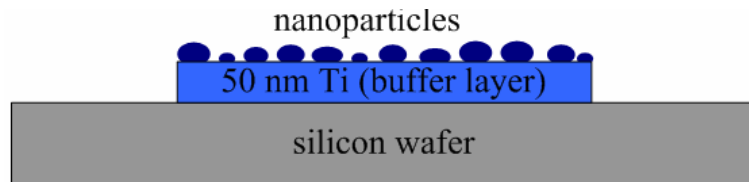


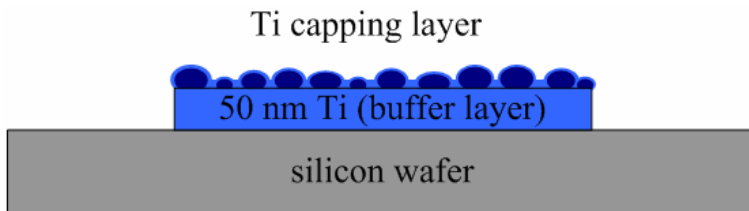
Figure 2.1 The schematic flowchart for the fabrication of experimental samples: (a) forming a 50×50 array of square holes with $10 \mu\text{m}$ in length and $10\text{-}\mu\text{m}$ inter-space by the lithography system, (b) depositing a 50-nm -thick Ti buffer layer and a 5-nm -thick Fe catalytic layer subsequently by the dual-electron-gun deposition system, (c) removing the photoresist with Ti buffer layer and Fe catalytic layer by a lift-off process, (d) loading the samples into the thermal-CVD to be pretreated in hydrogen and form Fe nanoparticles, (e) depositing a thin Ti capping layer with 1 to 20 nm in thickness by the dual-electron-gun deposition system, and (f) synthesizing CNTs in the thermal-CVD.



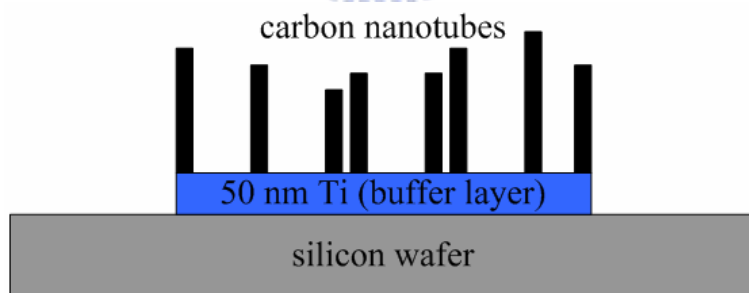
(c)



(d)



(e)



(f)

Figure 2.1 (cont.)

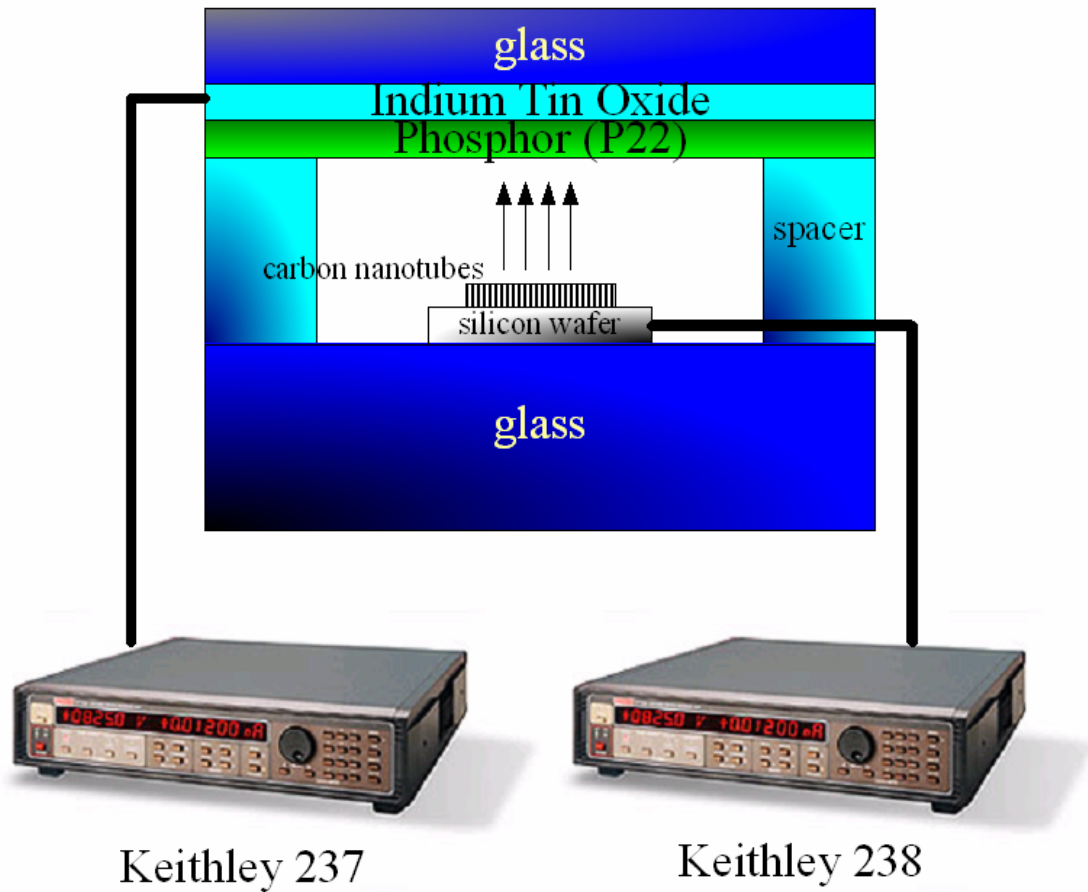
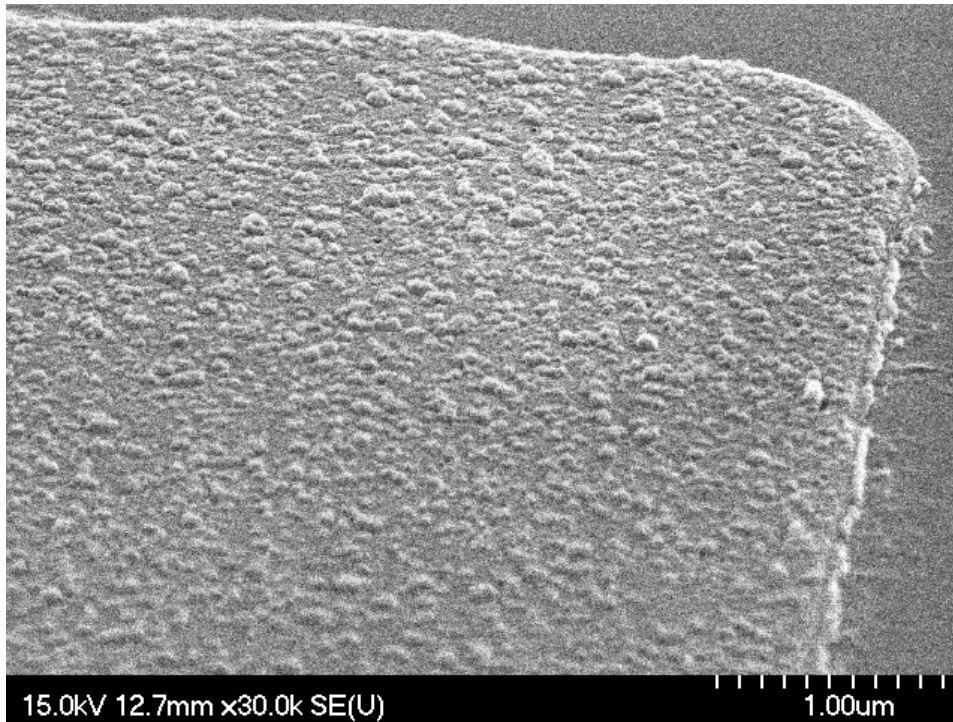
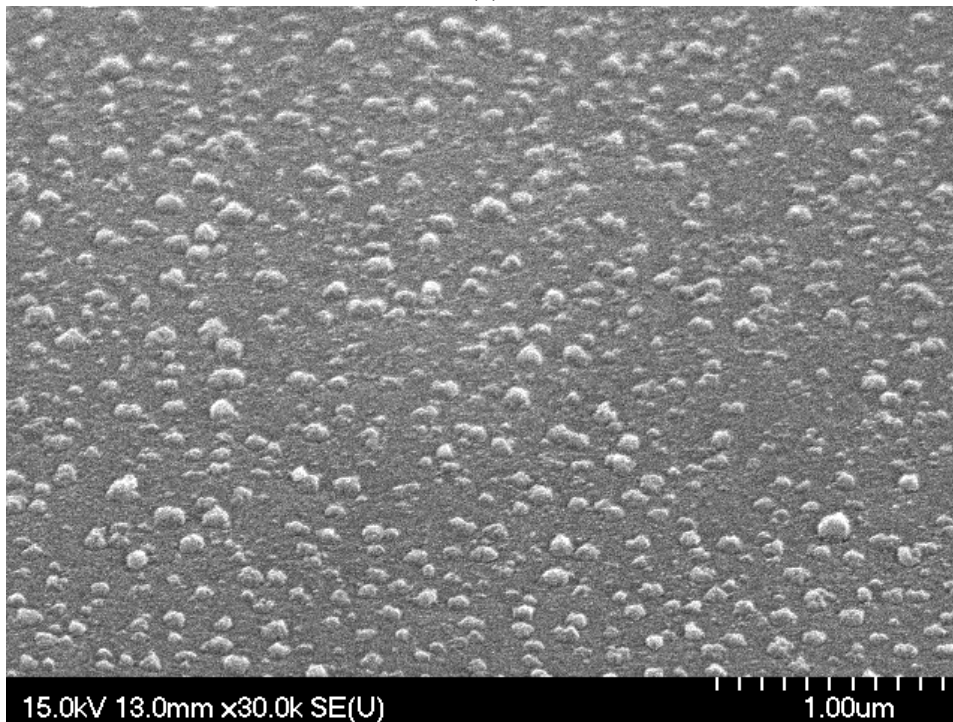


Figure 2.2 The samples were put on a glass substrate with a spacer of about 100 μm from the CNTs to the anode and the anode was a glass coated with a indium-tin-oxide (ITO) film and green phosphor (P22). The samples were loaded into a vacuum chamber with anode applied to the high-voltage source measurement unit, Keithley 237, and the cathode applied to the high-current source measurement unit, Keithley 238, to measure the field-emission current at high vacuum environment.

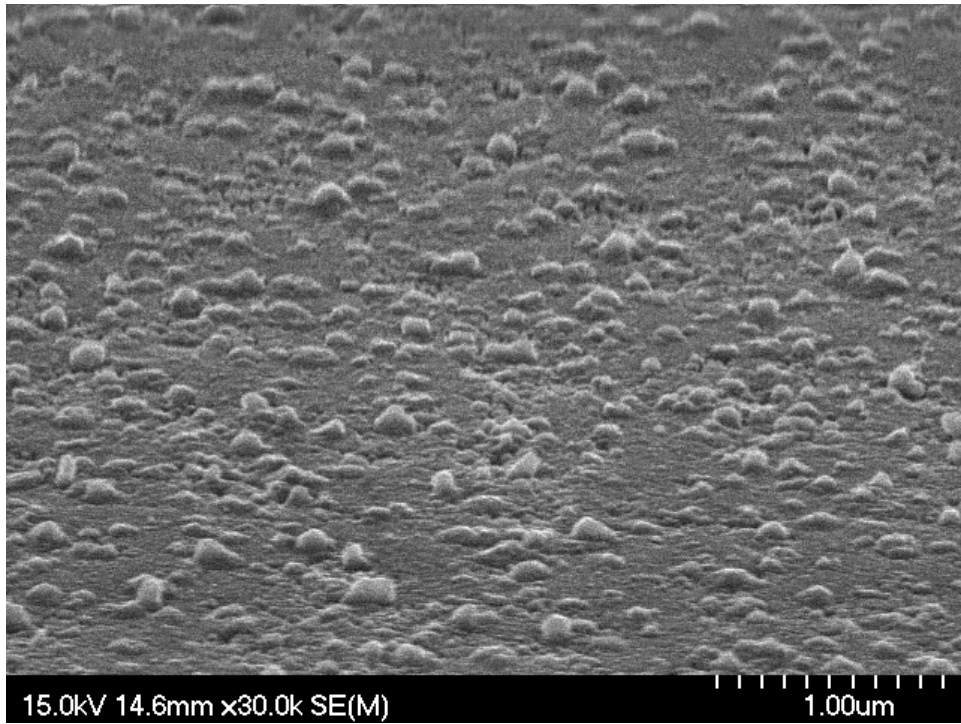


(a)

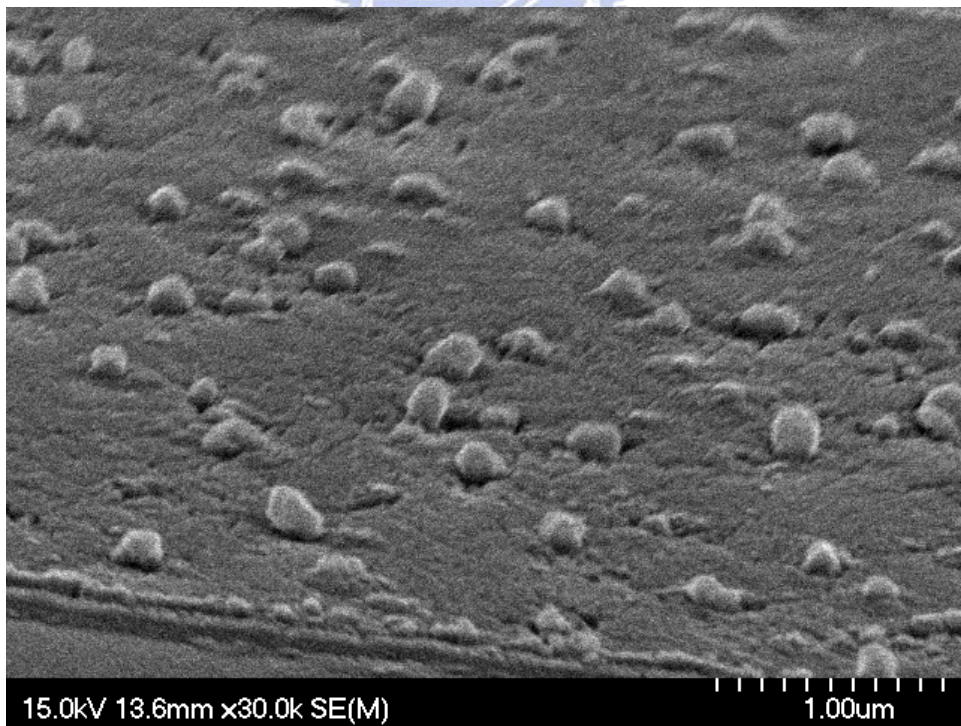


(b)

Figure 2.3 The pictures shown here were the images taken by SEM for the Fe nanoparticles that have been pretreated in hydrogen ambient for 5 min in the thermal-CVD with different thicknesses of the thin Ti capping layer: (a) 0 nm, (b) 1 nm, (c) 2 nm, (d) 4 nm, (e) 10 nm, and (f) 20 nm. With thicker Ti capping layer, the Fe nanoparticles were getting obscure in the micrographs due to being buried in the Ti capping layer.

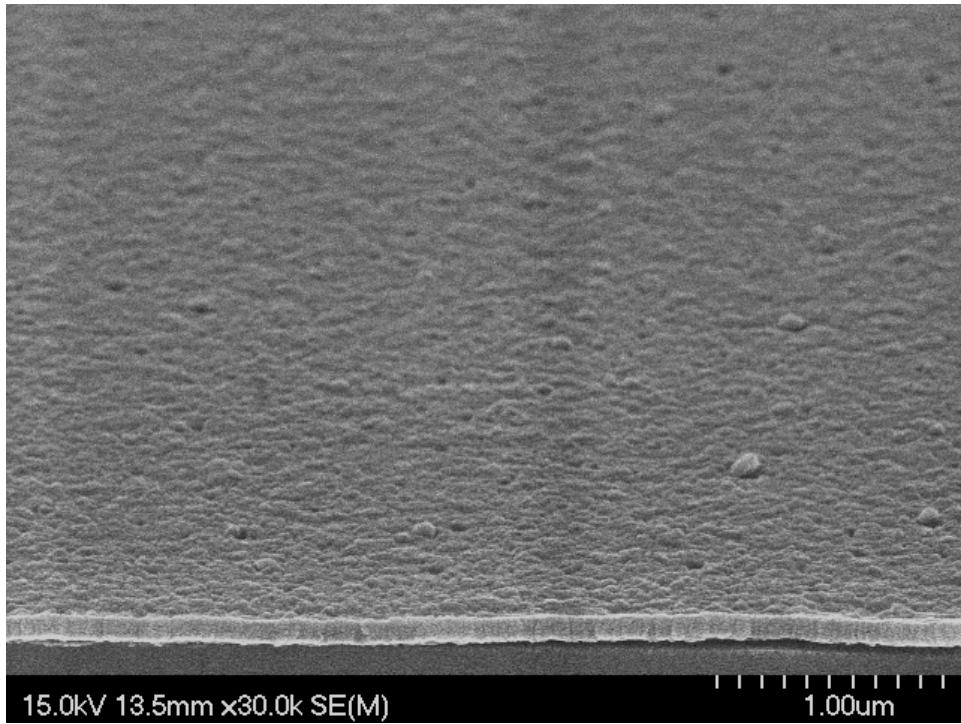


(c)

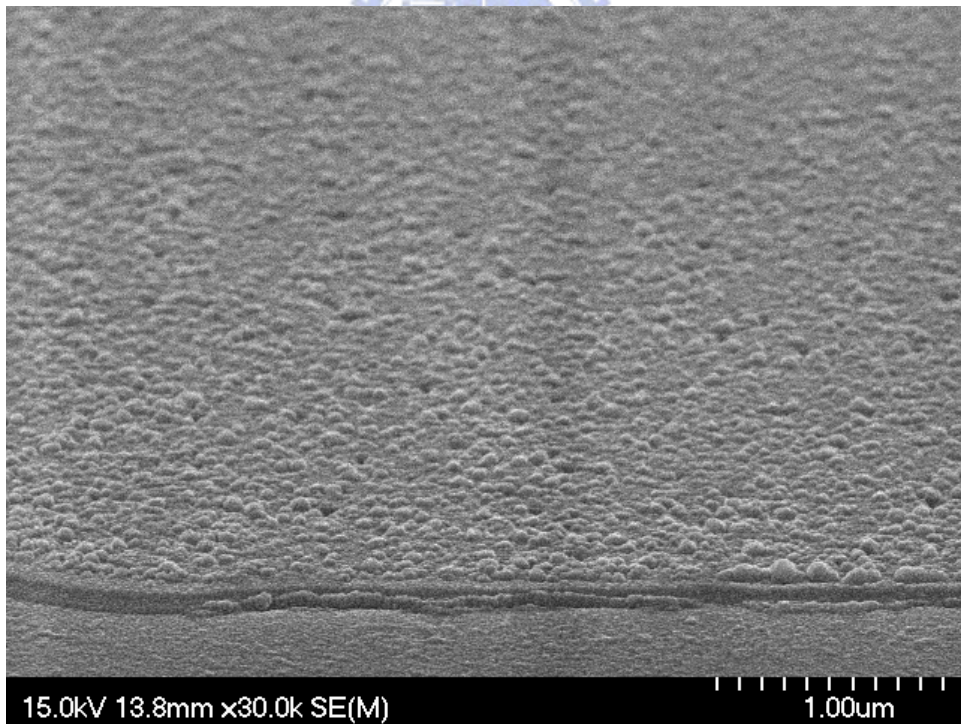


(d)

Figure 2.3 (cont.)

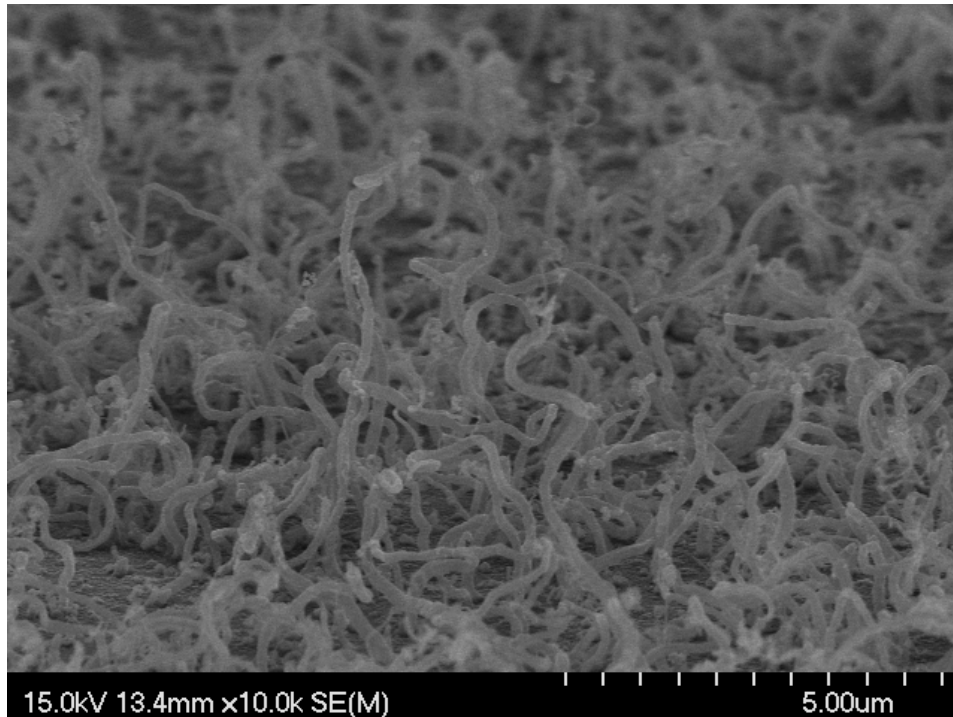


(e)

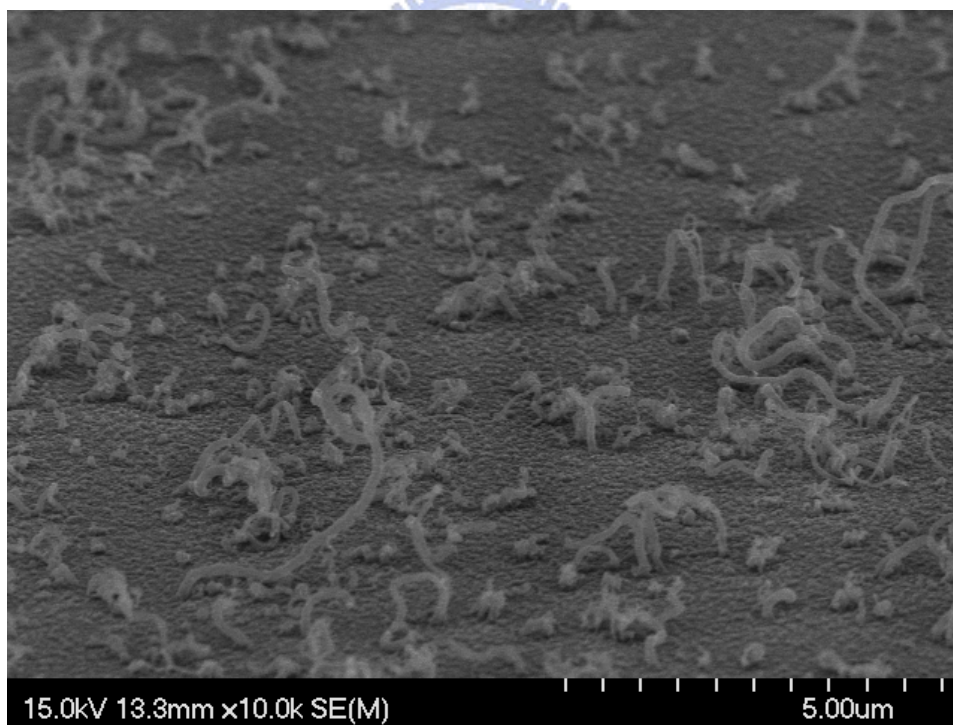


(f)

Figure 2.3 (cont.)

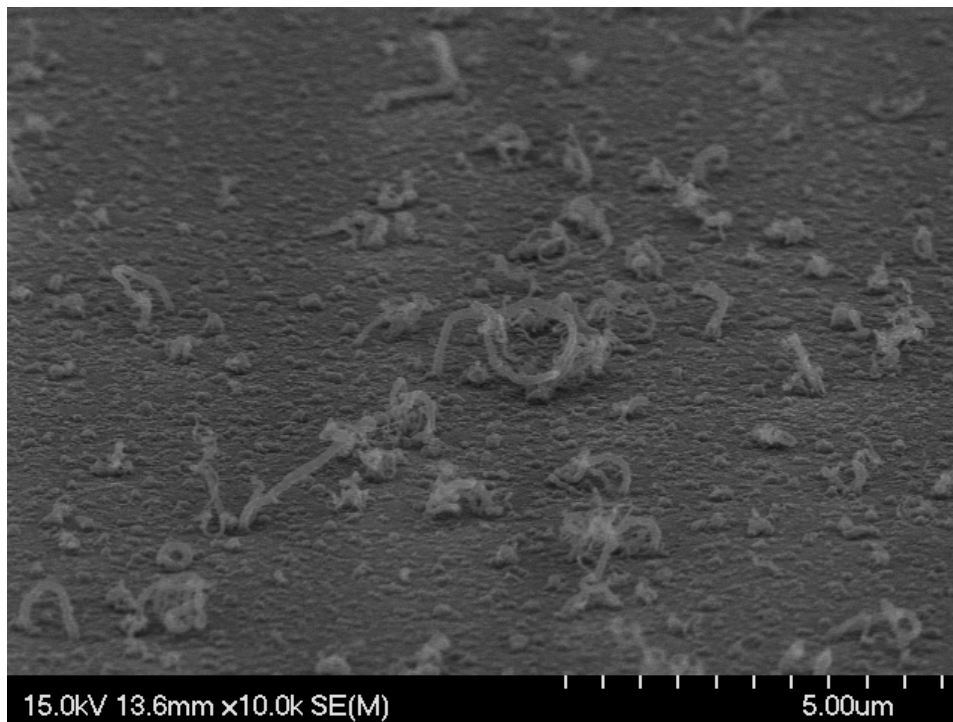


(a)



(b)

Figure 2.4 The surface morphologies taken by the SEM from top with 45° viewing angle for the CNTs of the samples with different thicknesses of the Ti capping layer: (a) 0 nm, (b) 1 nm, (c) 2 nm, (d) 4 nm, (e) 10 nm, and (f) 20 nm. It was obvious that the number density of the CNTs was decreased with the increasing thickness of the Ti capping layer.

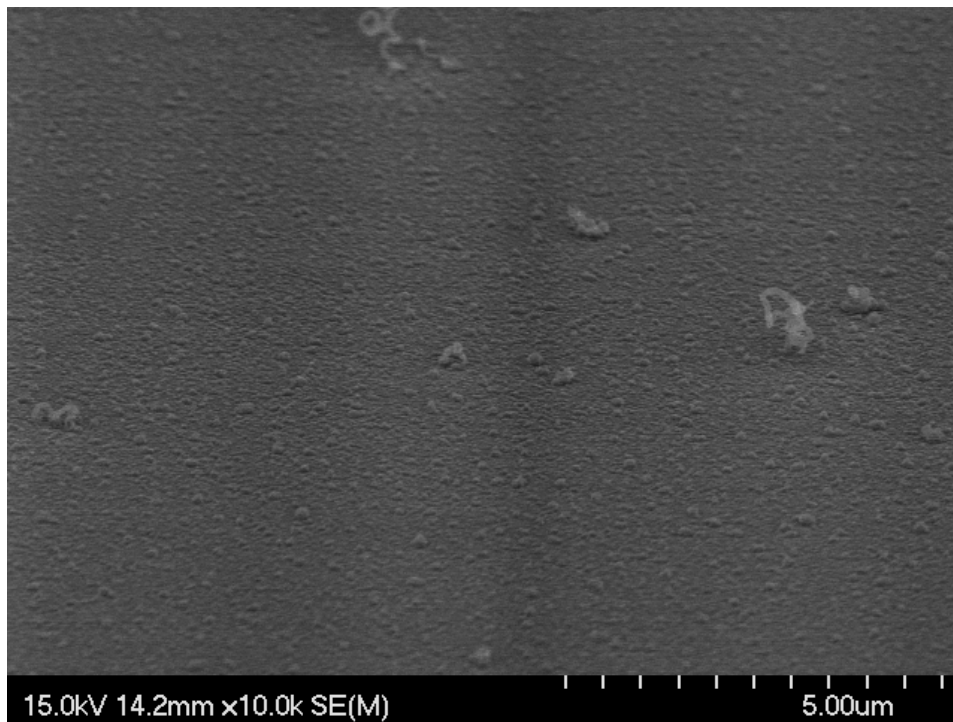


(c)

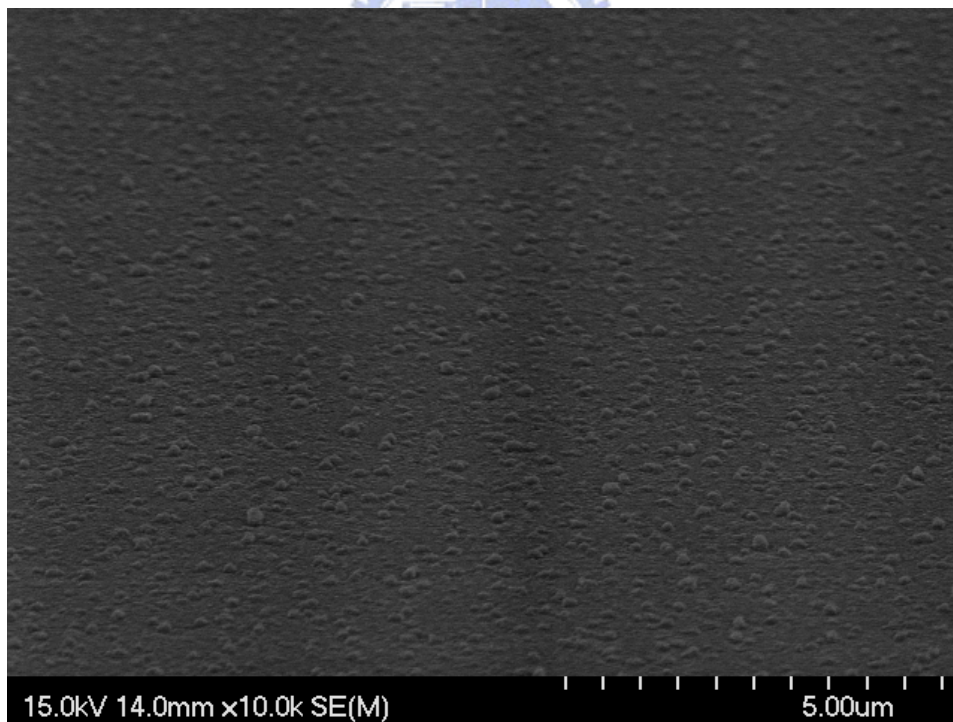


(d)

Figure 2.4 (cont.)

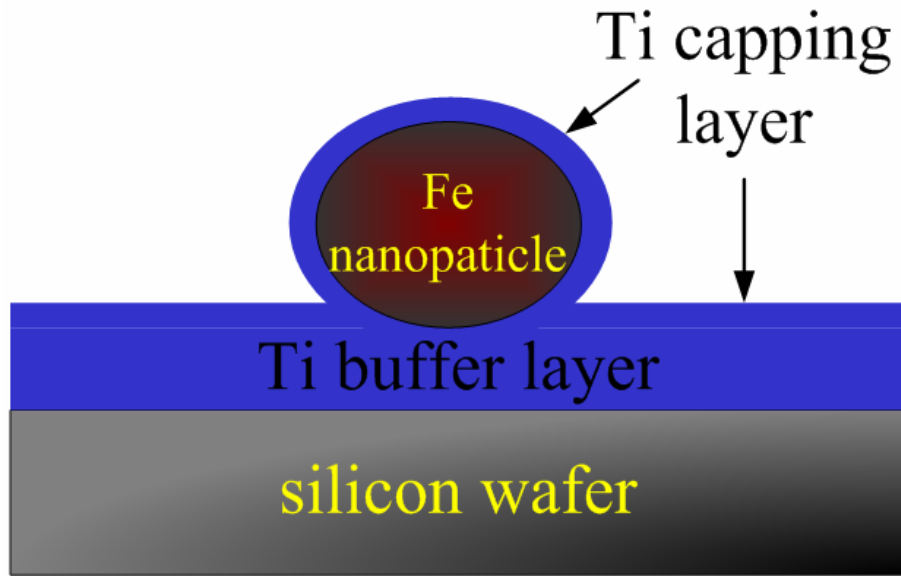


(e)

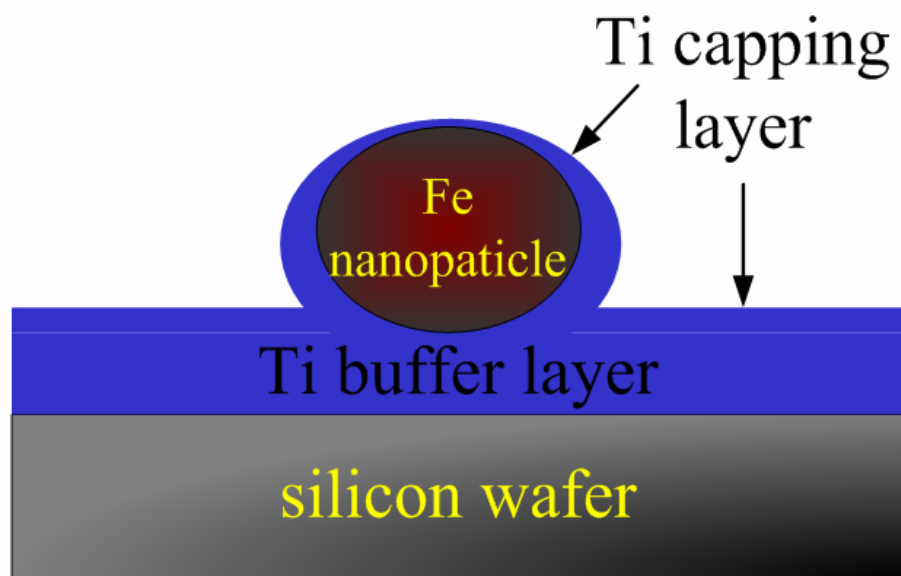


(f)

Figure 2.4 (cont.)

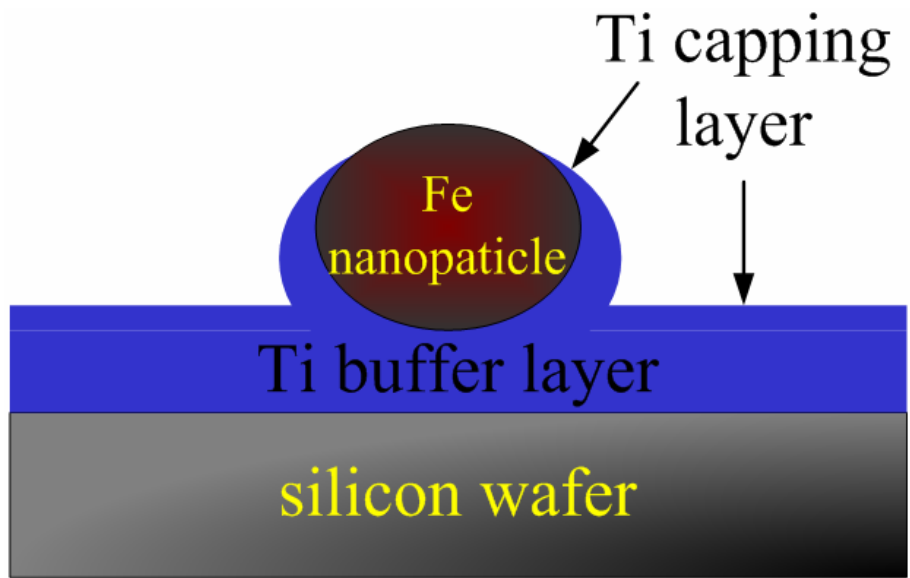


(a)



(b)

Figure 2.5 The scheme for the conditions of the Fe nanoparticles capped with thin Ti capping layer after being heated at 700 °C during the synthesis of the CNTs in the thermal-CVD: (a) the Fe nanoparticles capped with the thin Ti capping layer before growing the CNTs, (b) the deposited thin Ti capping layer was partially melted and getting thinner during the synthesis of CNTs at 700 °C, and (c) part of the Fe nanoparticle might even be exposed during the heating at 700 °C.



(c)

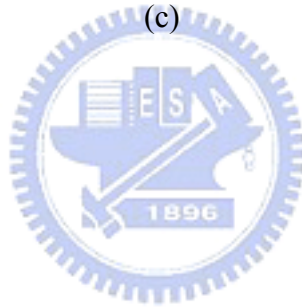
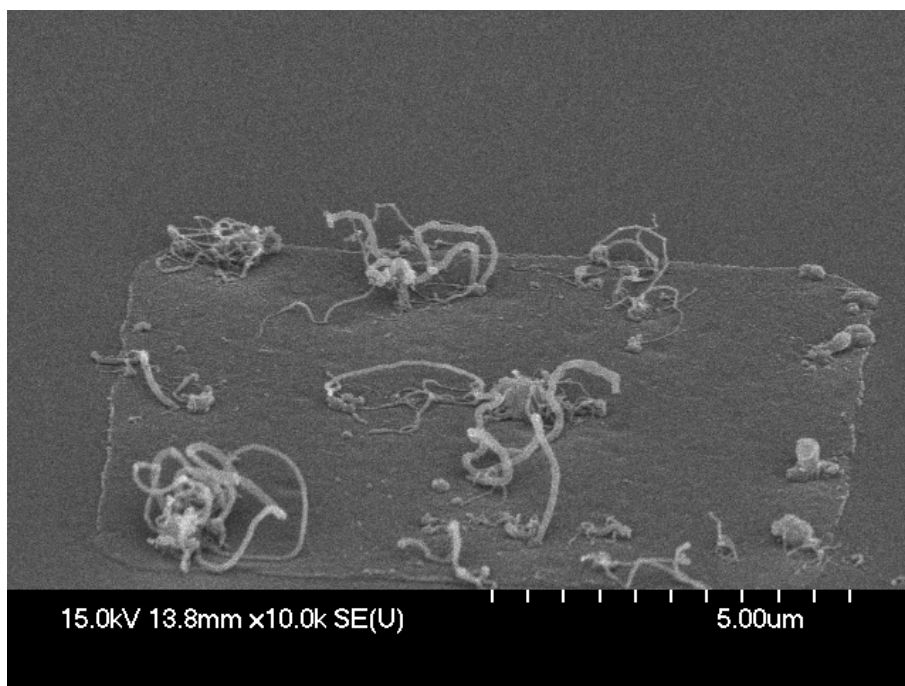
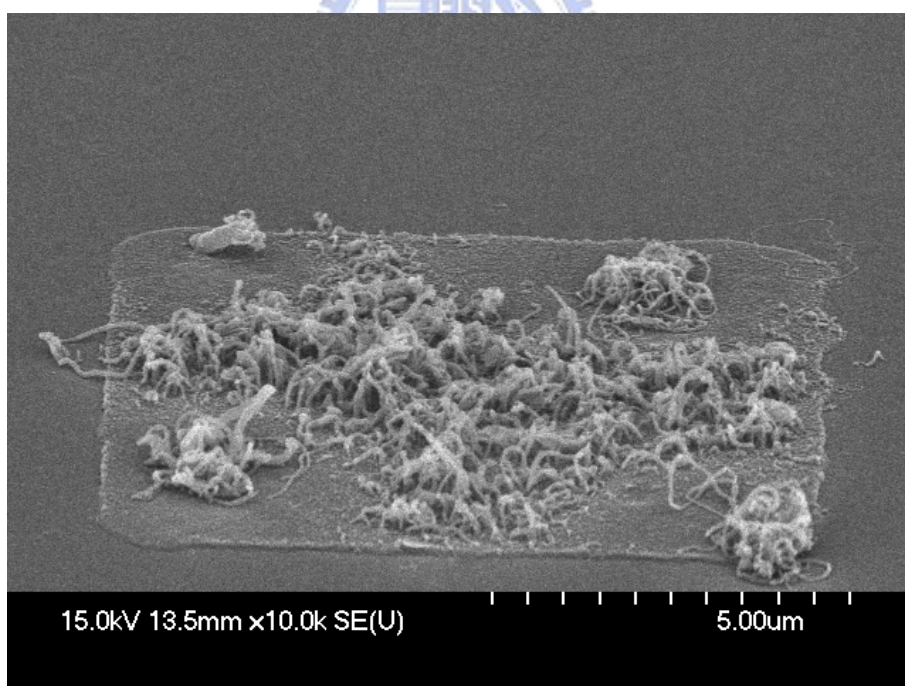


Figure 2.5 (cont.)

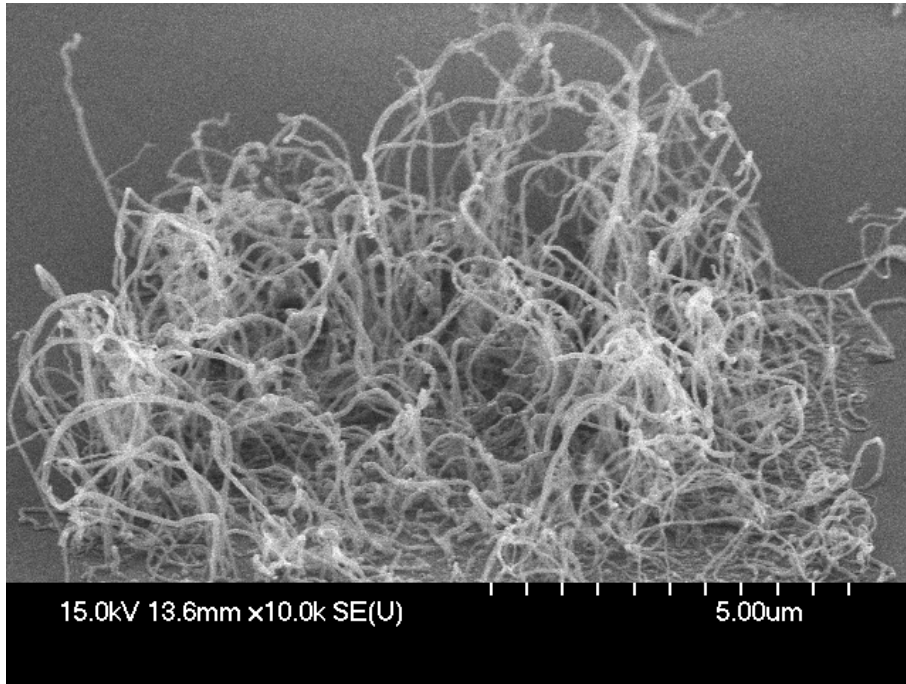


(a)

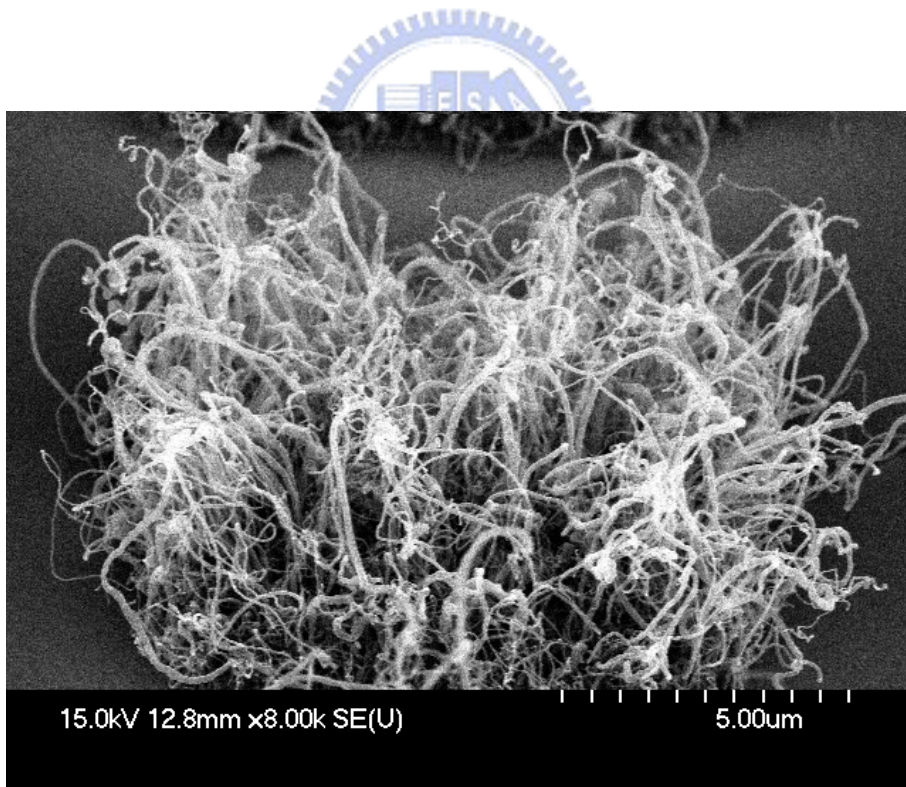


(b)

Figure 2.6 The morphologies of CNTs synthesized with different materials as the capping layer: (a) Mo, (b) Ti, (c) Al, and (d) without capping layer

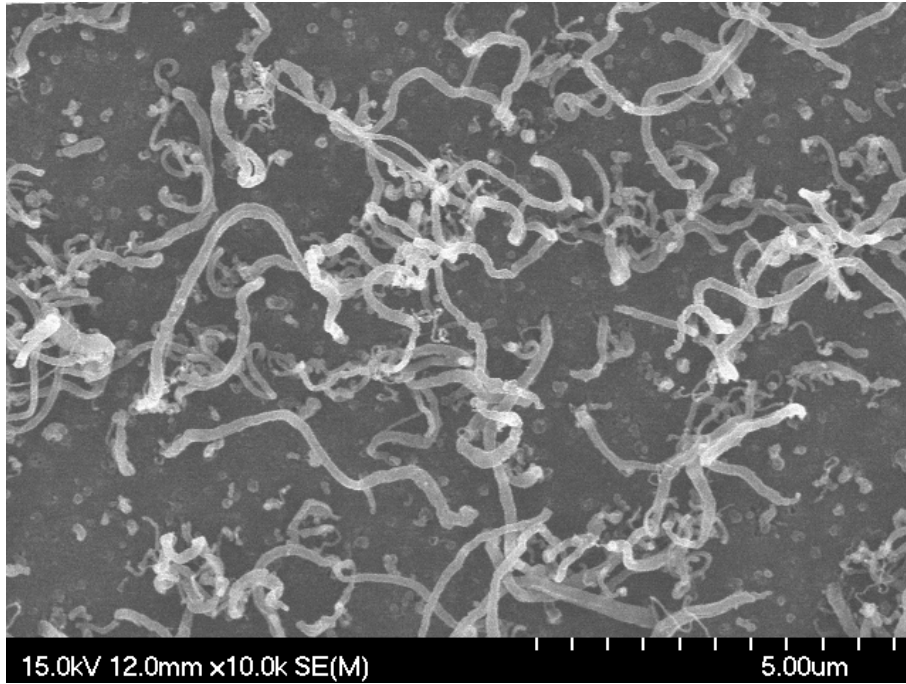


(c)

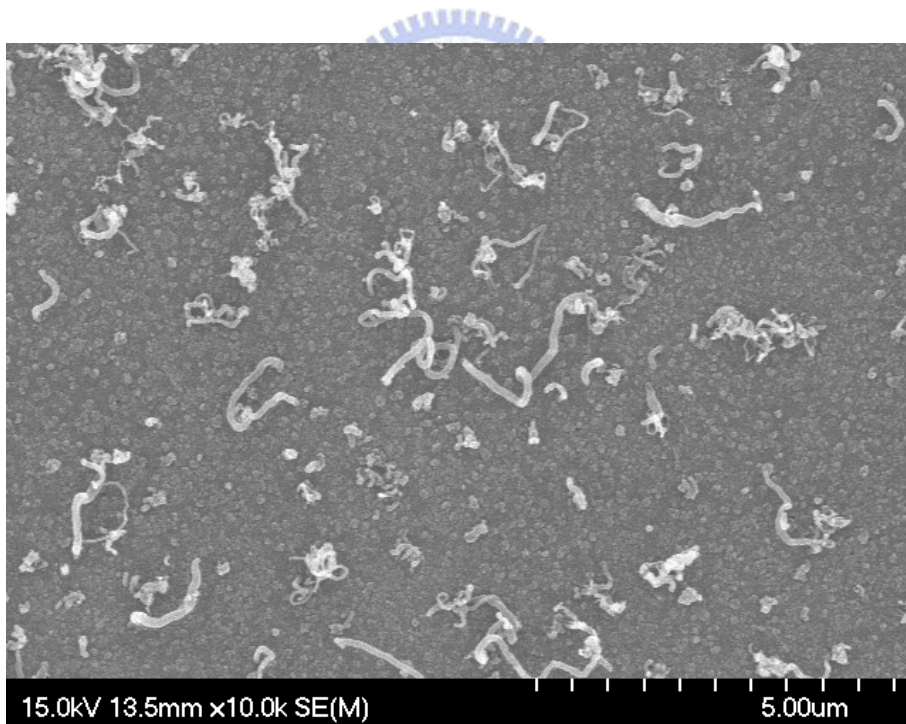


(d)

Figure 2.6 (cont.)

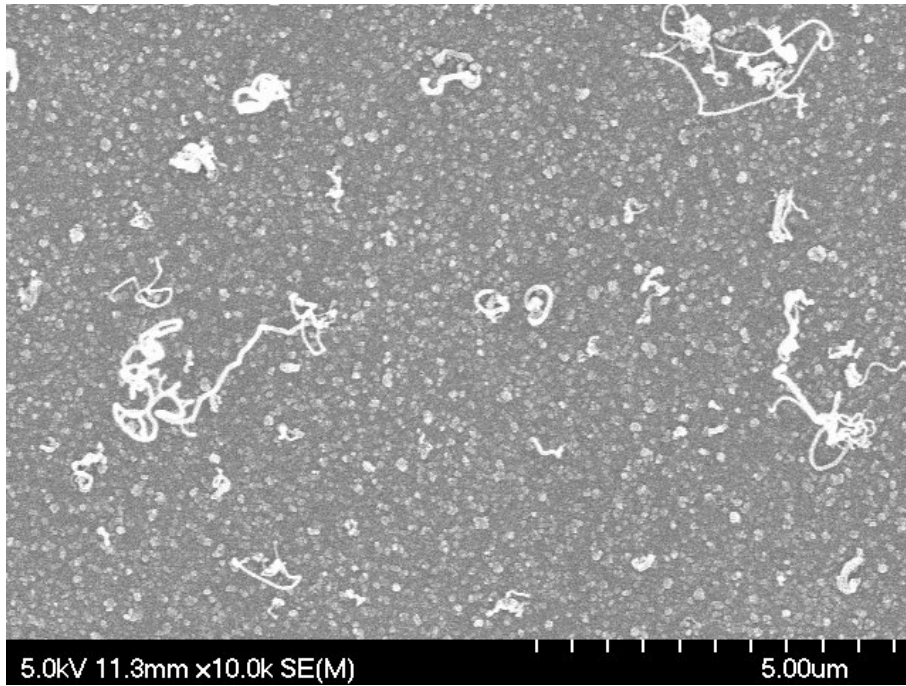


(a)

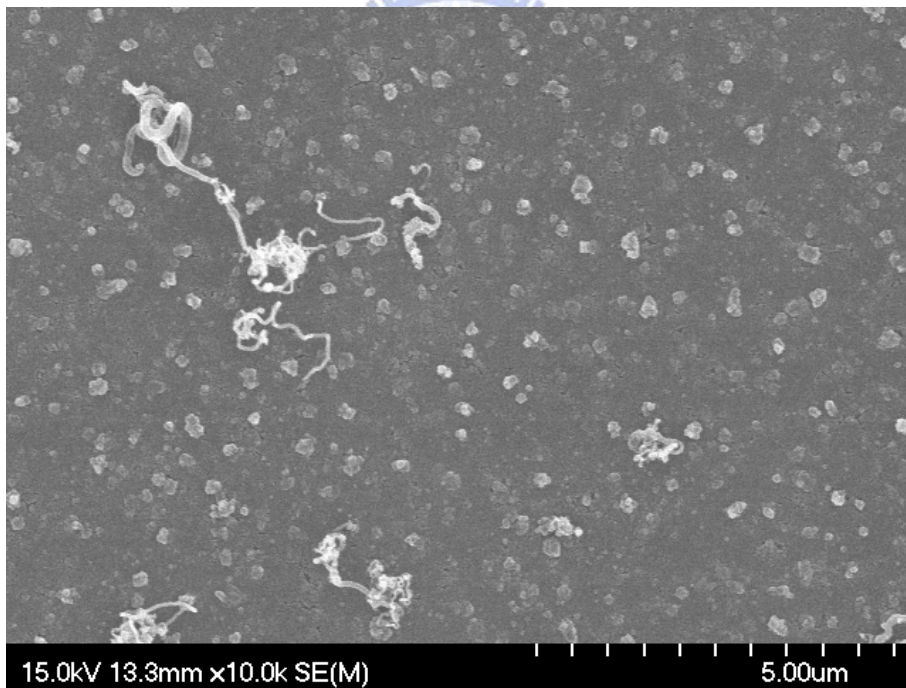


(b)

Figure 2.7 The SEM images of CNTs with different thickness of thin Ti capping layer from the top view: (a) 0 nm (b) 1 nm (c) 2 nm (d) 4 nm (e) 10 nm (f) 20 nm.

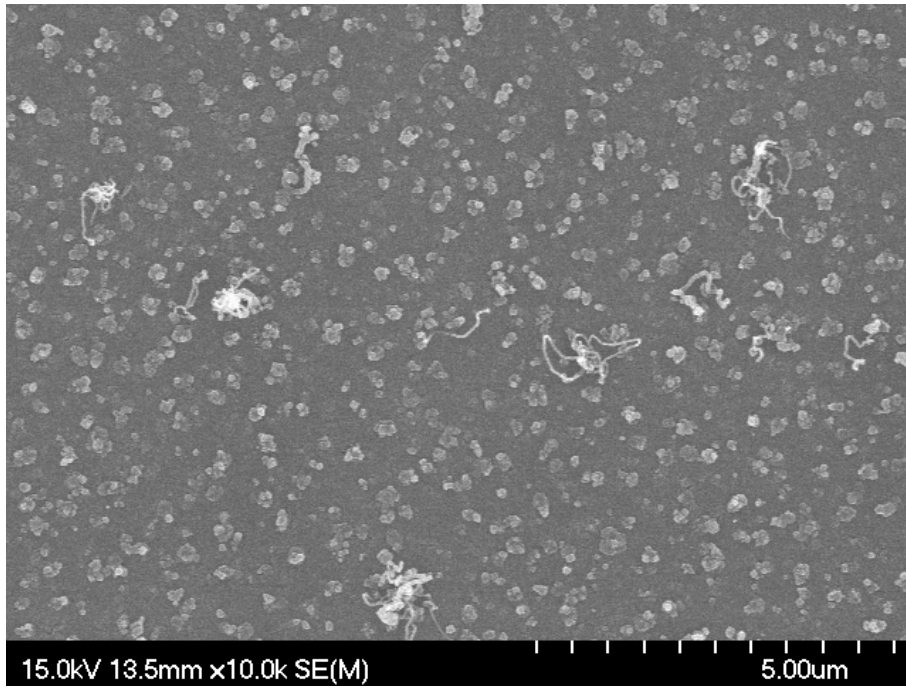


(c)

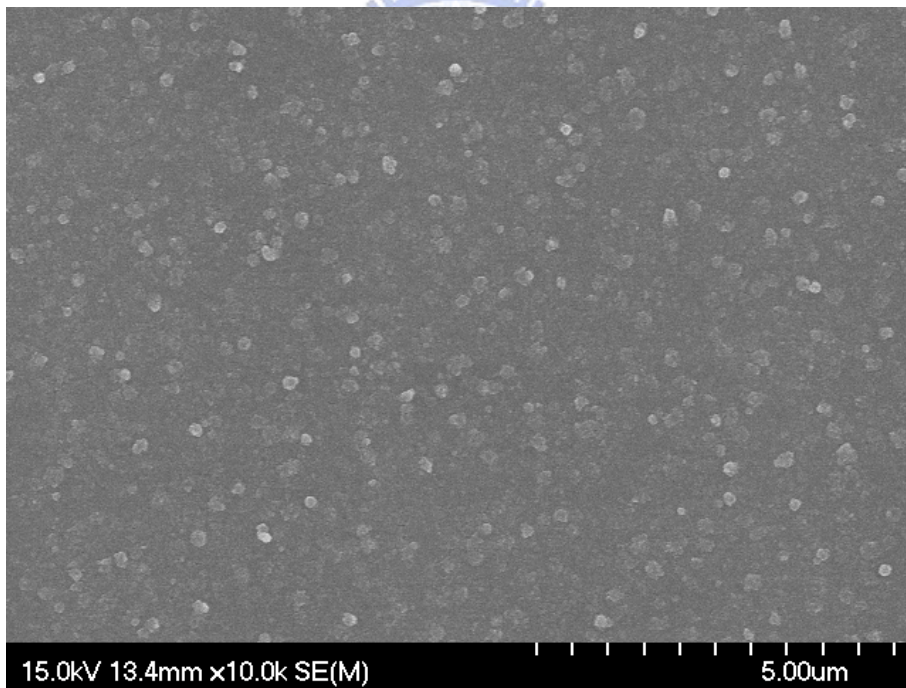


(d)

Figure 2.7 (cont.)

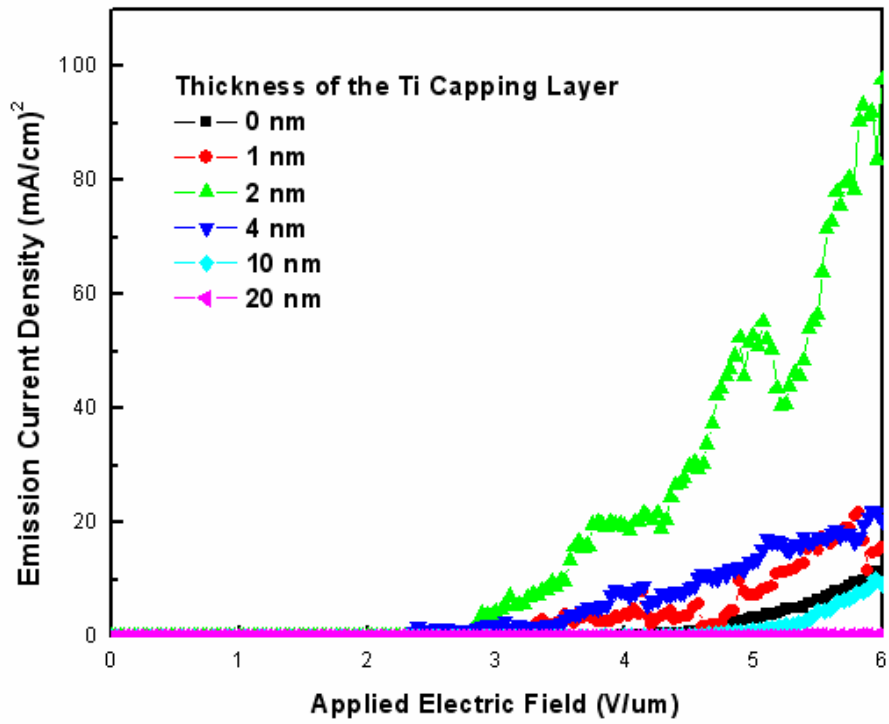


(e)

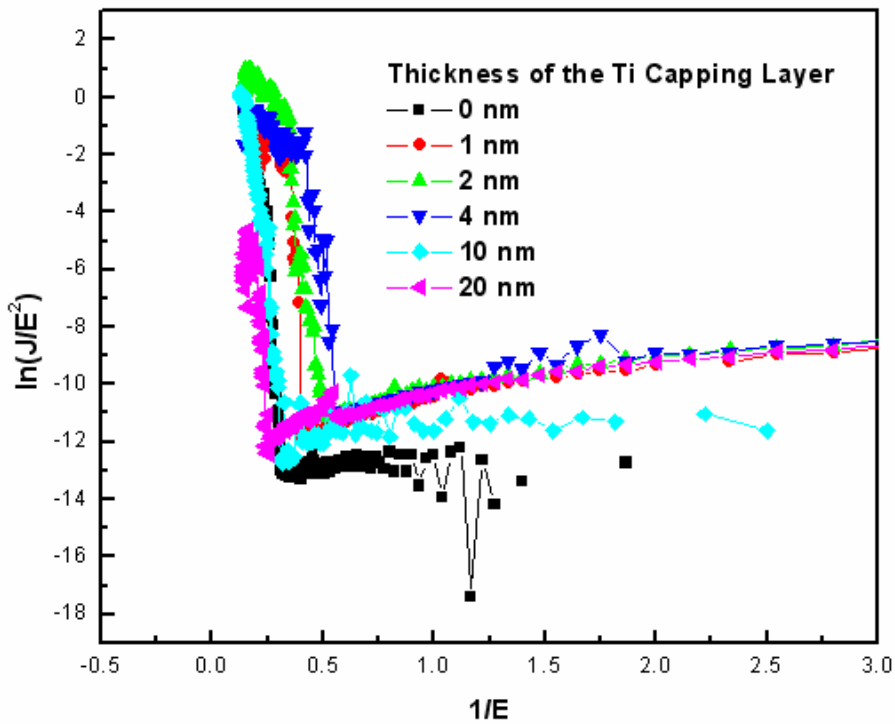


(f)

Figure 2.7 (cont.)



(a)



(b)

Figure 2.8 The field-emission characteristics for the samples with different thicknesses of the Ti capping layer: (a) the emission current density versus the electric field and (b) the F-N plot

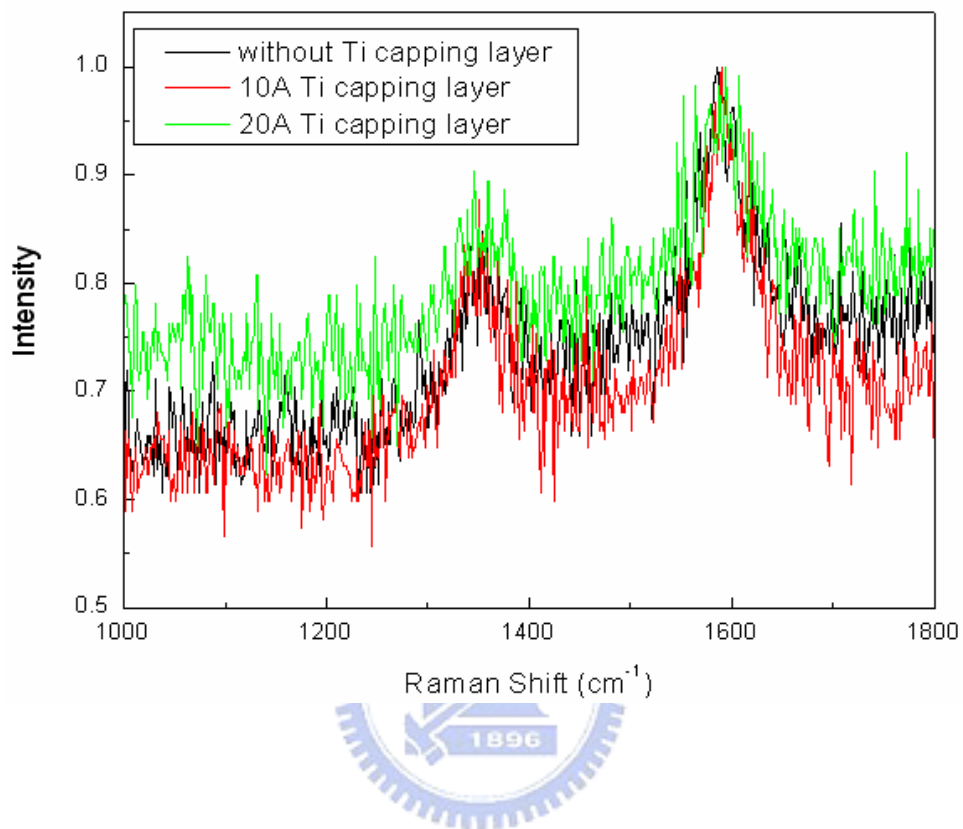


Figure 2.9 The Raman spectra of the CNTs with no Ti capping layer and with Ti capping layer of 1 nm and 2 nm. The Raman spectra for the samples with thicker Ti capping layer were too weak to be detected here.

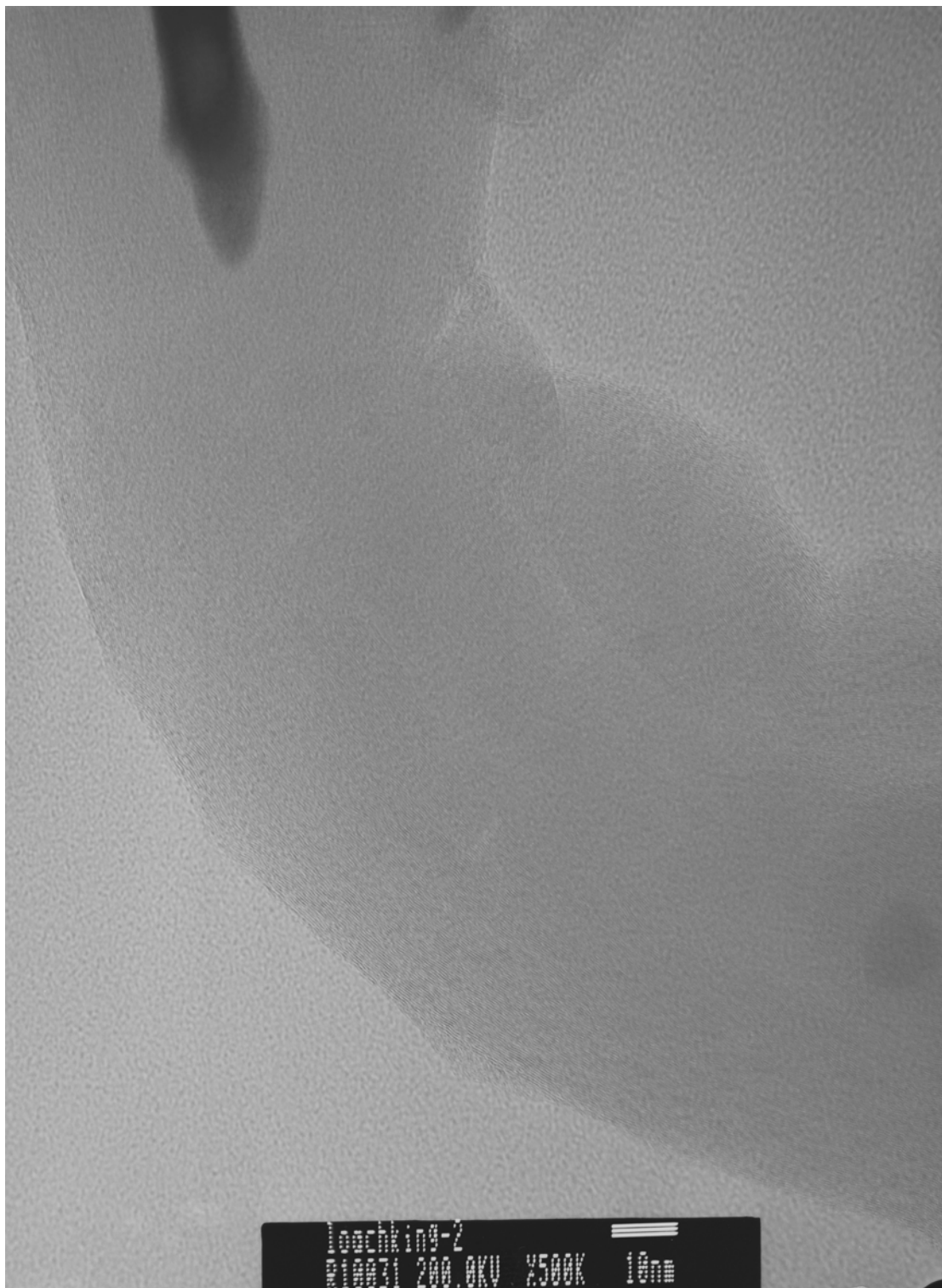


Figure 2.10 (a) The micrograph of the CNTs taken by TEM

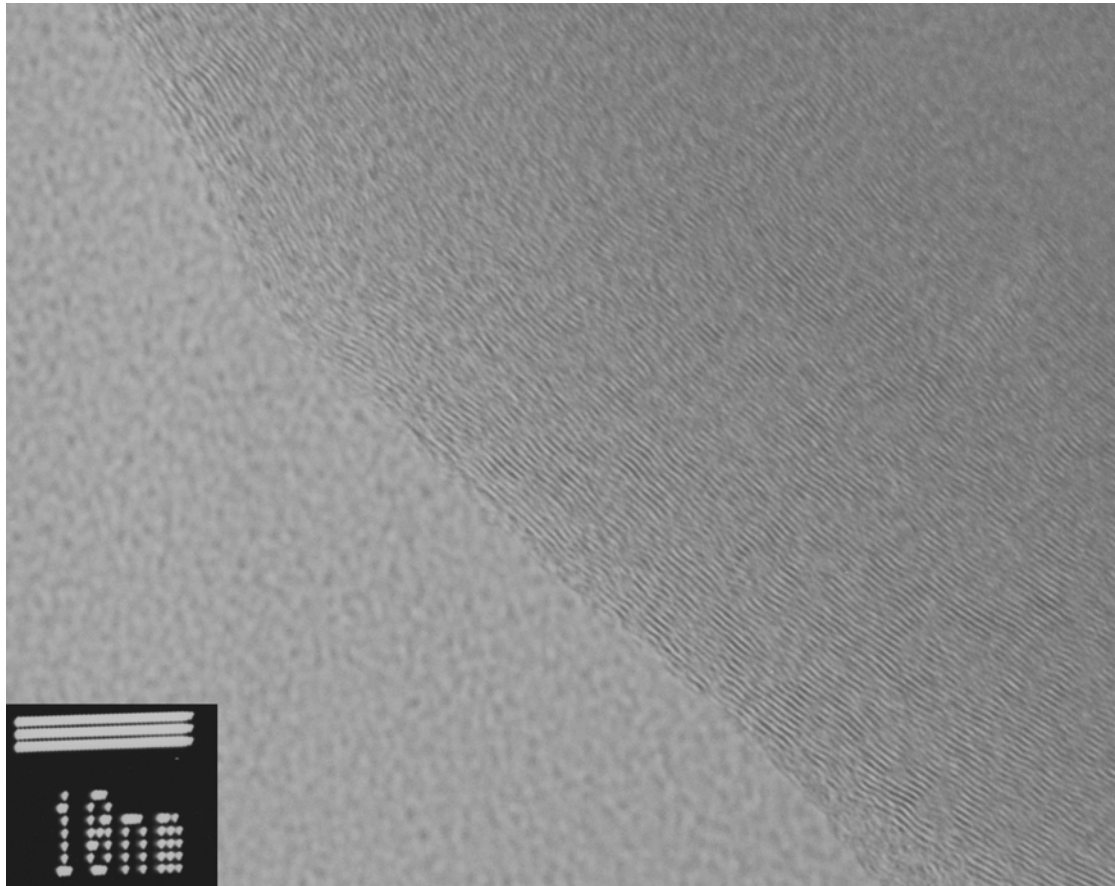


Figure 2.10 (b) The micrograph of CNTs taken by TEM with higher resolution

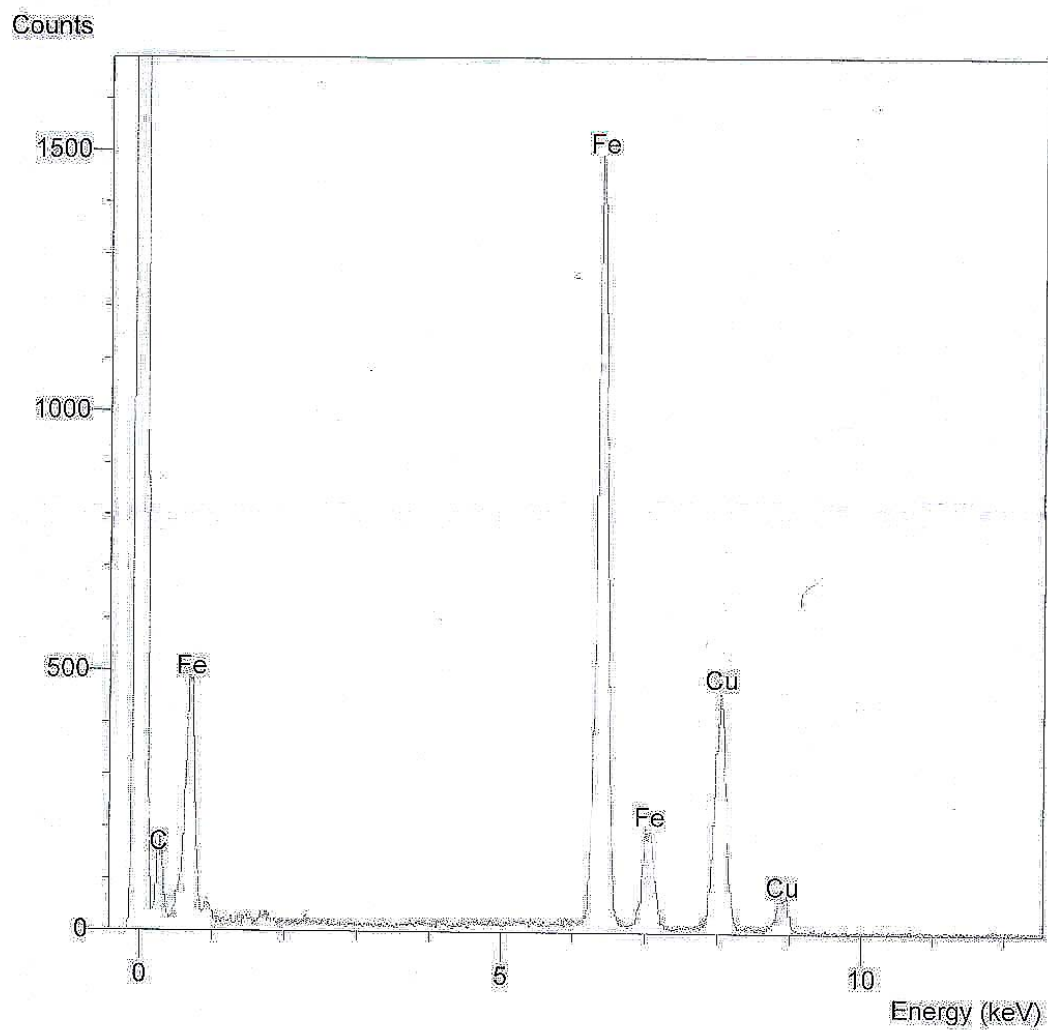


Figure 2.11 The analysis results of energy dispersive spectrometer for the nanoparticles enclosed in CNTs as shown in Fig. 2.10(a).

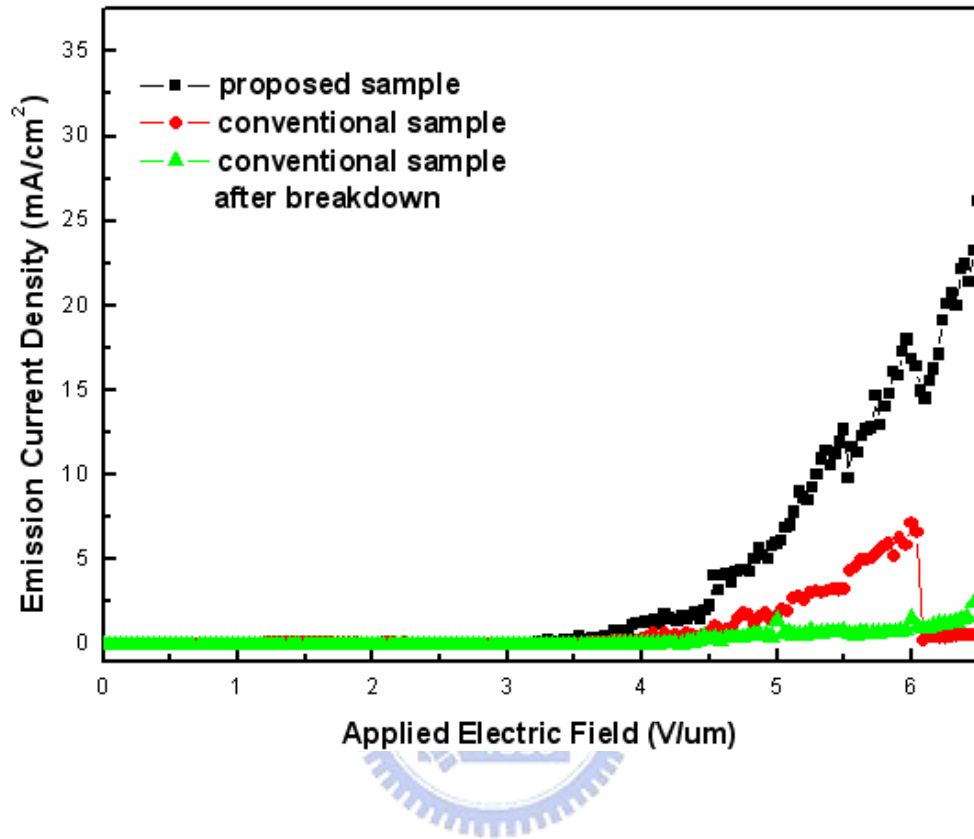
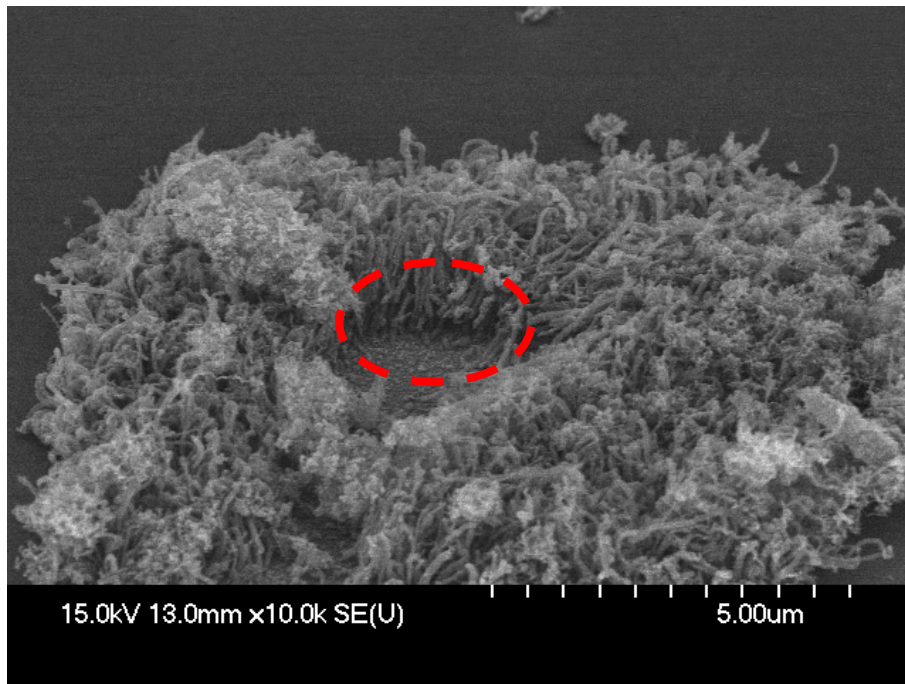
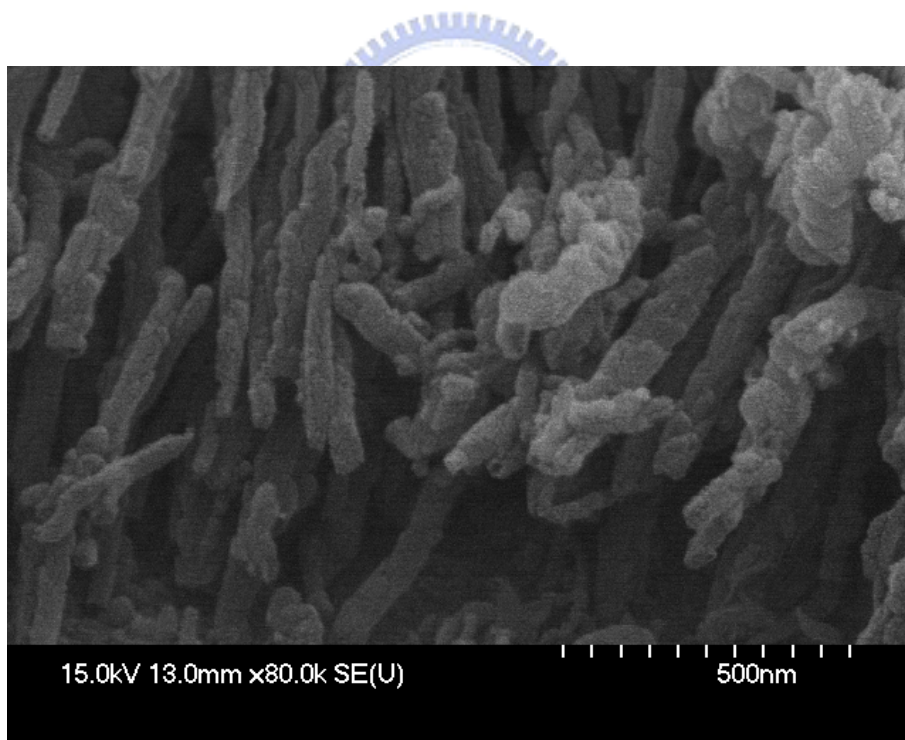


Figure 2.12 The emission current density versus electric field for the samples without Ti capping layer (the conventional samples) and the samples with 5-nm-thick Ti capping layer (the proposed samples). An abrupt decrease in emission current density was observed in the conventional samples and no obvious decrease in emission current density was observed in the proposed samples. After the breakdown in the conventional samples, almost no emission current density was measured in the second measurements.

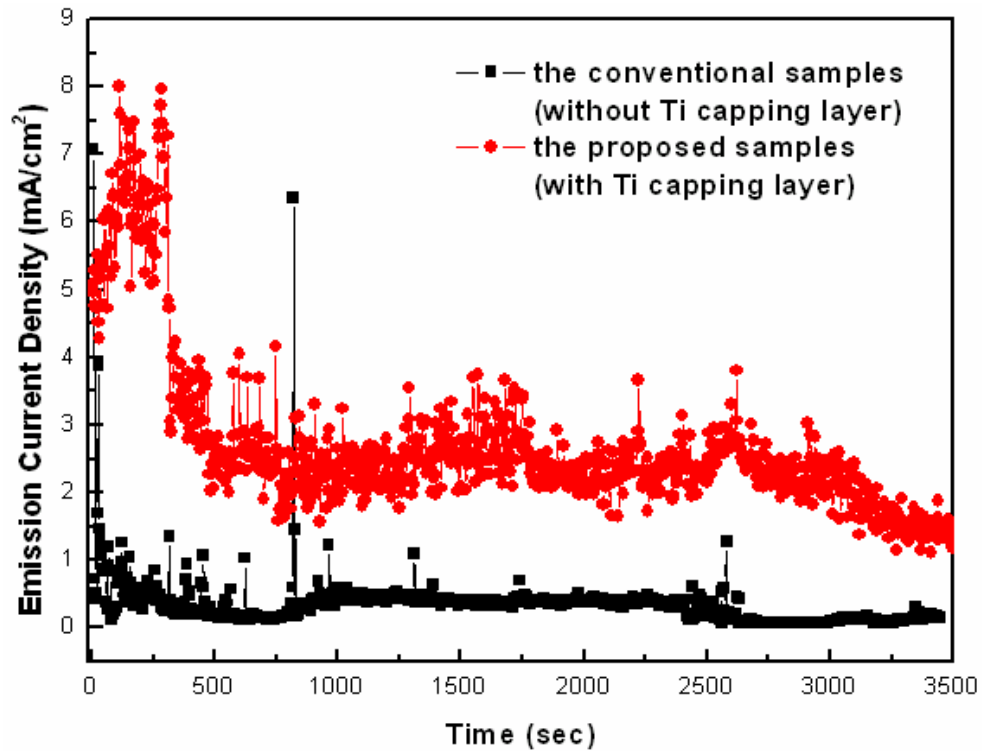


(a)

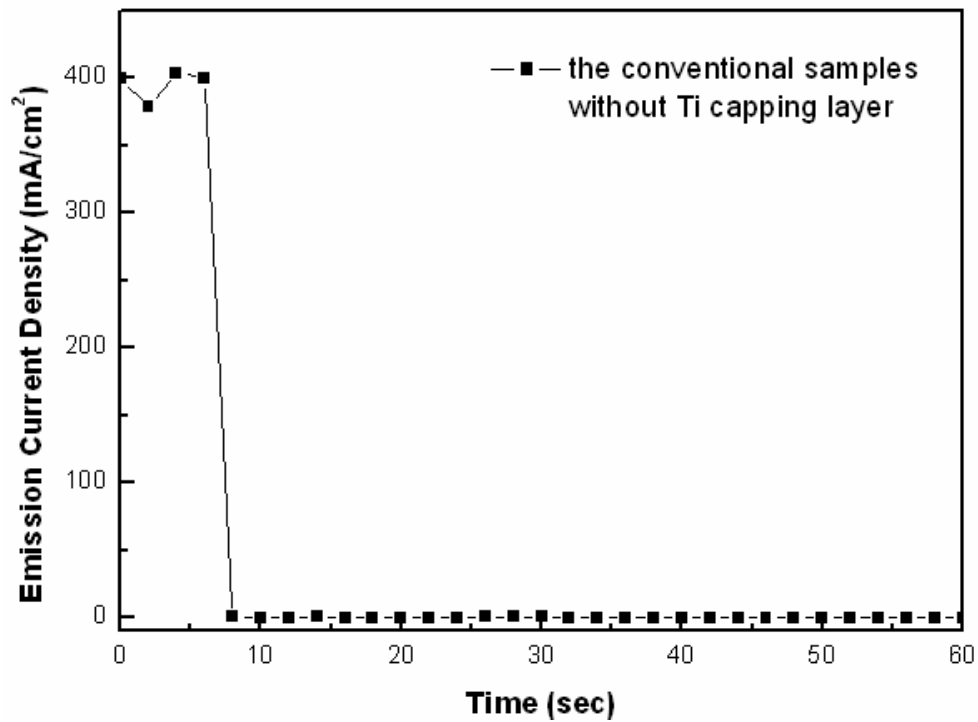


(b)

Figure 2.13 The micrographs taken by the SEM for (a) the morphologies of the CNTs in the conventional samples after the electric breakdown and (b) the image with higher resolution



(a)



(b)

Figure 2.14 (a) the emission current density of both the conventional and the proposed samples over one hour (the emission current density of the conventional samples in the first 6 sec was removed) and (b) the emission current density of the conventional samples for the first 6 sec

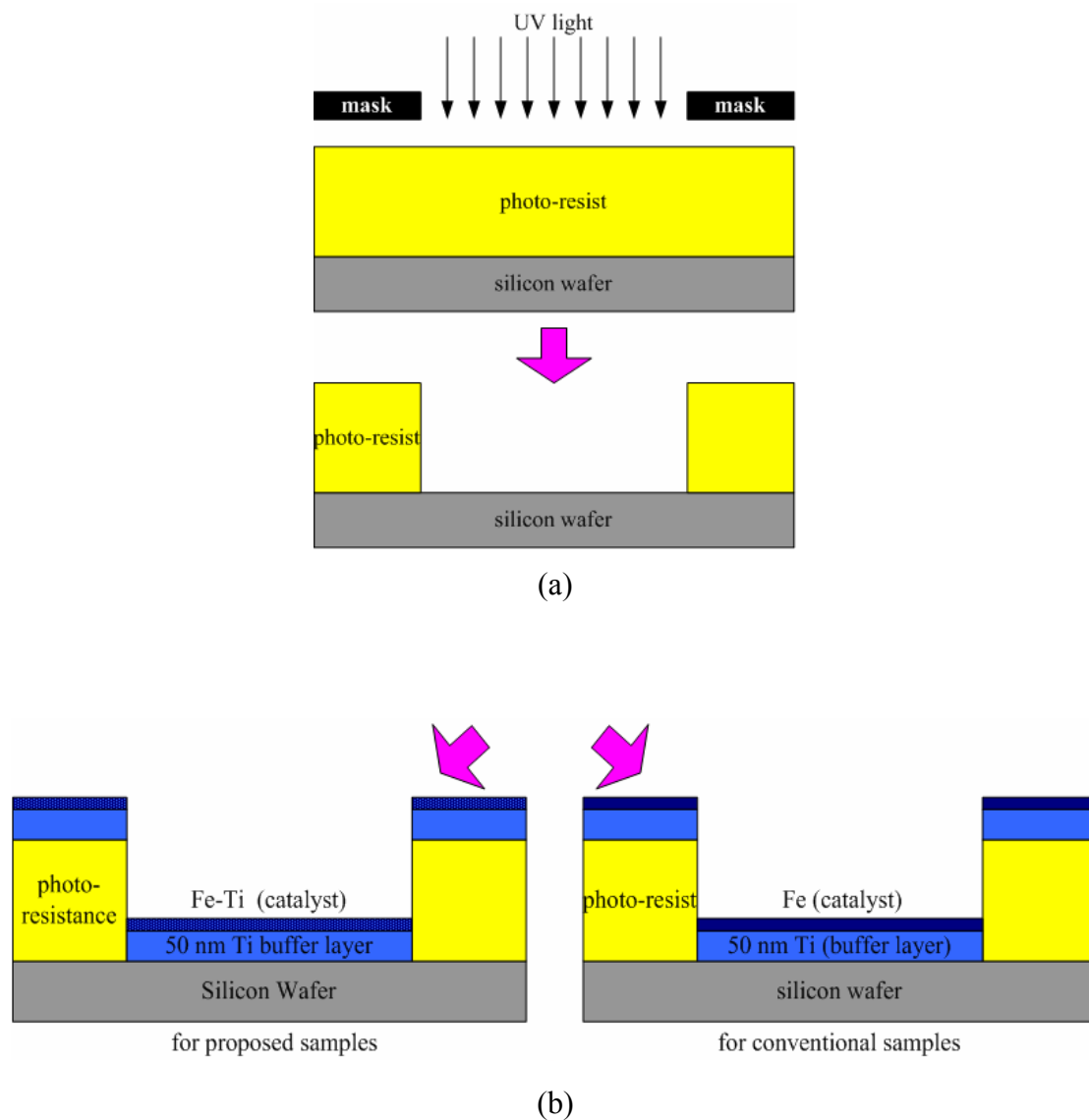
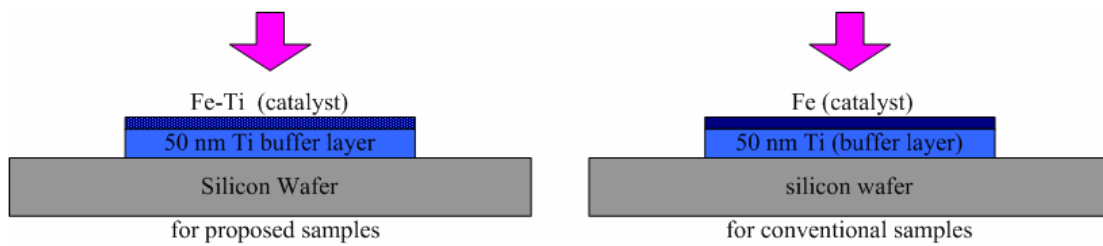
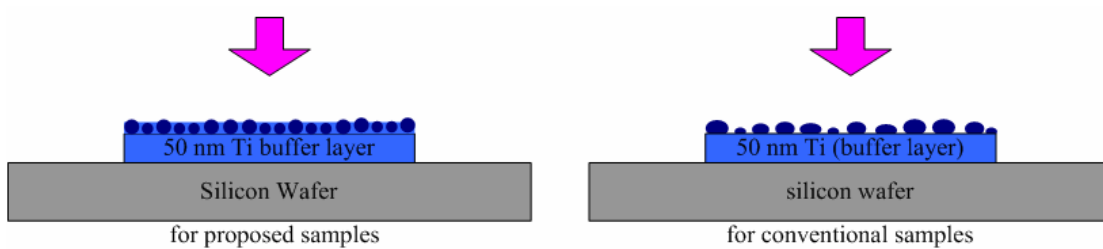


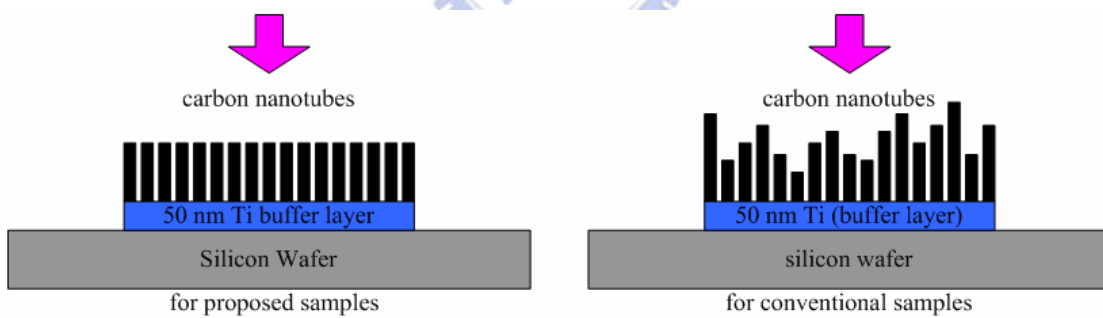
Figure 3.1 The flowchart of experiment: (a) an array of 5×5 square holes with 100 μm in length and 100 μm interspacing were patterned by the lithography system on a photoresist film, (b) a 50-nm-thick Ti layer was deposited by the dual-electron-gun physical vapor deposition system and a catalytic metal layer (Fe-Ti codeposited layer for proposed samples and pure Fe for conventional samples) was subsequently deposited in the same chamber, (c) the photoresist was removed by a lift-off process in acetone solution to leave the Ti buffer layer with the catalyst in the squared holes only, (d) loaded into the chamber of thermal-CVD to be pretreated in hydrogen ambient ($H_2/N_2 = 400/600$ s.c.c.m.) at 700 °C for 5 min, and (e) grew the CNTs in the same chamber with ethylene ($C_2H_4/H_2/N_2 = 5/100/10$ s.c.c.m.) at 700 °C for 15 min



(c)

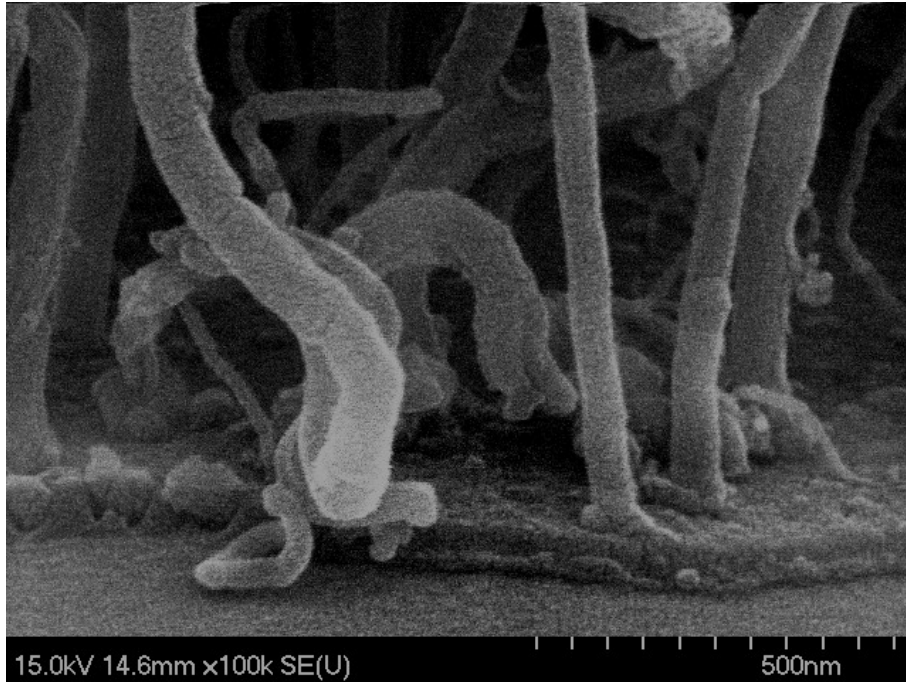


(d)

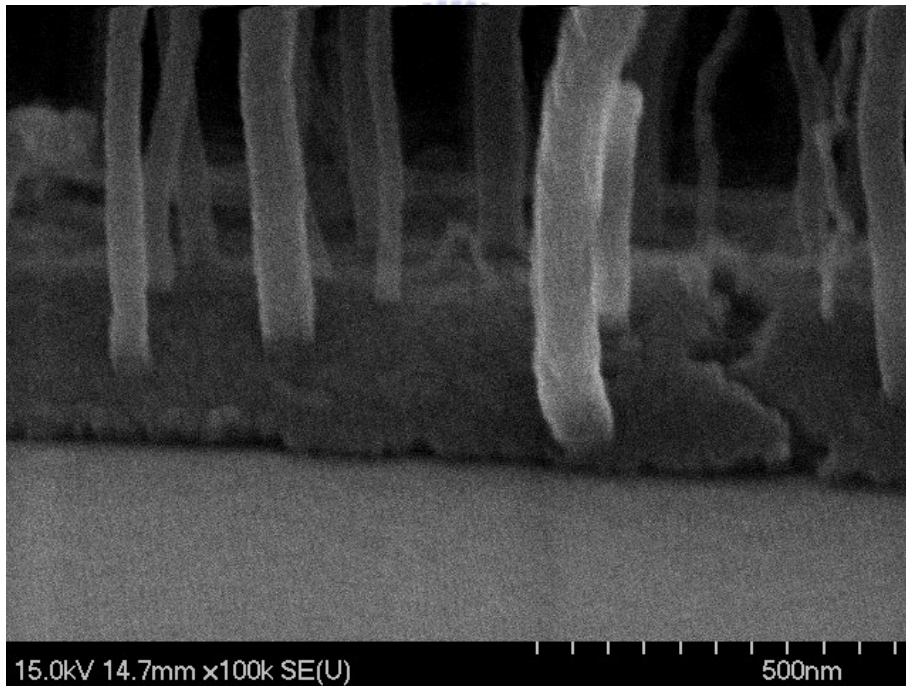


(e)

Figure 3.1 (cont.)

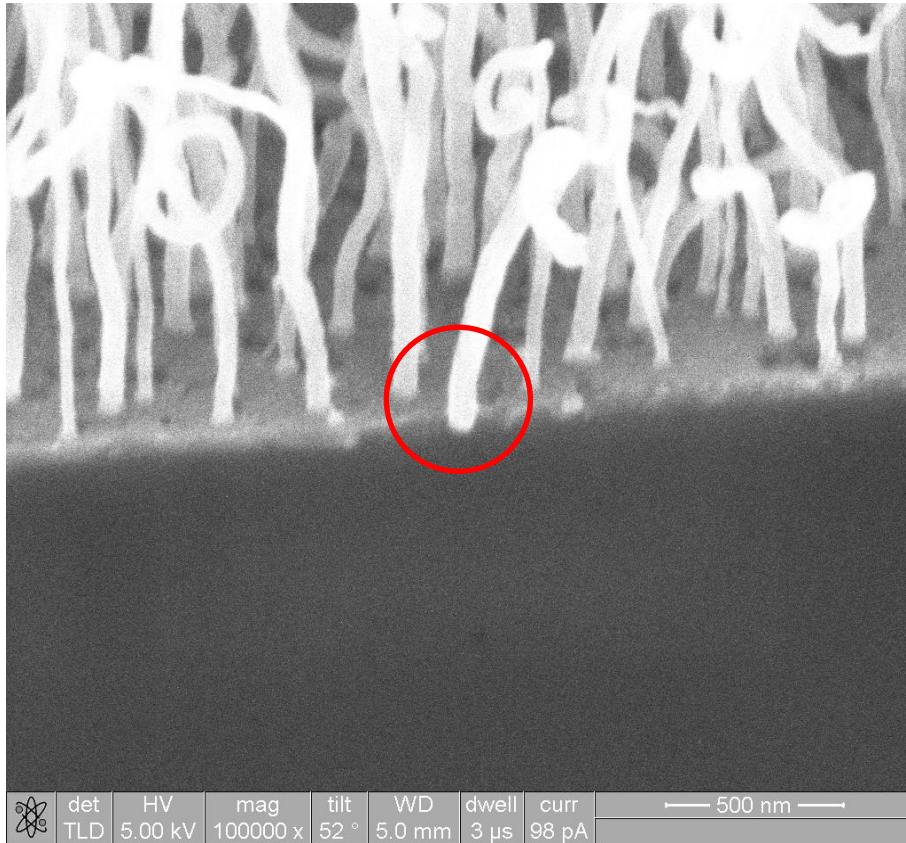


(a)



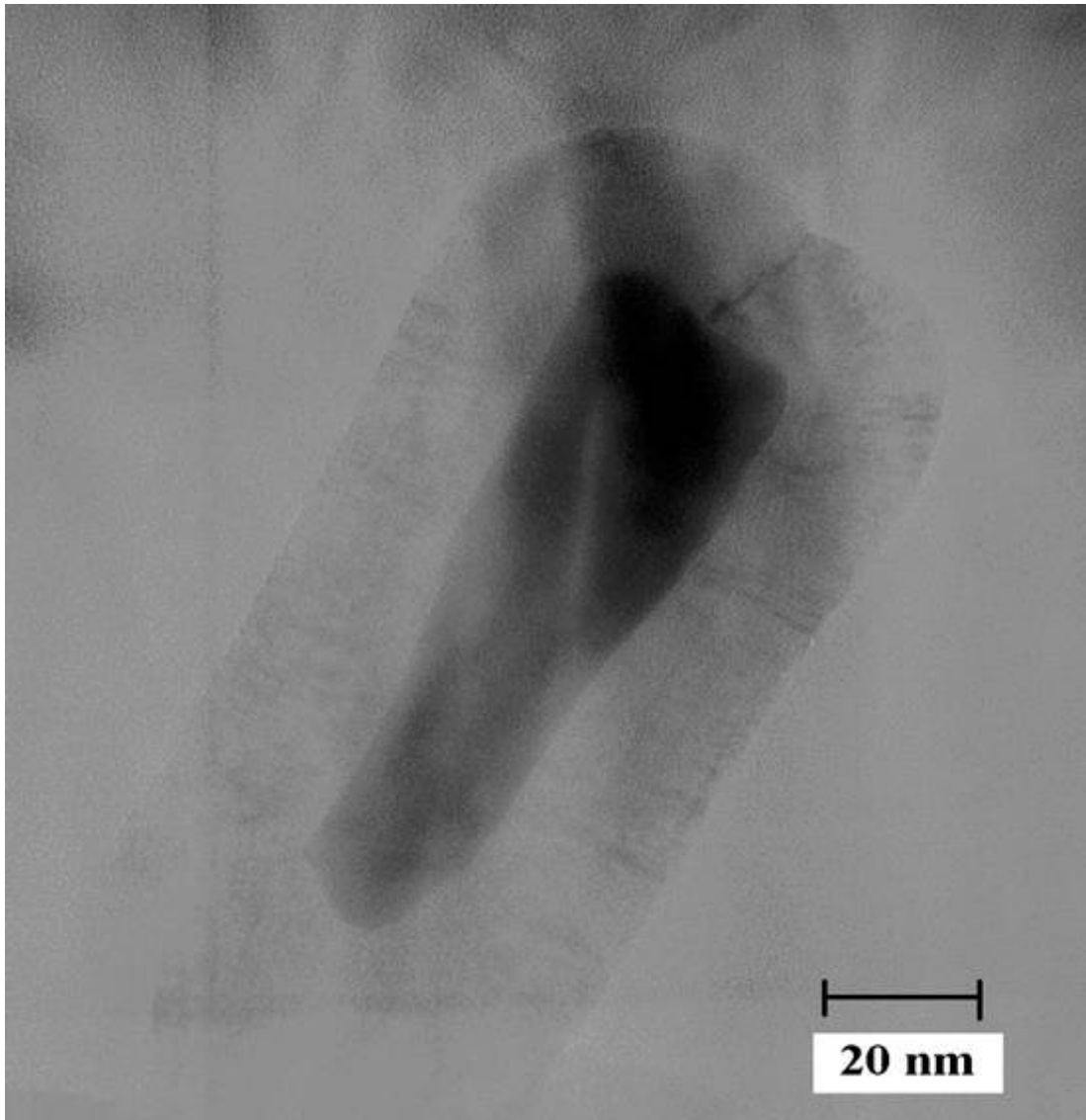
(b)

Figure 3.2 The images of SEM displayed the roots of the CNTs for both (a) the conventional specimens and (b) the proposed specimens with high resolution. The proposed specimens were cleaved across the patterned area and a CNT partially immersed into the codeposited metal layer on the cleaved edge was marked by a circle in (c).



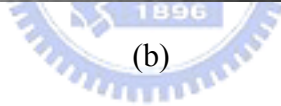
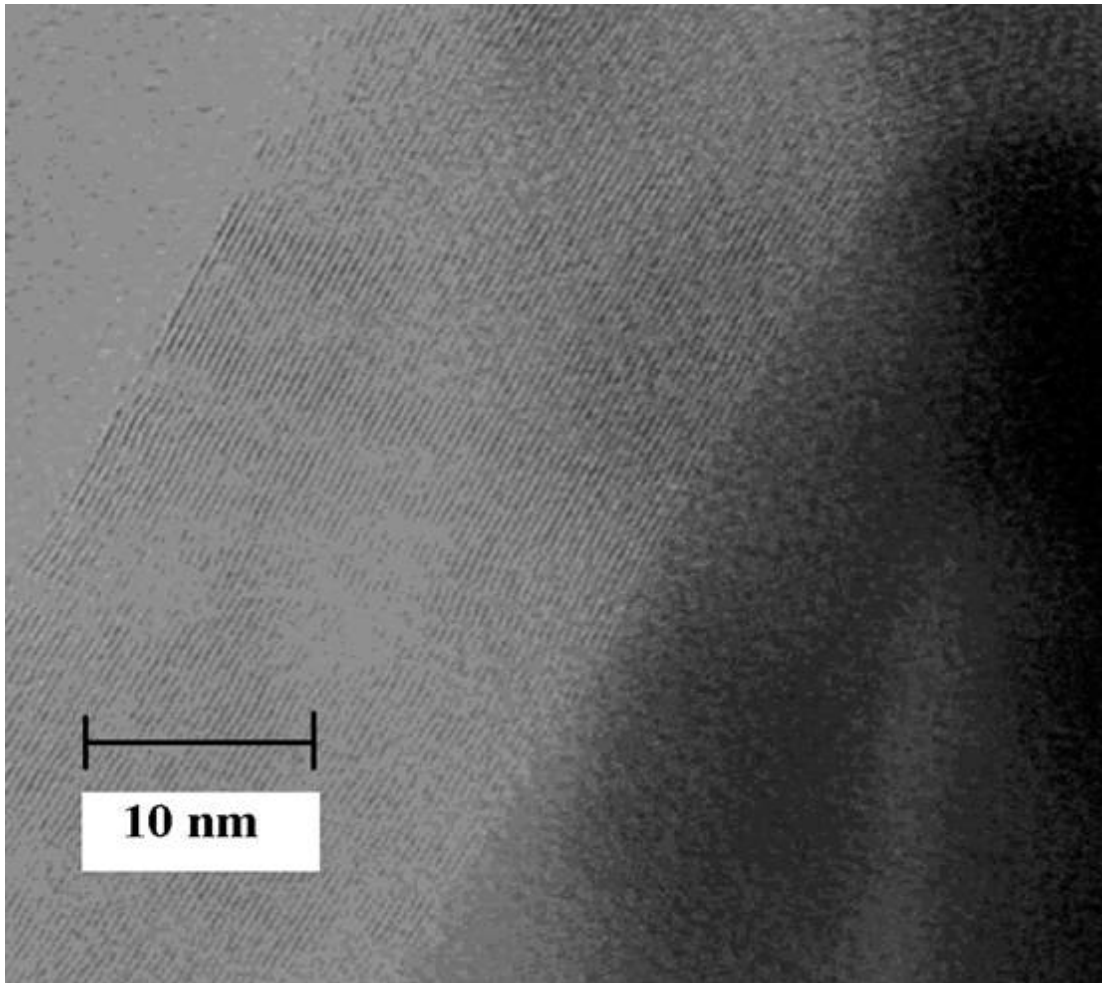
(c)

Figure 3.2 (cont.)



(a)

Figure 3.3 The micrographs of the CNTs synthesized from the Fe-Ti codeposited catalyst taken by the TEM: (a) a CNT with an enclosed nanoparticle and (b) the multiwalled structure of the CNTs with higher resolution



(b)

Figure 3.3 (cont.)

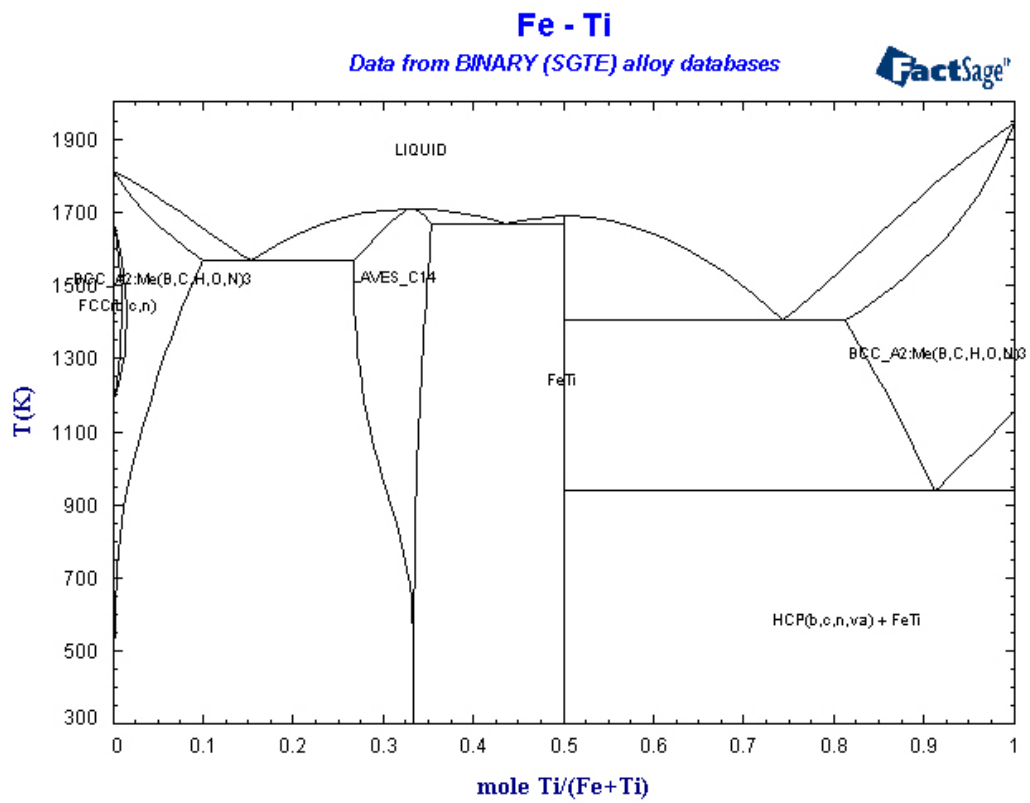


Figure 3.4 The phase diagram of Fe-Ti

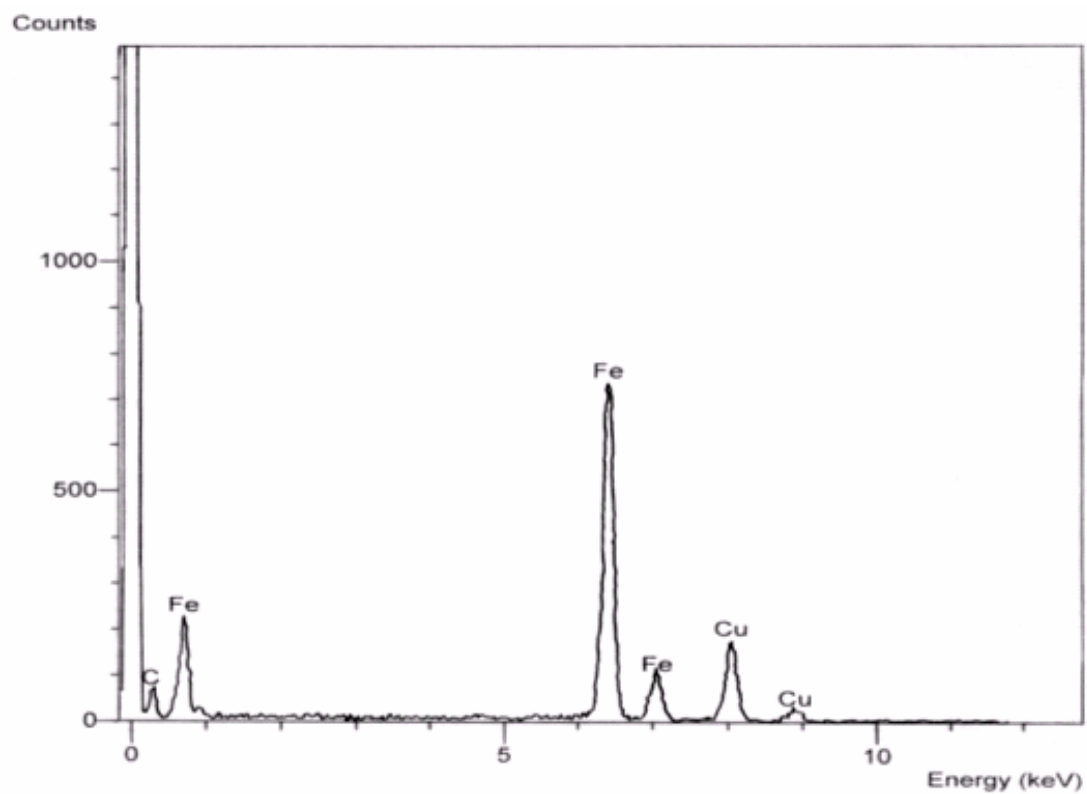


Figure 3.5 The results of energy dispersive spectrum for the enclosed nanoparticle in Fig. 3.3(a) where only signals of Fe, C, and Cu were detected

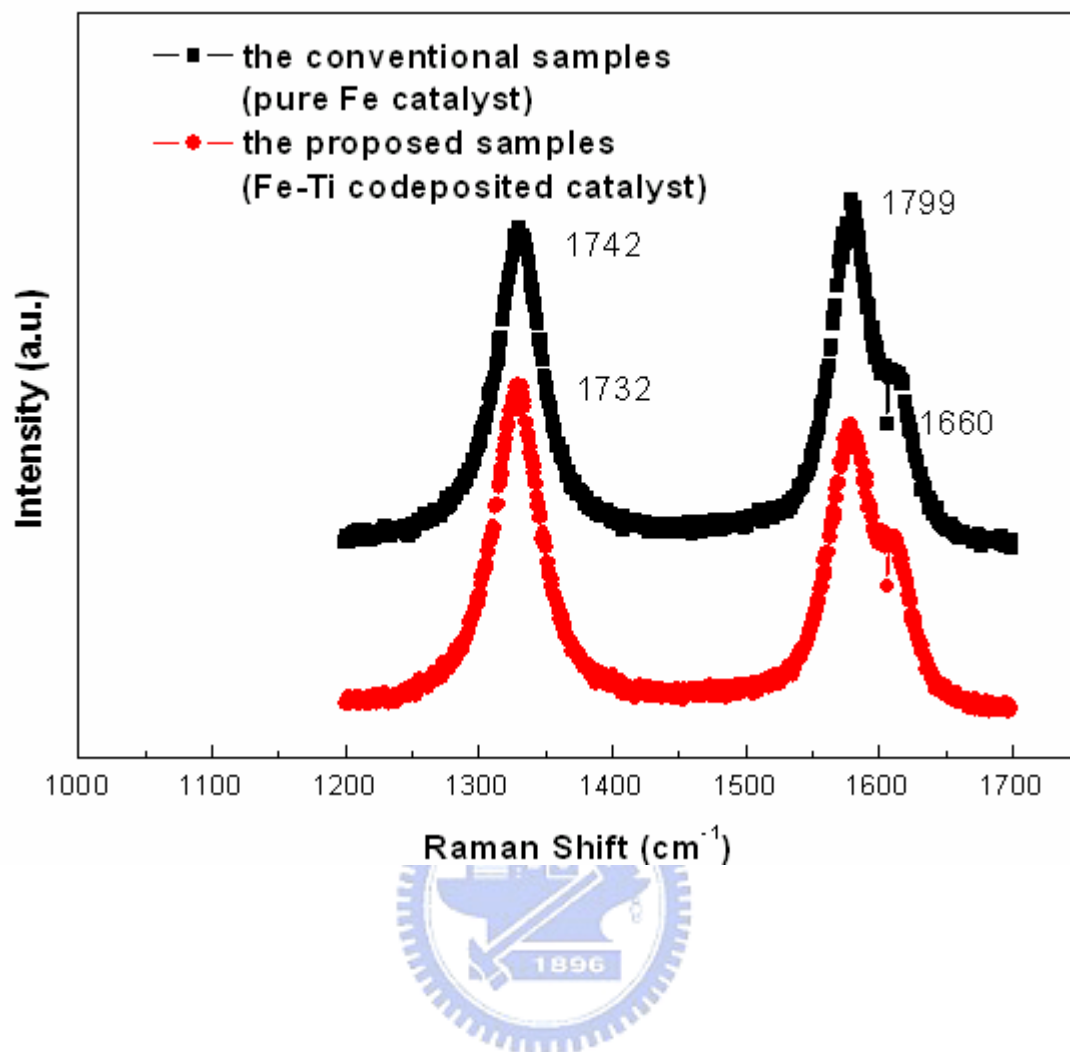
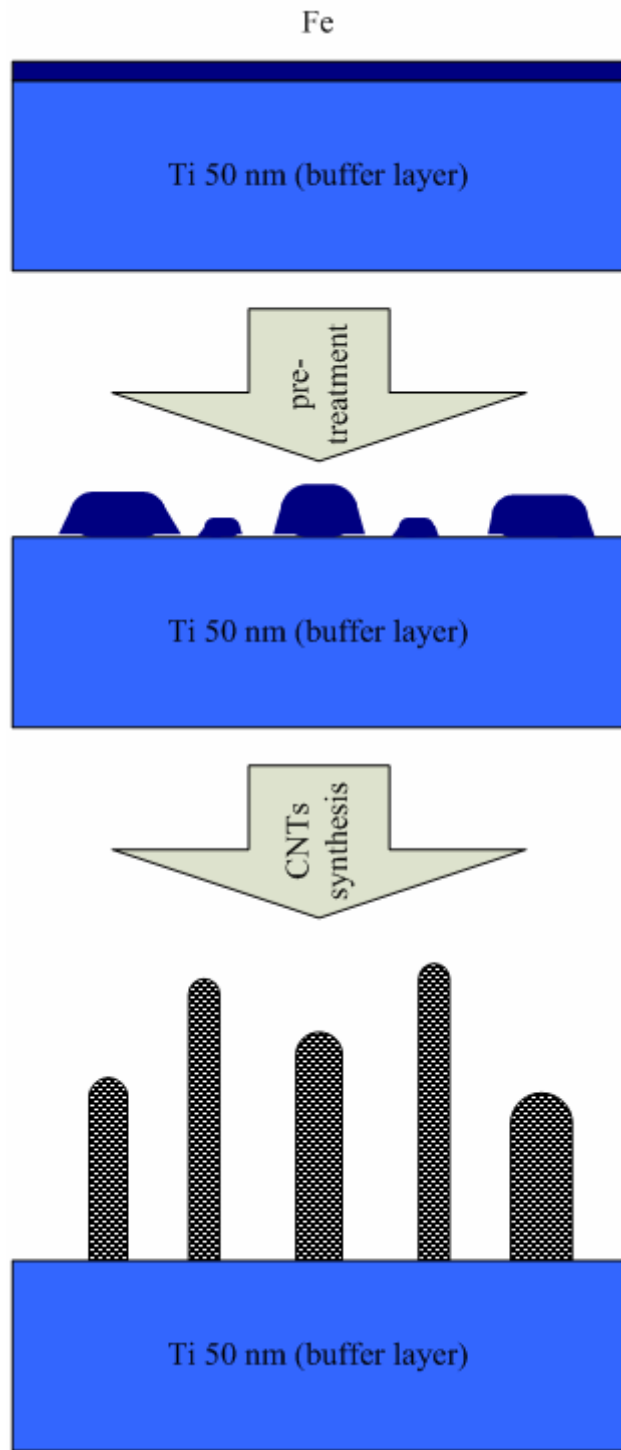
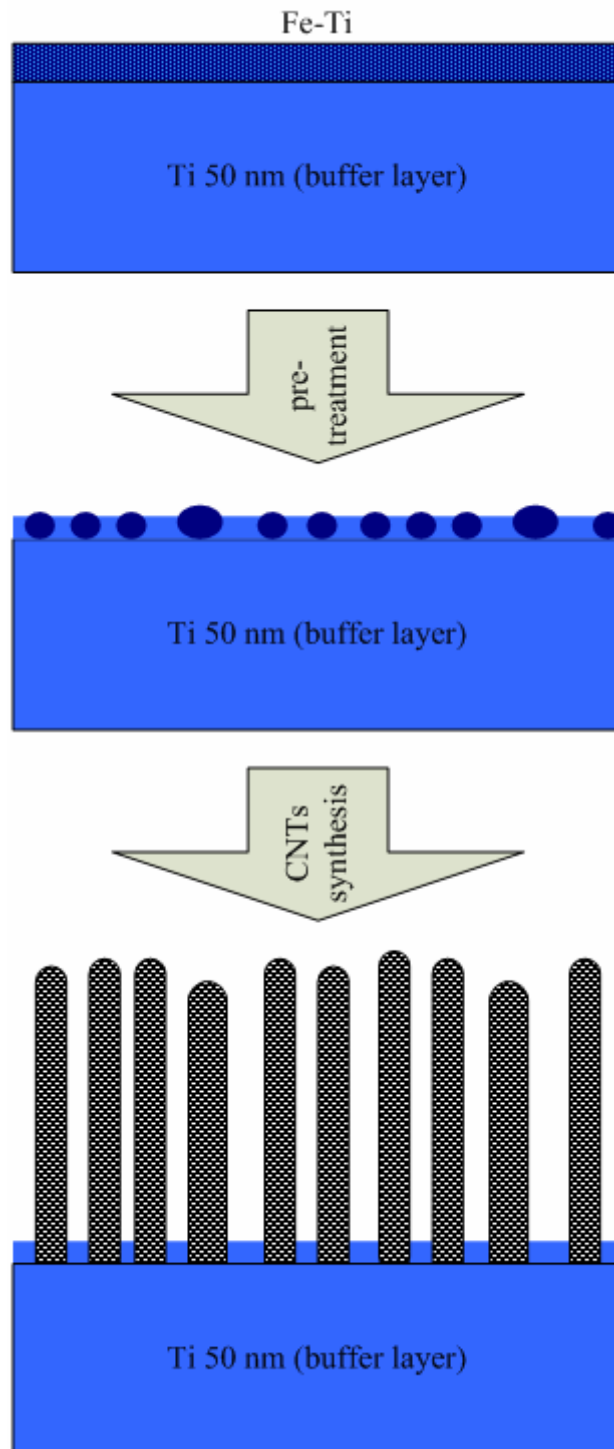


Figure 3.6 The Raman spectrum of the CNTs in the conventional samples and the proposed samples



(a)

Figure 3.7 The schemes of mechanisms illustrated the formation of nanoparticles during hydrogen pretreatment and the growth of CNTs for both (a) the conventional specimens and (b) the proposed specimens.



(b)

Figure 3.7 (cont.)

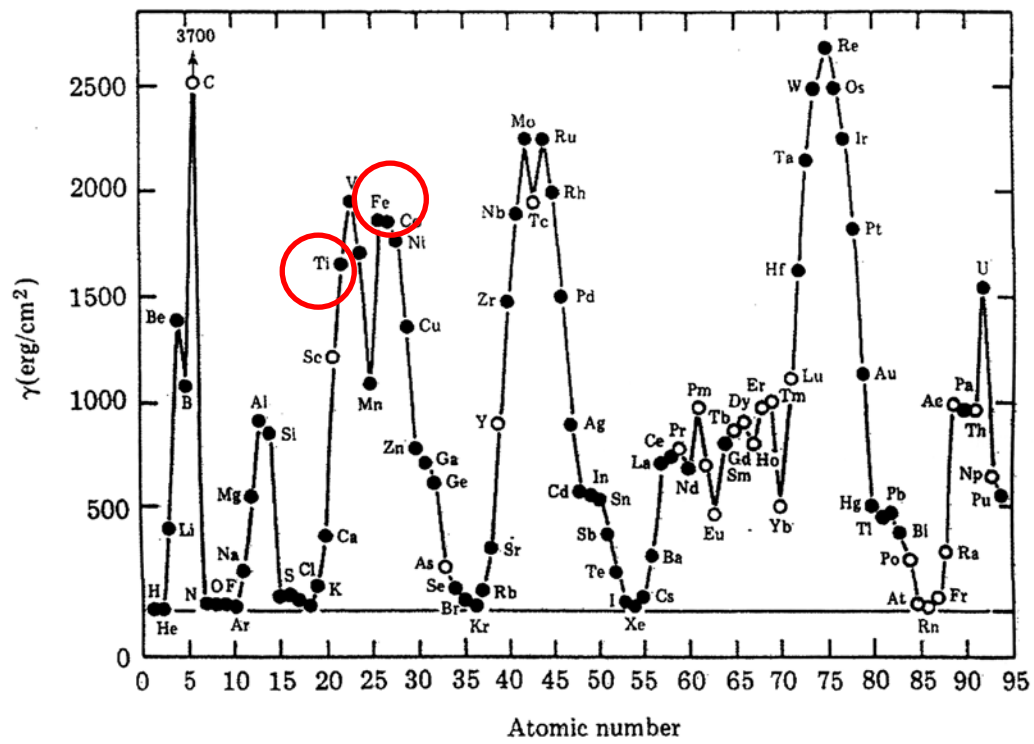
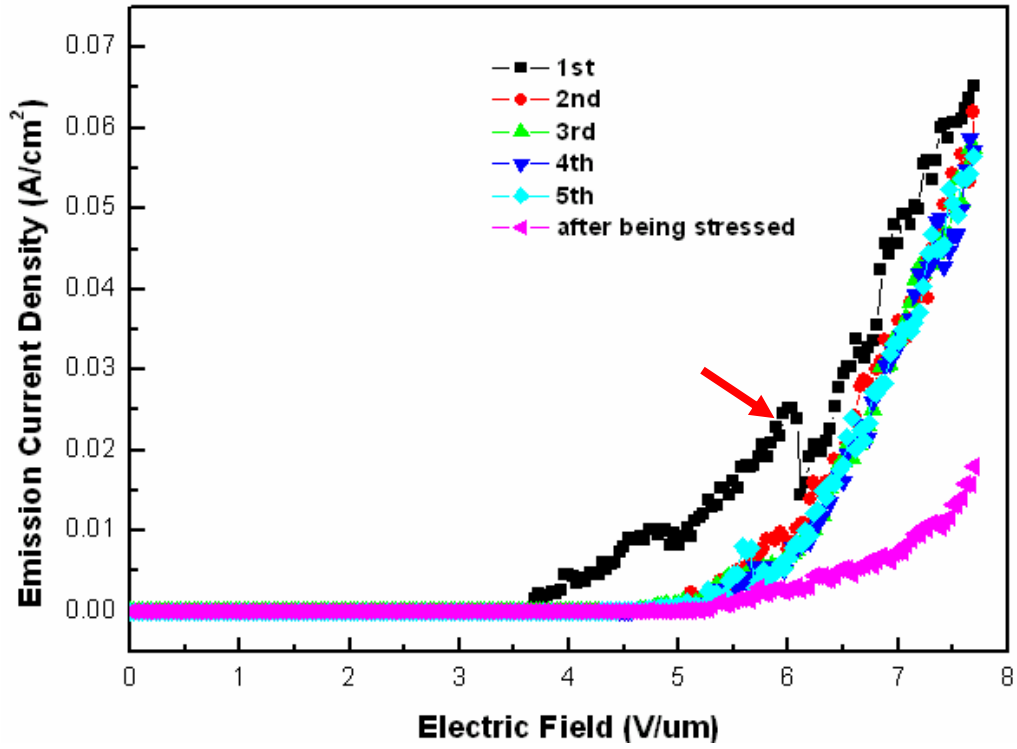
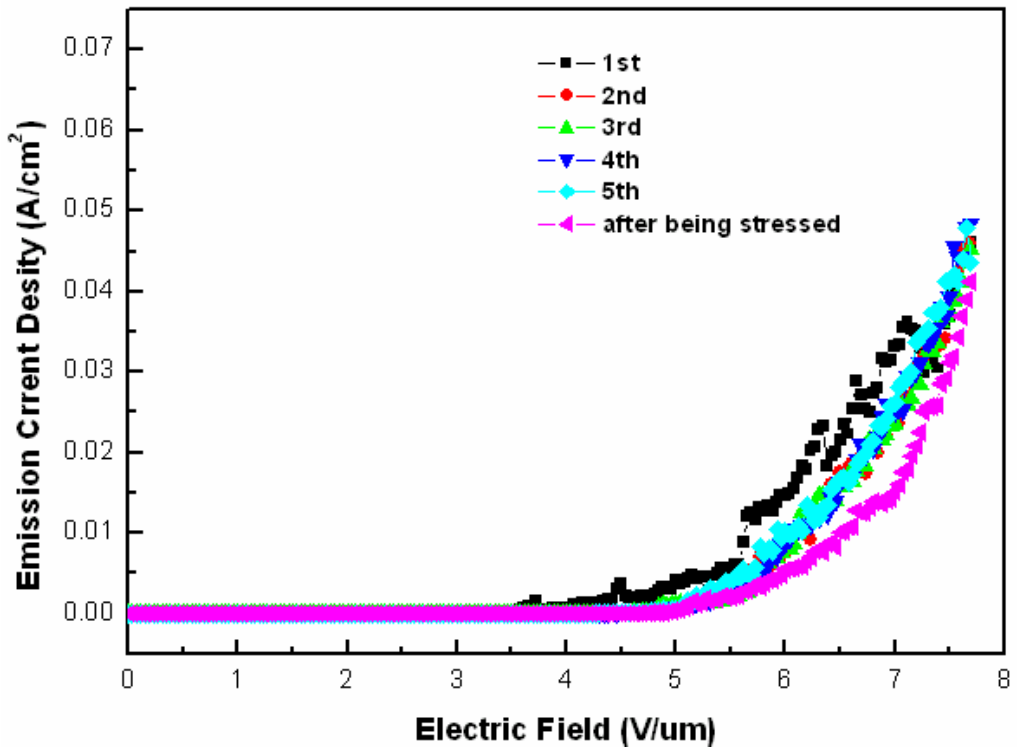


Figure 3.8 The surface energies of elements

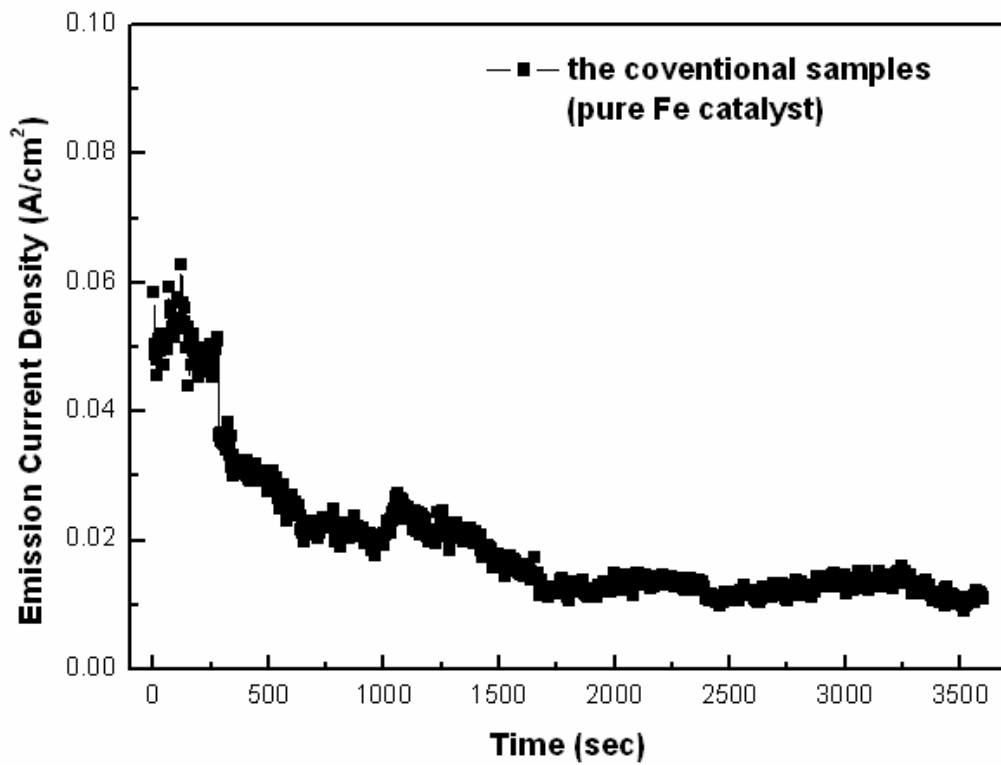


(a)

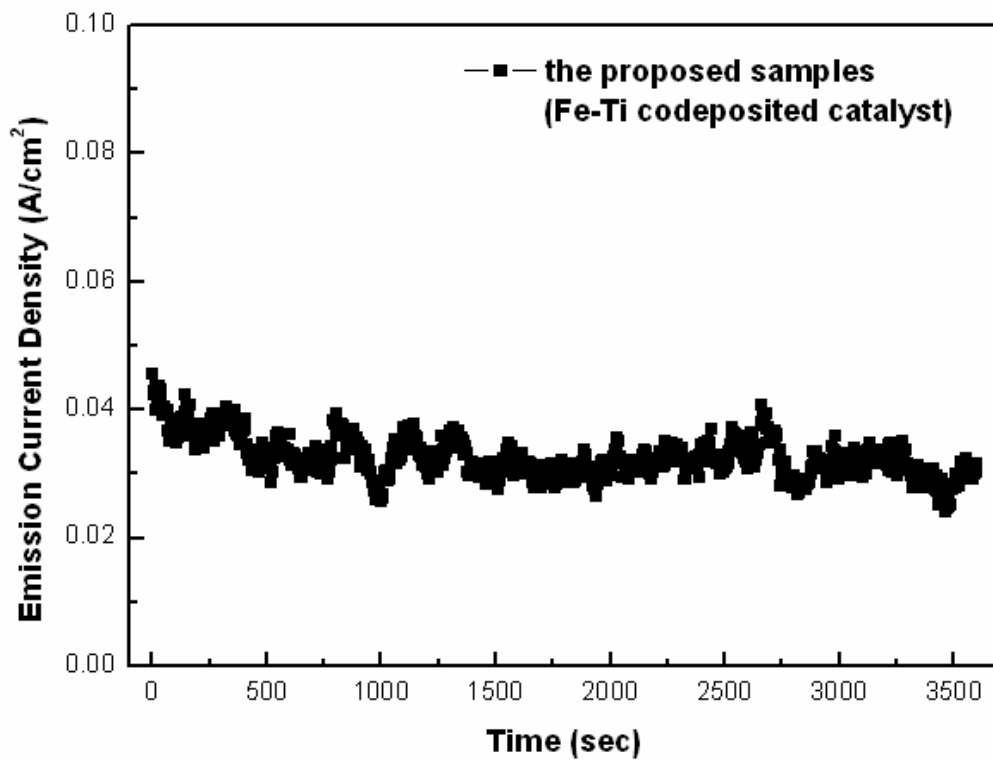


(b)

Figure 3.9 The curves of emission current density versus electric field from 0 to 7 $V/\mu m$ for (a) the conventional samples and (b) the proposed samples before and after being stressed



(a)



(b)

Figure 3.10 The emission current density versus operating time of (a) the conventional samples and (b) the proposed samples for 2,500 sec

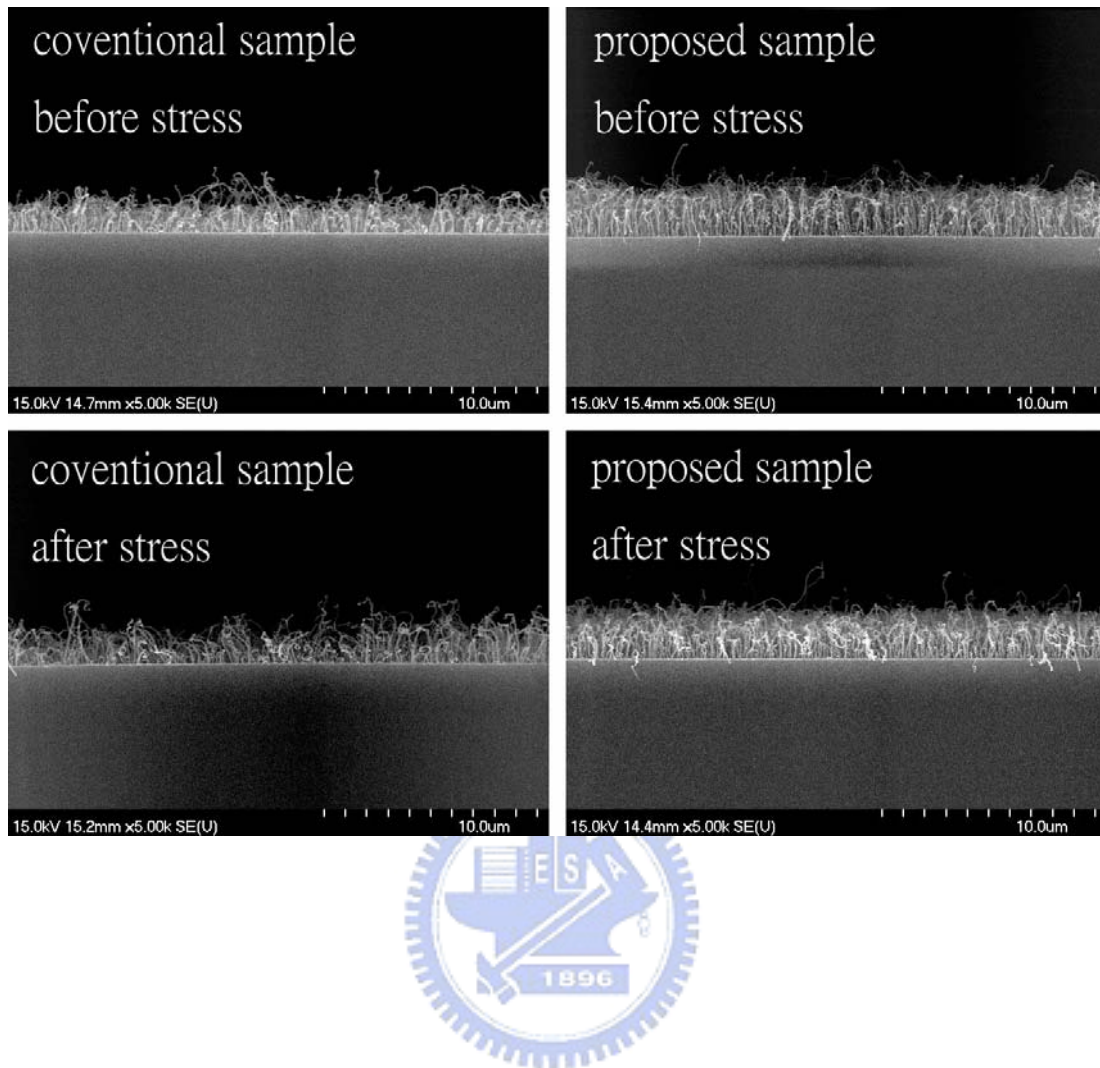
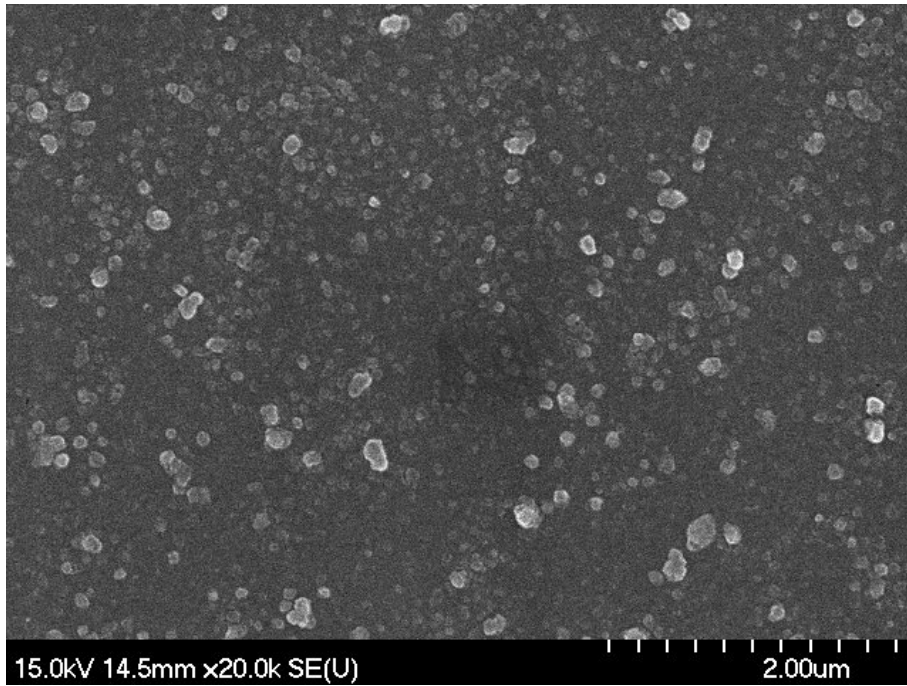
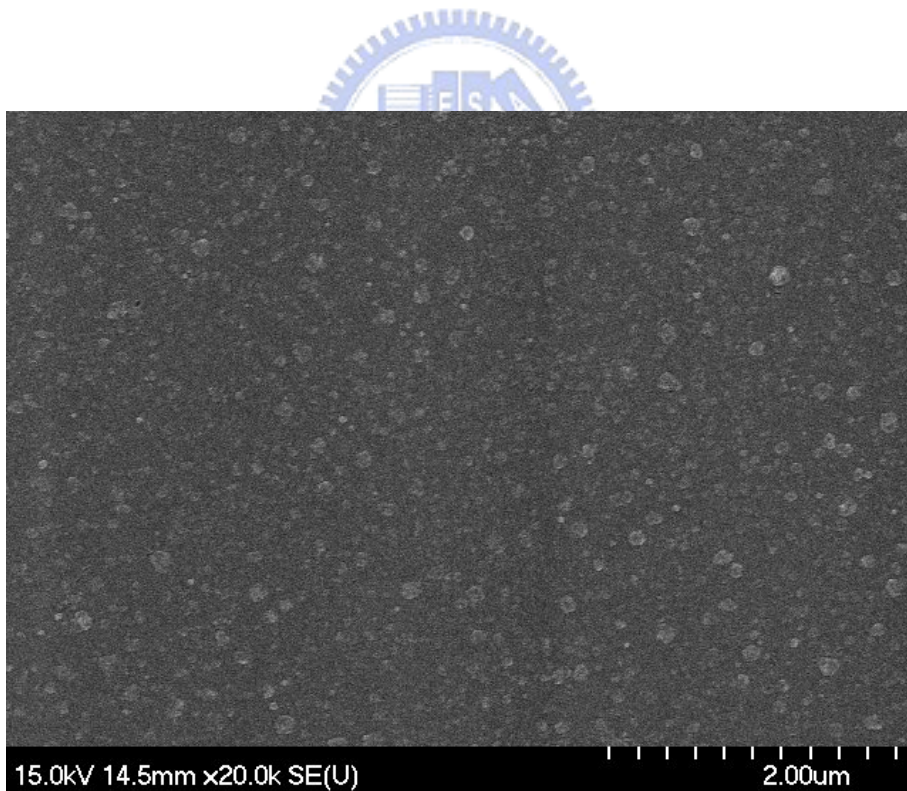


Figure 3.11 The micrographs taken by SEM displayed the morphologies of both the conventional and the proposed samples before and after being stressed

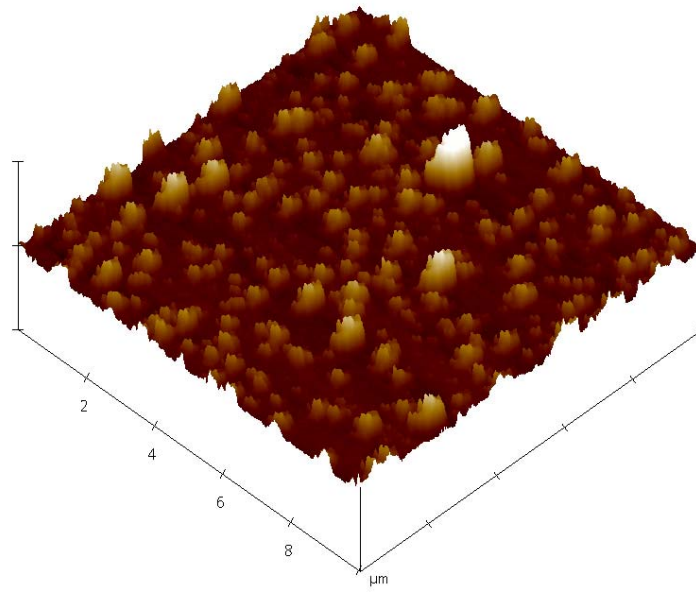


(a)

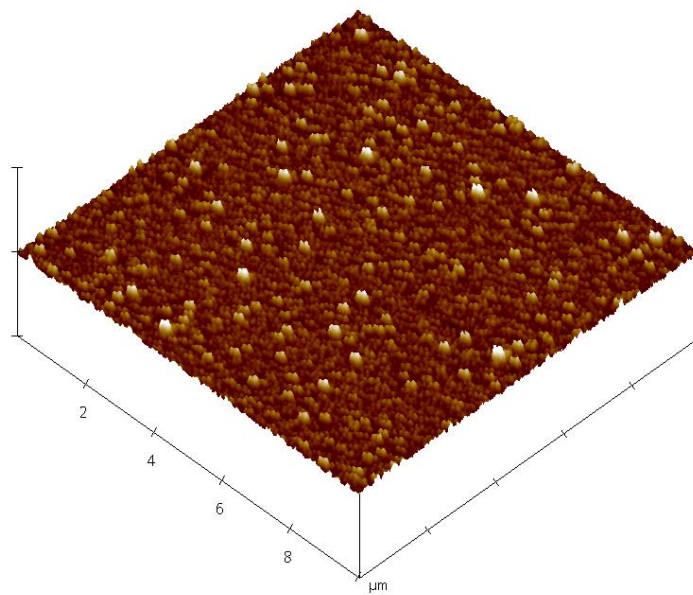


(b)

Figure 3.12 The micrographs of the catalytic nanoparticles taken by the SEM from top-view for (a) the conventional samples and (b) the proposed samples

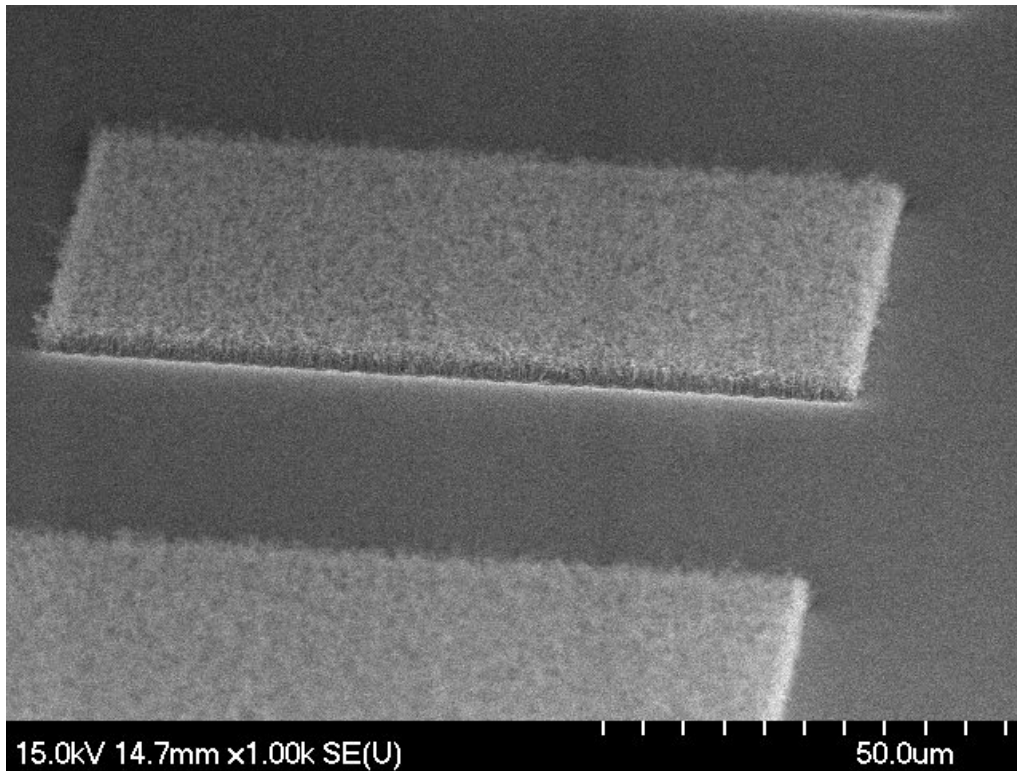


(a)

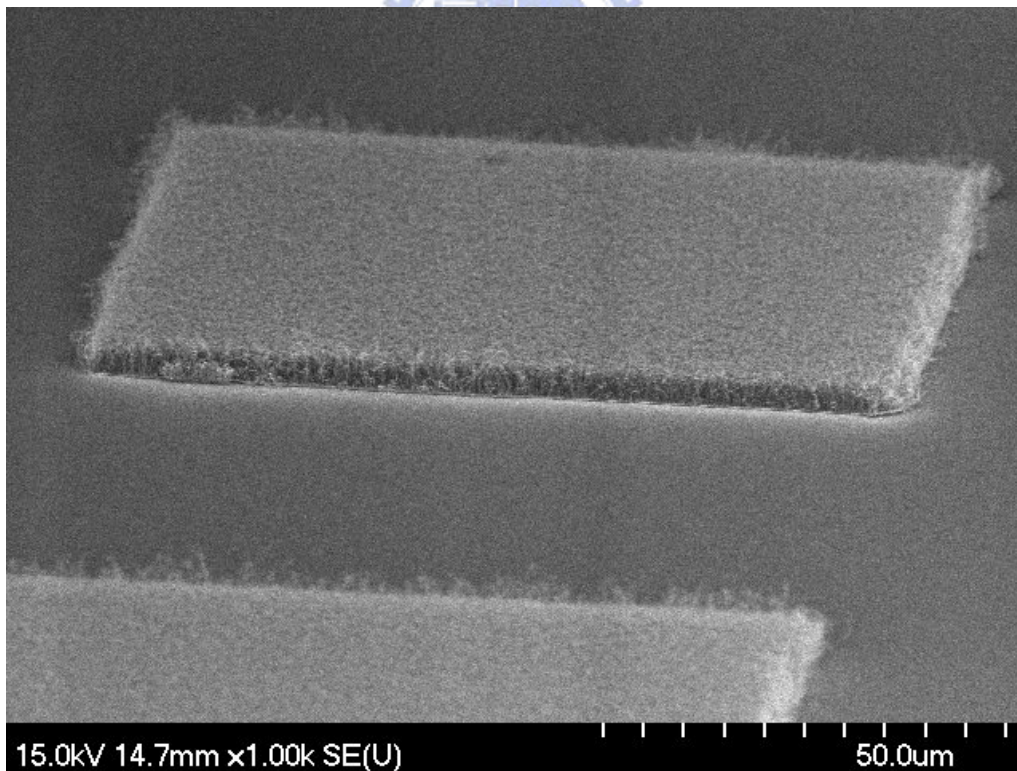


(b)

Figure 3.13 The atomic force microscope images (scanning area of $10\ \mu\text{m} \times 10\ \mu\text{m}$) of the catalytic nanoparticles for (a) the conventional samples and (b) the proposed samples

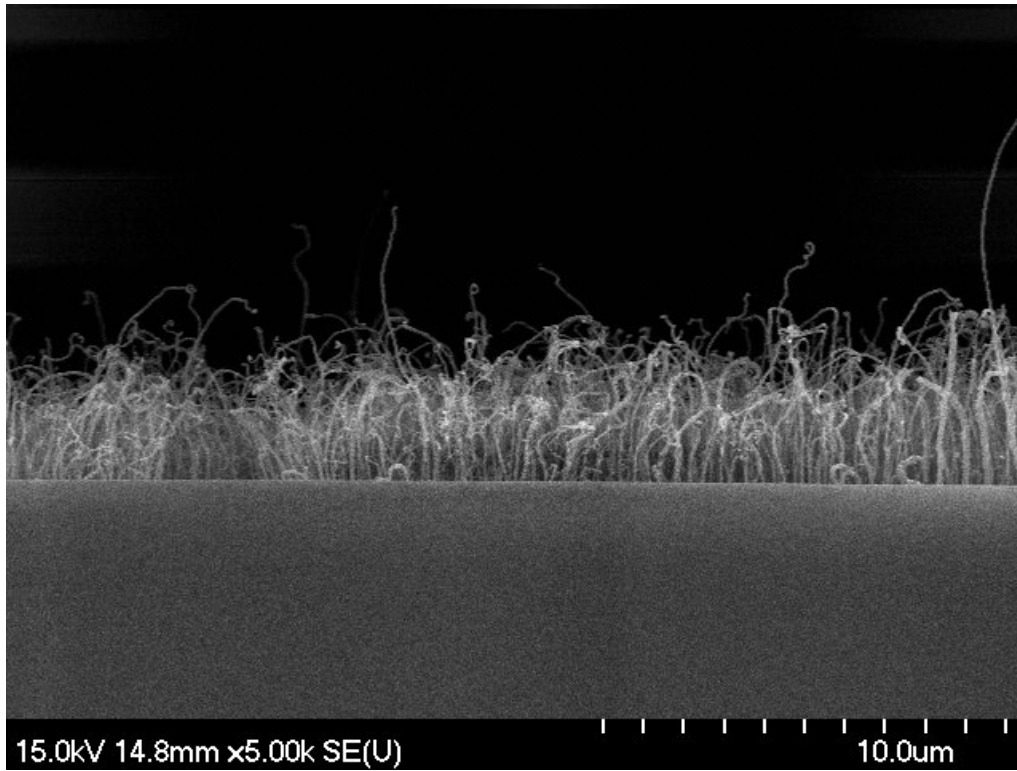


(a)

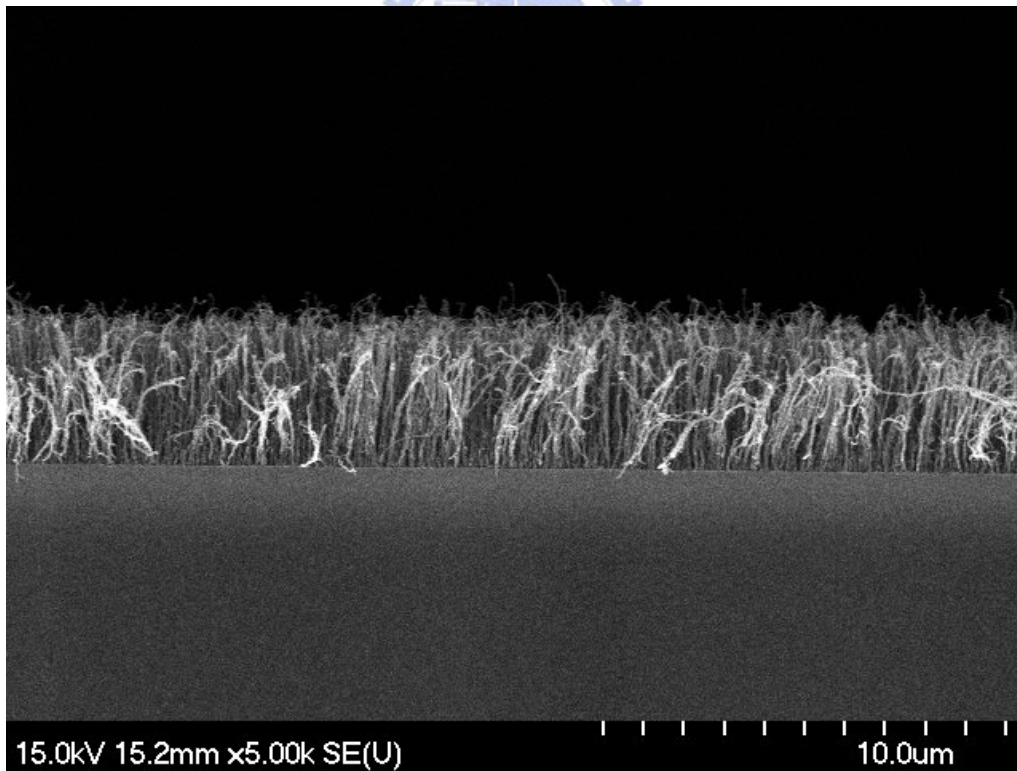


(b)

Figure 3.14 The micrographs of the CNTs taken by the SEM with 45° viewing angle for (a) the conventional samples and (b) the proposed samples

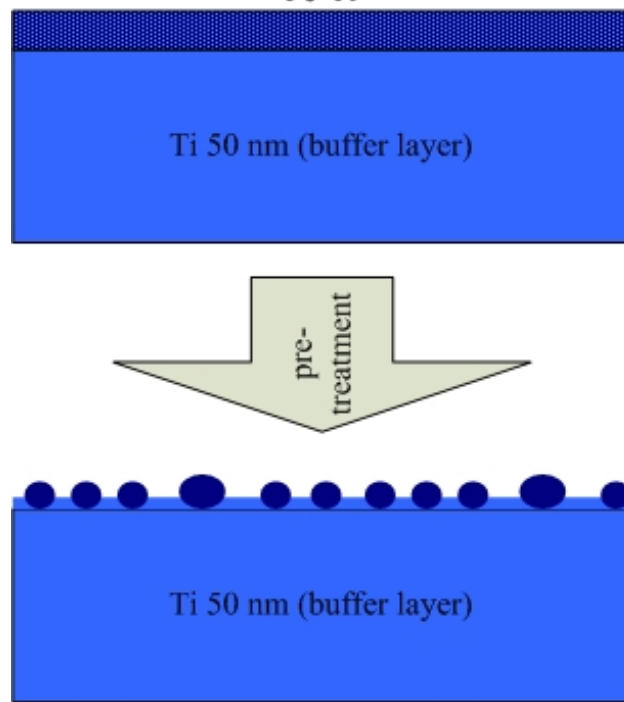
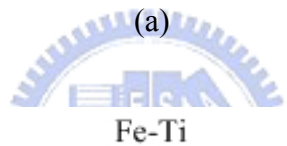
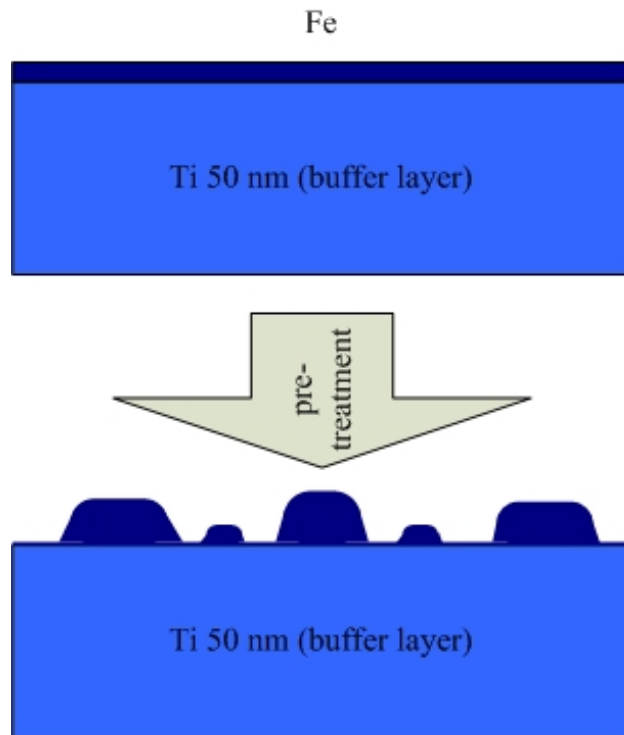


(c)



(d)

Figure 3.14 The cross-sections of the CNTs taken by the SEM: (c) the conventional samples and (d) the proposed samples



(b)

Figure 3.15 The scheme for the formation of the catalytic nanoparticles in (a) the conventional samples and (b) the proposed samples

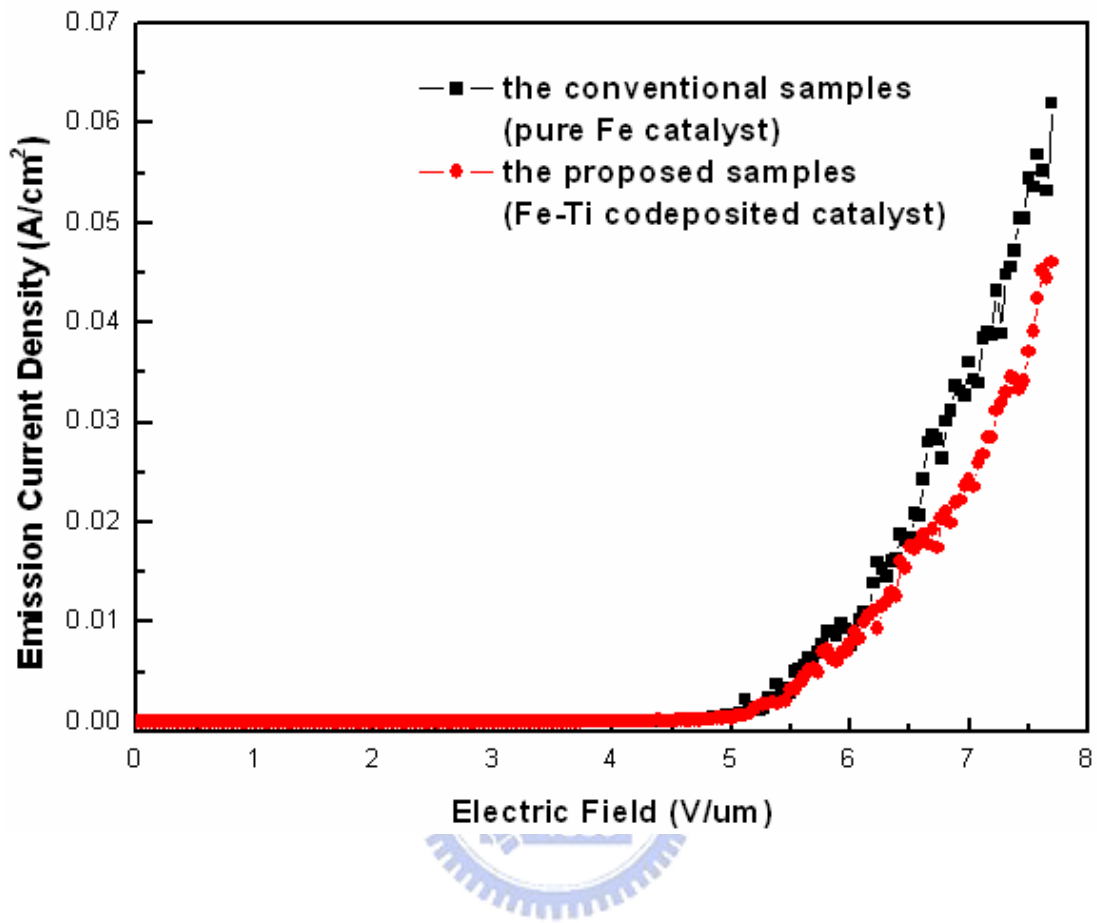
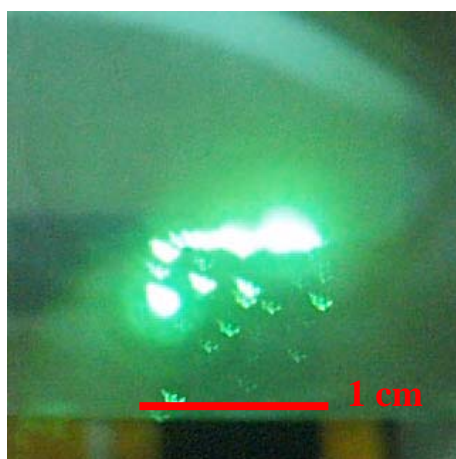


Figure 3.16 The curves of emission current density versus applied electric field for both the conventional and the proposed samples



500 V

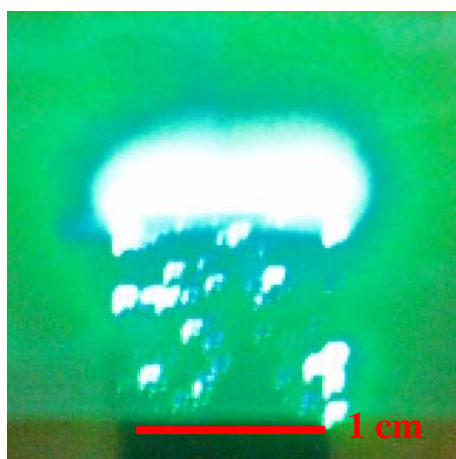


600 V



700 V

Figure 3.17 (a) The luminescent images for the conventional samples operated at 500 V, 600 V, and 700 V of anode voltages



500 V



600 V



700 V

Figure 3.17 (b) The luminescent images for the proposed samples operated at 500 V, 600 V, and 700 V of anode voltages

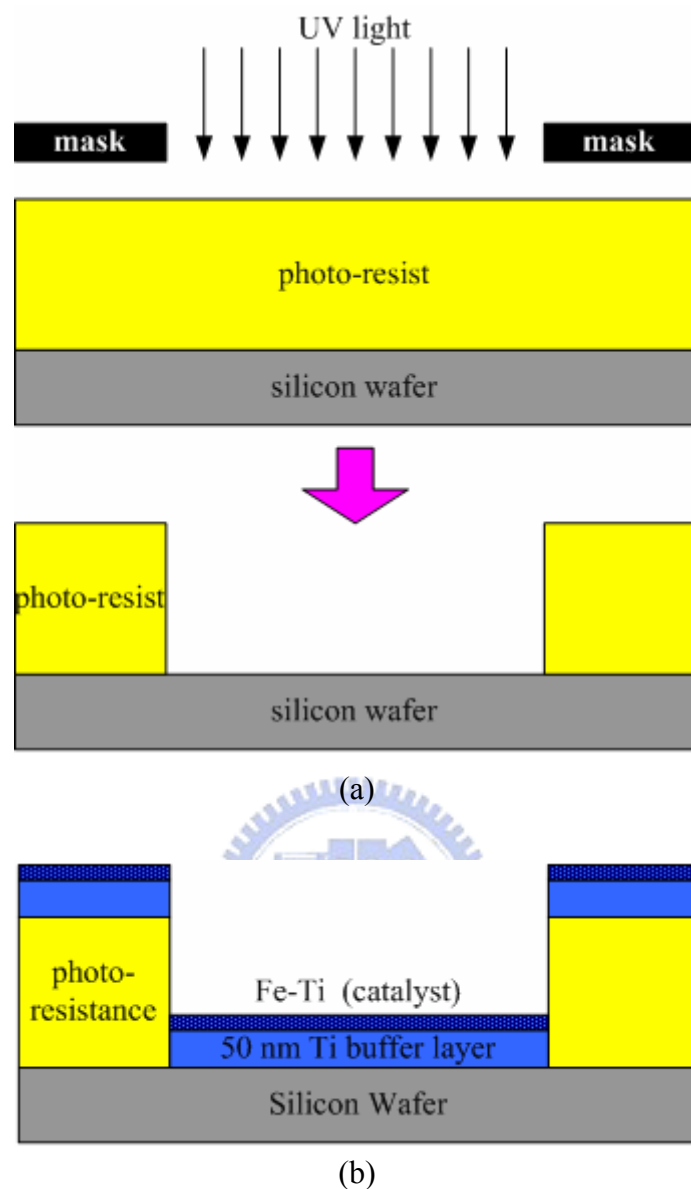
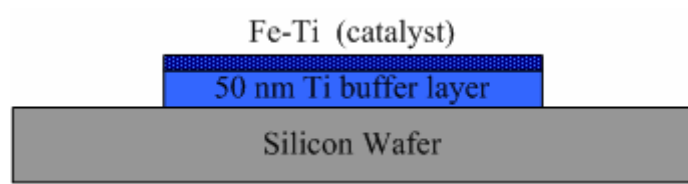
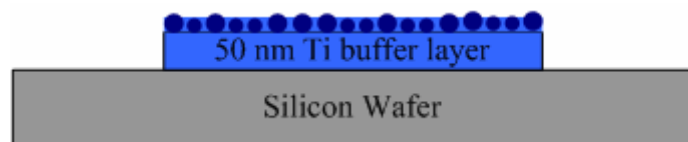


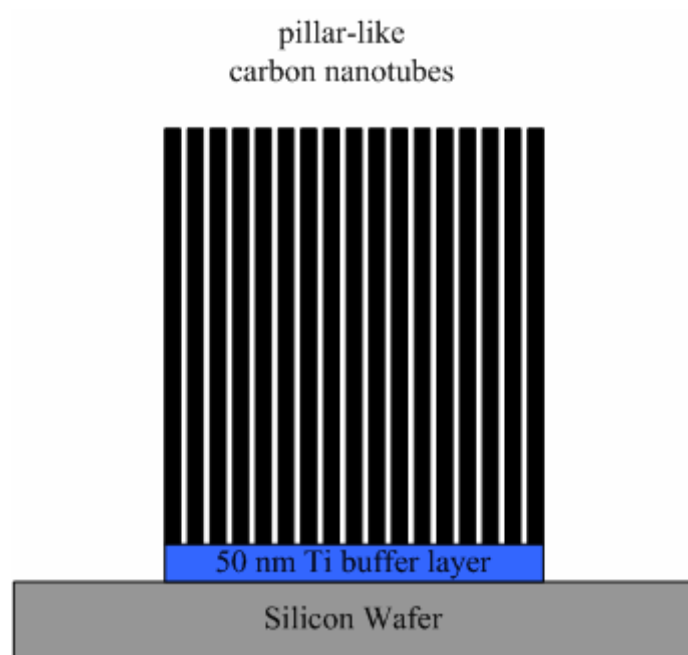
Figure 4.1 The flowchart of experimental processes: (a) spin photoresist on N-type silicon wafers and then form a hole-array of circles with 6 μm in diameter and different inter spacing of 12, 15, 20, 25, 30, and 35 μm in a rectangular of 1 mm in width and 2 mm in length, (b) depositing a 50-nm-thick Ti metal as a buffer layer by dual electron-gun physical vapor deposition system and subsequently codepositing a 10-nm-thick Fe and Ti film as the catalyst of CNTs (Fe 64% w.t.), (c) the photoresist was removed by a lift-off process in an ultrasonic cleaner with acetone solution and only Ti buffer layer and Fe-Ti codeposited catalyst were left in the circle holes, (d) the samples were loaded into a thermal-CVD to be pretreated in hydrogen ambient ($\text{N}_2/\text{H}_2 = 500/100$ s.c.c.m.) at 700 $^\circ\text{C}$ for 8 min, and (e) finally synthesized CNTs with ethylene ($\text{C}_2\text{H}_4/\text{N}_2/\text{H}_2 = 20/500/100$ s.c.c.m.) at 700 $^\circ\text{C}$ for 15 min.



(c)

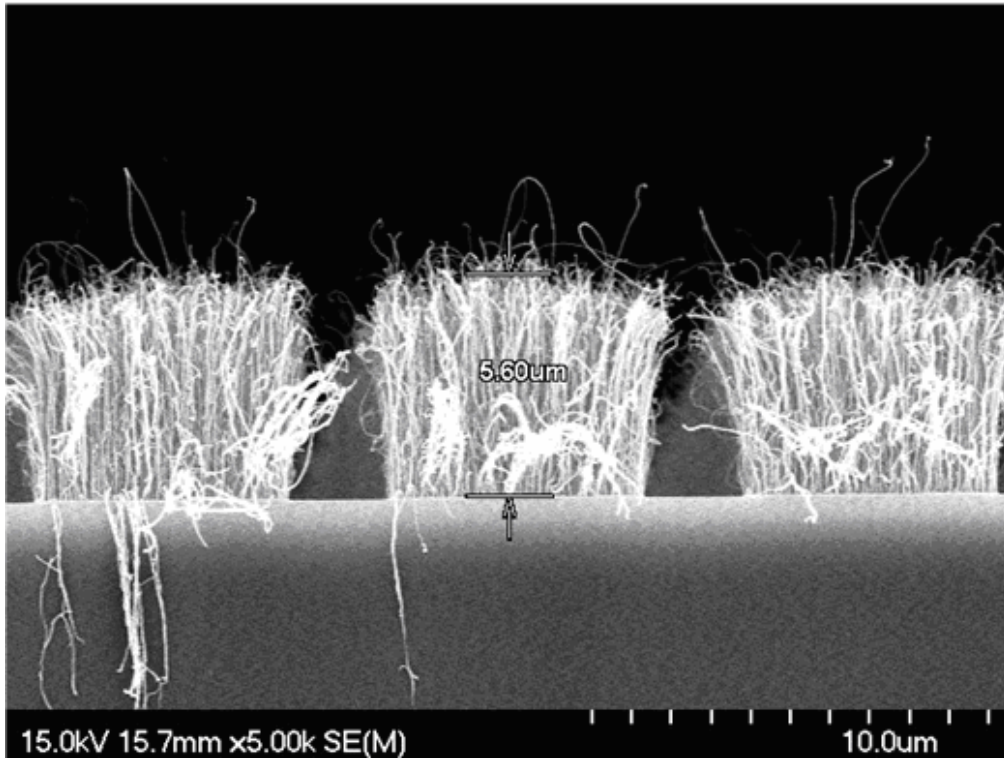


(d)

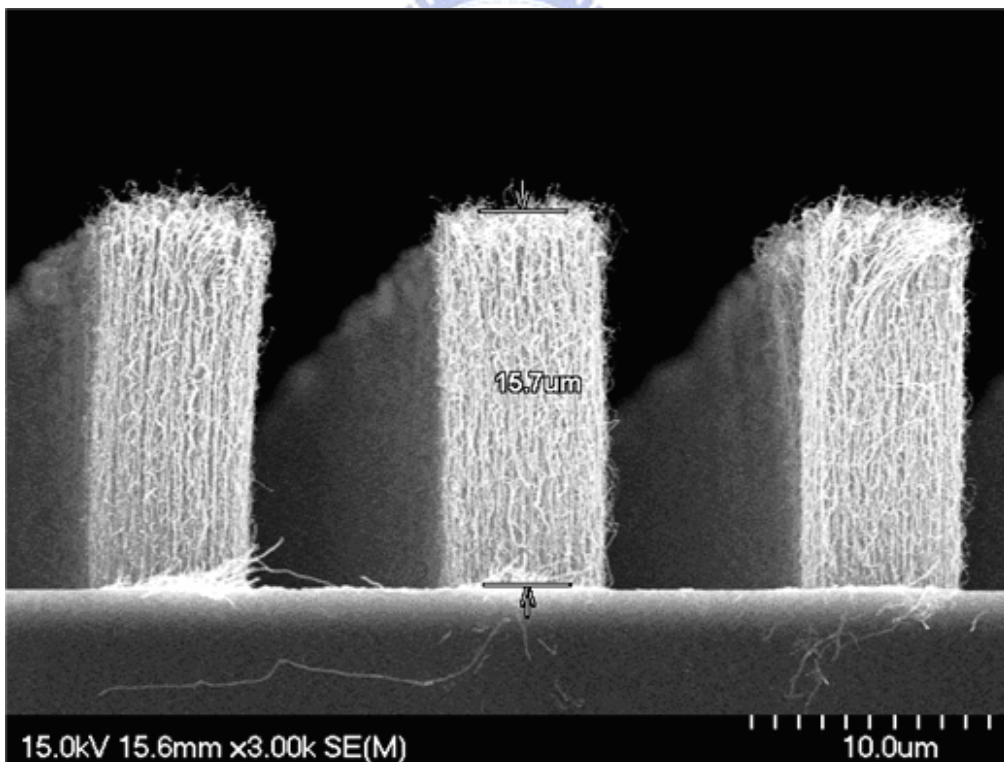


(e)

Figure 4.1 (cont.)

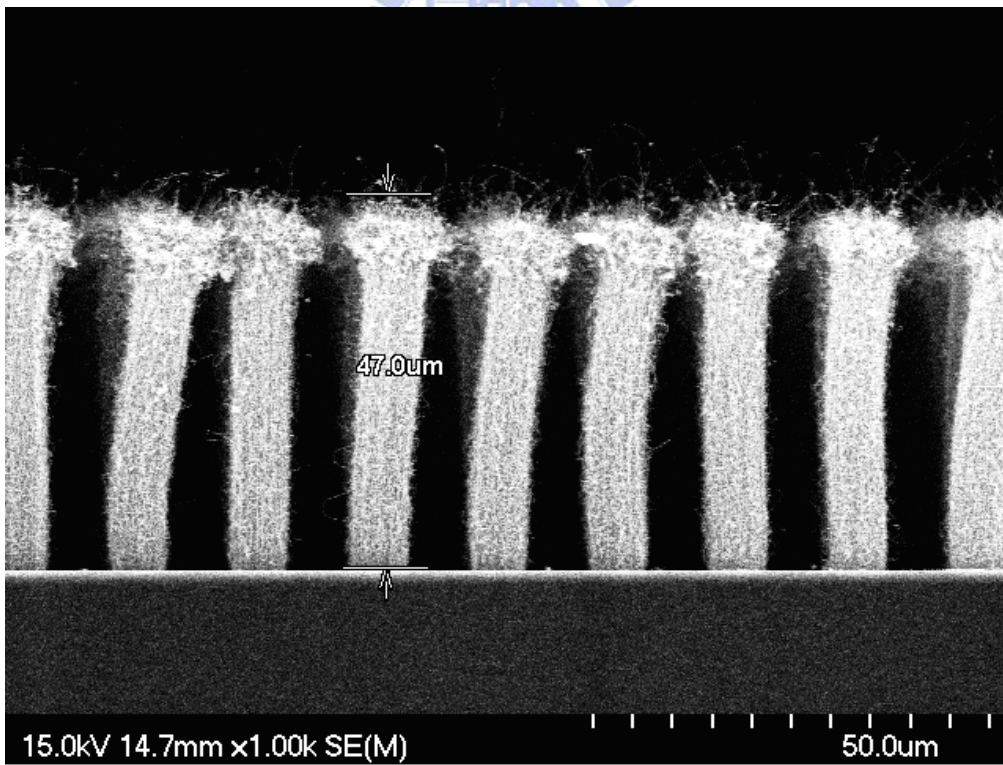
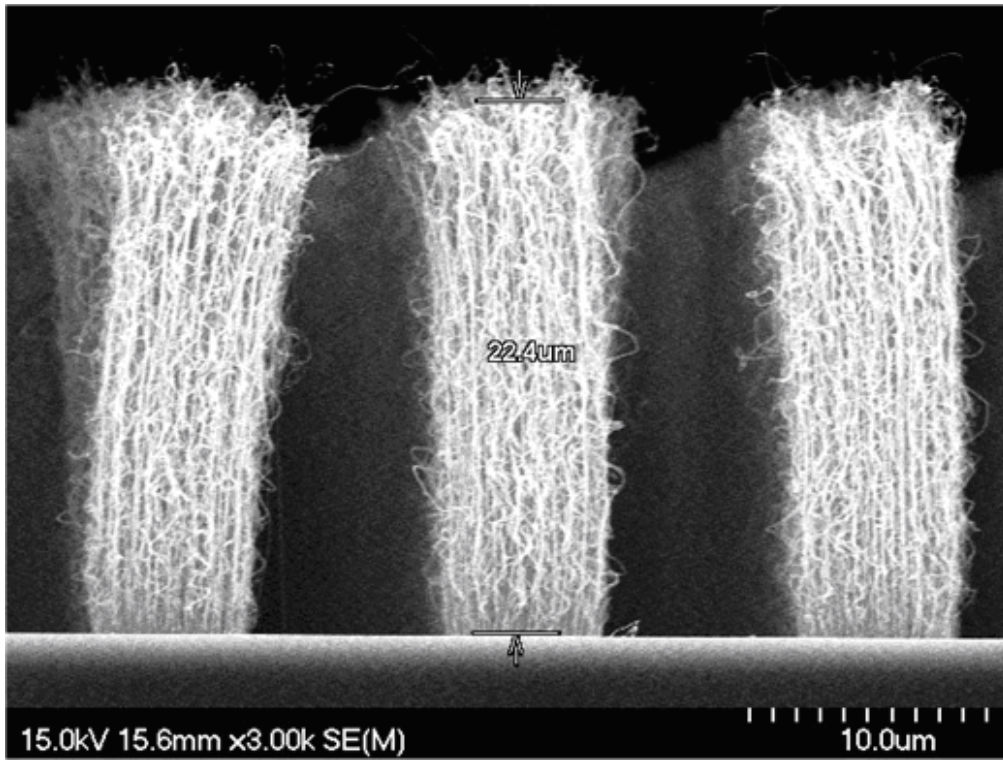


(a)



(b)

Figure 4.2 The cross-section view of pillar-like CNTs synthesized from the 5-nm-thick pure Fe catalytic film in the thermal-CVD for (a) 8 min, (b) 15 min, (c), 30 min, (d) 60 min, and (e) 120 min



(d)

Figure 4.2 (cont.)

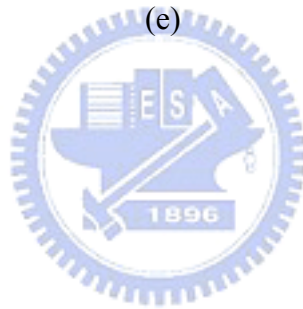
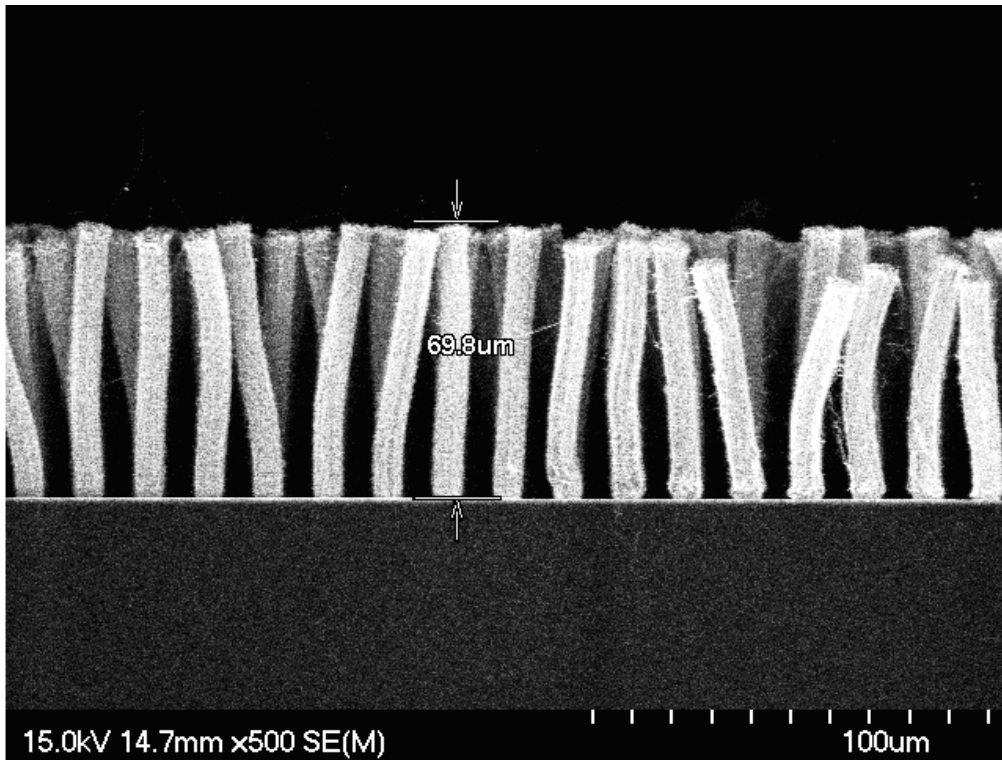
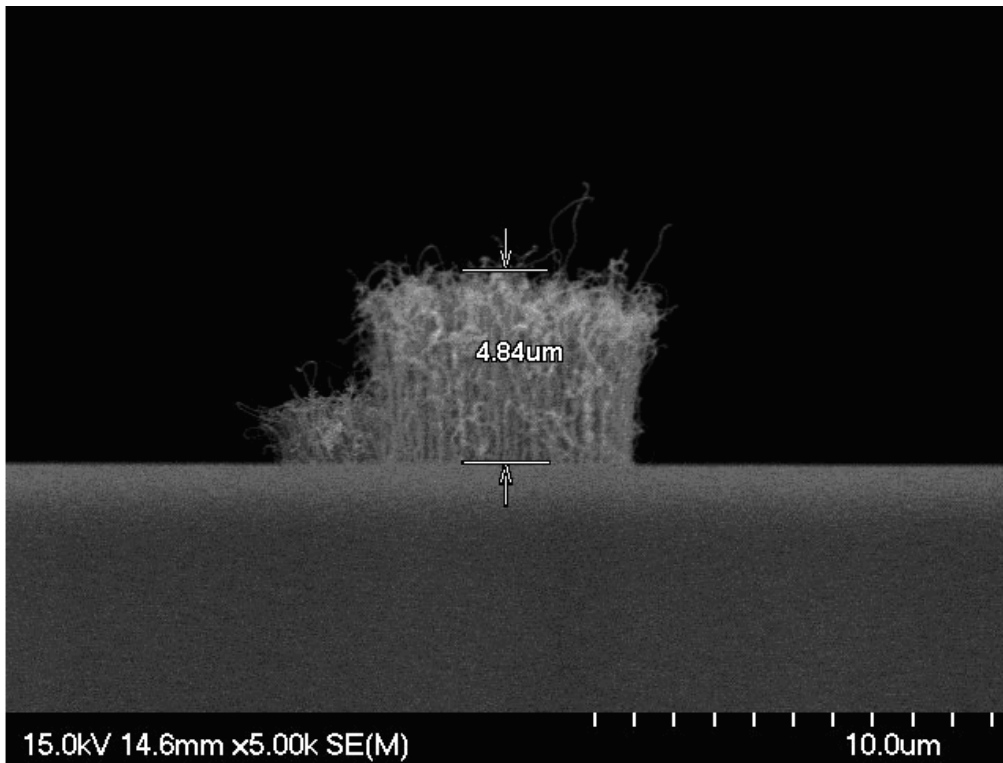
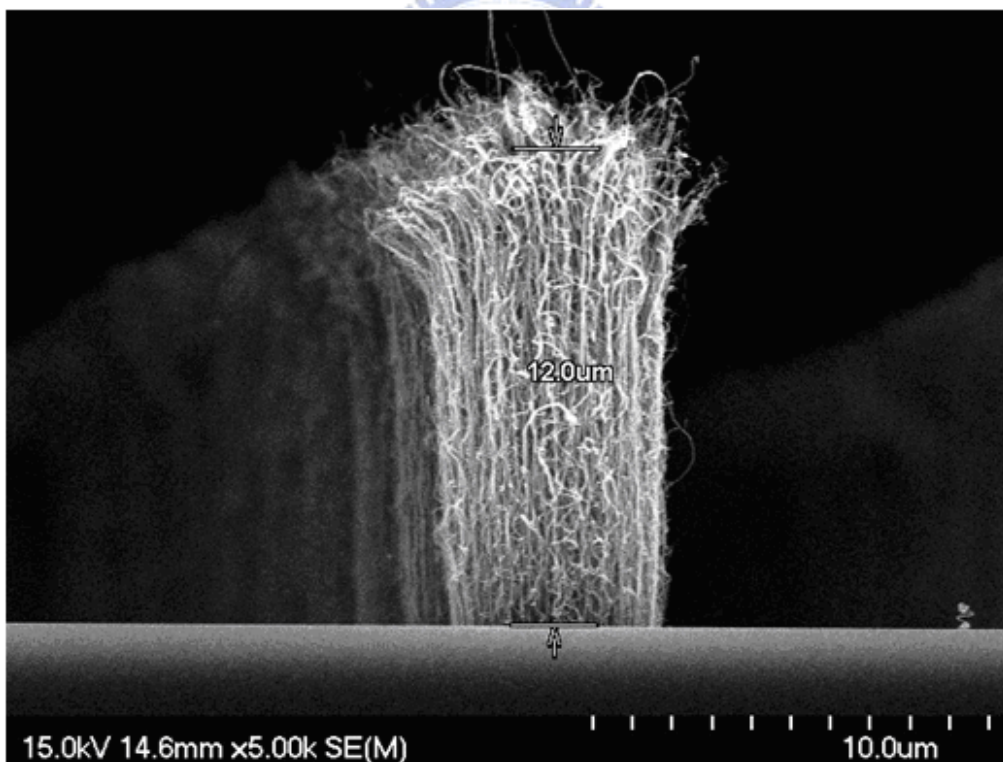


Figure 4.2 (cont.)



(a)



(b)

Figure 4.3 The cross-section view of pillar-like CNTs synthesized from the Fe-Ti codeposited catalytic film in the thermal-CVD for (a) 8 min, (b) 15 min, (c), 30 min, (d) 60 min, and (e) 120 min

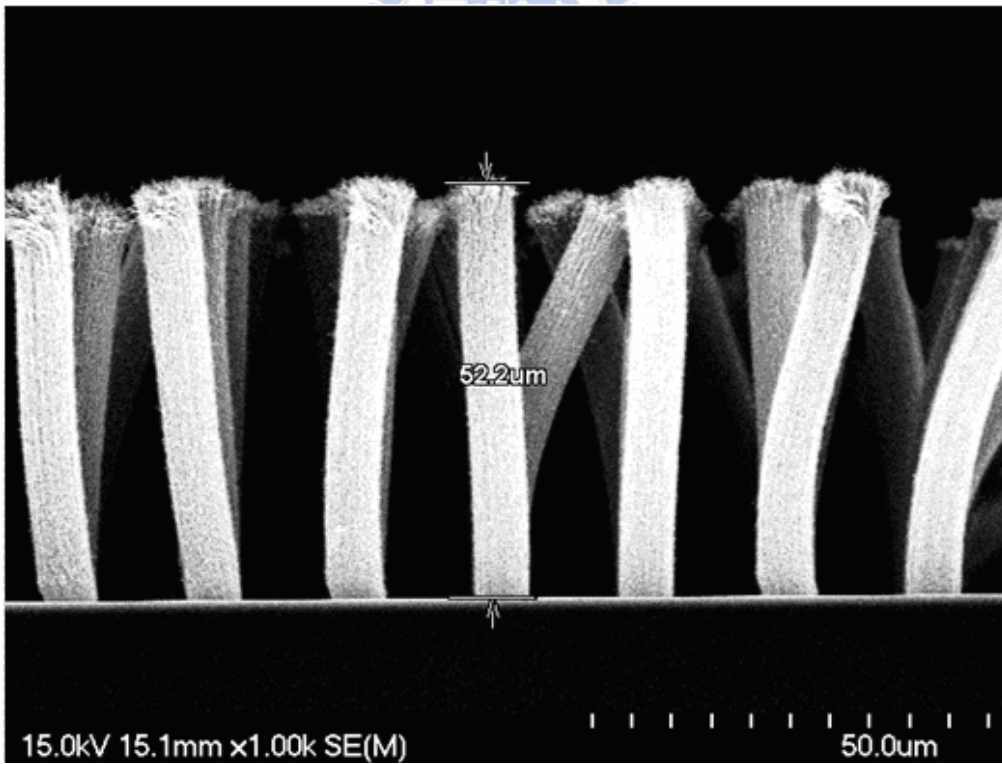
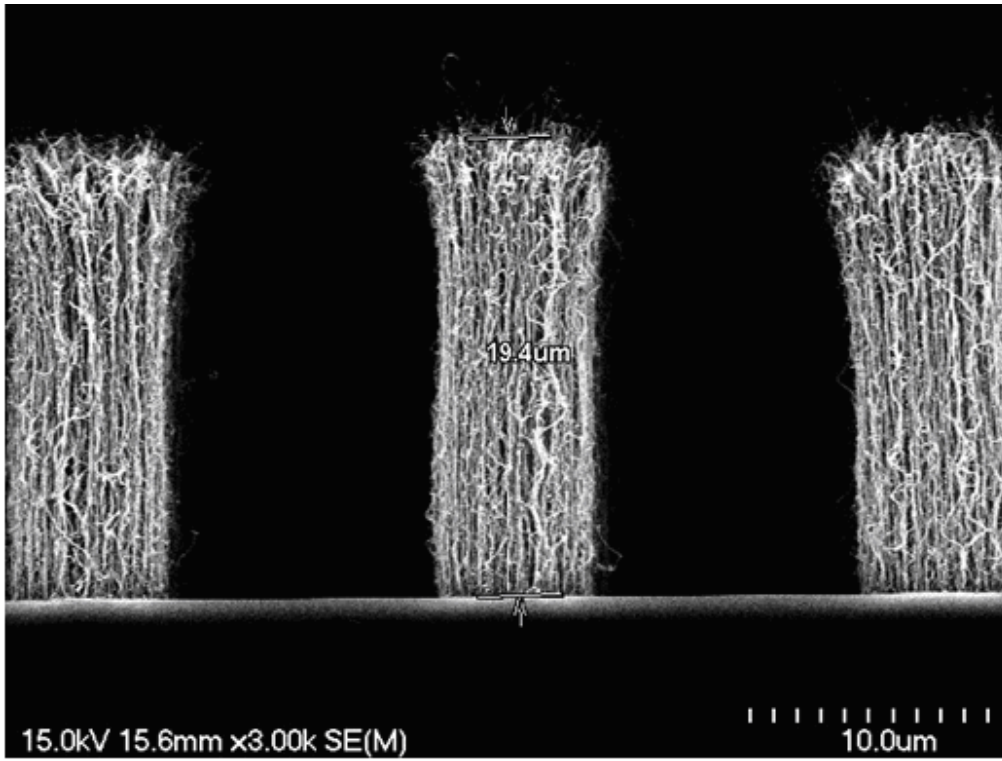


Figure 4.3 (cont.)

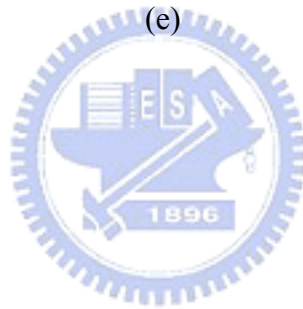
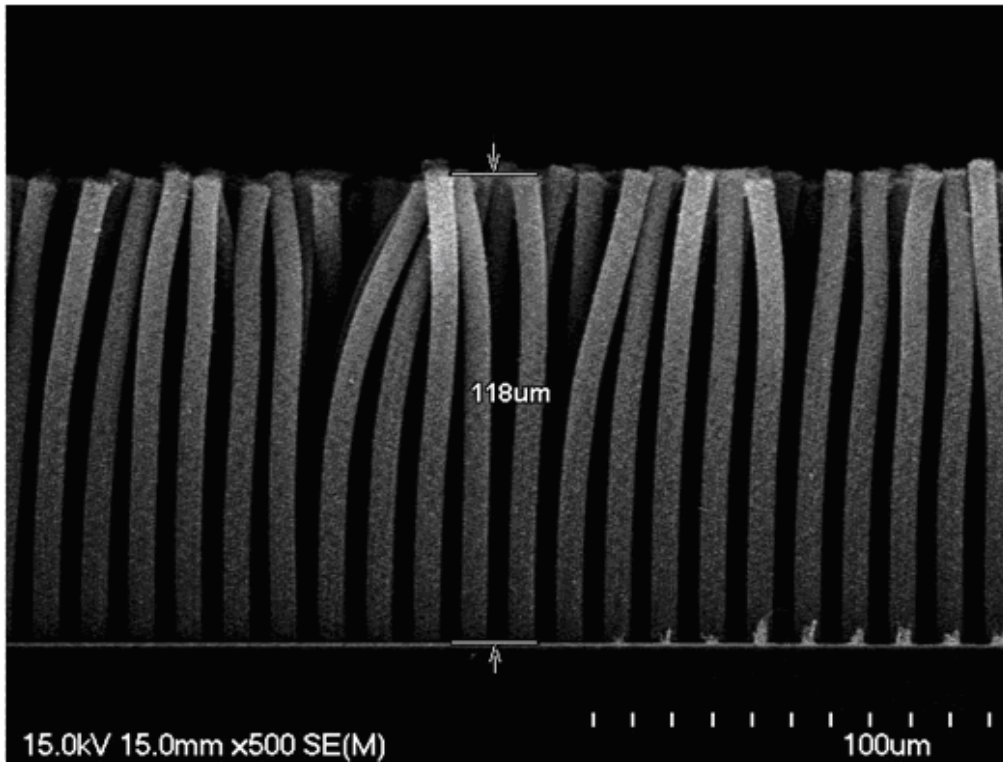


Figure 4.3 (cont.)

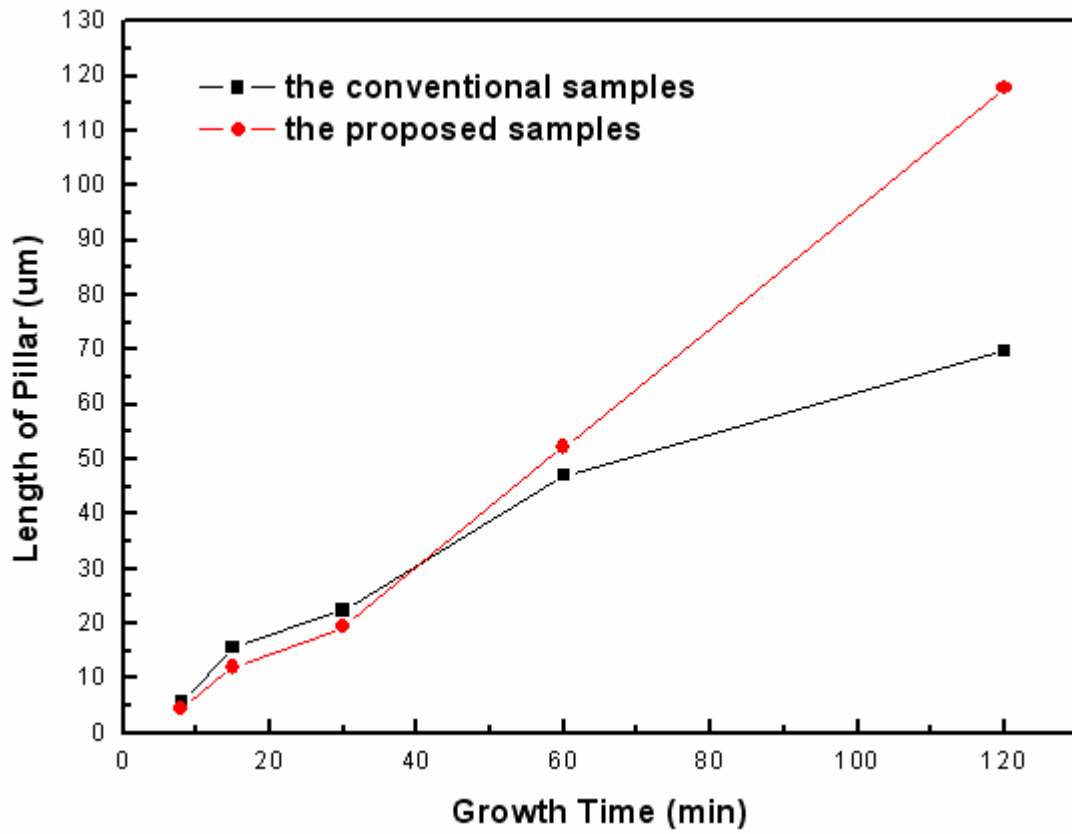
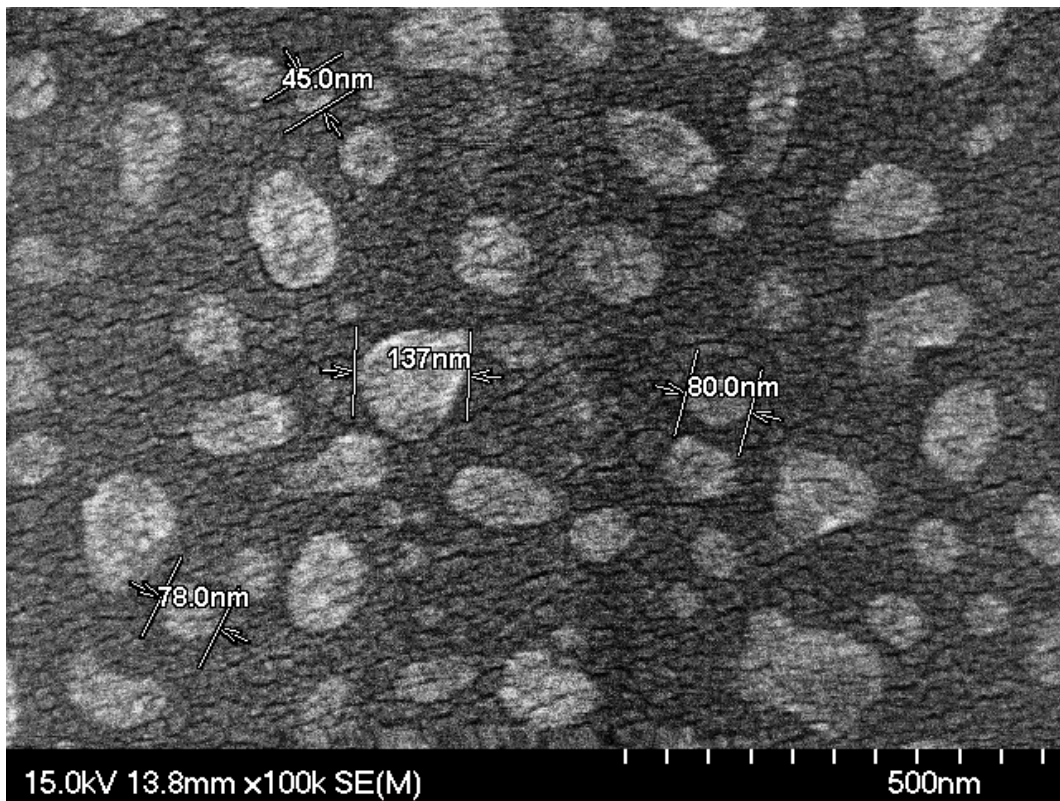
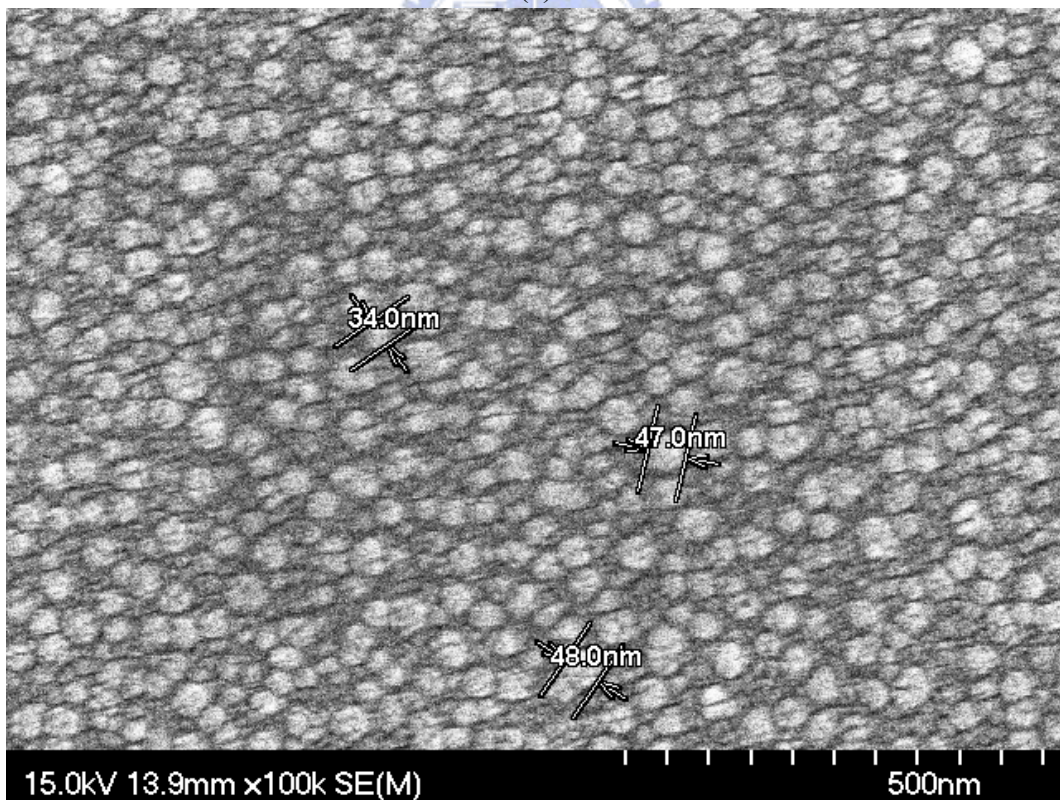


Figure 4.4 The relationship of the length of pillars versus the growth time for both the conventional and the proposed samples



(a)



(b)

Figure 4.5 The morphologies of the hydrogen pretreated catalytic nanoparticles for both (a) the conventional samples and (b) the proposed samples.

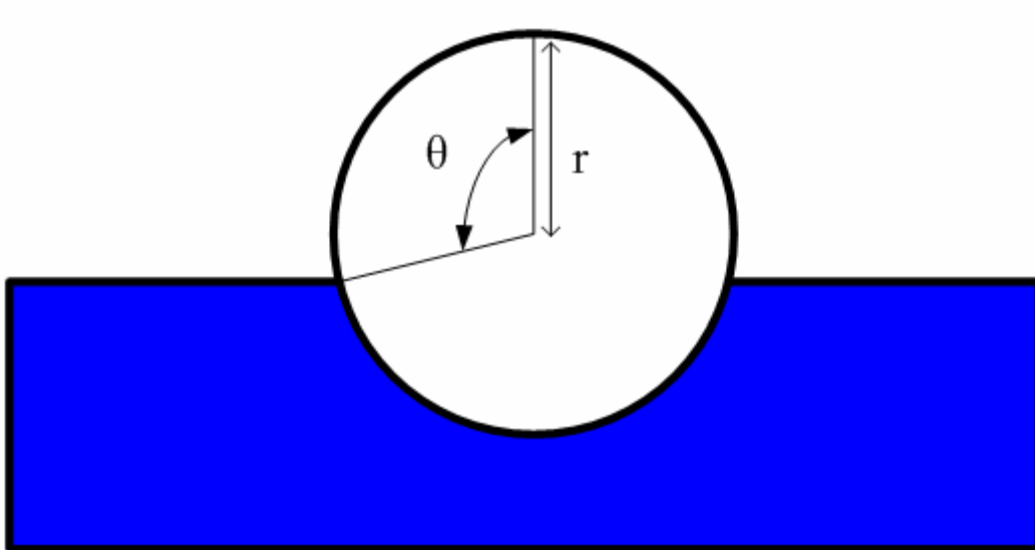


Figure 4.6 The scheme of a sphere partially immersed in the substrate

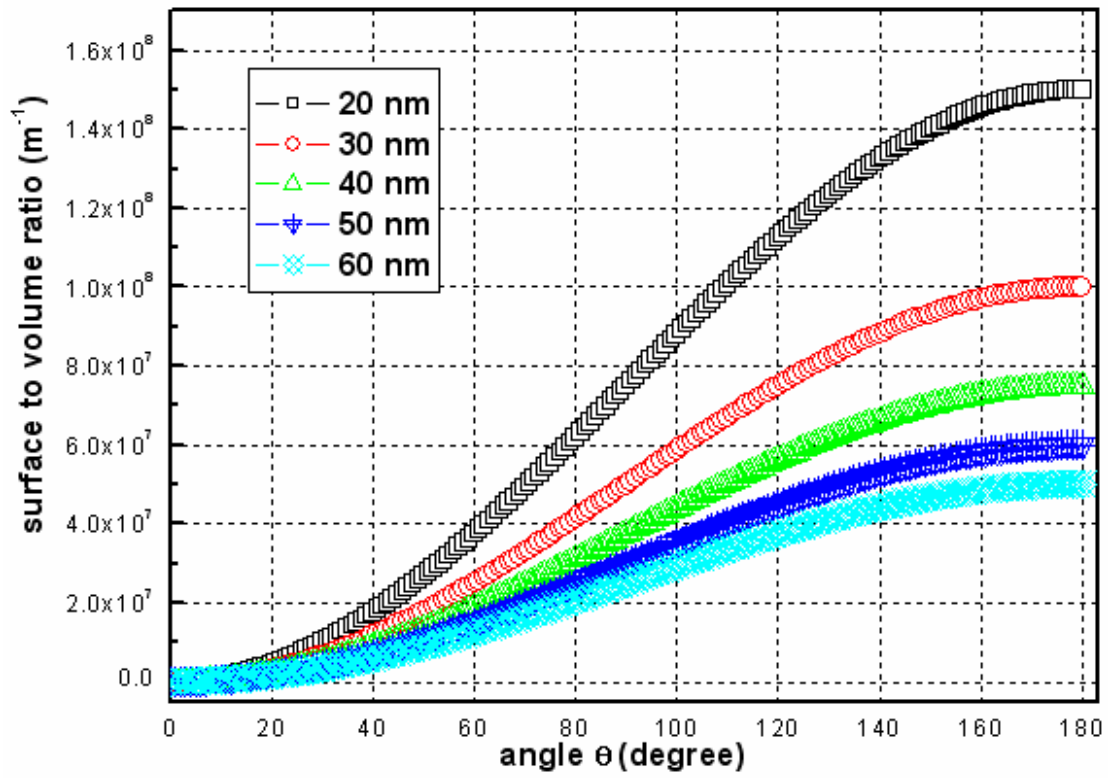
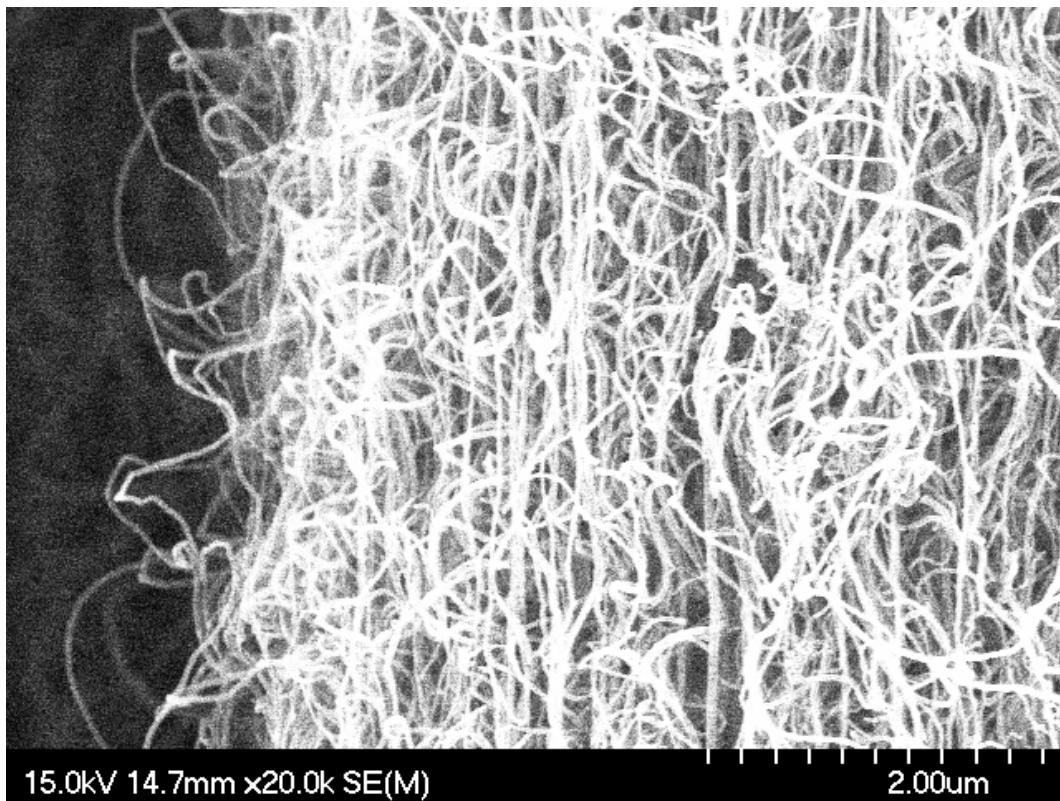
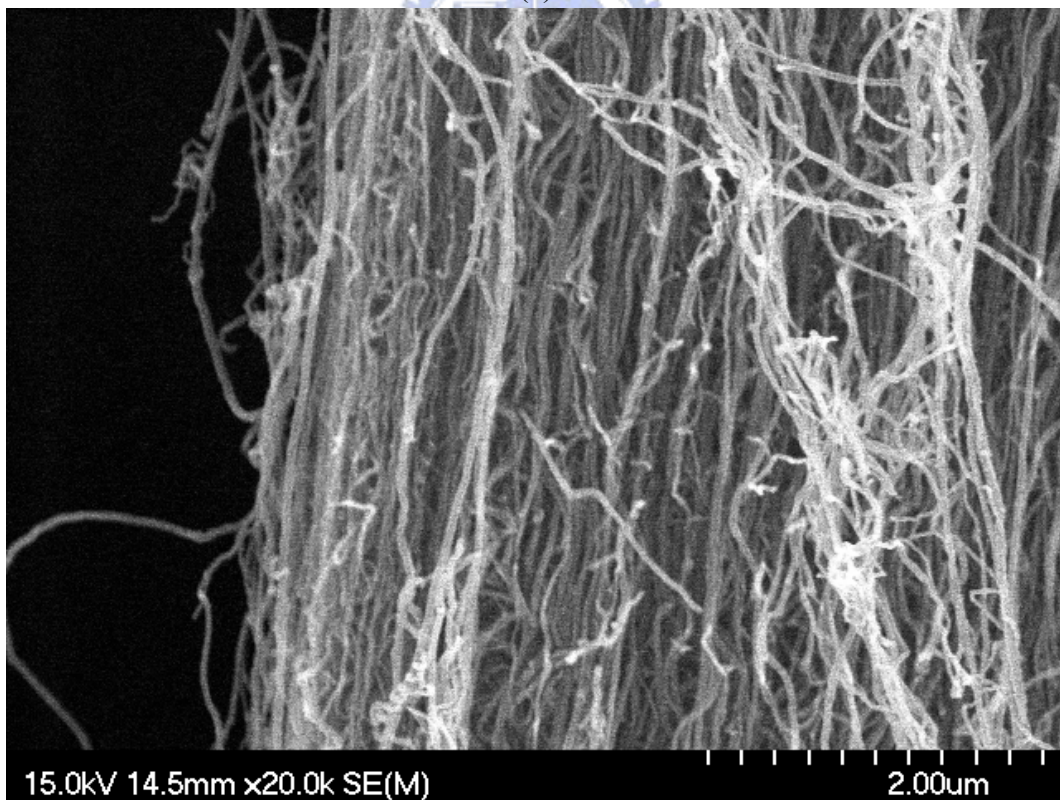


Figure 4.7 The surface to volume ratio of sphere in Fig. 4.6 versus the radius and the angle θ

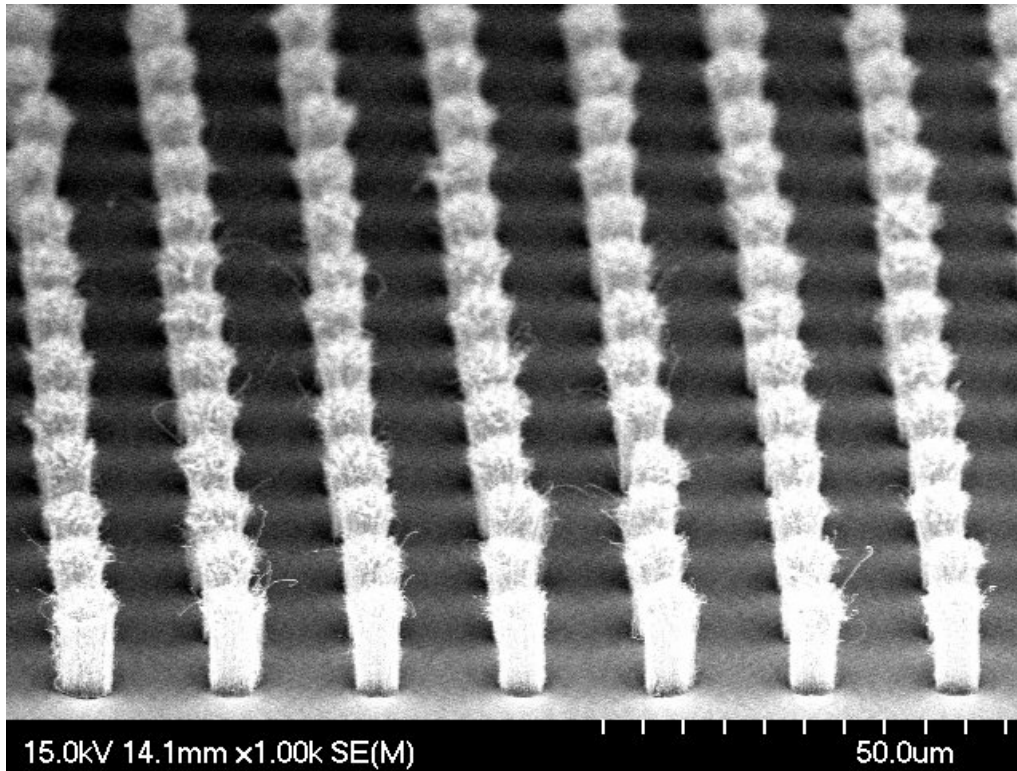


(a)

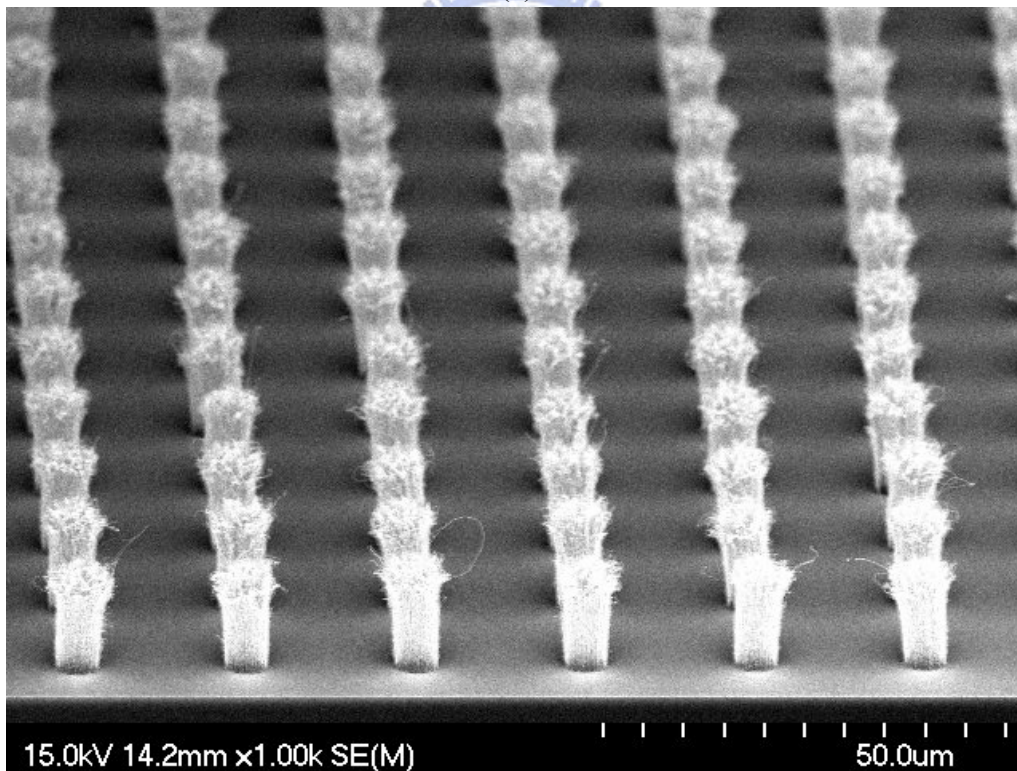


(b)

Figure 4.8 The images of CNTs with higher resolution for (a) the conventional samples and (b) the proposed samples



(a)



(b)

Figure 4.9 The micrographs of the pillar-like CNTs with different interpillar spacing, (a) 12 μm , (b) 15 μm , (c) 20 μm , (d) 25 μm , (e) 30 μm , and (f) 35 μm , taken by SEM with 45 ° viewing angle.

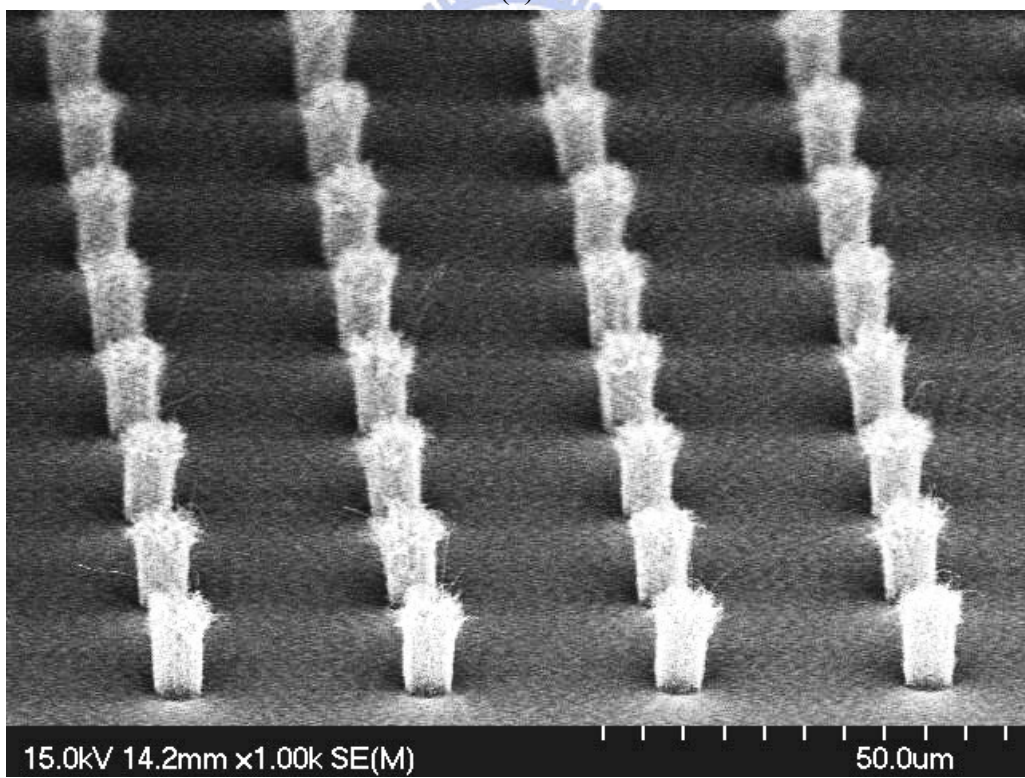
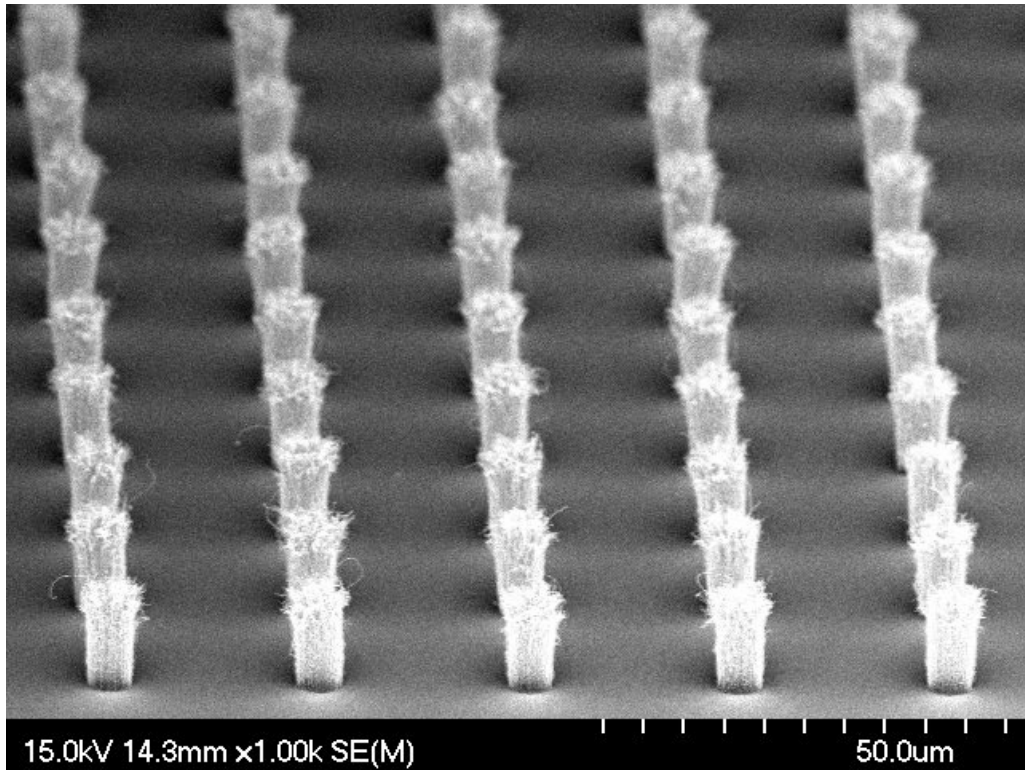


Figure 4.9 (cont.)

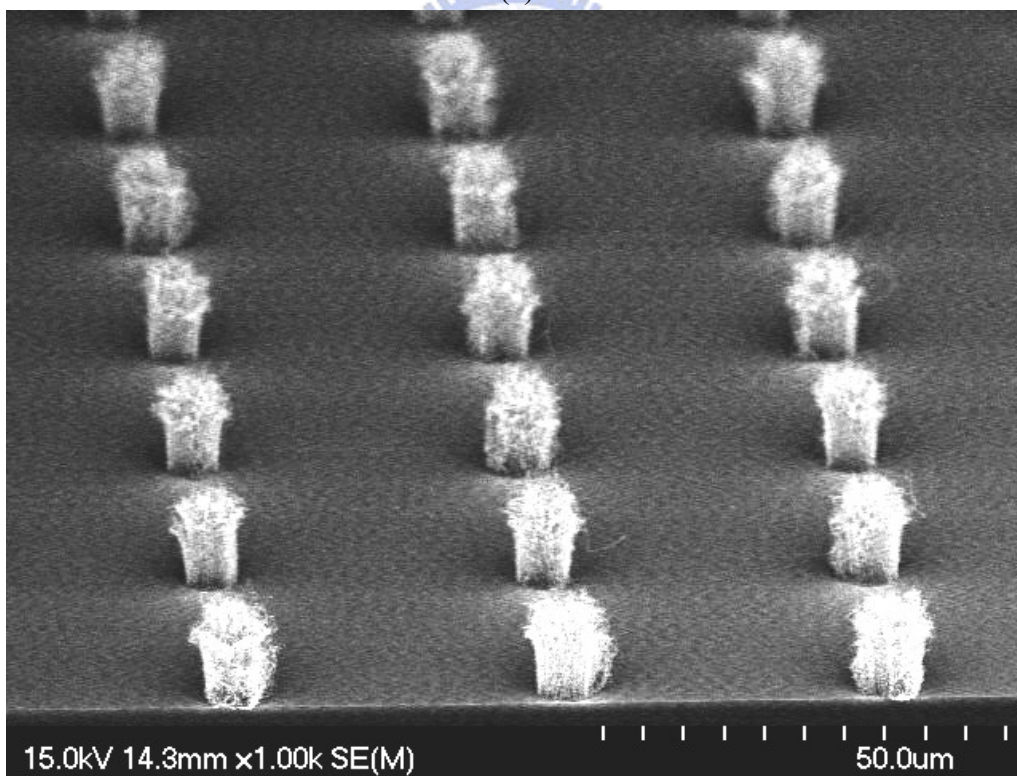
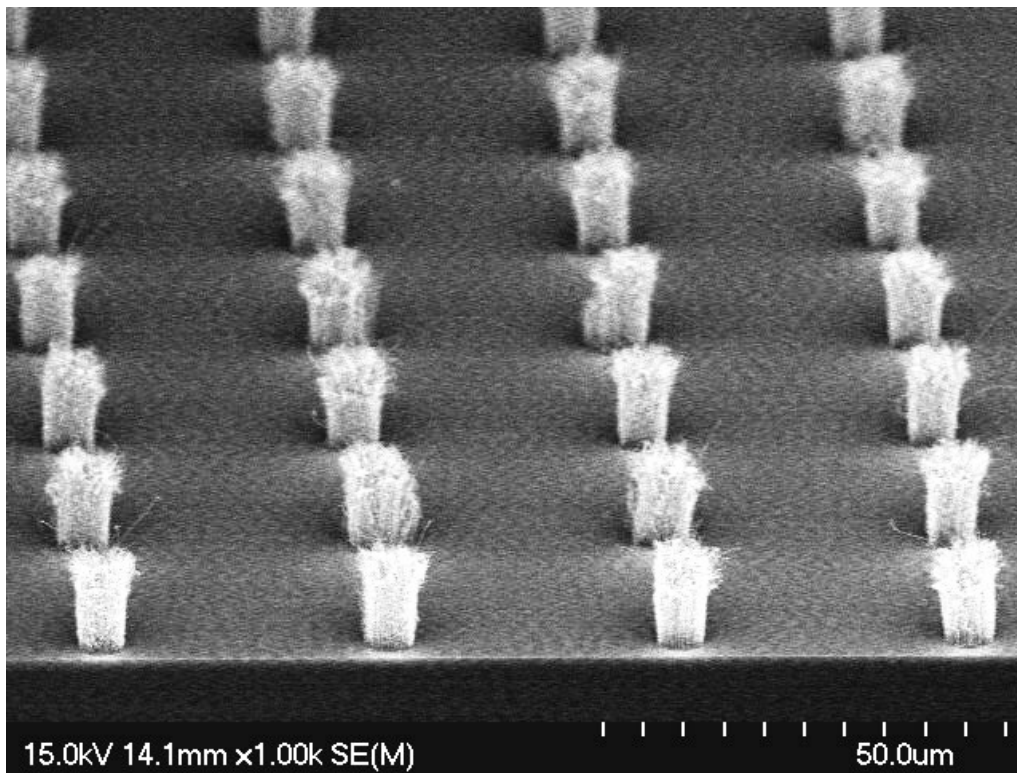
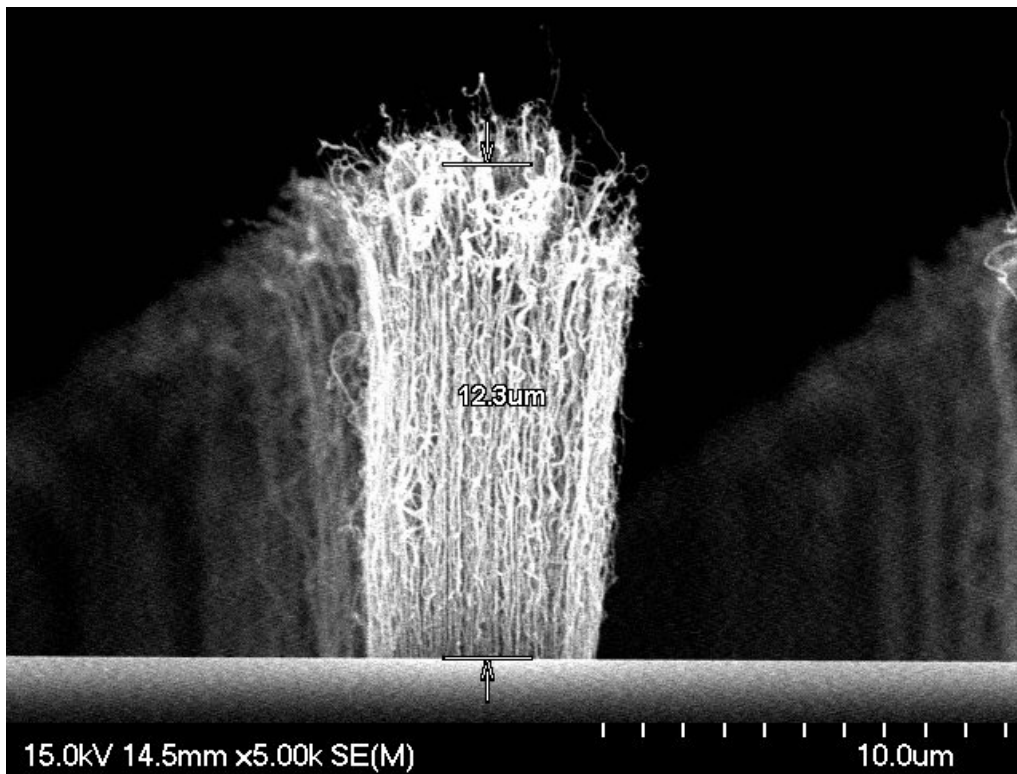
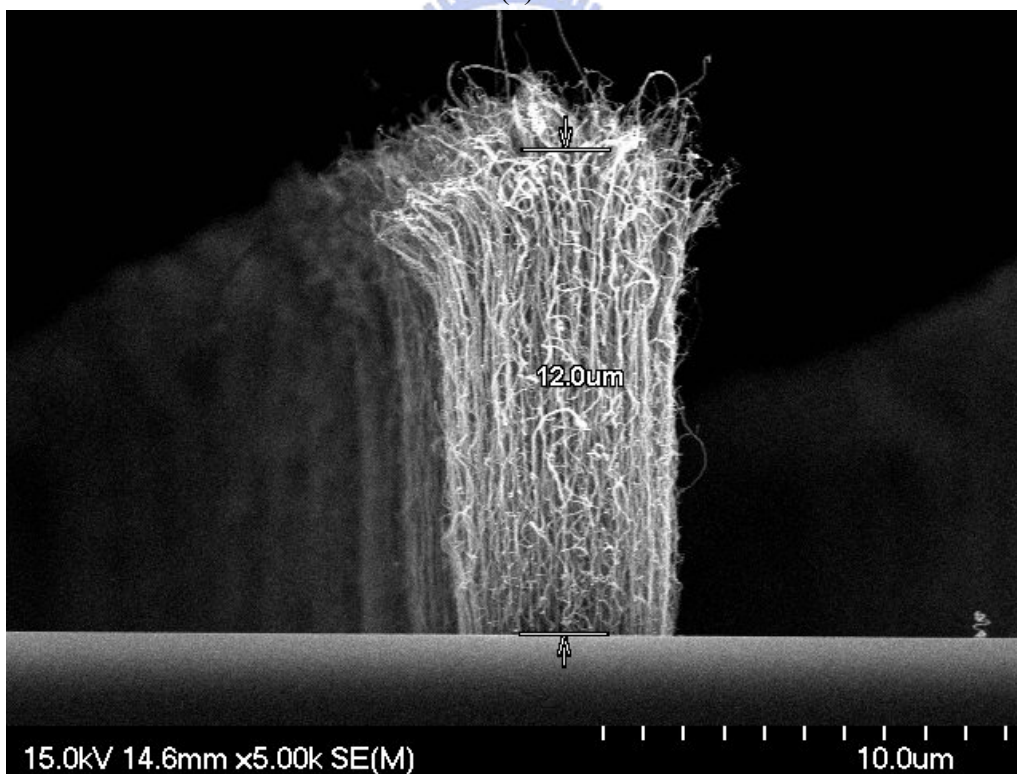


Figure 4.9 (cont.)



(a)



(b)

Figure 4.10 The cross-section views of the pillar-like CNTs with different interpillar spacing, (a) 12 μm, (b) 15 μm, (c) 20 μm, (d) 25 μm, (e) 30 μm, and (f) 35 μm.

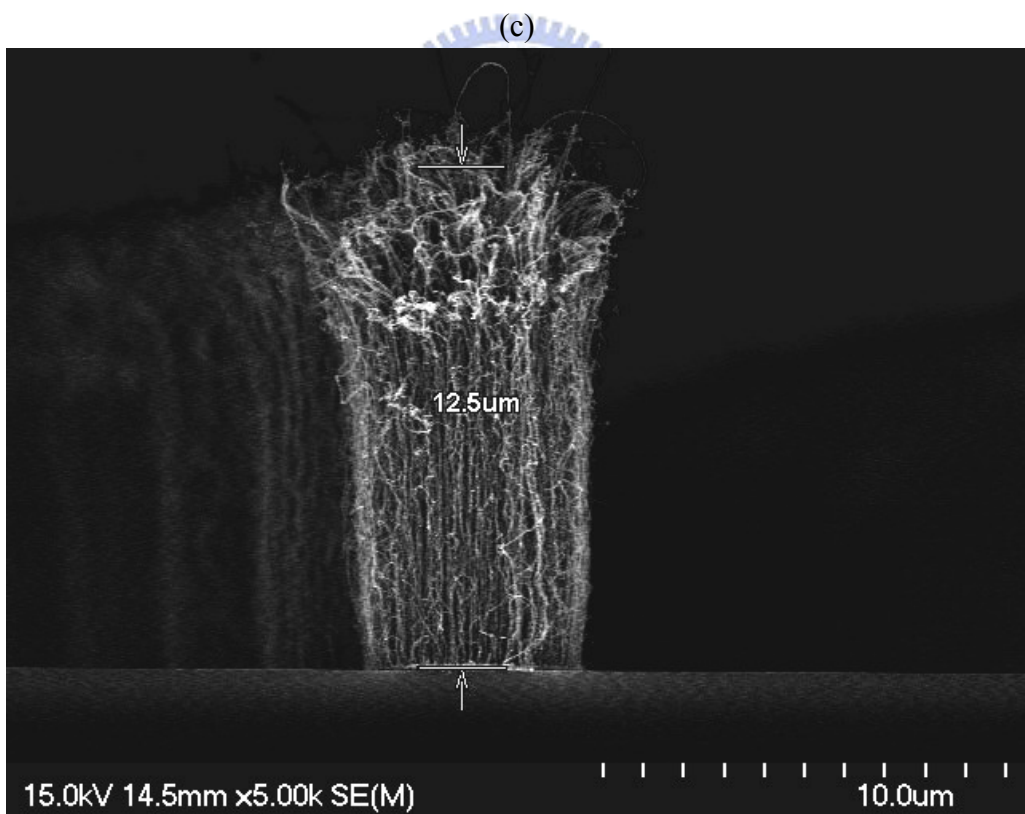
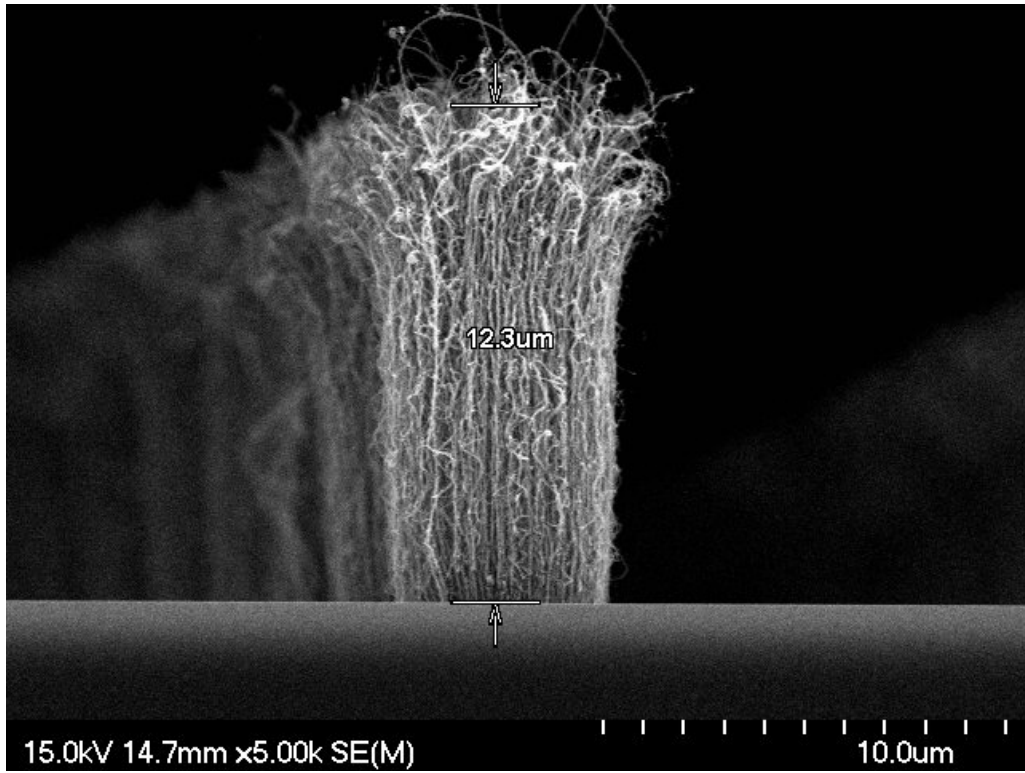


Figure 4.10 (cont.)

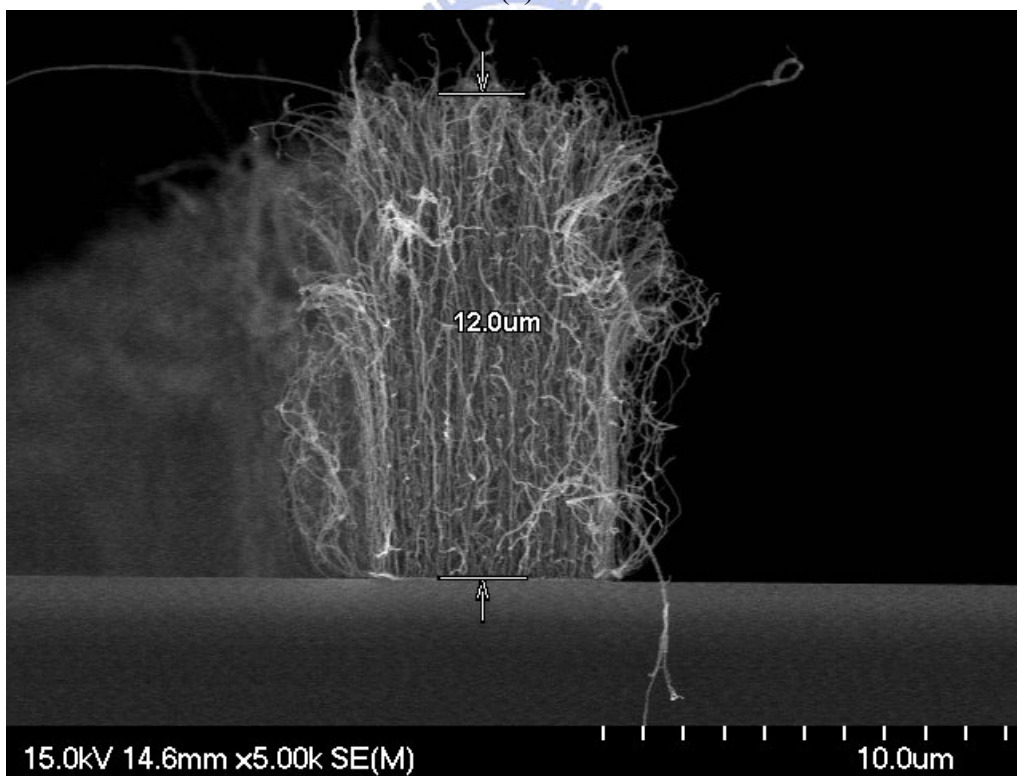
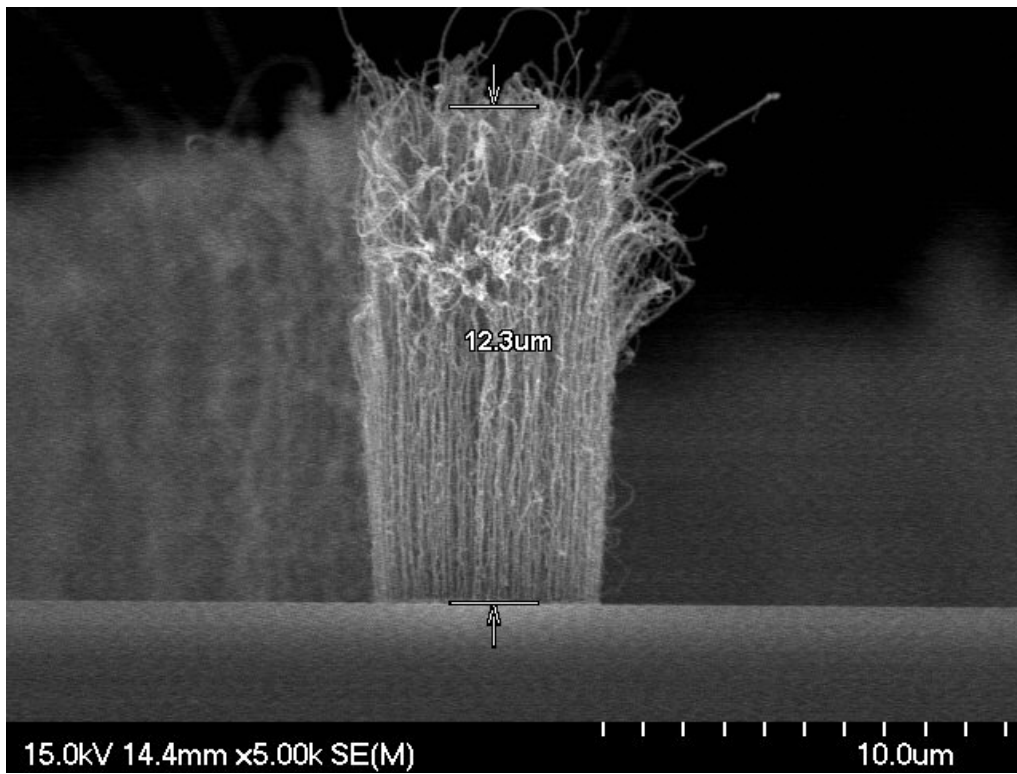
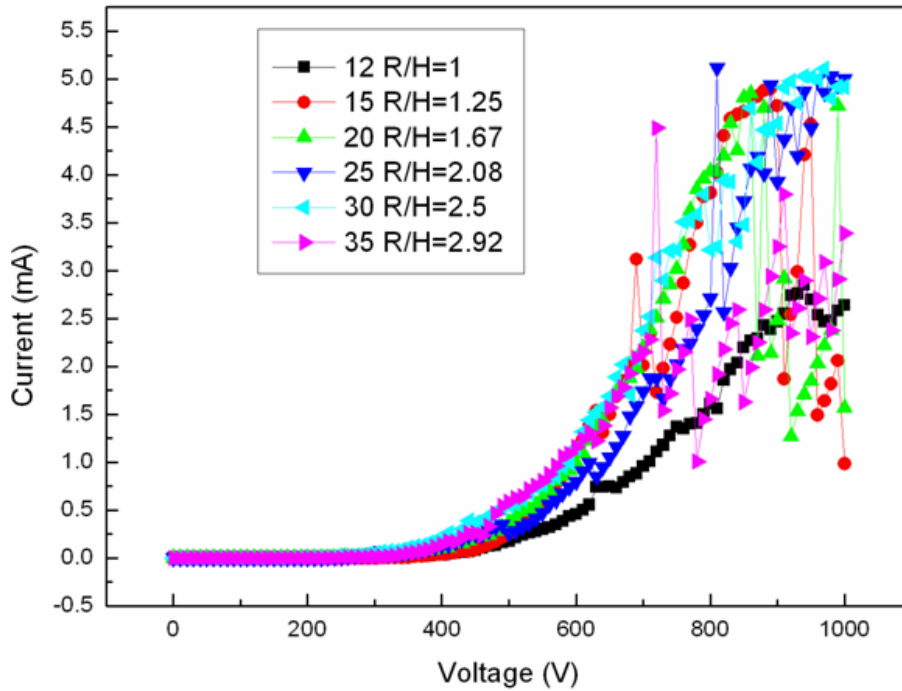
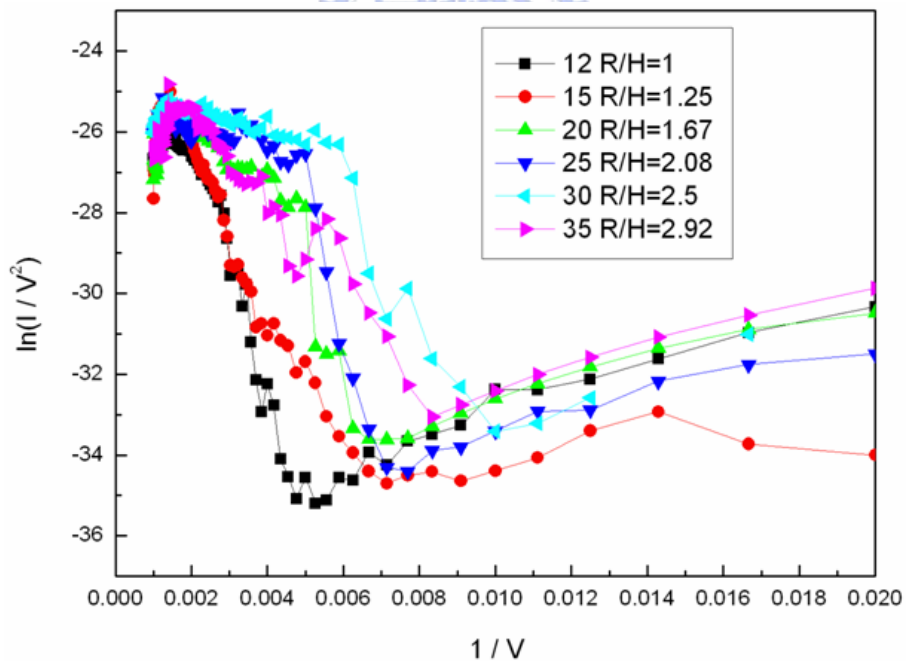


Figure 4.10 (cont.)



(a)



(b)

Figure 4.11 The field-emission characteristics of the pillar-like CNTs (a) the emission current of samples versus applied voltage and (b) the Fowler-Nordhiem plot of each samples

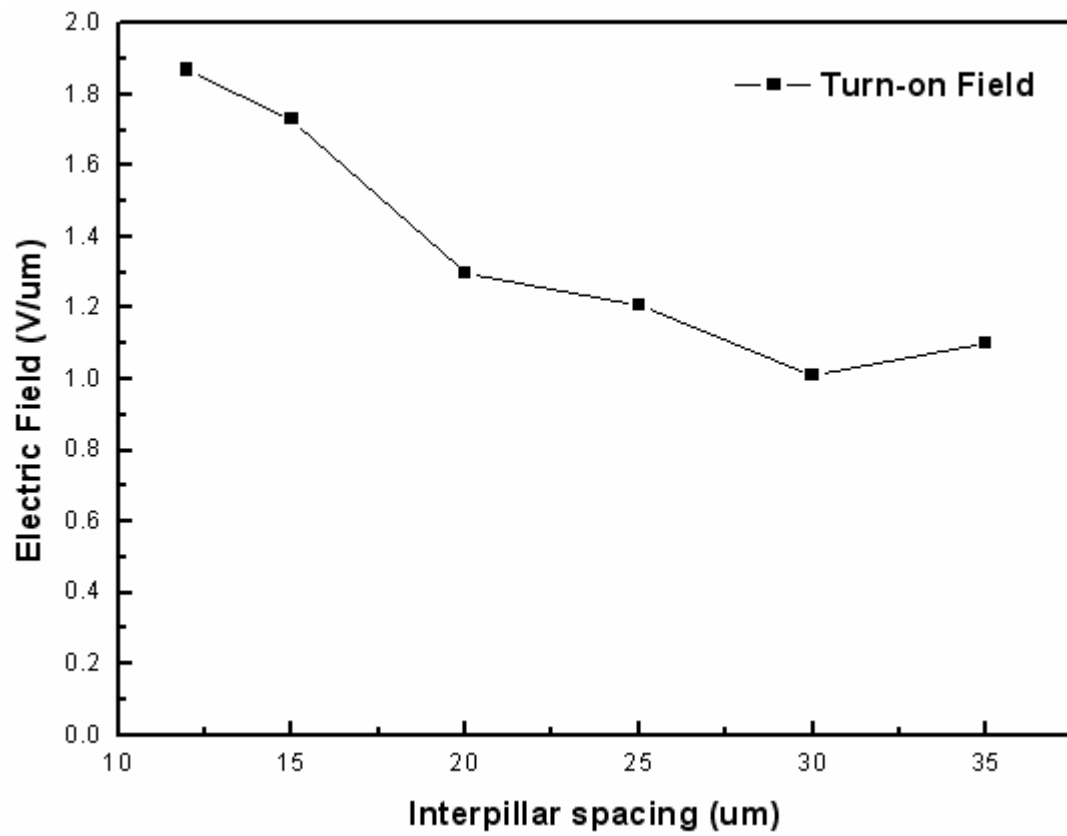


Figure 4.12 The curve of the turn-on field versus the interpillar spacing for the pillar-like CNTs with different interpillar spacing

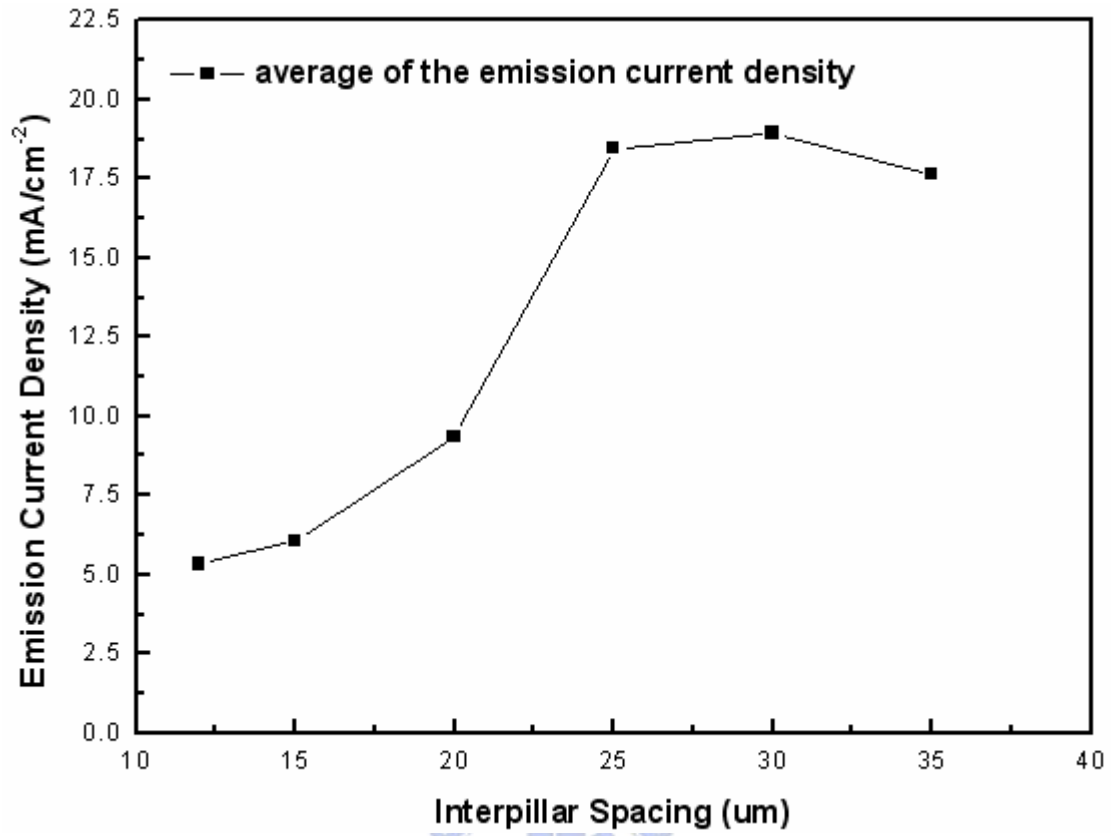
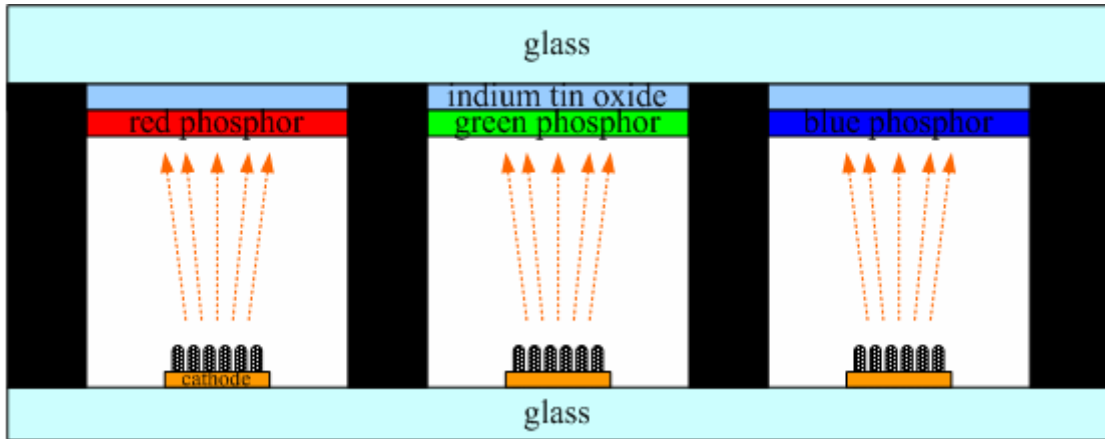


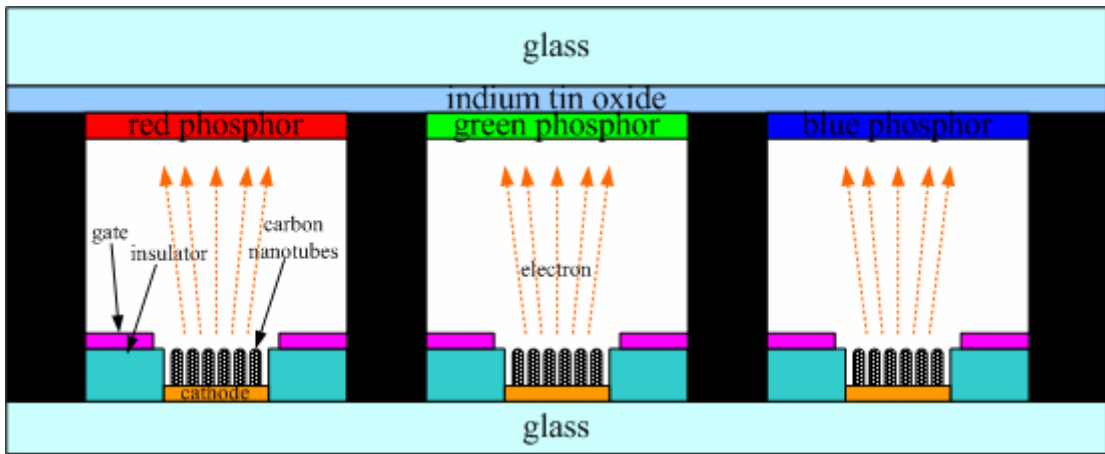
Figure 4.13 The average of the emission current density for all the samples with different interpillar spacing applied at 800 V for 1 hour



Figure 4.14 The luminescent image of the pillar-like CNTs applied at 800 V taken by digital camera



(a)



(b)

Figure 5.1 The scheme of device structures in field-emission displays for (a) the diode-type and (b) the triode-type

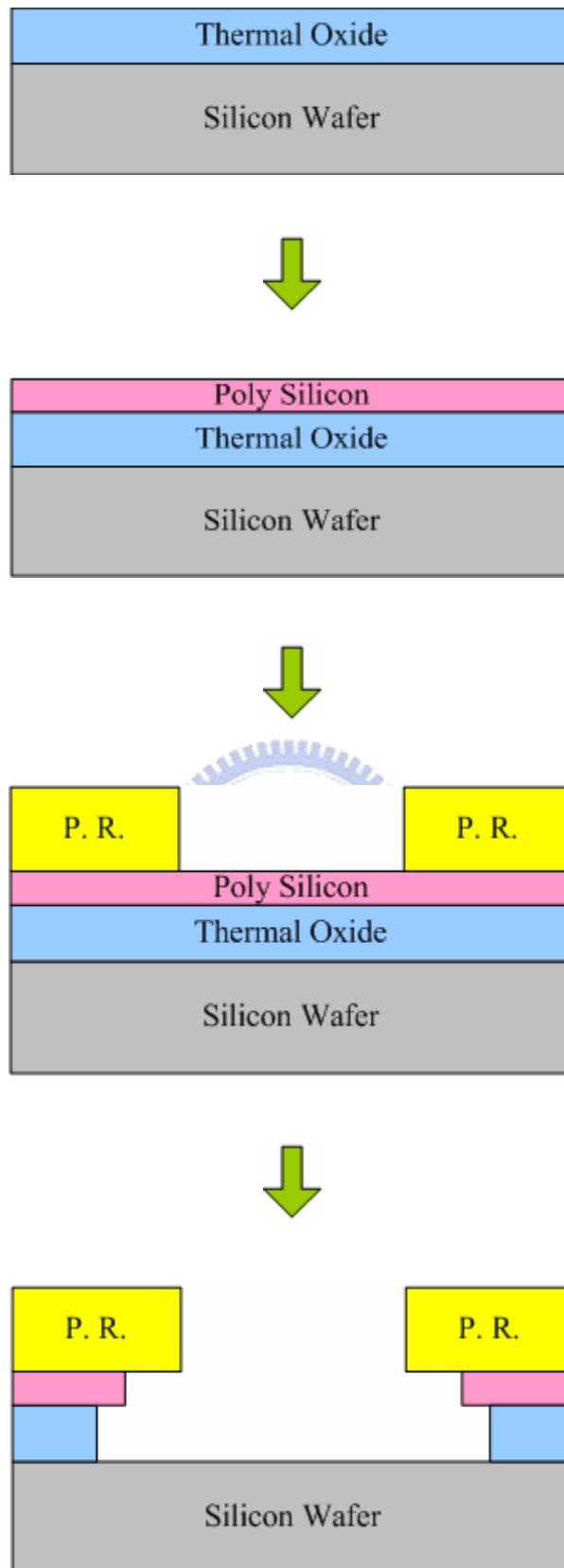
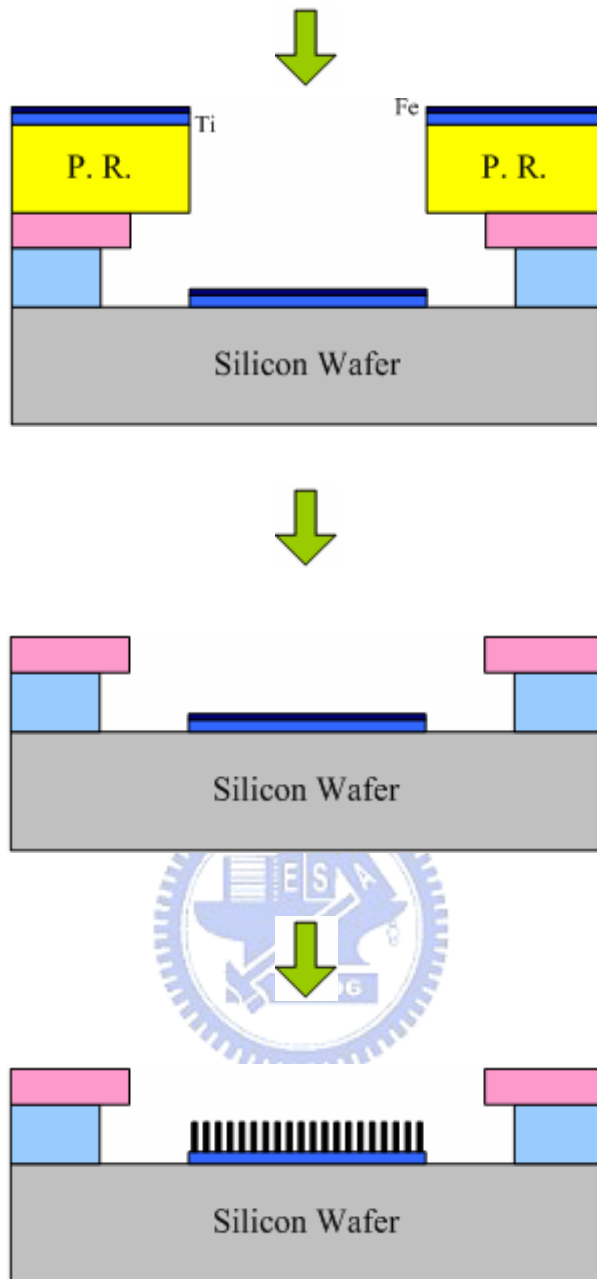


Figure 5.2(a) The flowchart of the conventional samples



(a)

Figure 5.2(a) (cont.)

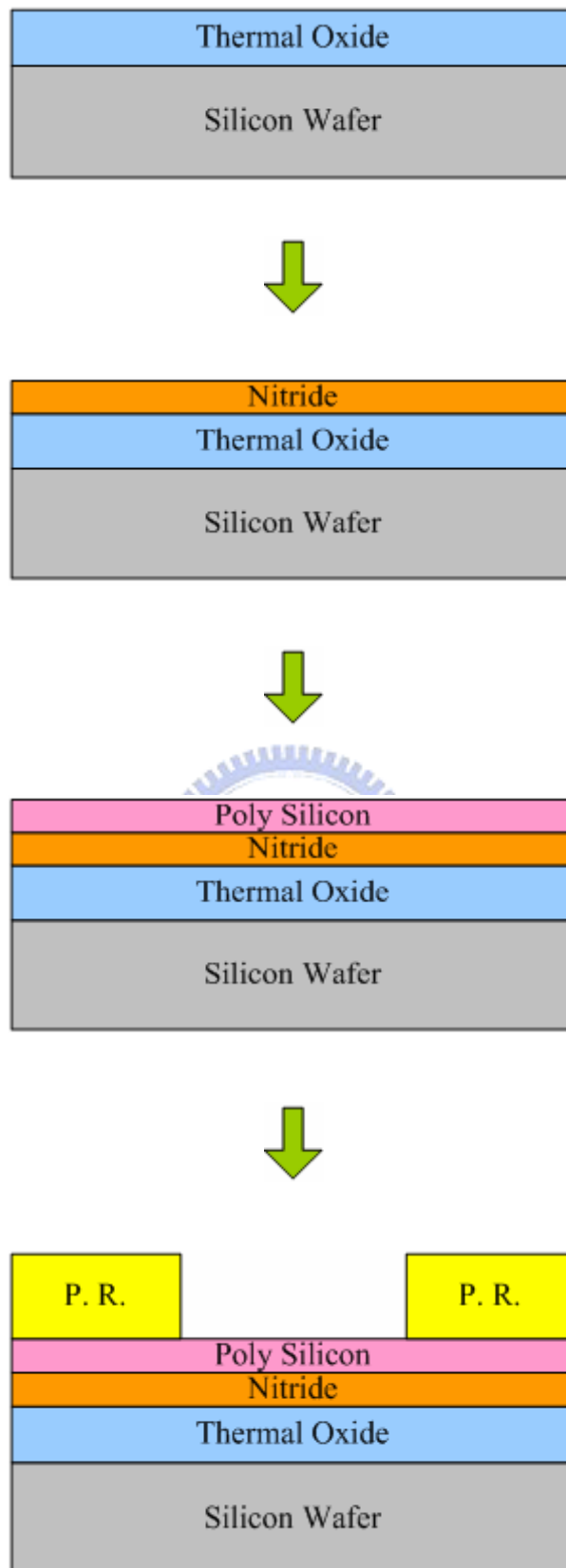


Figure 5.2(b) The flowchart of the OPN (oxide-poly-nitride) samples

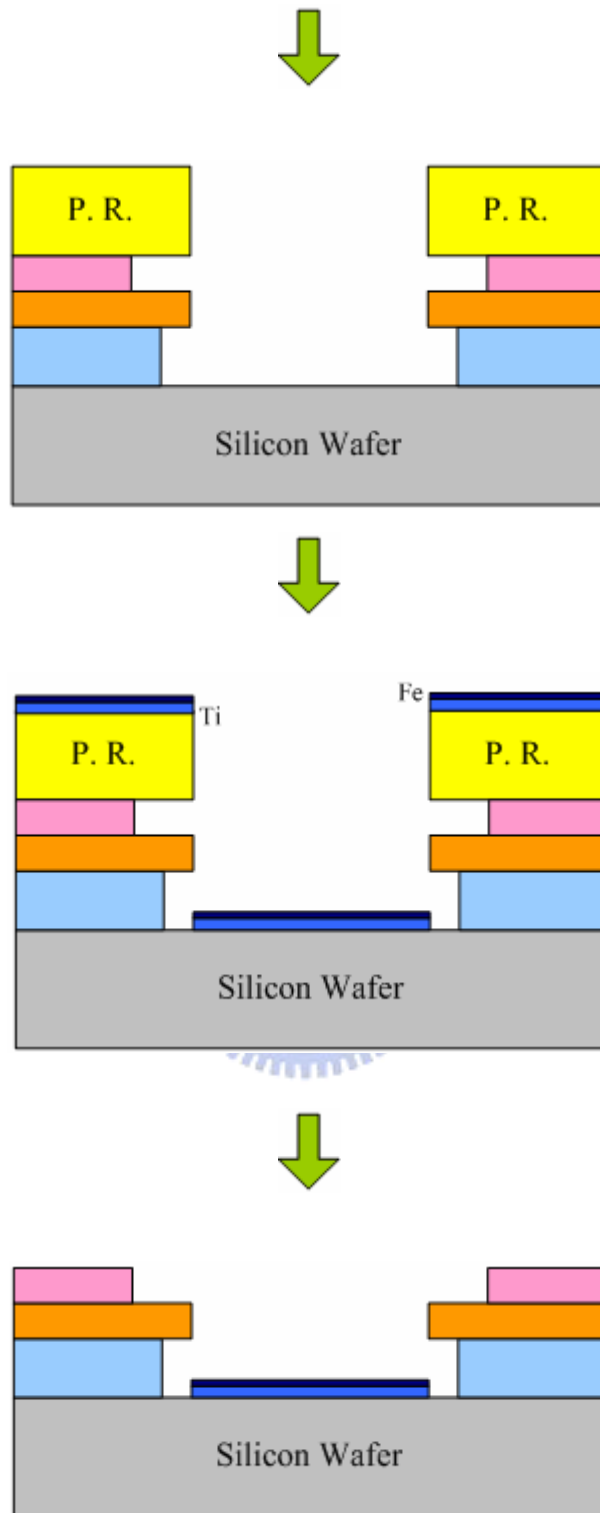


Figure 5.2(b) (cont.)

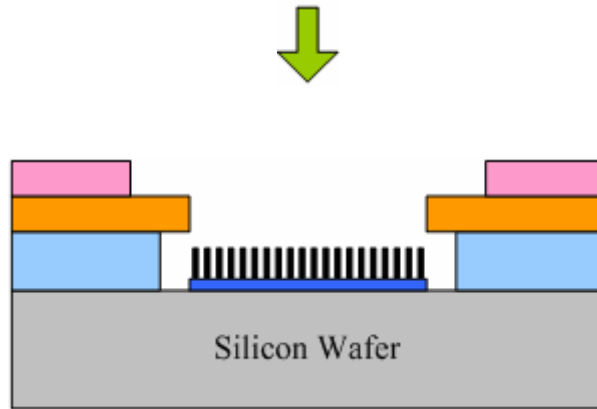


Figure 5.2(b) (cont.)

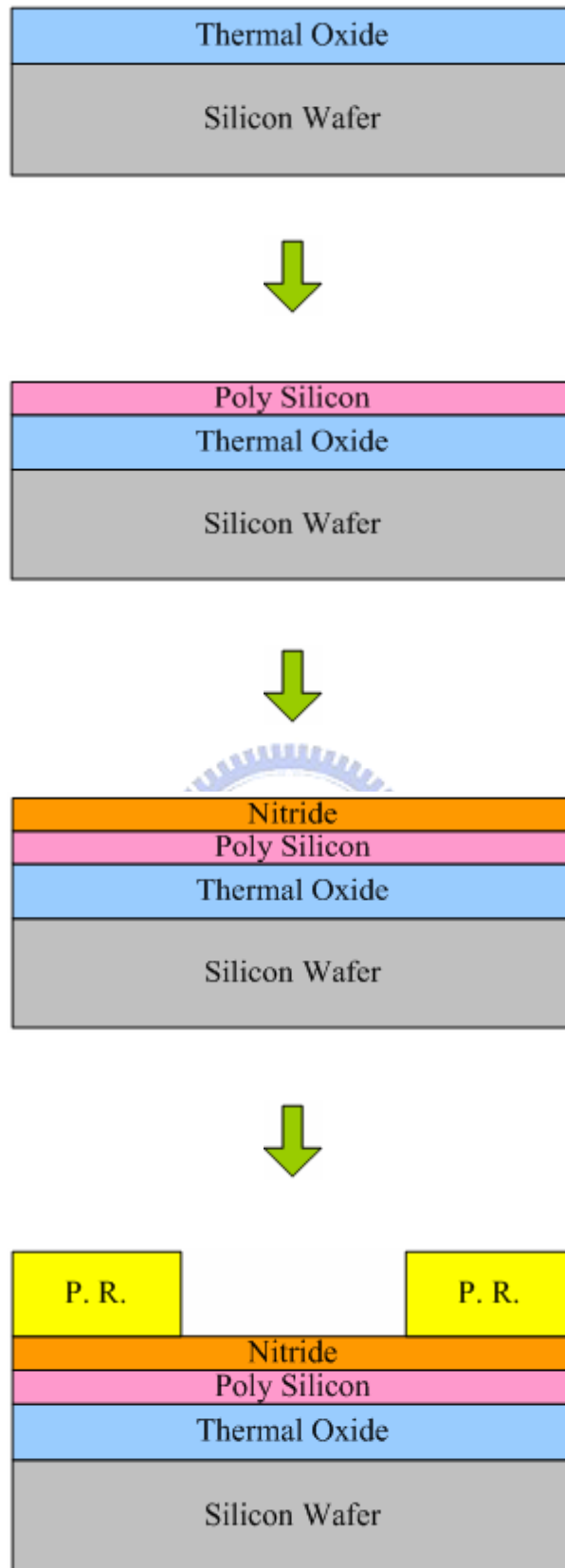


Figure 5.2(c) The flowchart of the ONP (oxide-nitride-poly) samples

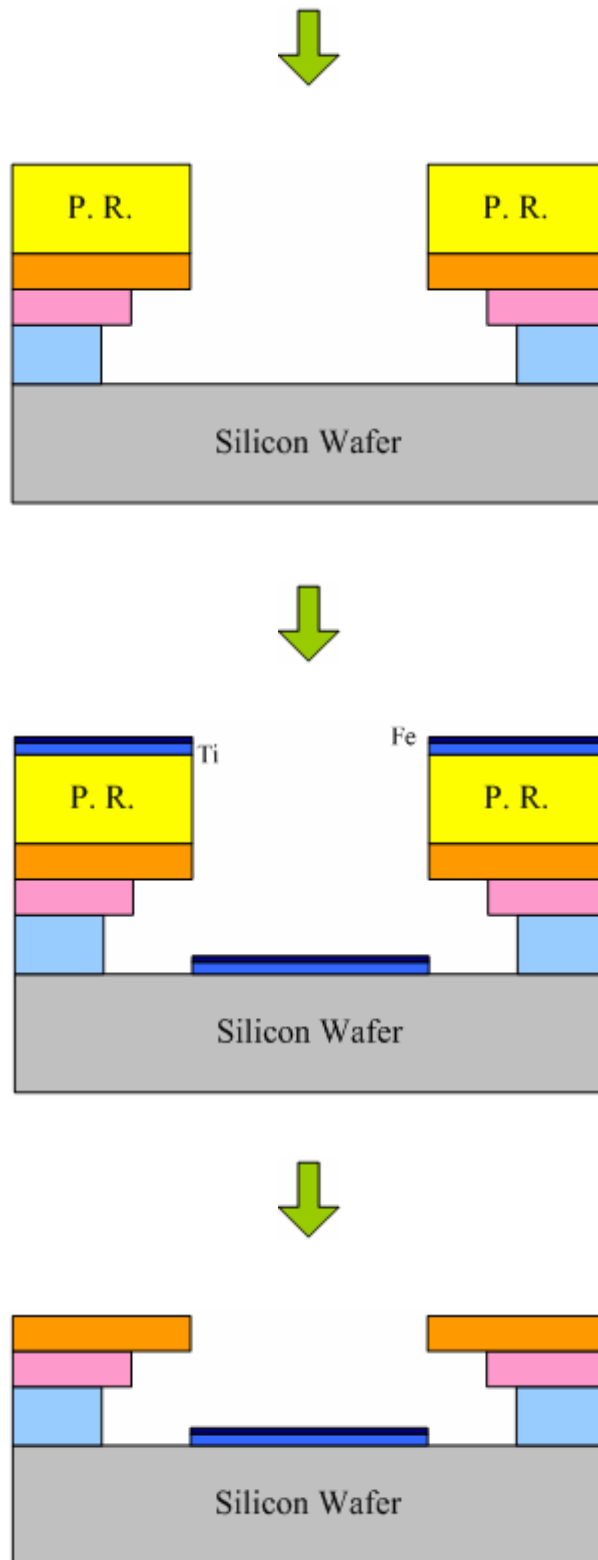


Figure 5.2(c) (cont.)

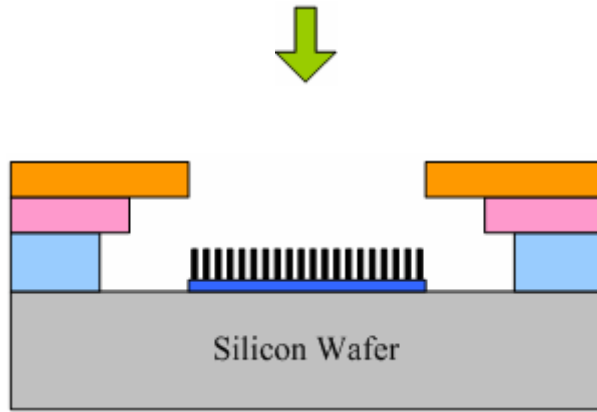
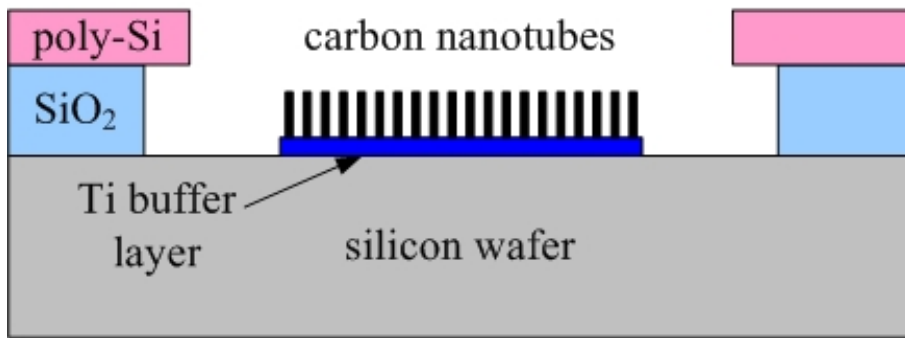
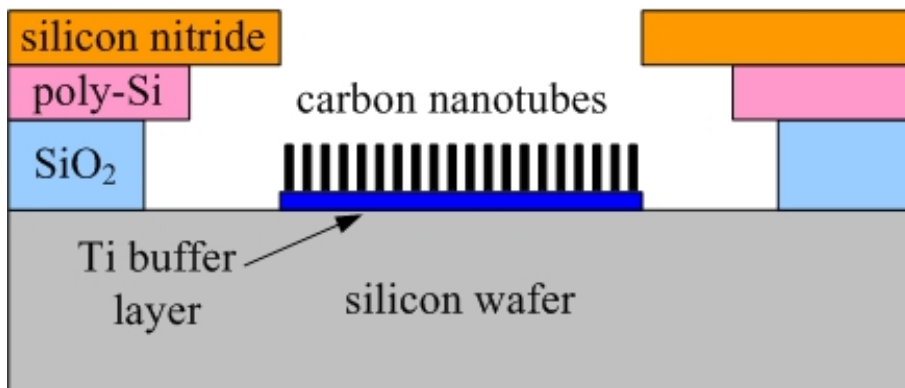


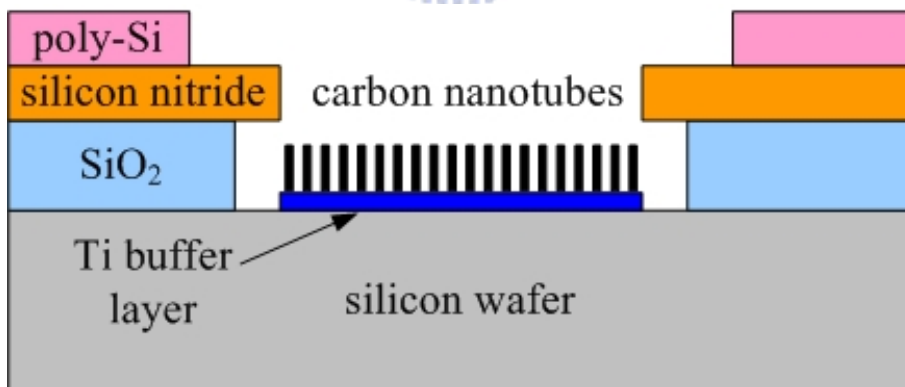
Figure 5.2(c) (cont.)



(a)



(b)



(c)

Figure 5.3 The device structures of the (a) conventional samples, (b) the OPN (oxide-poly-nitride) samples, and (c) the ONP (oxide-nitride-poly) samples

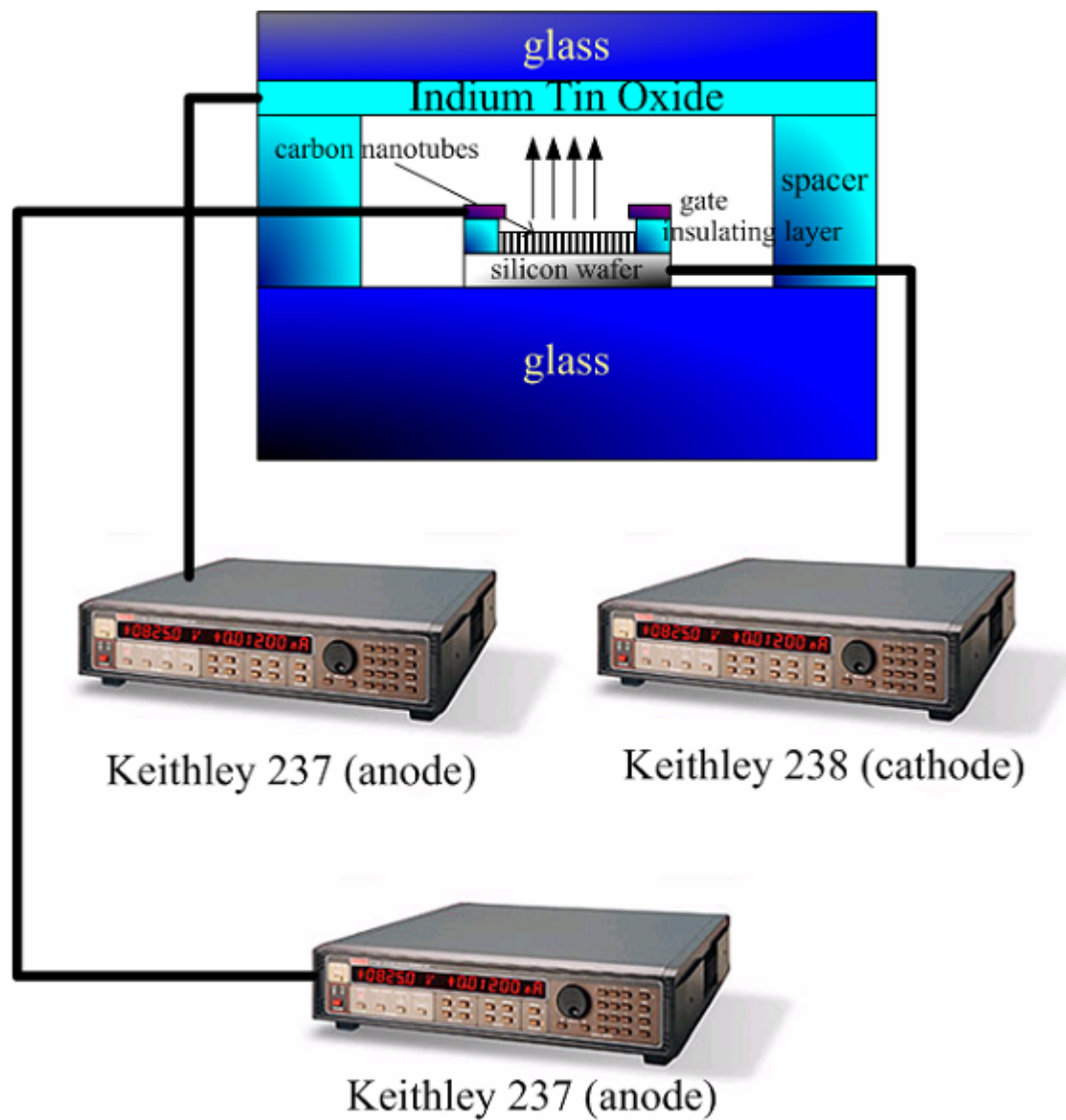
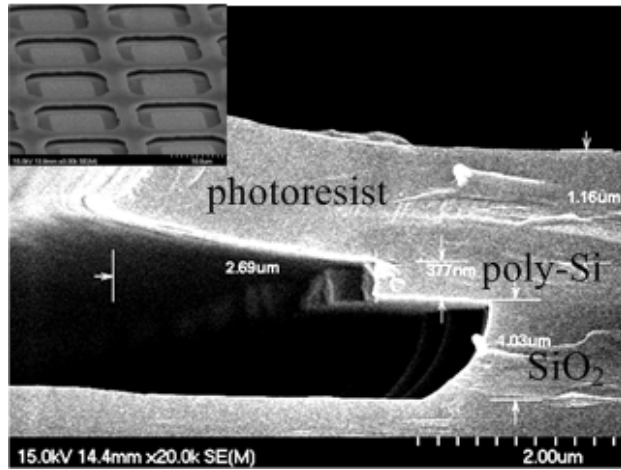
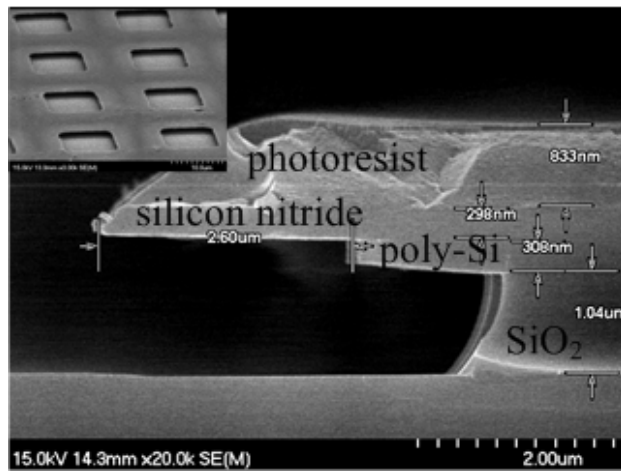


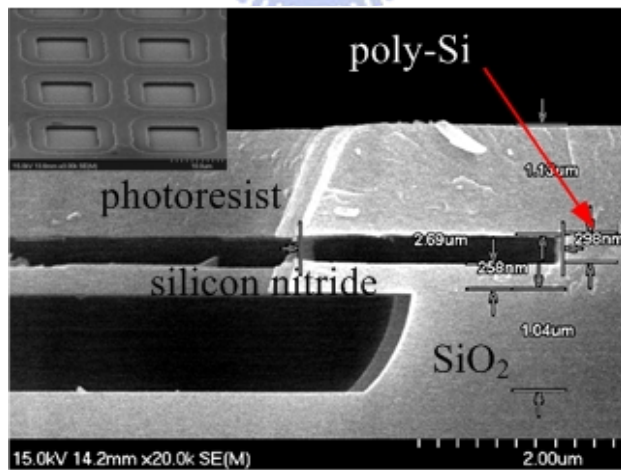
Figure 5.4 The vacuum measurement structure of the triode-type field-emission devices



(a)



(b)



(c)

Figure 5.5 The cross-section views of (a) the conventional samples, (b) the OPN (oxide-poly-nitride) samples, and (c) the ONP (oxide-nitride-poly) samples taken by SEM. The insets were top views with 45° viewing angle for those samples that have undergone the process of CNTs synthesis

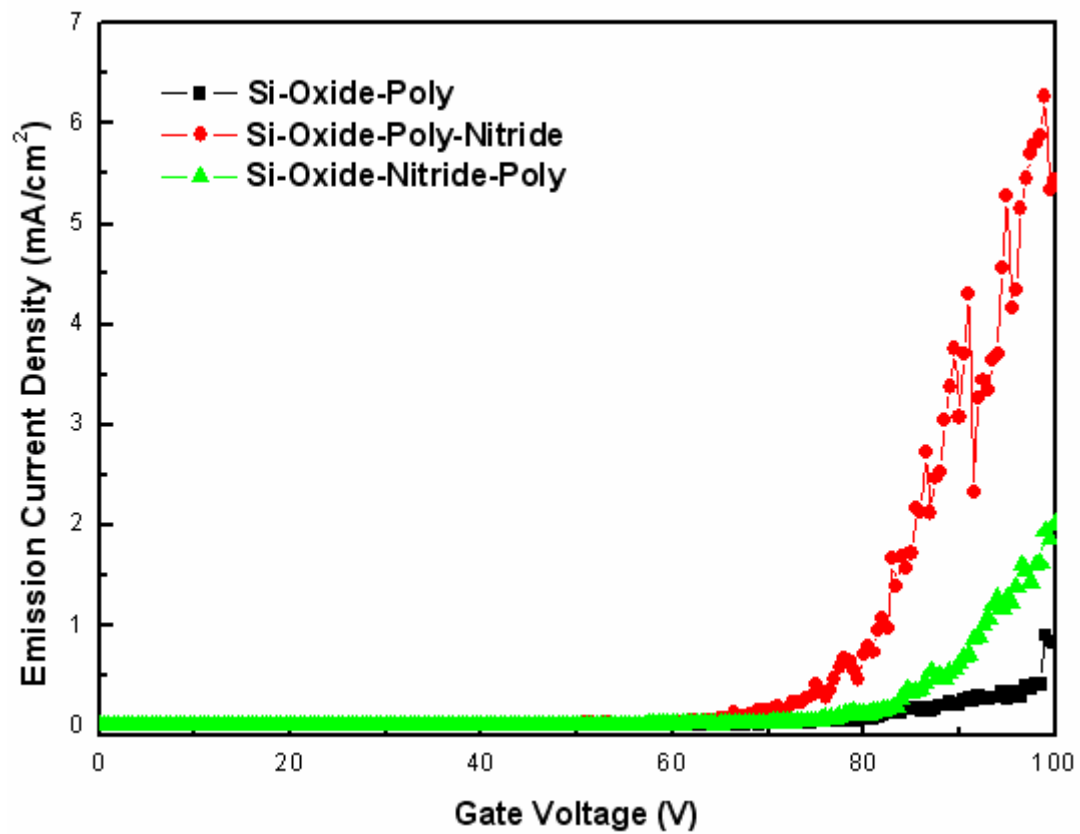
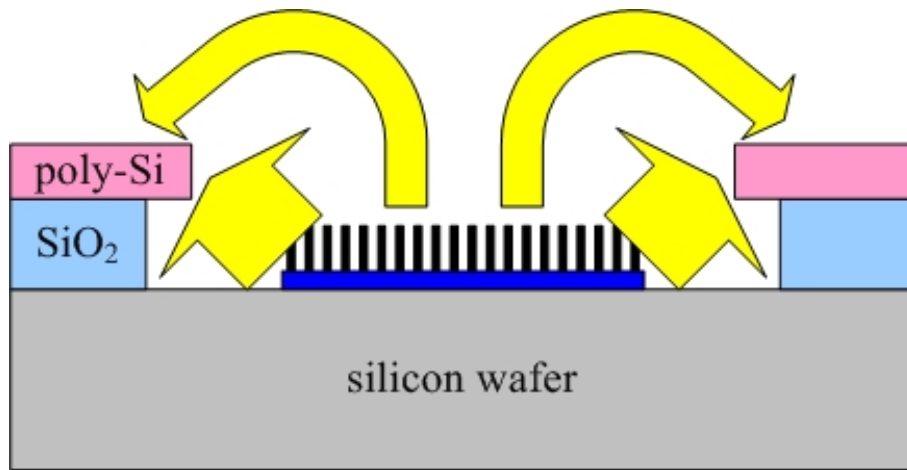
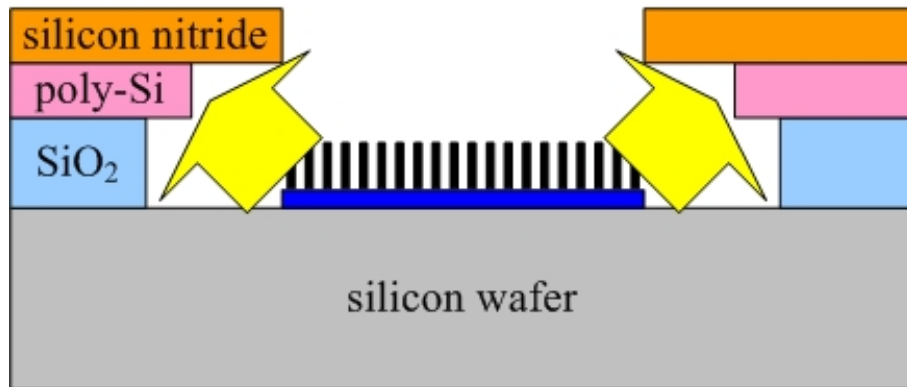


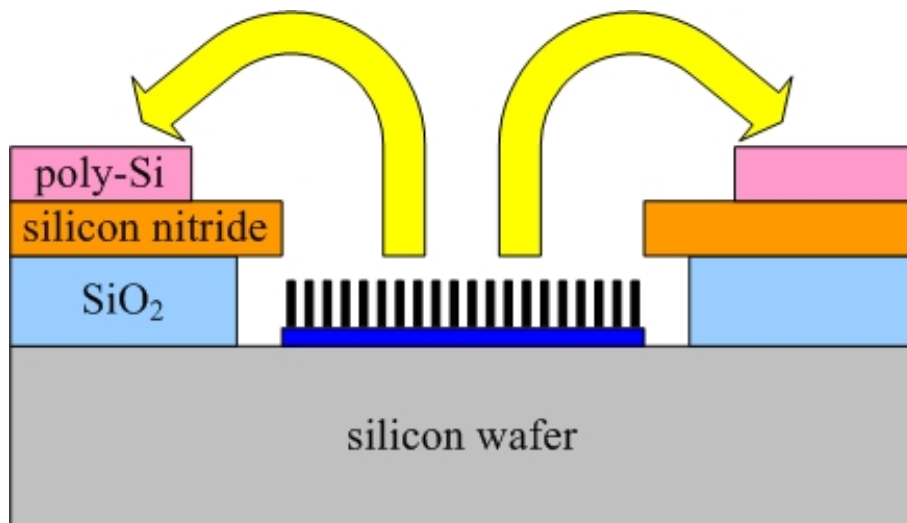
Figure 5.6 The emission current density of anode versus gate voltage for the conventional samples, the OPN samples, and the ONP samples



(a)



(b)



(c)

Figure 5.7 The leakage current paths between gate and cathode in (a) the conventional samples, (b) the OPN samples, and (c) the ONP samples

簡 歷

姓 名：賴瑞霖

性 別：男

出生年月日：民國六十八年十二月十二日

籍 貫：台灣省彰化縣

地 址：彰化縣和美鎮彰新路三段 636 巷 46 弄 94-1 號

學 歷：台灣省彰化高級中學

(84 年 9 月~87 年 6 月)

國立交通大學電子工程系

(87 年 9 月~91 年 6 月)

國立交通大學電子工程研究所碩士班

(91 年 9 月~92 年 6 月)

國立交通大學電子工程研究所博士班

(92 年 9 月~96 年 9 月)

論文題目：藉助催化金屬與元件結構以增進奈米碳管場發射
特性之研究

Study on the Improvements of Field-Emission Characteristics of
the Carbon Nanotubes via Modifying the Catalyst and Device
Structures

Publication Lists

A. International Letter:

- [1] **Rui-Ling Lai**, Jiun-Kai Shiu, Yao-Ren Chang, Kao-Chao Lin, Pei-Chi Chang, Chien-Yin Lee, and Huang-Chung Cheng, "Suppression of Gate Leakage via Adding a Silicon Nitride Layer as an Obstructor of Emission Current," submitted in *Electrochemical Solid-State Letters*.

B. International Journal:

- [1] Chuan-Ping Juan, Kuo-Ji Chen, Chun-Chien Tasi, Kao-Chao Lin, Wei-Kai Hong, Chen-Yu Hsieh, Wen-Pin Wang, **Rui-Ling Lai**, Kuei-Hsien Chen, and Huang-Chung Cheng, "Improved Field-Emission Properties of Carbon Nanotube Field-Emission Arrays by Controlled Density Growth of Carbon Nanotubes," *Jpn. J. Appl. Phys.*, Vol. 44, No. 1A, pp. 365-370, 2005.
- [2] **Rui-Ling Lai**, Jiun-Kai Shiu, Yao-Ran Chang, Kao-Chao Lin, Pei-Chi Chang, Chuan-Ping Juan, Han-Chung Tai, and Huang-Chung Cheng, "Properties of Carbon Nanotubes via a Ti Capping Layer on the Pretreated Catalyst," *J. Electrochem. Soc.*, Vol. 154, pp. J109-J115, 2007. (also be collected in the *Virtual Journal of Nanoscale Science & Technology*)
- [3] Chuan-Ping Juan, Kao-Chao Lin, **Rui-Ling Lai**, Kuo-Ji Chen, and Huang-Chung Cheng, "Field Emission Improvement through Structure of Intermixture of Long and Short Carbon Nanotubes," *Jpn. J. Appl. Phys.*, Vol. 46, No. 2, pp. 859-862, 2007.
- [4] Huang-Chung Cheng, **Rui-Ling Lai**, Yao-Ran Chang, Kao-Chao Lin,

Chuan-Ping Juan, Pei-Chi Chang, Chien-Ying Lee, and Jiun-Kai Shiu, "Improvement of Luminescent Uniformity via Synthesizing the Carbon Nanotubes on a Fe-Ti Co-deposited Catalytic Layer," *Jpn. J. Appl. Phys.*, Vol. 46, No. 2, pp. 863-866, 2007.

[5] Huang-Chung Cheng, Kao-Chao Lin, Han-Chung Tai, Chuan-Ping Juan, **Rui-Ling Lai**, Yaw-Shine Liu, Hsia-Wei Chen, and Yu-Ying Syu, "Growth and Field Emission Characteristics of Carbon Nanotubes Using Co/Cr/Al Multilayer Catalyst," *Jpn. J. Appl. Phys.*, Vol. 46, No. 7A, pp. 4359-4363, 2007.

[6] **Rui-Ling Lai**, Jiun-Kai Shiu, Yao-Ran Chang, Kao-Chao Lin, Pei-Chi Chang, Chuan-Ping Juan, Chien-Ying Lee, Hsia-Wei Chen, and Huang-Chung Cheng, "The Reliability Improvements of Carbon Nanotubes Emitters by Using an Fe-Ti Codeposited Catalyst," *Jpn. J. Appl. Phys.*, Vol. 46, No. 8A, 2007. (accepted)

C. International and Local Conference:

[1] Huang-Chung Cheng, **Rui-Ling Lai**, Ting-Kuo Chang, Chun-Chien Tsai, Jian, and Bo-Ting Chen, "A Novel Germanium Laser Doping Method for Fabrication of High-Mobility Poly-Si_{1-x}Gex TFTs," *15th International Conference on Ion Implantation Technology*, (B305 oral section), 2004.

[2] Chuan-Ping Juan, Chun-Chien Tsai, Kuo-Ji Chen, Chen-Yu Hsieh, Wen-Pin Wang, **Rui-Ling Lai**, and Huang-Chung Cheng, "Controlled Density Growth of Carbon Nanotubes and its Improvements on Field-Emission Properties," the *8th Asian Symposium on Information Display*, 3-126, 2004.

[3] Kao-Chao Lin, **Rui-Ling Lai**, Yao-Ran Chang, Chuan-Ping Juan,

Tsung-Ting Chuang, Jiun-Kai Shiu, Han-Chung Tai, and Huang-Chung Cheng, "Constraining the Direction of Carbon Nanotubes by Oxide Capping Layer," *the 2005 International Conference on Solid State Devices and Materials*, pp. 752-753, 2005.

- [4] **Rui-Ling Lai**, Yao-Ran Chang, Chuan-Ping Juan, Tsung-Ting Chuang, Kao-Chao Lin, Jiun-Kai Shiu, Han-Chung Tai, Kuei-Hsien Chen, Li-Chyong. Chen, and Huang-Chung Cheng, "Improvement of Breakdown Field of Carbon Nanotubes by a Ti-Capping Layer on Catalyst Nanoparticles," *the 2005 International Conference on Solid State Devices and Materials*, pp. 832-833, 2005.
- [5] Jiun-Kai Shiu, **Rui-Ling Lai**, Yao-Ran Chang, Chuan-Ping Juan, Kao-Chao Lin, Tsung-Ting Chuang, Han-Chung Tai, and Huang-Chung Cheng, "Density Control of Carbon Nanotubes by Ti-Fe Co-deposition," *Taiwan Display Conference*, 06-019, 2006.
- [6] Kao-Chao Lin, Tsung-Ying Chuang, Han-Chung Tai, Chuan-Ping Juan, **Rui-Ling Lai**, Yao-Ren Chang, Jiun-Kai Shiu, and Huang-Chung Cheng, "Low Temperature Growth of Carbon Nanotubes by Thermal Chemical Vapor Deposition using Novel Catalyst," *Taiwan Display Conference*, 06-018, 2006.
- [7] Huang-Chung Cheng, **Rui-Ling Lai**, and Kao-Chao Lin, "Carbon Nanotubes-Based Field Emission Displays," *the International Electron Devices and Materials Symposia 2006*, invited talk, 2006.
- [8] Han-Chung Tai, Tsung-Ying Chuang, Chuan-Ping Juan, Yao-Ren Chang, **Rui-Ling Lai**, Kao-Chao Lin, Jiun-Kai Shiu, Wen-Pin Wang and Huang-Chung Cheng, "Relatively Low Temperature Growth of Carbon Nanotubes by Thermal Chemical Vapor Deposition using Novel Catalysts,"

the Material Research Society 2006 Spring Proceedings, Vol. 922E, U7-16, 2006.

- [9] Chuan-Ping Juan, Kao-Chao Lin, Rui-Ling Lai, Jung-Yen Yang, and Huang-Chung Cheng, "Field Emission Improvement from Pillar Array of Aligned Carbon Nanotubes," *the 2006 International Conference on Solid State Devices and Materials*, pp. 722-723 (P-9-4), 2006.
- [10] Hsia-Wei Chen, Kao-Chao Lin, Yaw-Shing Leou, Yu-Ying Hsu, **Rui-Ling Lai**, Pei-Chi Chang, Chien-Ying Lee, Chuan-Ping Juan, and Huang-Chung Cheng, "Study on Carbon Nanotubes Synthesized at Low Temperatures Using Multilayered Catalytic Films," *the International Display Manufacturing Conference 2007*, P2-02, 2007.
- [11] Pei-Chi Chang, **Rui-Ling Lai**, Kao-Chao Lin, Hsia-Wei Chen, Chuan-Ping Juan, Chien-Ying Lee, Yu-Ying Hsu, Chia-Hao Chang, and Huang-Chung Cheng, "Pillar-shaped Carbon Nanotubes by Ti-Fe Codeposition," *the International Display Manufacturing Conference 2007*, P2-03, 2007.

D. Local Journal:

- [1] **賴瑞霖**、林高照、鄭晃忠, "平面顯示器新星-淺談奈米平面顯示器", 零組件雜誌 2003 年四月號
- [2] 林高照、**賴瑞霖**、鄭晃忠, "奈米碳管場發射顯示器元件技術", 電子月刊第十二卷第八期, 2006 年八月號
- [3] **賴瑞霖**、林高照、鄭晃忠, "場發射顯示器應用之奈米碳管技術", 電子資訊第十二卷第二期, 2006 年十二月
- [4] **Rui-Ling Lai**, Kao-Chao Lin, Pei-Chi Chang, Jiun-Kai Shiu, Yao-Ren Chang, Chuan-Ping Juan, Jien-Yin Lee, and Huang-Chung Cheng,

“Improvements of Uniformity and Reliability for the Electron Emission of Carbon Nanotubes in High Vacuum Environment,” 真空科技，2007 年十九卷第四期

E. Others:

[1] 九十六年中華民國真空科技學會年會論文佳作獎

